Abstract

This thesis is concerned with multi-wavelength observations of the prominent southern hemisphere high energy BL Lac object, (HBL), PKS 2155−304.

After a general introduction covering the particulars of Active Galactic Nuclei, the physical processes and models that are believed to play an important role in the observations and ground based $\gamma-$ray astronomy, the results and interpretation of 4 individual multi-wavelength campaigns on PKS 2155−304 are presented. Lead by observations of the High Energy Stereoscopic System (H.E.S.S.), these campaigns include observations with *RXTE*, NTT at ESO, ROTSE, *Spitzer*, JCMT and the NRT.

During all these campaigns, the source appeared to be in a quiescent state, allowing us to probe the jet parameters and emission models for a quiescent HBL for the first time. The models for VHE emission from HBLs have evolved over the last 14 years since Mkn 421 was detected as a VHE emitter. However, the sensitivity of the past generations of VHE telescopes has only been sufficient to observe VHE emission from HBLs during apparent active states. These evolved models are therefore essentially high active state emission models. Since the sensitivity of H.E.S.S. now allows us to detect these objects in a quiescent state, the obvious question is, do the 'active state' models still accurately predict the SED and in particular the VHE emission?

Very High Energy Emission and Multi-wavelength Campaigns of the BL Lac object PKS 2155−304

by

Anthony Murray Brown

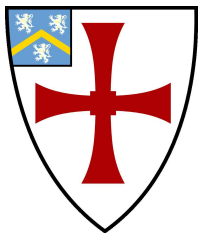

Submitted in conformity with the requirements
for the degree of Doctor of Philosophy

Department of Physics
University of Durham
South Road
Durham. UK.

Contents

Declaration

The material contained within this thesis has not previously been submitted for a degree at the Durham University or any other university. The research reported within this thesis has been conducted by the author unless indicated otherwise.

Copyright Notice

Dedication

I dedicate this to my parents, Sharon and Anthony, and my 10 siblings, Tammarra, Nicholas, Holly, Tenille, Alexander, Jemimah, Brydie, Lucy, Matthias and Thomas. No matter where you all are around the globe, your support, jokes, laughter and words of wisdom have always kept me going. I would not have been able to finish this without the little things you have all taught me through the years.

Acknowledgements

The author would like to acknowledge the help of several parties during the completion of this thesis.

Firstly I would like to thank my two advisors, Dr Paula Chadwick and Dr Lowry McComb, whose advice, letter writing, thesis reading, form filling and general scientific banter was very much appreciated. Thanks for putting up with my crazy ideas.

These thanks also extend to the Durham VHE $\gamma-$ray group in general. Whether it be Christos, Denise, Hugh, Ian, John, Joy, Sam or Steve, thanks for the help. Though I personally think we are even after 3 years of being the butt of the office jokes...

It should be pointed out that these thanks extend to the H.E.S.S. collaboration at large. With a nice bit of kit (the 4 telescopes), it was a great opportunity for me to work with such a great experiment. Nonetheless, thanks to the likes of Anita, Gavin, Guillaume and Berrie for putting up with my Q&As. On the optical front, thanks to Dieter for help with the ROTSE data and Mark for the help with the spectroscopic NTT observations.

Finally thanks to the footie teams, COSMIC and Ustinov. Always time for some footie...

This thesis has been brought to you with the support of PPARC and the University of Durham. The author would like to thank the head of the Department of Physics at the University of Durham, Professor Abram, for the use of the facilities within the department during the completion of this thesis.

Chapter 1

Active Galactic Nuclei

Active Galactic Nuclei, or AGN, is a general term used to describe the existence of extremely energetic phenomena, that cannot be attributed solely to stars, in the central region of some galaxies. First classified by Seyfert in 1943 using high-excitation emission lines in optical spectra, AGN are highly variable, producing vast amounts of energy in a very compact region, usually no greater then 1 cubic parsec. This energy is emitted over a large range of frequencies, from radio right through to VHE γ-rays, with luminosities that can be up to 10^4 times greater then the total luminosity of the host galaxy. In this chapter we give a brief introduction to the AGN family, the different observational characteristics that make up each sub-class of AGN, and the different components of the AGN phenomenon.

1.1 Observational history

While the original AGN classification was based on optical properties, as technology advanced and new observation techniques became available, AGN were classified by new observational characteristics. By the late 1950s, the angular resolution of radio telescopes had advanced to such a stage that the strongest radio sources could be identified with individual optically bright objects. The radio surveys of the late 1950s and 1960s, such as the Parkes survey in the Southern Hemisphere [67, 145, 27] and the third and fourth Cambridge sur-

vey in the Northern Hemisphere [111, 115, 86], offered the AGN community a wealth of information. When the radio surveys were cross correlated with optical surveys, a large number radio sources were found to be spatially coincident with known optical sources; often these sources were galaxies, but occasionally they appeared to be stellar in nature. Photometry of these 'stellar' looking objects revealed they were bluer than normal stars, with optical spectra revealing unrecognisable, strong emission lines.

The next breakthrough in understanding these unusual objects came with the realisation that the strong emission lines from the source 3C 273 were infact the hydrogen Balmer series, at a redshift of z = 0.158, [161]. The large distance to 3C 273 implied an extremely high luminosity. This required physical extremes that, at the time, were not found anywhere else in the universe. Since the physical nature of these extreme sources was unknown, they were named 'quasi-stellar radio sources'. This was subsequently shortened to the term 'quasar'.

It was quickly realised from the results of the photometric study that quasars could be identified by their excessive blue or UV emission. Optical surveys were completed, with the quasar candidates being selected by their blue excess. These surveys were however 'contaminated' by non-AGN sources, such as RR Lyrae stars and white dwarfs. This contamination from non-AGN sources biased the population of AGN to greater values and as such, the original estimation of up to 3 'blue stellar objects' per square degree had to be revised [159]. Nonetheless, there was still a large number of these optically selected objects that were shown to be quasar-like objects. The optically selected quasars were called quasi-stellar objects or QSO's for short.

When the optically selected objects were compared to the radio surveys, it was found that a large percentage of them appeared to be radio quiet. In short, the radio surveys didn't give us a complete census of the population of AGN, with only 10% of AGN being radio-loud [195]. What is more, of those radio loud AGN, over 60% showed no evidence of the strong, broad emission lines that were originally used to identify AGN [128]. Therefore the vast majority of the radio selected AGN would never have been selected by the original optical techniques, with only 10% of optically-selected AGN being 'radio-loud' and

less than 40% of radio-selected AGN being 'optically-loud'.

With the advent of X-ray astronomy, another tool for identifying AGN became available. First used in the early 1970's, when it was realised that a quarter of the high-latitude X-ray sources detected in the *Ariel-V* X-ray survey could be identified with known AGN [144], there are very few, if any, AGN that are not X-ray luminous. Using X-ray luminosities is, therefore, one of the least error prone methods of selecting AGN. It is also one of the most efficient methods of selecting AGN. For example, the *ROSAT* All-Sky Survey team, [87], found three times more AGN than the colour-selected Palomar-Green bright quasar survey [162], for the same patch of sky.

One of the most interesting developments in observational AGN studies came with the discovery of a class of AGN emitting γ-rays in excess of 100 MeV, the first of which was the nearby quasar 3C 273 detected in 1978 with the COS B satellite [177]. However, it was not until 1991, with the launch of the EGRET experiment onboard the Compton Gamma-ray Observatory, that the detection of these energetic extragalactic photons could be confirmed. During its lifetime, EGRET detected $\sim$70 AGN in the 20 MeV to 30 GeV range, all of them variable in nature. It should be noted that all bar one of the AGN sources detected by EGRET are blazars, Flat Spectra Radio Quasars or BL Lac objects; the other is a radio galaxy, Cen A.

AGN were first discovered as VHE sources in 1992 with the detection of photons >300 GeV from the northern hemisphere BL Lac object, Markarian 421, by the Whipple collaboration [148]. With the discovery of VHE emission from another northern hemisphere BL Lac object, Markarian 501 [149], the inclusion of AGN as extra-galactic VHE sources was confirmed. The catalogue of known VHE AGN sources currently stands at 13 (as of August 2006), with all bar one of these sources being high energy peaked BL Lac objects, HBLs, the other being M87, a type I Fanaroff-Riley radio galaxy (see Section 1.3). While M87 is believed to be a mis-aligned BL Lac object [183, 151], it is not clear whether the the VHE emission originates from the jet or the central supermassive black hole. The detection of VHE emission from AGN has opened up an exciting new area of AGN research. With the majority of emission from AGN occuring in the $\gamma-$ray regime, we are now able to compare models

to observations for the entire electromagnetic spectrum, from radio to VHE $\gamma-$rays.

1.2 Current AGN Model

The fundamental question about AGN is how they generate their vast quantities of energy in such a small volume of space. This question was first seriously tackled in the mid 1960's with suggestions of supernovae or matter being accreted onto a black hole as being possible energy sources, [158, 199]. Since these early suggestions, the observations and arguments in favour of the accreting black hole model have become more and more compelling.

Proposed by Urry & Padovani in 1995, the currently accepted model for AGN consists of a central engine of a supermassive black hole ($10^6 - 10^9 M_\odot$) surrounded by an accretion disc which extends out to around 1 pc, [187] (see Figure 1.1). Around the outside of the accretion disc a dusty torus is believed to exist, extending up to 100 pc from the central engine of supermassive black hole (SMBH) and accretion disc [136]. The torus can be used to explain the anisotropic emission of the AGN, with the dust absorbing radiation from the central engine when the AGN is viewed edge-on. In the inner regions of the AGN, above and below the accretion disc, is the Broad Line Region (BLR), so called for the population of dense gas clouds moving at velocities up to 20,000 km/s. Further out is the Narrow Line Region (NLR), in which less dense gas clouds orbit with considerably smaller velocities than the BLR clouds. If the AGN is radio loud, outflows of relativistic particles, in the form of jets, are also believed to be present. These jets extend out kiloparsecs from the central engine, perpendicular to the accretion disc.

1.2.1 Central Engine: Supermassive Black Hole & Accretion disc

All AGN are believed to be powered by the central engine of a SMBH accreting matter from the surrounding accretion disc. While the gravitational potential of the black hole powers the system, it has also been suggested that the spin

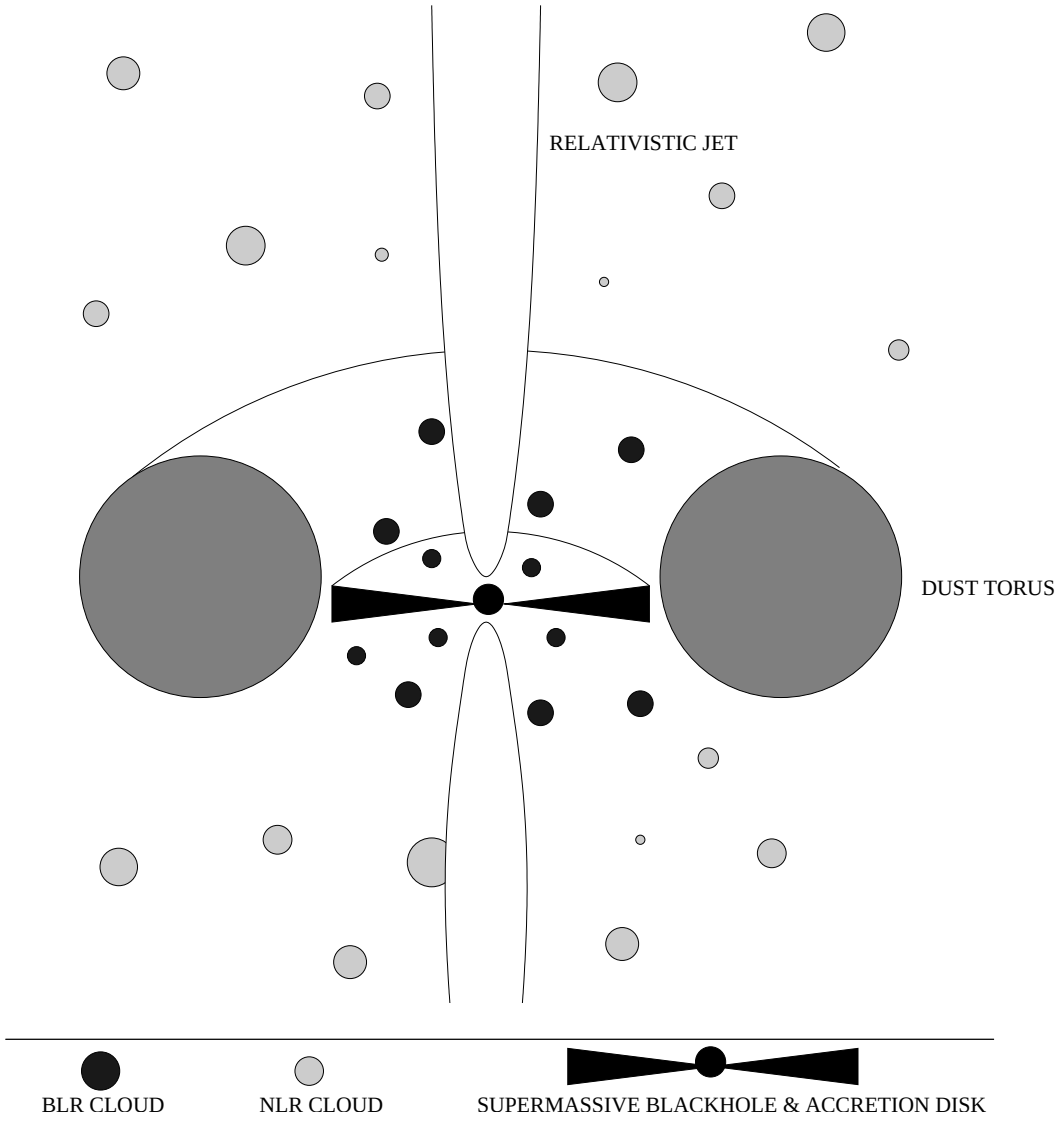

Figure 1.1: Schematic of current model for radio-loud AGN.

of the black hole can affect the system, with radio-loud AGN containing a rotating black hole and a radio-quiet AGN containing a non-rotating black hole. There is, however, no direct evidence for this.

The accretion disc, formed when gas with angular momentum is accreted onto a dense body, is another key ingredient in the current AGN model as it not only continually feeds the SMBH but also serves as a source of the continuum emission needed to maintain ionisation of the BLR and NLR clouds. Applying Kepler's third law to the accretion disc, we see that rather than rotating as a solid body, the inner regions of the disc orbit the black hole faster then the outer parts. This produces a vast amount of friction between gas particles within the disc as the inner regions fly past the outer regions. This friction has two major effects. First, the friction heats up the gas within the accretion disc, causing it to emit thermal radiation at IR/optical/UV wavelengths; the importance of this radiation will be discussed in Section 2.2.2. Secondly, as a result of the energy lost through the friction process, angular momentum will be transported out of the accretion disc system, allowing matter to accrete inwards onto the surface of the SMBH.

The accretion disc may also be a source of material to continually replenish the BLR and NLR. Through the processes of turbulence within the disc, photoionisation, and magnetically driven ejection events, material can be expelled into the BLR region, eventually travelling out to the NLR. This dynamic link between the accretion disc and in particular, the BLR, may have important implications for modelling the emission from blazars.

1.2.2 Relativistic Jets

Suggested in 1974 by Blandford & Rees as a possible method of transporting energy and/or material out to the radio lobes observed in some AGN, the radio emission from radio-loud AGN is believed to be dominated by bipolar outflows in the form of relativistic jets [23]. These relativistic jets cannot be considered in isolation from the accretion disc as they appear to be a natural by-product of it [25, 26].

While no consensus has been reached on the origin of AGN jets, the most

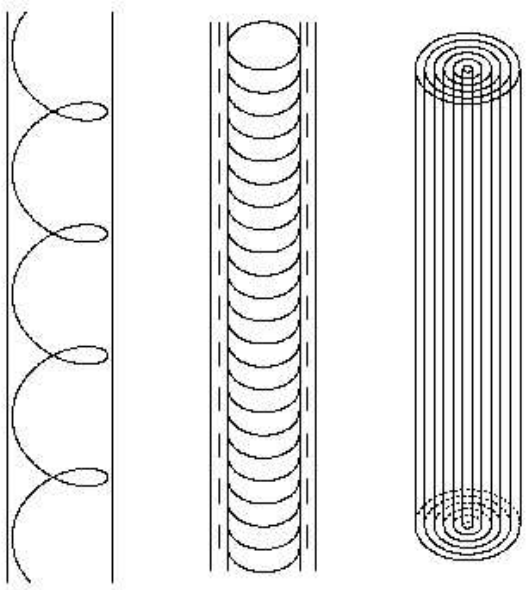

Figure 1.2: Sketches of three possible magnetic field configurations. Left: vector-ordered helix. Middle: perpendicular field spine surrounded by a longtitudinal-field. Right: two dimensional field sheets wrapped around the jet axis. Courtesy of [108].

promising scenario by which an AGN jet is launched and sustained involves the rotation of large-scale magnetic fields within the accretion disc, [171]. However, thereafter, a multitude of questions are raised about the characteristics of these jets. Dynamically, are they dominated by the magnetic fields that support the jets, or by the energy density of the matter being accelerated within the jet? What is more, how are the magnetic fields collimated over the vast parsec to kiloparsec distances of the jet, and what is the configuration of the magnetic field within the jet? Some examples of magnetic field configurations can be seen in Figure 1.2. Since the magnetic fields inhibit the motion of charged particles to along the field lines, the different configurations of the magnetic field seen in Figure 1.2 will impose different types of structure on the plasma in the jet.

While the mechanisms behind the formation of these relativistic jets are still an area of much interest and research, their importance to the overall VHE emission from AGN is clear to see. All bar one of the current known VHE AGN

emitters belonging to the HBL class of blazars, the overall emission from HBLs being dominated by the relativistic jet aligned close to the line of sight.

1.2.3 Gas Clouds

Believed to be classified into two main groups depending upon their relative position in the AGN, the role gas clouds play in the mechanics of the AGN is still an area of much debate. These clouds of dust and gas sit in either the broad line region, within 0.1 parsec of the blackhole, or the narrow line region that extends up to 1 kpc from the blackhole.

The broad line region, BLR, clouds have electron densities up to $N_e \sim 10^9$ cm^{-3} and velocities between 5000 and 30,000 km s^{-1}. The high densities of these BLR clouds allow the cloud to be held together by it's own gravitational force and are inferred from the presence of forbidden emission lines. The BLR clouds give rise to the broad emission lines seen in some AGN. The narrow line region, NLR, clouds move much more slowly, with velocities between 200 and 1000 km s^{-1}. With no forbidden emission lines from these NLR clouds, the electron density of these clouds is believed to be low, $N_e \sim 10^2 - 10^6$ cm^{-3}.

1.2.4 Dusty Torus

Around the central regions of many AGN appears to be an obscuring structure, believed to be composed primarily of dust. This dust is thought to be distributed in the form of a torus [136, 137]. With its inner radius at a distance of around 0.1pc from the central engine, the dusty torus is believed to reprocess some of the UV radiation from the inner parts of the accretion disc into IR radiation, giving rise to the IR bump seen in the spectra of some AGN. More over, as we will see in Section 1.4, a dusty torus helps to explain the anisotropic distribution of observational characteristics of the unified AGN family; a key ingredient in the unification model of AGN proposed by Urry & Padovani.

1.3 AGN Taxonomy

The different observational properties of AGN and the fact that there is no set definition of what observational properties define an AGN, have resulted in a rather muddled and confused taxonomy of AGN, creating a 'zoo' of AGN sub-classes. Since the majority of AGN have not been observed over the full spectral range, it is difficult to classify and group different types of AGN. However, much like the original Hubble diagram for galaxies, we can draw a simple 'family tree' of AGN sub-classes that can give us an insight into how the different types of AGN can be related, (see Figure 1.3).

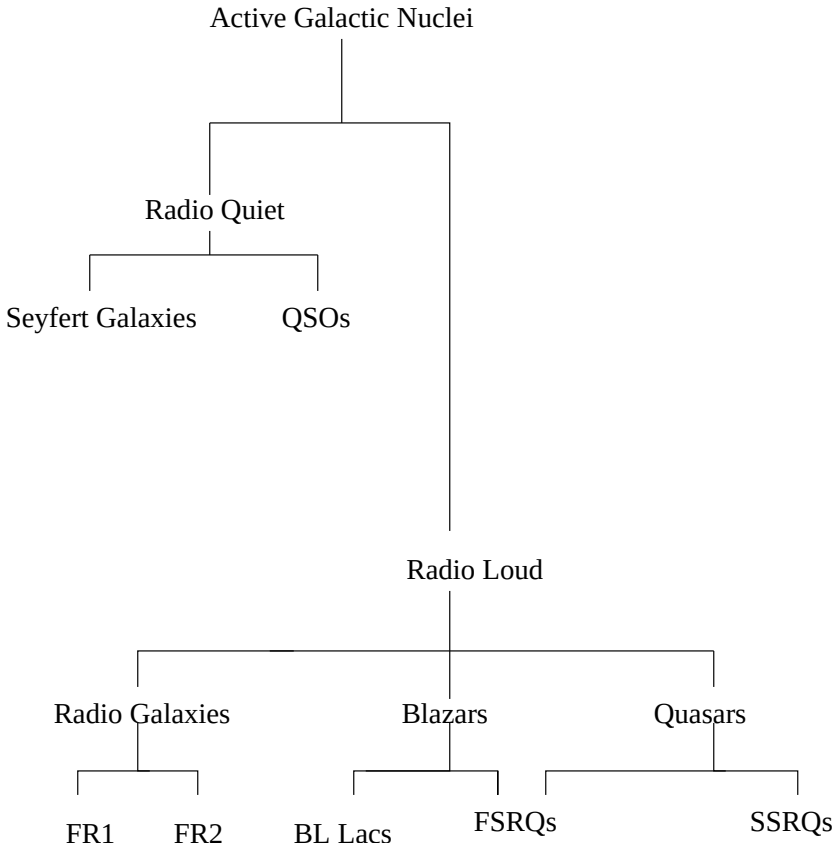

Figure 1.3: Family tree of the different sub-classes of AGN.

1.3.1 Seyfert Galaxies

Seyfert Galaxies are relatively low luminosity, radio quiet AGN. Due to this low luminosity, the host galaxy of the AGN is clearly detectable. Seyfert Galaxies are defined by the presence of strong ionisation emission lines, with the sub-classification of Seyfert galaxies depending upon the type of emission lines present in their spectra.

Seyferts are further classified into two groups: Seyfert 1 and Seyfert 2 Galaxies. Seyfert 1 Galaxies have both broad and narrow emission lines in their spectra, while the spectra of Seyfert 2 Galaxies only contain narrow emission lines. The narrow emission lines are believed to originate from low density ionised gas, travelling at several hundred kilometers per second (NLR clouds). The broad emission lines are believed to originate from high density gas travelling up to 30,000 km per second (BLR clouds).

1.3.2 QSOs

One of the most luminous subclasses of AGN, QSOs have both radio-loud and radio-quiet 'flavours'. Due to their brightness, the host galaxy of the AGN usually appears as a fuzzy blob of diffuse star light. Similiar to Seyfert galaxies in many ways, the observational properties of Seyfert galaxies and radio-quiet QSOs show a lot of overlap. This is obvious when comparing QSO and Seyfert spectra, with both being quite similiar. However, due to the luminous nature of QSOs, the stellar absorption lines of the host galaxy are usually very weak, if present at all. Due to the similarities between radio-quiet QSOs and Seyfert galaxies, the possibility of both being the same phenomenon cannot be ruled out, the difference between the two possibly being accretion rate, with the radio-quiet QSOs having a higher accretion rate then that of the less luminous Seyfert galaxies.

A small percentage ($\sim$10%) of QSOs are radio-loud quasars. Believed to originate from a jet, the radio emission contains a few percent of the total luminosity of quasars. Quasars are further divided into two subclasses, Flat Spectrum Radio Quasars, FSRQ, and the Steep Spectrum Radio Quasars, SSRQ, depending upon the nature of their radio emission. FSRQs have a

flat, compact, radio spectrum, while SSRQs have a more extended, steep radio spectrum. Quantitatively, FSRQs have a radio spectral indices less than 0.5, while SSRQs radio spectral indices is greater than 0.5.

1.3.3 Radio Galaxies

Strong radio sources, often with extended jets, radio galaxies are usually elliptical. Depending upon their radio luminosity and morphology, radio galaxies are subdivided into two groups; Fanaroff-Riley 1 (FR1) and Fanaroff-Riley 2 (FR2) radio galaxies. FR1 galaxies are low luminosity radio galaxies, with the radio brightness peaking in the vicinity of the central source, close to its optical counter part. FR2 galaxies are the high luminosity radio galaxies with the radio emission dominated by the outer lobes of the radio jet. The difference between the two types of radio galaxies can be seen in Figure 1.4 & 1.5.

1.3.4 Blazars

Blazars form a small subset of AGN that seem to exhibit the most extreme characteristics. Of all AGN subclasses, blazars are the brightest, emitting radiation over the full electromagnetic range. They are the most variable and the most polarised of AGN. The extreme nature of blazars is believed to be due to their orientation with respect to the observer, with there being less than 10° between the line of sight and the axis of the relativistic jet. This small angle maximises the observed relativistic effects of the jet. These effects include Doppler shifting of the radiation emitted to higher energies, temporal contraction, such that the variability appears on an even smaller timescale than the intrinsic variability timescale, and Doppler boosting of the energy radiation density. Arguably, these characteristics make blazars the most interesting of AGN groups to observe.

Originally blazars were identified from other AGN by their extreme variability and their featureless optical spectra with weak, or even non-existent, emission and absorption lines. This was originally believed to be due to the dominance of the relativistic jet 'drowning out' any spectral features present. However, there is now a growing belief that the lack of emission/absorption

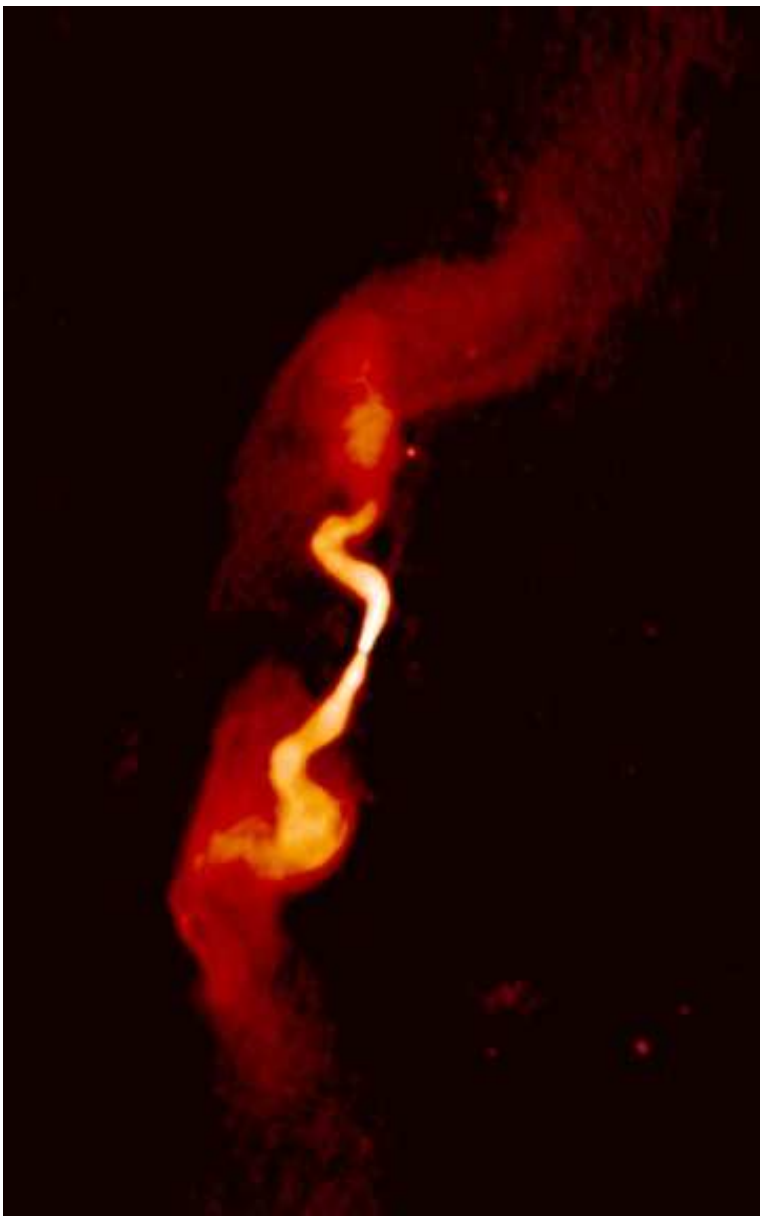

Figure 1.4: Radio image of the FR 1 radio galaxy, 3C 31 (Image courtesy of NRAO/AUI).

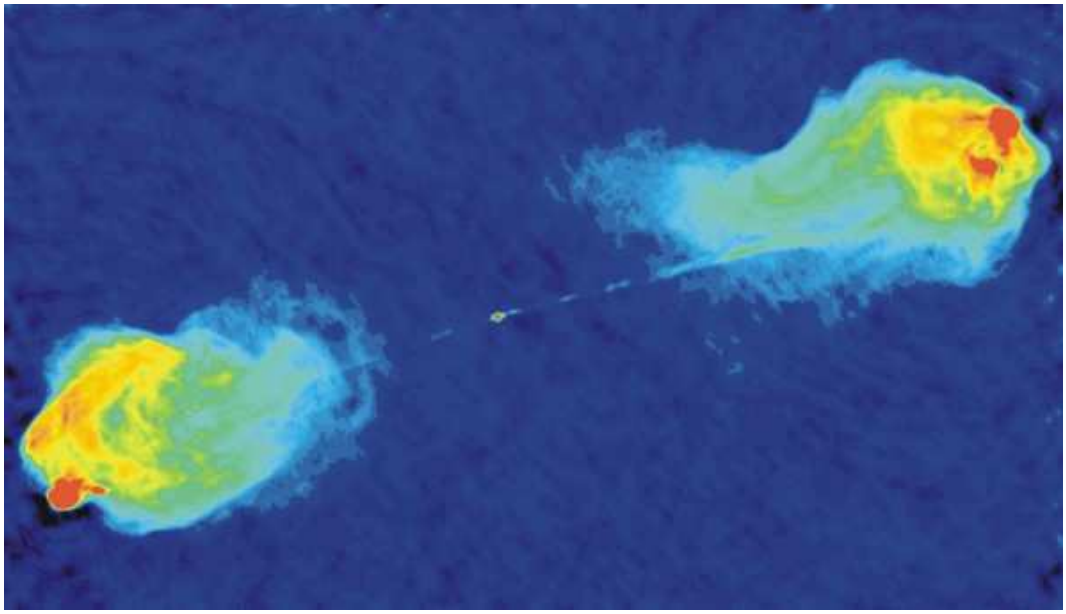

Figure 1.5: Radio image of the FR 2 radio galaxy, Cyg A (Image courtesy of NRAO/AUI).

lines is due to a lack of gas clouds to produce them. This can have profound implications for the unification theory for blazars as we will see in Chapter 9. Due to the featureless nature of blazars' optical spectra, 95% of blazars have been identified through radio and X-ray observations.

Blazars are further classified into 2 main subclasses, FSRQs and BL Lac objects; with BL Lac objects being subclassified further to low energy BL Lac objects (LBLs) and high energy BL Lac objects (HBLs). There is a general trend in observational characteristics of these sources, with FSRQs being brightest and exhibiting spectral features, to HBLs being 'dimmest' and having no detectable spectral features. Quantitatively, the difference between HBLs and LBLs in particular is the ratio of the spectral slope at X-ray energies to the spectral slope at radio energies, α_{RX}. HBLs have a $\alpha_{RX} < 0.75$, while LBLs have a $\alpha_{RX} > 0.75$ [54]. This general trend has lead to a unification theory for blazars, with FSRQs having a high accretion rate and large external photon field and HBLs having a low accretion rate and no significant external photon field [72].

Table 1.1: The 3 main groups of AGN

	Type 2 (narrow line)	Type 1 (broad line)	Type 0 (unusual)
Radio-Loud	NLRG	BLRG FSRQ SSRQ	BL Lac Objects (FSRQ)
Radio-Quiet	Seyfert 2	Seyfert 1 QSO	

1.4 Unified Models

The multitude of free variables in the AGN model means that unification of the different sub-classes of AGN is very difficult. Size of the central black hole, amount of matter in the accretion disc and the accretion rate are just a few of the different parameters of AGN which, when altered, can vary both the observed luminosity and the type of radiation emitted. Not only that, but the high anisotropy of the current AGN model means that the observational characteristics of a given AGN are highly dependent on the orientation of the AGN with respect to the observer. The unification of AGN models is primarily concerned with the latter point

AGN can be divided into 3 broad groups, based upon the orientation at which we observe them (Table 1.1). Since varying the angle of observation changes the amount of either the broad line region or narrow line region we see, or whether we see it at all due to the dust torus, this simple classification is primarily done using optical emission lines. However, as seen in Section 1.1, this can introduce a selection bias, as not all AGN exhibit these optical properties.

Type 2 AGN have narrow emission lines and usually a rather weak continuum. As seen in Figure 1.6, it is believed that Type 2 AGN are AGN that are viewed side on, such that the dusty torus obscures the inner regions of the AGN, the central engine and the BLR, and thus attenuates the radiation from

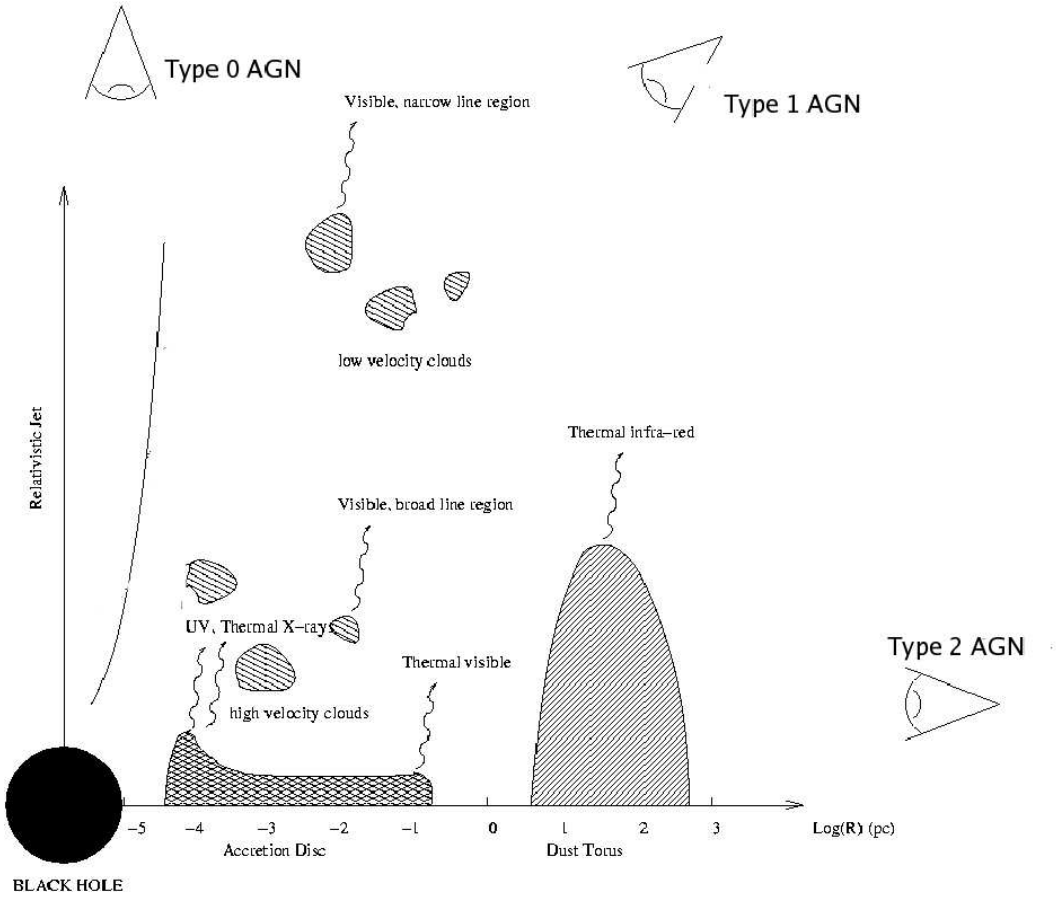

Figure 1.6: Diagram showing the approximate angle of observation for each AGN type. Notice that as the angle between the relativistic jet and the observer decreases, a larger amount of BLR is observed and thus the Broad Line features become easily detected.

the inner regions. Type 2 AGN include Narrow Line Radio Galaxies (NLRG) and Seyfert 2 galaxies.

Type 1 AGN have both strong broad and narrow emission lines as well as a bright continuum. Including Seyfert 1 galaxies, Broad Line Radio Galaxies (BLRG) and Quasars, Type 1 AGN are believed to be viewed closer to the pole of the dust torus than Type 2 AGN, such that the BLR can be viewed without obstruction.

Type 0 AGN are a small subset of AGN that exhibit unusual and extreme characterisitics. Suggested by Urry and Padovani to be AGN observed with the relativistic jet aligned close to the line of sight, blazars are currently the only group of AGN that can be classified as Type 0 AGN. The blazar subgroup consists of both BL Lac objects, which are radio-loud, highly variable and lacking any absorption or emission features, and FSRQ, a subgroup of Type 1 Quasars. FSRQ exhibit the same extreme variability as BL Lac objects, and while more luminous, they also exhibit fairly strong emission and absorption features (Equivalent Width (EW) < 5Å). These slight differences aside, the extreme characteristics of both BL Lac objects and FSRQ are consistent with the continuum emission being due to a population of relativistic particles directed close to the line of sight.

1.5 Observational History of PKS 2155−304

PKS 2155−304 is the archetypal X-ray selected high frequency peaked BL Lac object (see Section 1.2.4). With an elliptical galaxy as a host galaxy, PKS 2155−304 is located in the southern hemisphere, at a redshift of z = 0.117 [30]. With its extreme observational characteristics, typical of HBLs, PKS 2155−304 has been the target of numerous multi-wavelength campaigns (e.g. Smith et al. 1992, Urry et al. 1993, Brinkmann et al. 1994, Courvoisier et al. 1995, Edelson et al. 1995, Pian et al. 1997, Urry et al. 1997 & Aharonian et al. (H.E.S.S. Collaboration) 2005b)[173, 186, 31, 55, 66, 138, 188, 5]. These campaigns have found PKS 2155−304 to be one of the brightest BL Lac objects at optical, UV and X-ray energies [92].

1.5.1 TeV γ-ray Observations

PKS 2155−304 was first detected as a source of VHE gamma rays by the University of Durham VHE γ-ray group, during September/October/November 1996 and October/November 1997, using the Mark 6 telescope. The combined significance of this detection was 6.8σ [43], with a flux above 1.5 TeV of $2.1 \pm 0.2_{sys} \pm 0.5_{stat} \times 10^{-7}$ m^{-2} s^{-1} [14]. The CANGAROO collaboration was however, unable to confirm these findings [153, 132, 129], perhaps not surprisingly, as PKS 2155−304 appeared to have been in a quiescent state during the CANGAROO observations. In fact, the Durham group were unable to detect PKS 2155−304 in 1998 either, due to the source being in an apparent quiescent state.

The original detection with the Mark 6 telescope has, however, subsequently been confirmed by the H.E.S.S. collaboration with a high significance ($> 45\sigma$) [4]. Observations by the H.E.S.S. collaboration have also showed PKS 2155−304 to be a variable source of VHE γ-rays, with variability on timescales as short as an hour.

1.5.2 GeV-MeV γ-ray Observations

PKS 2155−304 was observed with the Energetic Gamma Ray Experiment Telescope (*EGRET*; 30 MeV - 10 GeV), onboard the Compton Gamma Ray Observatory *CGRO* numerous times throughout the early 1990's [190]. These observations were only able to gain upper limits on the flux >100 MeV, until a strong flare during November 1994, when a flux of $2.73 \pm 0.70 \times 10^{-7}$ photons cm^{-2} s^{-1}, with a hard spectral slope of 1.74 ± 0.24, was detected. Other detections with EGRET of PKS 2155−304 in an apparent quiescent state have since proven PKS 2155−304 to be a variable source at MeV-GeV energies, [190].

1.5.3 X-ray Observations

PKS 2155−304 was first identified as an X-ray source by the *HEAO-1* satellite [88, 165]. However, it was first detected at X-ray energies as 'confused'

emission with the *Ariel V* satellite [50]. The angular resolution of the modulated collimator of *HEAO-1* allowed the identification of PKS 2155−304's X-ray emission with its optical counterpart [88].

As one of the brightest BL Lac objects at X-ray energies, PKS 2155−304 has been observed regularly with X-ray observatories since the first X-ray observations in 1978. *Einstein*, *EXOSAT*, *ROSAT*, *BeppoSax*, *RXTE*, *ASCA*, *Chandra*, and *XMM-Newton* have all been used to observe PKS 2155-304 at some stage or another [39, 125, 82, 48, 191, 179]. PKS 2155−304 was even one of the few BL Lac objects to be observed with the short lived Broad-Band X-ray Telescope, *BBXRT*, that was operational for 9 days, 2-11th December 1992, onboard the space shuttle Columbia, (STS-35).

All these X-ray observations have found PKS 2155−304 to be a highly variable X-ray source. The fastest X-ray flare detected was with *ASCA* in 2000, displaying a doubling timescale of 3×10^4 seconds [102]. Likewise Zhang et al. (2002) detected a similiar increase in 5×10^4 seconds [197].

1.5.4 UV Observations

PKS 2155−304 has also been found to be the brightest BL Lac object at UV wavelengths, with the majority of its energy emitted in the hard UV, soft X-ray regime [193]. As such, PKS 2155−304 was the subject of numerous observations with the *International Ultraviolet Explorer* satellite throughout the mid-1990's [188, 138]. These observations discovered significant UV variability at timescales from hours to days, with no strong correlation between flux and spectral slope. However, a strong correlation between the UV, optical and X-ray flux has been detected [66]. This correlation indicates a common origin for the emission in these energy bands.

Observations of PKS 2155−304 with the Extreme Ultraviolet Explorer, *EUV* also show a strong correlation between the flux level of EUV photons and that of X-rays. However, the magnitude of the variability in the EUV flux continuum is marginal compared to that of other wavelengths, such as X-rays [120].

1.5.5 Optical Observations

One of the brightest BL Lac objects in the optical regime, PKS 2155−304 also exhibits a high degree of optical variability. To this end, there have been numerous studies investigating the optical variability of PKS 2155−304 [88, 123, 89, 41, 181, 63]. These campaigns have reported a wide range of variability patterns, with variations of a few percent on the minute length timescale to several hundred percent on timescales of months to years [41, 196]. On the small scale, Carini & Miller and Paltini et al. both report variability timescales as small as 15 minutes, though due to limitations of their detectors they were unable to rule out variability on smaller scales. As we will see in Chapter 9, recent observations by Brown et al. [34] display evidence for significant variability on minute timescales.

These studies have also reported the optical emission of PKS 2155 − 304 to be well described by a power law ($F_\nu \propto \nu^\alpha$), with an spectral index ranging from -0.62 to -0.84. Some of these studies found variations in the spectral index to be correlated with flux, while others didn't. This may be an indication that, in some instances, there is an underlying component to the optical emission from the VLBI core of PKS 2155 − 304 [92].

1.5.6 IR Observations

PKS 2155−304 has been observed in the past with the *IRAS* and *ISO* satellites and recently with the *Spitzer* space telescope [98, 22, 7]. All these observations found the infrared flux to be fairly constant with time, a flux of ∼100 mJy at a wavelength of 100 microns, and there to be negligible contribution to the infrared flux from the elliptical host galaxy.

1.5.7 Radio Observations

While radio observations can be used to pin down the low energy tail of the spectral energy distribution of PKS 2155−304, the strength of radio observations, through the use of very long baseline interferometry (VLBI), are their ability to detect apparent superluminal motion and thus probe the Doppler

factor of the jet. VLBI observations by Piner & Edwards (2004) have found features within the jet of PKS 2155−304 to have an apparent speed of 4.37±2.88c, which implies only a modest Doppler factor ($\sim$ a few) [140].

Chapter 2

Astrophysical Processes and Emission Models of Blazars

In this chapter the astrophysical processes that are believed to play important roles in the non-thermal emission from relativistic jet-dominated AGN, such as BL Lac objects, are described. Some of these processes are directly related to the emission of VHE photons, the inverse Compton process for example, while other processes, such as synchrotron radiation, play a secondary role. This secondary role can involve providing seed photons for Comptonisation up to very high energies. The importance of these 'secondary processes' depends upon the model in which they are invoked. The Synchrotron Self Compton model (SSC), for example, is more dependent on synchrotron seed photons than, say, the external Compton model.

After reviewing the main astrophysical processes, the current favoured models for VHE emission from BL Lac objects will be discussed. These models not only have to predict the VHE emission from these objects, but also their overall broadband spectral energy distribution. Finally the pair production of the VHE radiation off the extragalactic background light (EBL) will briefly be discussed. Travelling over cosmological distances, VHE photons interact with the EBL, annihilating both photons and producing a positron-electron pair. This process attenuates the VHE flux, and therefore must be taken into consideration.

2.1 Astrophysical Processes

2.1.1 Synchrotron Radiation

As a charged particle interacts with a magnetic field, of field strength B, it is continually accelerated as it spirals around the magnetic field lines, and thus emits radiation. If an electron is travelling relativistically or ultra-relativistically along a magnetic field line, with energy $\gamma m_e c^2$, then the radiation produced is called synchrotron radiation. The peak frequency of this synchrotron radiation is given by:

$$\nu_c = \frac{3}{4\pi}\gamma^2 \frac{eB}{m_e c}\sin\phi \tag{2.1}$$

where γ is the local Lorentz factor of the electron, $\beta = \frac{v}{c}$ where v is the velocity of the electron, B is the magnetic field strength, and ϕ is the angle between the velocity vector of the electron and the direction of the magnetic field, often referred to as the pitch angle [113, 157]. The total energy lost by the electron as it emits synchrotron radiation is given by:

$$-\frac{dE}{dt} = \frac{2}{3} r_o^2 c \gamma^2 \beta^2 B^2 \sin^2\phi \tag{2.2}$$

where $r_o = \frac{e^2}{m_e c^2}$ and the other variables are as before. Averaging over an isotropic distribution of the pitch angle, ϕ, such that $p(\phi)d\phi = \frac{1}{2}\sin\phi d\phi$, gives:

$$-\frac{dE}{dt} = \frac{4}{3} c \sigma_T \beta^2 \gamma^2 U_{mag} \tag{2.3}$$

where σ_T is the Thompson cross-section ($\sigma_T = \frac{8\pi r_o^2}{3}$) and $U_{mag} = \frac{B^2}{8\pi}$ and is the energy density of the magnetic field. This synchrotron radiation is emitted in a narrow cone along the velocity vector of the emitting particle and is linearly polarised, see Figure 2.1. The half opening angle of this cone, θ, is inversely related to the Lorentz factor of the emitting particle, $\theta = \frac{1}{\gamma}$. The faster the particle is moving, the smaller the opening angle and the greater the amount of beaming that is applied to the radiation. An interesting point is that the amount of energy emitted by a particle is inversely proportional to the square of the mass of the relativistic particle. Therefore, for the same velocity and

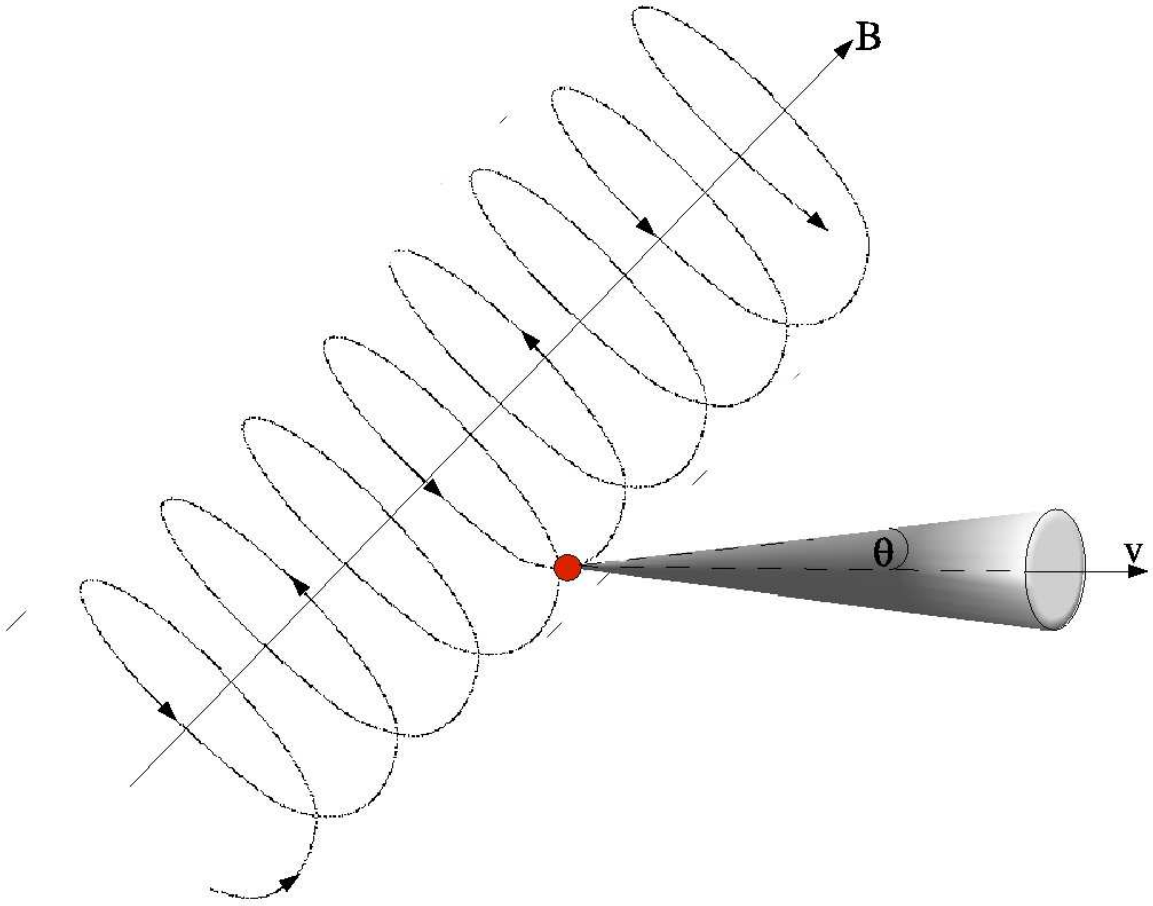

Figure 2.1: Synchrotron radiation emitted by a relativistic particle spirally along a magnetic field, B. This radiation is beamed into a cone along the velocity vector, with a opening half angle of $\theta = \frac{1}{\gamma}$.

magnetic field, an electron produces much more radiation than a proton. Thus in an electrically neutral plasma in a magnetic field, the synchrotron radiation emitted is dominated by the electron population.

It should be noted that with the emission of synchrotron radiation, the electrons are cooled. The cooling time of a relativistic synchrotron-emitting electron is given by:

$$t_{cool} = \frac{\gamma m_e c^2}{P_s} \sim 5 \times 10^8 \frac{1}{\gamma B^2} \tag{2.4}$$

where B is measured in Gauss, and P_s is the total power of the synchrotron radiation ($P_s = -\frac{dE}{dt}$), [122]. Since the cooling time is inversely proportional to the Lorentz factor of the electrons, the most energetic electrons cool most quickly. Likewise, since the total power of the synchrotron radiation is dominated by electrons, with $P_s \propto m^{-2}$, then electrons are cooled quicker than protons when emitting synchrotron radiation.

2.1.2 Inverse Compton Scattering

Electrons can interact with photons and in doing so can either impart energy to the photon or gain energy from it. Compton scattering is the latter and can be seen in Figure 2.2. Inverse Compton, IC, scattering is the former and occurs when a relativistic electron interacts with a low energy photon, imparting some of its energy to it and 'bumping' it to higher energies.

The efficiency of the interaction, i.e. the amount of energy that is transferred from the electron to the photon, depends upon the cross-section of the interaction, which in turn depends upon the energy of the electron. If an electron with velocity βc and Lorentz factor γ interacts with a photon of frequency ν', then in the rest frame of the electron, the photon appears to have a frequency, ν_e of:

$$\nu_e = \nu' \gamma (1 + \beta cos\theta) \tag{2.5}$$

- If $h\nu_e \ll m_e c^2$ then the scattering process occurs in the Thompson regime (see Figure 2.3). IC scattering in the Thompson regime results in photons

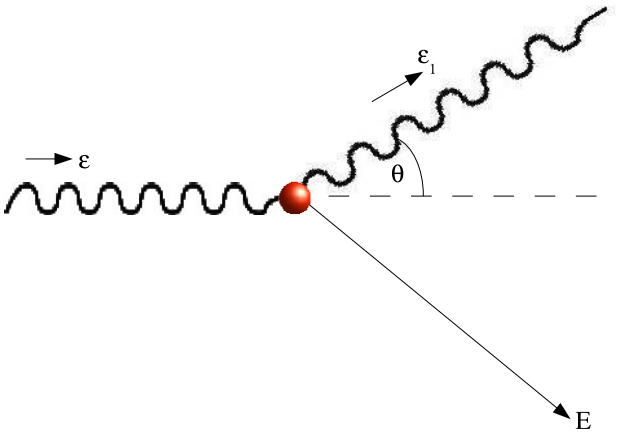

Figure 2.2: Compton scattering of a low energy electron and a photon. During the interaction, the photon imparts some of its energy to the electron.[109]

being scattered isotropically over a wide range of angles and the photon's energy being increased by a factor of γ^2, where γ is the Lorentz factor of the electron that does the upscattering. It should be noted that during these interactions, the energy transferred by the electron to the photon is small compared to the electron's total energy. Thus the same population of relativistic electrons is able undergo multiple IC interactions.

- If $h\nu_e \gg m_e c^2$ then the scattering process occurs in the Klein-Nishina (K-N) regime, (see Figure 2.3). In the K-N regime, the efficiency of the IC process decreases due to the decrease in the interaction cross-section. IC scattering that occurs in the K-N regime is not isotropic and the energy of the photon is only increased by a factor of γ. The energy imparted by the electron during the IC interactions in the K-N regime is a much larger fraction of its total energy and thus the electron usually only undergoes one IC interaction in the K-N regime before it needs to be re-accelerated.

The properties of the IC process in the K-N regime have important implications for the production of VHE photons through IC scattering. Due to the difference in energy increase between IC scattering in the different regimes, an increase by a factor of γ for the K-N regime compared to γ^2 for the Thomp-

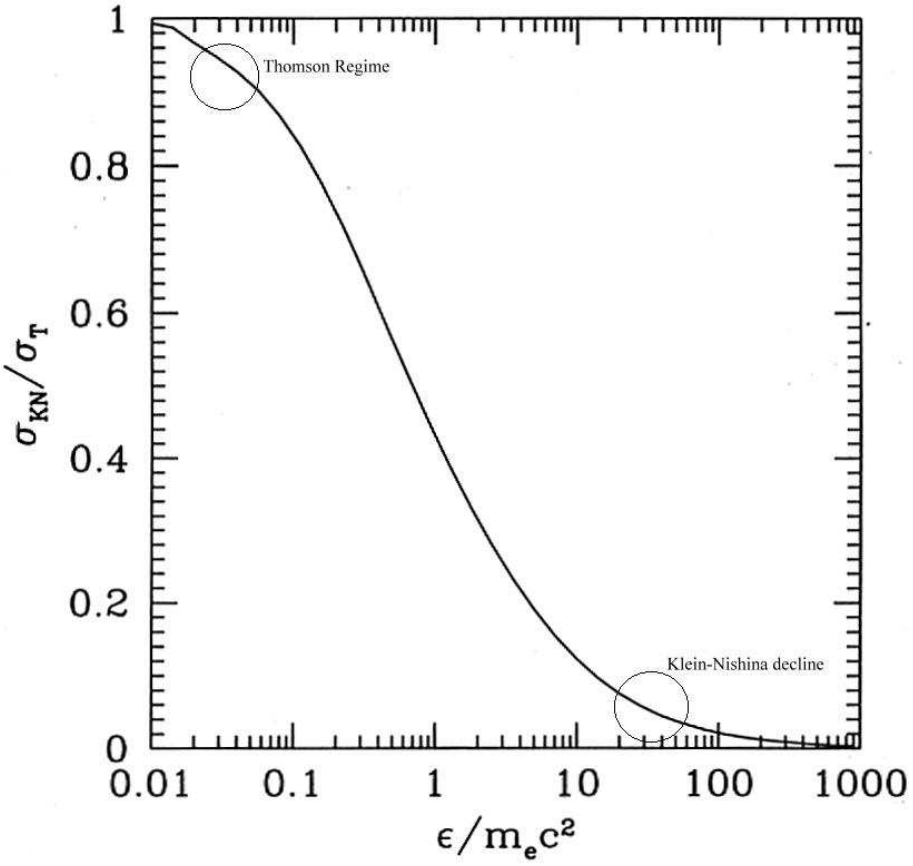

Figure 2.3: The variation of the scattering cross-section as a function of photon energy. [109]

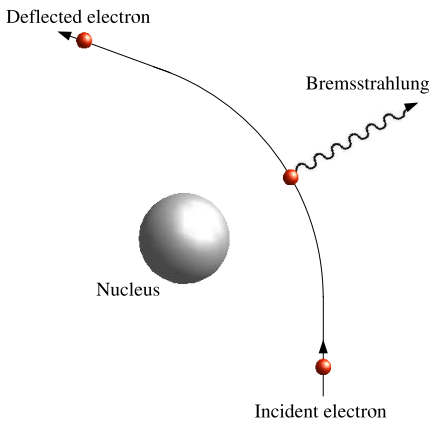

Figure 2.4: Bremsstrahlung produced by the acceleration of an electron in the electrostatic field of an ion or atomic nucleus. [109]

son regime, the majority of the seed photons for IC scattering are limited to infrared and optical energies.

The total energy loss rate of an electron due to the IC process is given by:

$$-\frac{dE}{dt} = \frac{4}{3} c \sigma_T \beta^2 \gamma^2 U_{rad} \tag{2.6}$$

where U_{rad} is the energy density of the radiation field the electron interacts with, (assumed to be isotropic). Comparing the energy loss rate for the IC process, Eq. 2.6, to that of the energy loss rate for the Synchrotron process, Eq. 2.3, we note a surprising similiarity between the two, with the only difference being the energy density of the magnetic field and the energy density of the radiation field. This has implications for the different models which will be described in Section 2.2.

2.1.3 Bremsstrahlung

Bremsstrahlung is produced when a charged particle passes close to an ion or the nucleus of an atom and is accelerated in its electrostatic field, (see Figure 2.4) [112]. An important process to consider when a population of relativistic electrons and dense atomic or molecular material are co-spatial, the spectrum and energies of Bremsstrahlung are of the same order as that of the electron

population that produced them.

An in-depth discussion about Bremsstrahlung can be found in [112]. It should be noted that not only is non-thermal Bremsstrahlung an important process within the AGN [157, 28], but its also important in the production of the Extended Air Showers used to detect VHE photons (see Chapter 3).

2.1.4 Pion Production

With a half life of 10^{-16} seconds, π^0 particles can be produced by interactions between relativistic protons and either other ambient protons, Eq. 2.7, or ambient photons, Eq. 2.8. An example of a proton-proton interaction can be seen in Figure 2.5.

$$p + p \rightarrow \pi^{\pm,0} + 2N \tag{2.7}$$

$$p + \gamma \rightarrow p + \pi^0 \tag{2.8}$$

Invoked in hadronic models, the decay of π^0 results in the emission of 2 γ-rays of energy $\sim$70 MeV in the rest frame, Eq. 2.9.

$$\pi^0 \rightarrow 2\gamma + e^{\pm} pair \tag{2.9}$$

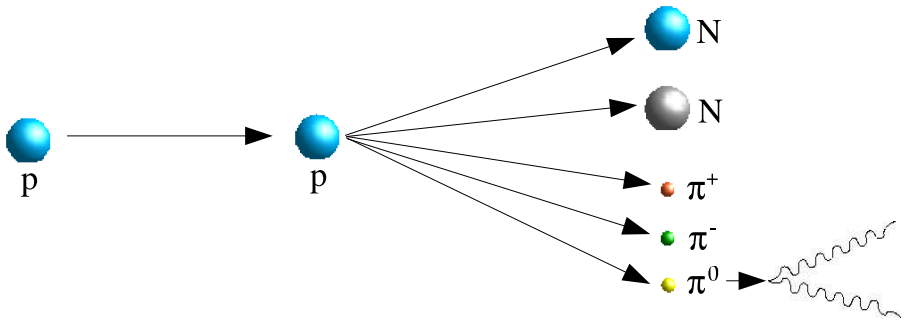

Figure 2.5: An interaction between a relativistic proton and another proton, producing a π^0 which then decays into γ-rays. [109]

It should be noted that for proton-proton interactions, $\pi^{\pm}$ particles are also produced. With a half life of 2.6×10^{-8} seconds, $\pi^{\pm}$ particles decay into muons

and neutrinos. Thus detecting BL Lac objects as sources of neutrinos would indicate an underlying hadronic component to the VHE emission from these sources.

2.1.5 Pair Production

While VHE γ-rays are highly penetrating due to their extreme energy, they can be absorbed through photon-photon interactions, $\gamma\gamma \rightarrow e^+e^-$. First suggested in the mid 60's as a method for attentuating VHE photons [100], photon-photon pair production has implications for VHE emission both locally within the VHE source, and externally over cosmological distances.

When a VHE photon and a low energy photon interact, satisfying Eq. 2.10, they annihilate each other through the pair production process. For a 'head-on' interaction the cross-section of a 1 TeV photon peaks in the infrared regime, $\sim$0.5 eV, while for a 10 MeV photon, it peaks in at 0.5 keV. However, the EBL at keV energies is not dense enough to absorb MeV photons, while the EBL at Near-Infrared (NIR) and Optical (O) energies energies is sufficiently dense to absorb VHE photons.

$$E_{\gamma 1}E_{\gamma 2}(1 - cos\theta) \sim 2(m_e c^2)^2 = 0.52 \text{ MeV}^2 \tag{2.10}$$

Locally, the VHE emission region cannot be too dense at near-infrared and optical energies or else the free mean path of the VHE photons between $\gamma\gamma$ interactions will be smaller than the size of the emission region and thus the VHE photons will be absorbed soon after they are produced. We can use this property to deduce parameters about the emission region (see Chapter 5).

Over cosmological distances VHE emission can also be attentuated quite severely, resulting in a steepening of the spectrum at VHE energies until it cuts off [175]. This also produces, in effect, a VHE horizon within our local Universe, past which no VHE emission can be observed. The distance to this horizon depends upon the density of the EBL at both NIR and O energies.

A point of interest is that, assuming a standard intrinsic spectrum in the VHE regime from BL Lac objects, we are able to use our observed VHE spectra to determine how many VHE photons have been absorbed. This in turn allows

us to probe the strength of the EBL at NIR/O energies, something we have been unable to do directly due to the strength of the Zodiacal light [164, 8].

2.1.6 Acceleration Mechanisms

The cooling time of the relativistic particles within the jet, particularly the electrons, is generally smaller than the dynamical timescale of the jet. This means the the particles must be continuously accelerated along the jet to account for the observed synchrotron emission from blazars. This acceleration can be due to magnetic fields, Fermi acceleration in shock fronts, or electric fields.

Magnetic fields can accelerate charged particles not only as they spiral along the magnetic field, but also through magnetic reconnection events, [91, 110, 143]. Highly probable in the turbulent inner region of the AGN, magnetic reconnection events convert magnetic energy into bulk kinetic energy and heat. Differential rotation in the accretion disc, plasma in the accretion disc corona or twisting of the field lines in the jet itsef can all result in a magnetic reconnection. Irrespective of the method by which the reconnection event occurs, the resulting accelerated particles have a power law distribution, [163, 124].

In the absence of suitable magnetic fields, material can be accelerated by shock waves. First proposed by Fermi in 1949 [70] as the source of cosmic rays, Fermi acceleration is widely used in astrophysics. From the Earth's magnetosphere to supernova remnants, Fermi acceleration has successfully explained the existence of non-thermal electron and ion populations [17].

First-order Fermi acceleration occurs as particles diffuse back and forth across a shock front. As the particles do this, there is a net increase in their kinetic energy. This increase in energy is proportional to the square of the bulk Lorentz factor of the material in the relativistic jet. Fermi acceleration also results in a power law distribution of accelerated particles [18]. It should be pointed out that Fermi acceleration of electrons is much less efficient than that of protons [168]. In the case of AGN, a sudden increase in the rate of accretion or plasma/obstacle interactions (such as BLR clouds entering the jet), can result in a shockwave travelling up along the jet. If this shockwave

is *collisionless*, that is, if energy and momentum transfer between particles along the jet are caused purely by plasma processes, then the Fermi acceleration mechanism can be applied. These plasma processes involve the particles interacting with magnetic fields, which are amplified by the shock front, and undergo scattering and diffusion.

It is also possible that charged particles are accelerated by the induction of strong electric fields. These electric fields can be created by a black hole surrounded by a differentially rotating accretion disc with an embedded perpendicular magnetic field [26, 114, 24].

2.2 Emission models

Models for emission from blazars are different from other AGN because the total emission is dominated by the relativistic jet aligned close to the line of sight. A successful model for the non-thermal emission from blazars should not only reproduce the double humped shape of the broadband spectral energy distribution (SED), but also other characteristics such as the rapid variability observed in the source, especially at high energies, and the time-lag observed between emissions in some energy bands [34, 75, 77]. In this section we will investigate the current models used to predict the multi-wavelength behaviour of BL Lac objects.

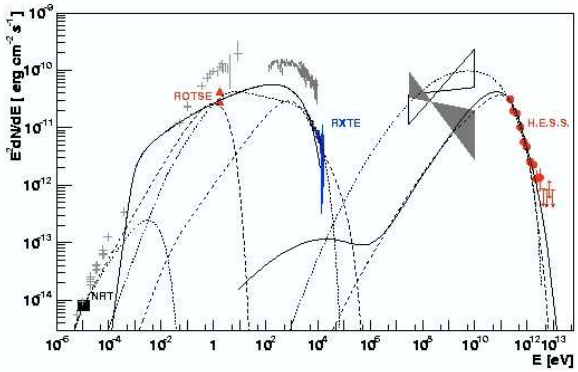

Figure 2.6: An example of the SED of PKS 2155-304, [5]. The double humped structure is clearly visible, with the low energy peak occurring in the UV/soft X-ray region, while the high energy peak occurs just short of the VHE regime.

2.2.1 Synchrotron Self-Compton

While the origins of the Synchrotron Self-Compton (SSC) model were first proposed by Ginzburg & Syrovatskii in 1969 [83], and subsequently incorporated into a relativistic jet scenario [104, 119, 79, 170], the beauty of the SSC model is its simplicity. In the SSC model, the same population of relativistic electrons are responsible for both producing the synchrotron photons, and then upscattering the synchrotron photons to very high energies, thus producing the IC peak.

As the same population of electrons produces both the synchrotron and IC peak, the SSC model makes two simple predictions that can be use to test the validity of the model [101, 118, 78]. These predictions are:

- The continuum of the IC emission should be similiar to the continuum of the seed synchrotron photons.

- Any variation in the flux of the seed synchrotron photons should result in a quasi-simultaneous variation in the flux of the IC emission.

It should also be noted that, since for a given magnetic field strength the synchrotron flux is proportional to the electron number density, $F_{syn} \propto N_e$, and the flux of the IC flux is proportional to the product of the electron number density and synchrotron flux, $F_{IC} \propto N_e F_{syn}$, then the IC flux is proportional to the square of the synchrotron flux, $F_{IC} \propto F_{syn}^2$. So even a small increase in the electron number density, or synchrotron flux, will result in a large increase in the IC flux.

There is evidence both for and against the SSC model. On numerous occasions, a single zone SSC model has been used to successfully describe the emission from the BL Lac objects Mkn 421, Mkn 501 and PKS 2155−304 among others [180, 105, 103]. There is, however, evidence that the SSC model is not always the dominant model for emission from BL Lac objects. During a multi-wavelength campaign on the HBL 1ES 1959+650, Krawcynski et al. detected an 'orphan' γ-ray flare; that is, an increase in the VHE emission was observed, with no associated increase in synchrotron X-ray emission [106]. The

detection of this orphan flare contradicts the second prediction made by the SSC model mentioned above. Other models must therefore also be considered.

2.2.2 External Compton

Similar to the SSC model, the External Compton (EC) mechanism requires a population of relativistic electrons as the primary particle species responsible for the overall broadband SED. This electron population is still responsible for the lower energy synchrotron peak up to X-ray energies, and the higher energy peak is still due to seed photons being IC scattered to higher energies by the relativistic electrons. However, the difference between the SSC and the EC models is the dominant source of seed photons for Comptonisation.

As the name suggests, the seed photons for the EC model originate from sources external to the jet. The source of external photons can include thermal photons from the accretion disc [59, 60], from the accretion disc radiation reprocessed by wind photoionisation of the accretion disc, disc radiation reprocessed by the broad line clouds [169, 61], thermal radiation from the dusty torus [174] or radiation from the jet being reflected by the broad line clouds [80]. There will also be a contribution to the external photon field from the cosmic microwave background (CMB). It should be noted that the energy density, U, of the CMB increases with redshift, such that $U \propto (1+z)^4$ [166].

Figure 2.7 is an example of how the BLR clouds reprocess the accretion disc radiation [169]. Notice that the clouds re-radiate approximately 50% of the incident radiation back into the jet. It should be noted that, just like the second prediction made by the SSC in Section 2.2.1, the EC model predicts a correlation between a rise in the seed photon flux and that of the VHE flux. However, the correlation predicted by the EC model is more complex than that of the SSC model, with a length of the time-lag and strength of the correlation depending upon the dominant source of seed photons. For example, a rise in the BLR flux seen in Figure 2.7, which would be observed as an increase in broad line strength, would be accompanied by a VHE flare with up to a 120 day time lag between the two.

Understanding the origin of the external photons is extremely important

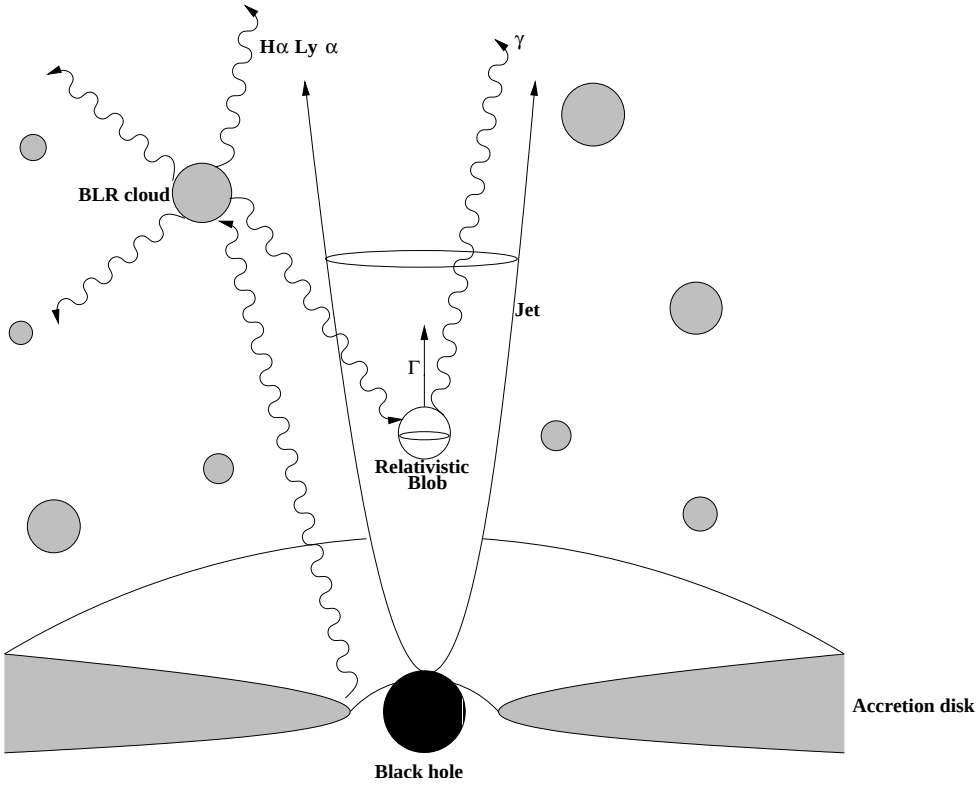

Figure 2.7: Diagram of the inner region of an AGN. The inner part of the accretion disc emits thermal UV/X-ray radiation which is reprocessed by the BLR clouds back towards the jet. The energy of the reprocessed light depends upon the composition and state of the BLR clouds.

due to the relativistic nature of the jet. Upon entering the jet, the radiation is either redshifted or blueshifted, depending upon its direction with respect to the relativistic material responsible for the IC upscattering (see Eq. 2.5). So, for example, hard UV/soft X-ray radiation from the inner accretion disc will be redshifted to lower energies, and in doing so, will go from the K-N regime to the Thompson regime for IC scattering.

An equally important point that must be considered as the external radiation transforms from an external reference frame to one co-moving with the relativistic material within the jet, is the energy density of the radiation field. The energy density of the photon field can be increased or decreased depending upon the angle between the propagation vector of the photon and the propagation vector of the relativistic electron. The change in energy density is given by:

$$U'_{rad} = \gamma^2(1 - \beta cos\theta)^2 U_{rad} \tag{2.11}$$

where U_{rad} is the radiation energy density in reference frame of the jet, U'_{rad} is the radiation energy density in the reference frame of the external radiation and θ is the angle between the propagation of the external radiation and the relativistic material within the jet.

As these two effects, relativistic Doppler shift and relativistic Doppler energy density boosting, are both a function of angle θ, the 'type' of radiation and the radiation energy density of external photons seen by the relativistic material within the jet varies as it travels up the jet. This has important implications for considering whether the EC model is dominant over the SSC model. For example, as the relativistic material, or 'blob', travels up the jet, a smaller and smaller percentage of the BLR clouds are located ahead of it. Therefore, if the dominant source of seed photons for the EC model is radiation reflected by the BLR clouds, then the contribution of the EC model to the overall VHE emission would steadily decrease, and the SSC model may become dominant.

It should be noted that not only does the external photon field seen by material within the jet change as a result of the material travelling up along the jet, but the intrinsic external photon field itself changes due to the anisotropic

distribution of matter within the BLR. A rather messy environment, the BLR is believed to contain dust, gas photoionised off the surface of the accretion disc and over-densities of gas in the form of the BLR clouds. The distribution of this matter is anisotropic with, for example, the accretion disc photoionised wind having its maximum densities at angles greater than 60° with respect to the jet [146, 147]. Therefore the majority of radiation reprocessed by the accretion disc wind will be 'behind' the relativistic blob and thus will be redshifted in the reference frame of the relativistic material.

2.2.3 SSC versus EC

While there is no doubt that both the SSC and EC models are occuring simultaneously within the jet, to determine which model best describes the overall emission from BL Lac objects we need to determine which is the dominant source of seed photons. As mentioned in Section 2.1.2, the energy lost by an electron during synchrotron emission and an IC interaction are remarkably similiar. The energy lost during these interactions is in fact the total power of the radiation emitted during the interactions [112, 113]. Therefore, for a given relativistic jet at any given moment in time, we can determine what is the dominant mechanism simply by considering the ratio of the energy density of the magnetic field and the energy density of the external radiation field, $\frac{U_{mag}}{U_{rad}}$. For the SSC model to be dominant over the EC model, the energy density of the magnetic field must be greater than the energy density of the external radiation field measured in the co-moving frame of the relativistic material, not forgetting the increase in photon energy density due to Eq. 2.11.

2.2.4 Hadronic based models

While a correlation between X-ray and VHE emission would support the dominance of the leptonic SSC model, as described in Section 2.2.1, it doesn't necessarily rule out other possibilities such as hadronic models. In such models the VHE emission is associated with a population of relativistic protons. These relativistic protons can emit VHE $\gamma-$rays through interactions with the magnetic field (synchrotron radiation) [1], or through interactions with

ambient matter or soft photons [127, 168, 116, 117, 20, 57, 18, 141].

Proton Synchrotron Model

The theory of synchrotron emission described in Section 2.1.1 can also be applied to a population of relativistic protons in a magnetic field, with a certain amount of re-scaling associated with the different mass of the proton. For example, the Larmor frequency, $\nu_L = \frac{eB}{2\pi m_e c}$, is re-scaled by the ratio of the proton's mass to that of the electron, $m_p/m_e \approx 1836$ [1]. This re-scaling factor follows through the other parameters of synchrotron emission, such as the energy loss rate and the characteristic frequency of the synchrotron radiation. The energy loss rate of a synchrotron-emitting proton is decreased by a factor of $(m_p/m_e)^4 \approx 10^{13}$ [1]. Thus the cooling time for a proton is much longer than for an electron and any hadronic model used to describe the overall emission from BL Lac objects does not need to consider re-acceleration of the particle population nearly as much as the leptonic models.

In fact, the difference in cooling times is the critical factor when considering synchrotron radiation from protons. The maximum energy a particle can achieve is limited by the point at which the energy loss associated with synchrotron emission is equal to the energy imparted to it through whatever acceleration mechanism. Since the energy lost rate is 10^{13} times greater for electrons, they reach this limiting point, where loss=gain, a lot sooner than protons and hence have a smaller maximum energy compared to the proton population. Therefore, while the critical frequency of the synchrotron radiation for the proton population is $\approx 6 \times 10^9$ smaller, when compared to the electrons, the maximum energy of the proton population is much greater and hence, synchrotron radiation from protons is possible.

Invoking a hadronic synchrotron model does pose a few problems, namely the extreme energy the protons need to reach and the strength of the magnetic field needed for the protons to gyrate around. The proton synchrotron model implies magnetic field strengths greater than 1 Gauss, yet multi-wavelength studies of BL Lac objects have shown the magnetic field from the VHE emitting region to be of the order of 0.1-0.3 Gauss, [81, 178]. Likewise, the energy of the proton has to be extremely high, $E \geq 10^{19}$ eV. This extremely large energy can,

however, be over come by invoking some of the many acceleration mechanisms described in Section 2.1.6.

Proton-Proton Interactions

The proton−proton mechanism for VHE emission, through the process of π^o decay as described by Eq. 2.7, can only realistically be dominant in a 'relativistic jet meets gas target' scenario [126, 1]. Work by Aharonian showed that for a reasonably accelerated proton beam, with power $L_p \leq 10^{45}$ erg s^{-1}, the 'target' gas density needs to exceed 10^6 cm^{-3} [1]. This can only really be achieved during gas cloud−jet interactions. Numerous models invoke gas cloud−jet interactions as the source of VHE flaring, with some models explaining high and low activity states as changes in the density of the target gas cloud [57, 20, 18, 19, 130].

The obvious gas cloud targets are the BLR and NLR clouds described in Section 1.2.3. The BLR cloud is the more favourable of the two due to its higher density and because the BLR clouds are in the inner regions of the AGN, so the protons have not had time to cool significantly and are therefore believed to be at their most energetic. While the origins of the BLR cloud−jet model stem from work by Burbidge (1956) and Felten (1968), the implications for proton−proton interactions and subsequent VHE emission have only seriously been considered recently by Dar & Laor and Beall & Bednarek, [38, 69, 57, 18].

Another gas cloud−jet interaction model was proposed by Bednarek & Protheroe, in which the gas cloud target consists of stars [20]. While the presence of the stars in the jet will increase the likelihood of proton−proton interactions, it is in fact the shock wave caused between the stellar wind and the jet plasma that is responsible for the VHE emission. The shock front accelerates electrons from the jet and the star to extremely high energies, through first-order Fermi acceleration. These energetic electrons, collimated by the downstream magnetic field of the shock front, interact with the stellar radiation field through the IC process to emit VHE photons. Thus this model is in fact a leptonic model invoked during a hadronic based gas cloud−jet interaction rather than a true hadronic model.

Proton Initiated Cascade Model

Proposed by Mannheim & Biermann in 1992, the Proton Initiated Cascade Model (PIC) has the interaction of extremely energetic protons with ambient soft photons as the origin for the γ-ray emission [116], as described by Eq. 2.8. One of the key assumptions of the PIC model is the extremely high energy of the protons, $E \geq 10^{19}$ eV. This assumption is due to the fact that, as the energy of the incident proton increases, the efficienty of the PIC model increases as well [1]. During the proton−photon interaction, the extremely energetic proton is cooled. Thus, while the synchrotron cooling times for protons are much greater than that of electrons, we also need to consider proton−photon cooling as well.

It should be noted that the 'reprocessed' proton secondaries of this interaction can then interact with other soft photons, provided that they have sufficient energy. Thus the PIC contribution from a population of relativistic protons can be quite appreciable, without any drastic need for re-acceleration of the protons.

The PIC model also associates the lower energy synchrotron peak with a population of relativistic electrons. During the proton−photon interaction, apart from γ-rays and reprocessed protons, $e^{\pm}$ pairs are also produced. These leptons can then be accelerated to emit synchrotron radiation.

Chapter 3

VHE $\gamma-$ray Astronomy

Arguably $\gamma-$ray astronomy began with the balloon experiments of Goeckel and Hess during the early twentieth century [85, 93]. Using simple particle detectors, these experiments found that the Earth was being continually bombarded with high energy radiation. The strength of this radiation was found to increase with altitude and thus believed to be cosmic in origin. The radiation was consequently dubbed 'cosmic rays'.

Today we know that cosmic rays are composed primarily of protons (90%), with the remainder being predominantly alpha particles and heavier nuclei. While the extra-terrestrial origin of cosmic rays is clear, we are currently unable to conclusively associate their emission with known astronomical objects. This is primarily due to the cosmic rays interacting with interstellar magnetic fields and losing information about their place of origin. However, $\gamma-$rays are not 'bent' by magnetic fields and thus travel straight from their point of origin. Since $\gamma-$rays are believed to be produced in the same location as the cosmic rays, $\gamma-$ray astronomy allows us to associate possible astronomical sources with cosmic ray emission.

In general, $\gamma-$ray astronomy allows us to probe the most extreme environments within the Universe, environments that we are unable to reproduce on Earth. In this chapter VHE $\gamma-$ray astronomy, the physics of Cherenkov radiation and the techniques that are used by the H.E.S.S. telescope array will be reviewed.

3.1 Cherenkov Radiation

Akin to the sonic boom of an aircraft travelling faster than the speed of sound, Cherenkov radiation occurs when a charged particle travels through a dielectric medium at a velocity greater than the phase velocity of light in that medium. As the charged particle travels through the atmosphere, localised polarisation occurs. This localised polarisation is due to the charged particle disturbing the neutrality of the air molecules it passes by. If the charged particle is travelling with a velocity that is less than the speed of light in the medium in which it is travelling, then the polarisation is symmetric, as can be seen in the left panel of Figure 3.1, and there is no net electromagnetic field.

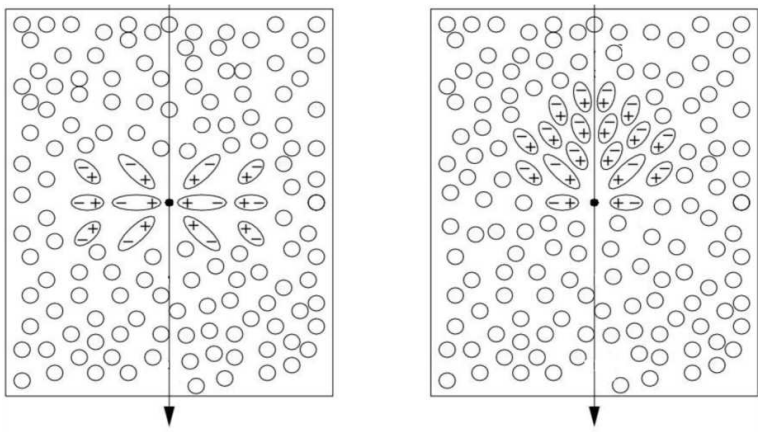

Figure 3.1: The effects a charged particle has on the surrounding air molecules as it travels with velocity less than (left) and greater than (right) the speed of light in the medium in which its travelling [109].

However, if the charged particle is travelling faster than the phase velocity of light in the medium, the electromagnetic field of the charged particle propagates more slowly than the particle itself, resulting in an asymmetric polarisation of the air molecules around the charged particle and a net electromagnetic field, see right hand panel of Figure 3.1. This electromagnetic field results in the emission of Cherenkov radiation, emitted at an angle θ with respect to the direction of motion. Travelling through the atmosphere, the individual Cherenkov wavefronts constructively interfere to produce the observed Cherenkov light cone, see Figure 3.2.

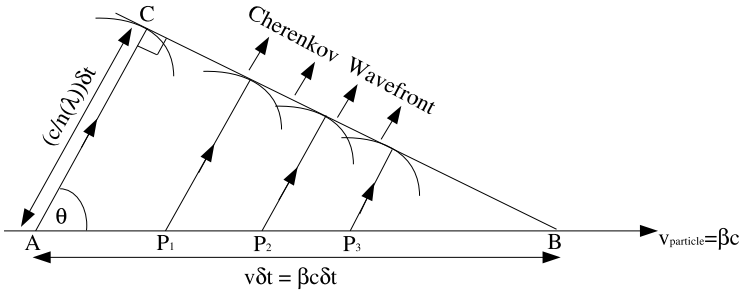

Figure 3.2: A charged particle travelling with velocity βc, moving through a medium with refractive index $n > 1$, emits individual Cherenkov wavefronts at points P_1, P_2 and P_3. These wavefronts constructively interfere to produce the observed Cherenkov radiation cone, with opening angle θ [109].

The opening angle of the Cherenkov radiation light cone, θ, often referred to as the Cherenkov angle, is given by:

$$\cos\theta = \frac{1}{\beta n} \tag{3.1}$$

where βc is the velocity of the charged particle and n is the refractive index of the medium through which the charged particle is travelling. From Eq. 3.1 we can deduce the following characteristics about Cherenkov radiation:

- For a given medium of refractive index n, there is a threshold velocity below which no Cherenkov radiation is emitted. This threshold velocity is given by $\beta_{min} = \frac{1}{n}$.
- For an ultra-relativistic particle, ($\beta \sim 1$), in a medium of refractive index n, there is a maximum Cherenkov angle, given by $\cos\,\theta_{max} = \frac{1}{n}$.
- Cherenkov radiation can only be produced at frequencies for which $n > 1$. For media such as the atmosphere, the refractive index is greater than 1 only for frequencies smaller than that of UV radiation. Thus Cherenkov radiation in the form of X-rays and $\gamma-$rays does not occur in our atmosphere.

It should be noted that work by Frank and Tamm [74] showed that the

number of Cherenkov photons produced, between wavelengths λ_1 and λ_2, from a charged particle moving along length l, is given by:

$$N = 2\pi l(\frac{1}{\lambda_1} - \frac{1}{\lambda_2})\sin^2\theta \tag{3.2}$$

Since the number of photons produced is inversely proportional to the wavelength, Cherenkov photons of shorter wavelength are preferentially produced. Therefore, considering that the Earth's atmosphere is only able to emit Cherenkov radiation at energies less than X-ray energies, Cherenkov radiation produced in the Earth's atmosphere peaks in the UV/blue region of the electromagnetic spectrum.

3.2 Extensive Air Showers

When a high energy ($>$ 10 GeV) photon or nucleon interacts with the atmosphere, it can initiate a cascade, or avalanche, of sub-atomic particles. Referred to as Extensive Air Showers (EAS), it is the sub-atomic particles in these EAS that emit Cherenkov radiation. Upon reaching the ground, the Cherenkov light pool from the shower can extend over a large area (up to 10^5 m^2). Placing a Cherenkov telescope in this light pool gives the telescope a large effective detection area. While both $\gamma-$rays and hadronic cosmic rays can initiate EAS, there are differences between the two types of showers that allow us to discriminate between them.

3.2.1 $\gamma-$ray-induced EAS

Upon encountering the Earth's atmosphere, a VHE $\gamma-$ray can interact with the Coulomb field of an atmospheric atom, X, to produce an $e^{\pm}$ pair.

$$\gamma + X \longrightarrow X + e^{\pm} \tag{3.3}$$

The electrons and positrons produced in Eq. 3.3 then emit further high energy photons through the process of Bremstrahlung, Eq. 3.4.

$$e^- + X \longrightarrow e^- + X + \gamma \tag{3.4}$$

If energetic enough, these high energy photons can in turn produce an $e^{\pm}$ pair as described in Eq. 3.3. The shower continues down through the atmosphere in this fashion until the Bremstrahlung photons aren't energetic enough to pair produce, $\sim$1 MeV. Note however, that 84 MeV is the critical energy at which the loss of energy by electrons becomes dominated by ionisation; below this energy progessively fewer Bremstrahlung photons are produced. Figure 3.3 shows the cascade of sub-atomic particles in a $\gamma-$ray-induced EAS. Each successive 'radiation length' sees the electrons and positrons undergoing both Coulomb-induced pair-production and Bremsstrahlung. As can be seen in Figure 3.3, a $\gamma-$ray induced EAS is a well ordered, 'clean' shower, with the overall direction of propagation of the EAS the same as that of the primary $\gamma-$ray. This 'clean' characteristic of $\gamma-$ray-induced EAS allows us to discriminate between $\gamma-$ray and hadronic cosmic ray induced showers.

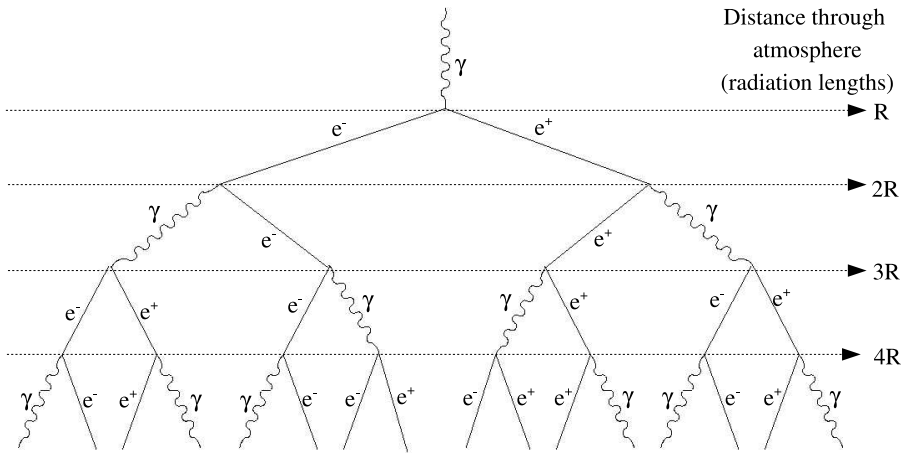

Figure 3.3: A $\gamma-$ray induced EAS. Composed of only two processes, a $\gamma-$ray induced EAS has a well ordered pattern, with the overall direction of propagation of the EAS being in the same direction as that of the primary $\gamma-$ray [109].

3.2.2 Hadron-induced EAS

Hadronically-induced EAS are more complex, involving many more physical processes. The initial hadronic interaction involves atmospheric nuclei, producing pion triplets and other high energy nucleons, see Eq. 3.5 & Eq. 3.6.

$$p + p \longrightarrow \begin{cases} p + n + \pi^+ \\ p + p + \pi^o \end{cases} \tag{3.5}$$

$$n + p \longrightarrow \begin{cases} n + n + \pi^+ \\ n + p + \pi^o \\ p + p + \pi^- \end{cases} \tag{3.6}$$

The pion triplets possess a large amount of transverse momentum, with further transverse movement being imparted to the hadron-induced EAS when the pion triplets decay, as described in Eq. 3.7-3.9. With this large amount of transverse, or lateral, momentum, hadron-induced EAS don't possess the characteristic of the overall direction of propagation of the EAS being the same as that of the primary hadron.

$$\pi^o \longrightarrow \gamma + \gamma \tag{3.7}$$

$$\pi^{\pm} \longrightarrow \mu^{\pm} + \bar{\nu}_{\mu} \tag{3.8}$$

$$\mu^{\pm} \longrightarrow e^{\pm} + \bar{\nu}_e + \nu_{\mu} \tag{3.9}$$

It should be noted that the secondary $e^{\pm}$ pair produced during the pion and muon decay processes, quickly attentuate due to ionisation loses. The low energy $\mu^{\pm}$ are able to decay into $e^{\pm}$ pairs and neutrinos. The high energy $\mu^{\pm}$ are able to penetrate to ground level before they decay, producing localised muon rings in the detectors of the telescope. The majority of the Cherenkov radiation from hadron-induced EAS is produced by the photons produced in Eq. 3.7; these photons producing a 'soft' component to the hadron-induced EAS in a fashion similiar to the γ-ray induced EAS. As seen in Figure 3.4, besides the soft electromagnetic component that is present in both $\gamma-$ray and hadron induced EAS, hadron induced showers also contain a hard component

due to nucleons and mesons. In a stereoscopic system, the localised muon rings, associated with the hard component of the hadron induced shower would only trigger one telescope and thus can be used to discriminate between hadron and $\gamma-$rays induced EAS.

The tranverse momentum of the hadron-induced EAS results in a rather 'messy' Cherenkov image, with no well defined shape and pointing in a direction that isn't necessarily towards the source. The Cherenkov images of γ-ray induced EAS are well defined, with the shape being well constrainted by an oval, pointing in the general direction of the γ-ray source. The difference in shape and orientation of the two Cherenkov images can also be used to discriminate between the two.

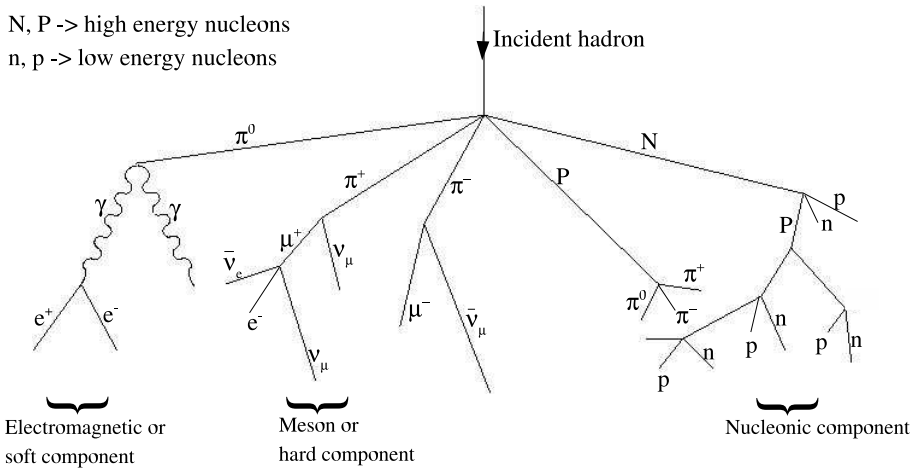

Figure 3.4: A hadron-induced EAS. With more physical processes occurring than in a $\gamma-$ray-induced EAS, the development of the hadron induced EAS is much more disorganised, containing more lateral movement, with an additional hard meson and nucleonic component [109].

3.3 Ground Based $\gamma-$ray Astronomy

The origin of modern day Cherenkov telescopes lies in the work of Galbraith and Jelley during the 1950s [76]. Using a dustbin, an army surplus search light mirror and a single photomultiplier tube, Galbraith and Jelley we able to detect flashes of Cherenkov radiation from the night sky.

Table 3.1: Summary of characteristics of other ground based VHE telescopes.

	VERITAS	CANGAROO	MAGIC
location	Arizona, USA	Woomera, Aus.	La Palma
altitude (m)	$\sim$ 2300	$\sim$ 160	$\sim$ 2000
diameter (m)	4×12	4×10	1×17
	$\sim$ Oct 2006		
F.O.V.	3.5°	4.0°	3.75°
Energy threshold	50 GeV	100 GeV	30 GeV

The first generation of ground based Cherenkov telescopes began with an array of 12 small detectors in the Crimea. Operated by the Lebedev Institute, observations with the Crimean array were unable to detect any evidence of VHE $\gamma-$ray emission above the background noise of cosmic rays. However, other first generation VHE telescopes, such as the University of Durham 'Mark' series and the Haleakala telescope, were able to claim detection of variable sources such as Cygnus X-3 [42, 152]. Unfortunately, due to the variable nature of these sources, and the poor sensitivity of the first generation VHE telescopes, these detections were not able to be simultaneously confirmed by multiple VHE groups.

In fact, even with other major ground based VHE telescopes coming online, such as 10 m Whipple telescope, it took the VHE community until 1989 to confirm the Crab Nebula as a VHE emitter [194]. Indeed, pioneering the imaging atmospheric Cherenkov technique, the detection of the Crab by the Whipple collaboration saw the beginning of a new era for ground based VHE $\gamma-$ray astronomy, an era that is now being eclipsed by the next generation of ground based VHE telescopes. The detection of the Crab as a constant, bright VHE source allowed the VHE community a source that it could calibrate existing and new telescope arrays against.

The next generation of ground based VHE telescopes is dominated by the 'big four' of H.E.S.S., CANGAROO, VERITAS and MAGIC. These telescopes exhibit greatly improved sensitivity and a lower energy threshold compared to previous generations [90]. A few points of interest for the latter three arrays

are summarised in Table 3.1.

It should be noted that the energy threshold quoted in Table 3.1 is the detection energy threshold. The imaging energy threshold is usually higher. For example, while the detection energy threshold of MAGIC is ∼30 GeV, a conservative cut is placed on this limit and MAGIC papers usually quote fluxes and spectra above ∼ 100 GeV. The performance of some past, present and future $\gamma-$ray experiments can be seen in Figure 3.5.

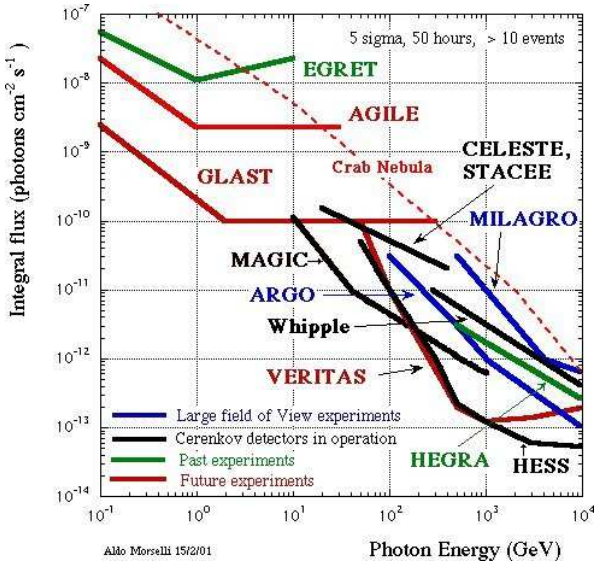

Figure 3.5: Energy flux sensitivities of a sample of past, present and future $\gamma-$ray experiments [109].

3.4 H.E.S.S.

Completed in December 2003, H.E.S.S. Phase 1 is an array of four 13m (flat to flat) imaging atmospheric Cherenkov telescopes. Located in the Khomas Highlands of Namibia (latitude 23°16′18″ south, longtitude 16°30′00″ east), at an altitude of 1800 metres above sea level, H.E.S.S. is situated in an area of excellent astronomical quality [9]. The four identical telescopes of Phase 1 are placed in a square formation, with side lengths of 120 m. This distance is optimised for maximum sensitivity at the 100 GeV energy threshold. Indeed,

the observing energy range of a stereoscopic system such as H.E.S.S., depends upon the distance between telescopes, the field of view of the telescope's camera and the energy of the EAS [156]. Tuning these parameters allows us to tune the energy range in which the telescope array observes [156].

3.4.1 Telescope Structure

The four identical Phase 1 telescopes are of steel construction, with altitude/azimuth mounts. Mounted on a 15 m diameter circular rail, the telescopes are able to track an object from 0.0° to 89.9° zenith angle, with a slew rate of 100° per minute around the circular rail. A schematic of the telescope is shown in Figure 3.6.

The dish stucture is a Davies-Cotton design, in a hexagonal arrangement [9, 58]. The Davies-Cotton design, with individual mirrors, allows us to take advantage of the excellent off-axis properties of the spherical dish and the excellent timing properties of the parabolic dish.

3.4.2 Mirrors

Composed of 382 individual round mirrors, each 60 cm in diameter, the total mirror surface area of each telescope is 107 m^2. With a focal length of 15 ± 0.25 m and reflectivity in the optical range of 80-90%, the single mirrors are made of low expansion glass that has been ground to a spherical profile, and coated with aluminium and quartz, the latter for protection against weathering.

Each individual mirror is mounted on the dish structure via two alignment motors. Using a bright star in the field of view, these allow fine adjustment to the position of each mirror, the uncertainty being minimised when the 382 single bright star images from the 382 individual mirrors form one single image, as shown in Figure 3.7. For a full description of the mirror alignment, see [53].

3.4.3 Camera

Weighing close to 1 metric tonne, each H.E.S.S. camera consists of 960 Photomultiplier tubes (PMT). PMTs are the detector of choice in ground based

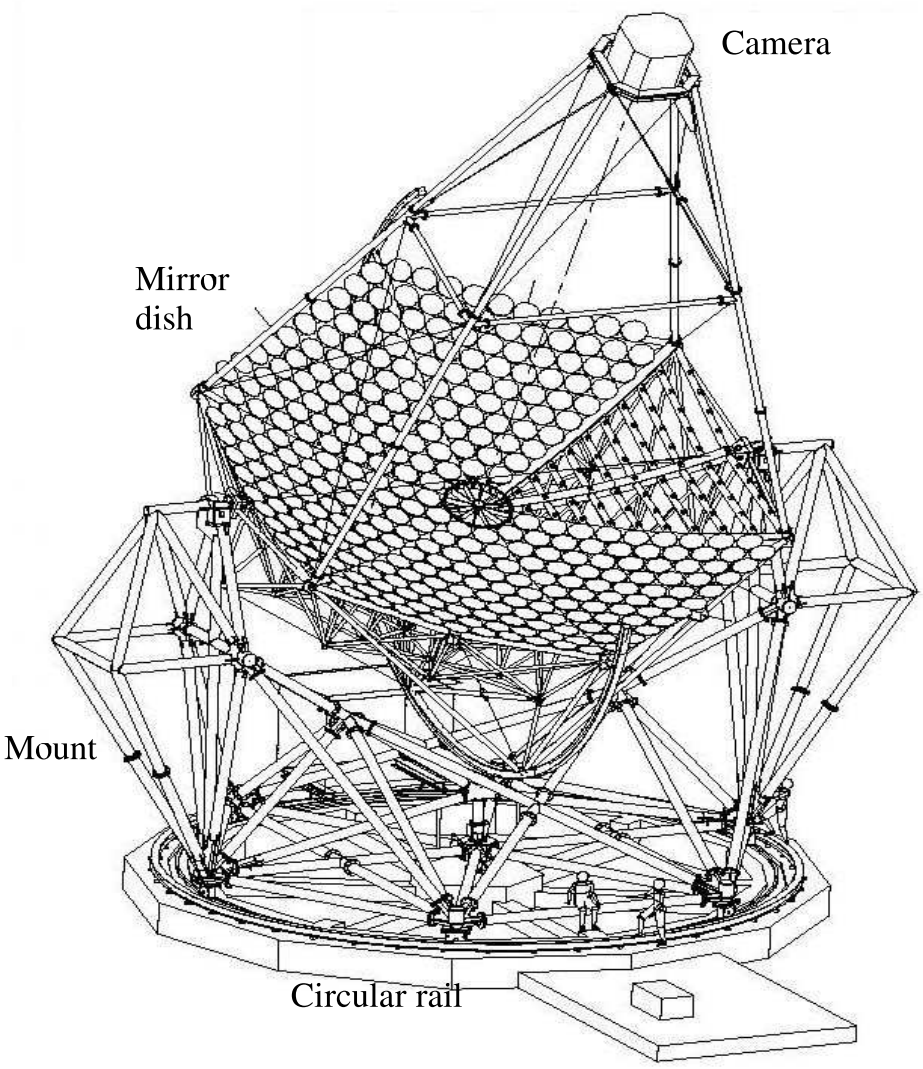

Figure 3.6: Schematic of a H.E.S.S. telescope.

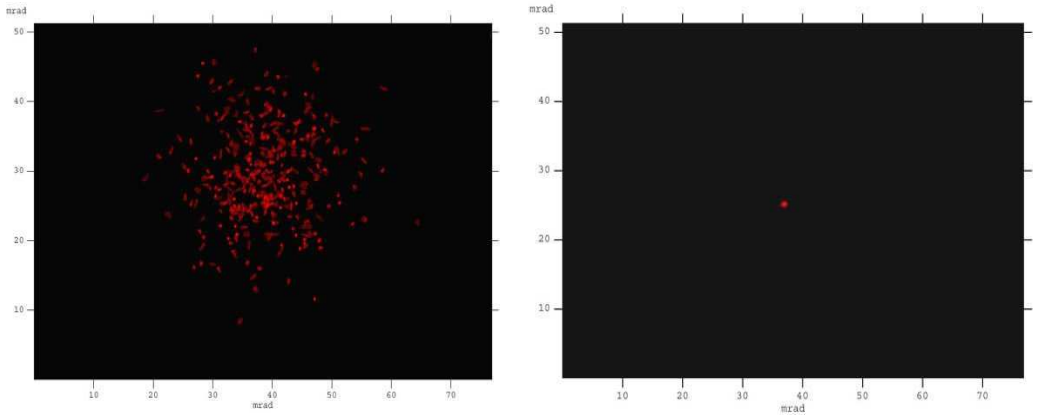

Figure 3.7: Image of bright star before (left) and after (right) mirror alignment.

VHE astronomy due to their rapid response time and their small dead-time. The rapid response time is needed to catch the faint, few nanosecond pulses of Cherenkov light. Each PMT has an angular extent of 0.16°, giving the camera a total field of view of 5°. Each PMT is also fronted by a Winston cone designed to re-direct light that would have otherwise fallen between the PMTs into them, as well as minimising the amount of background light entering the PMTs.

The PMTs are grouped into 60 'drawers'. Each draw consists of 16 PMTs, two acquisition cards (each card reading 8 PMTs) and a control or interface card. Each PMT has 3 channels, one trigger channel and two acquisition channels of different gains. The High Gain (HG) channel is used to detect signal charges up to 200 photo-electrons, and the Low Gain (LG) channel is used to detect signal charges over the broader range of 15 to 1,600 photo-electrons. For a detailed description of the camera see [3].

The system trigger for the recording of the signal from the H.E.S.S. cameras consists of 3 steps. These are as follows:

- A single PMT must detect at least 4 photo-electrons in a time interval of 1.5 ns.
- 3 PMTs from a sector must be triggered by the above criteria.
- When taking stereoscopic observations, two telescopes must trigger using

the above two criteria within a time interval of 80 ns.

A more in-depth description of the H.E.S.S. trigger system can be found in [3, 73].

3.5 Systematic Uncertainties

Since the atmosphere is a principal component of the Imaging Atmospheric Cherenkov (IAC) technique, it is necessary to understand the relationship between the energy of the initial VHE $\gamma-$ray and the Cherenkov signal recorded by the cameras. While Monte Carlo simulations can be used to accurately predict the amount of Cherenkov light detected by the cameras for a given VHE $\gamma-$ray energy, experimentally speaking, there are still a number of uncertainties in the IAC technique. The three main uncertainties are as follows:

- The optical response of the overall instrument. This includes the mirrors, Winston cones and shadowing of the telescope structure. This response degrades over timescales of years, due to, for example, the ageing of the mirrors due to weathering. The optical response of the telescope can be measured by studying the Cherenkov light from muons that travel close to the individual telescopes.

- The response of the cameras. Not only is the quantum efficiency of the individual PMTs known to deteriorate over time, but over shorter timescales the gain of each PMT is known to vary strongly, due to variations in voltage within the camera. An LED system is used to measure these relative variations and thus we are able to correct for them to a certain extent.

- Attenuation of the Cherenkov light as it travels through the atmosphere. The atmosphere is the largest and least understood component of the overall IAC technique. Variations in the dust content, pressure, humidity and temperature can all effect the amount of Cherenkov light attenuation as it travels through the atmosphere. For example, the absorption of Cherenkov light due to clouds and dust particles directly results in

a reduction of Cherenkov light recorded by the cameras, and hence a reduced telescope trigger rate. An array of atmospheric monitoring devices has been employed locally at the H.E.S.S. site by the University of Durham to better understand this effect [15, 36, 37].

These uncertainties must be taken into consideration, particularly the uncertainty in the atmosphere. Variations in the atmospheric conditions can lead to rapid variations in the response of the H.E.S.S. telescope array. Likewise, variations in the gain of the PMTs due to voltage fluctuations can mimic VHE $\gamma-$ray variations and must be taken into consideration, as will be discussed in Section 3.6.1.

3.6 H.E.S.S. Data Analysis

The H.E.S.S. data used within this thesis were analysed using the most up-to-date standard H.E.S.S. analysis software, which is largely provided by the Max-Planck-Institut für Kernphysik, Heidelberg, Germany. It should be noted that continual improvements are being made to the atmospheric models and look-up tables used by this software. This improvements can result in slight differences in the calculated flux level between runs reduced with different versions of the analysis software.

The H.E.S.S. observation runs used within this thesis are all 28 minutes in length, taken in stereoscopic *wobble* mode. Replacing the ON/OFF technique, *wobble* mode involves taking observations with the target offset from the centre of the field of view by some small amount. This allows us to simultaneously observe the source and estimate the background using different regions of the field of view, thus allowing us to double the amount of time available for on-source observations. The amount of offset used in the observations used here is predominantly $\pm 0.5^{\circ}$ in declination, with a small sample wobbled $\pm 0.577^{\circ}$ in right ascension. (The wobble in RA is given by the wobble in declination divided by the cosine of the declination of the target). The sign of the offset is alternated in successive observing runs to reduce the systematic effects of the technique.

3.6.1 Data quality control

The first step of the H.E.S.S. data reduction process is to produce a list of accepted observing runs of the intended target. To this end, we impose severe cuts on the parameters affected by the uncertainties described in Section 3.5. By not considering observations that have been made in less than perfect conditions, it is possible to remove the majority of the systematic uncertainty of the IAC technique. The data quality control checks consist of the following 3 criteria:

- A stable atmosphere. The atmospheric stability is checked using sky temperature readings, taken with radiometers, operating between 8 & 14 μm, attached to each telescope [45, 15]. When a cloud passes across the field of view, the radiometers observe an increase in temperature, and hence the run is rejected. The run is rejected if the rms variation of the trigger rate within the observing run is greater than 10%.

- A good trigger rate. If the observed trigger rate is less than 70% of the predicted rate (as discussed in [73]), then the run is rejected. The lower than expected trigger rate could be due to a layer of dust, cloud or high humidity.

- A stable telescope system. If there are problems with the hardware or software during the observations, then the run is rejected. This is to minimise the effects of such things as fluctuating PMT voltages etc.

Some examples of both good and bad trigger rates and radiometer readings can seen in Figure 3.8 & Figure 3.9. Both of these examples are observing runs taken on PKS 2155−304, with run 28786 taken during the optical spectroscopic campaign of September 2005, and run 23255 taken during the weather-affected campaign of November 2004.

3.6.2 $\gamma-$ray/Hadron Separation

To differentiate between $\gamma-$ray-induced EAS and hadron-induced EAS, the image parameters such as image length and width are used. Before information

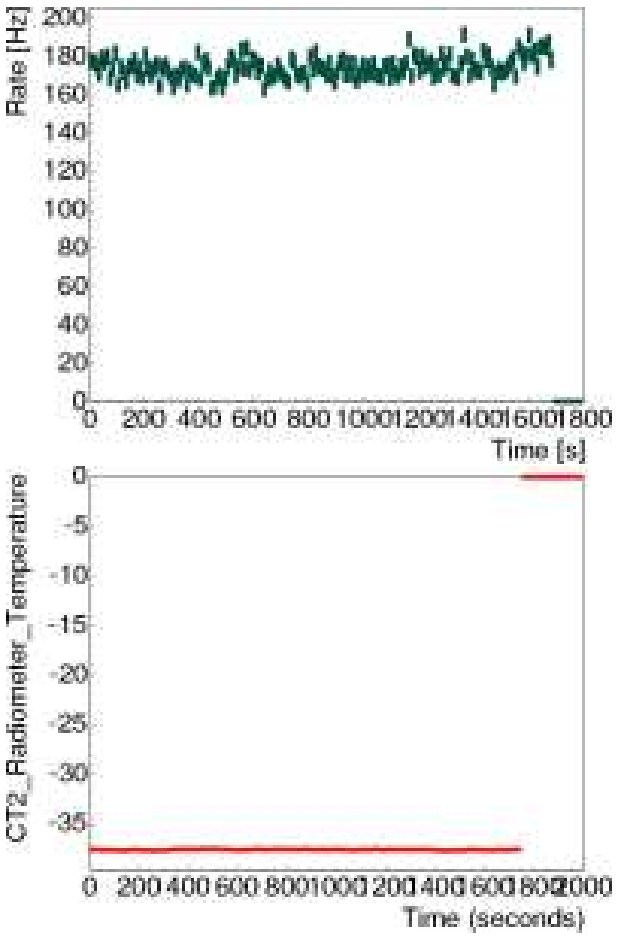

Figure 3.8: Central trigger rate (top) and radiometer readings (bottom) for the Run 28786 of PKS 2155-304. Taken as part of the optical spectroscopic campaign, this run was accepted as both the trigger rate and sky temperature are stable and acceptable.

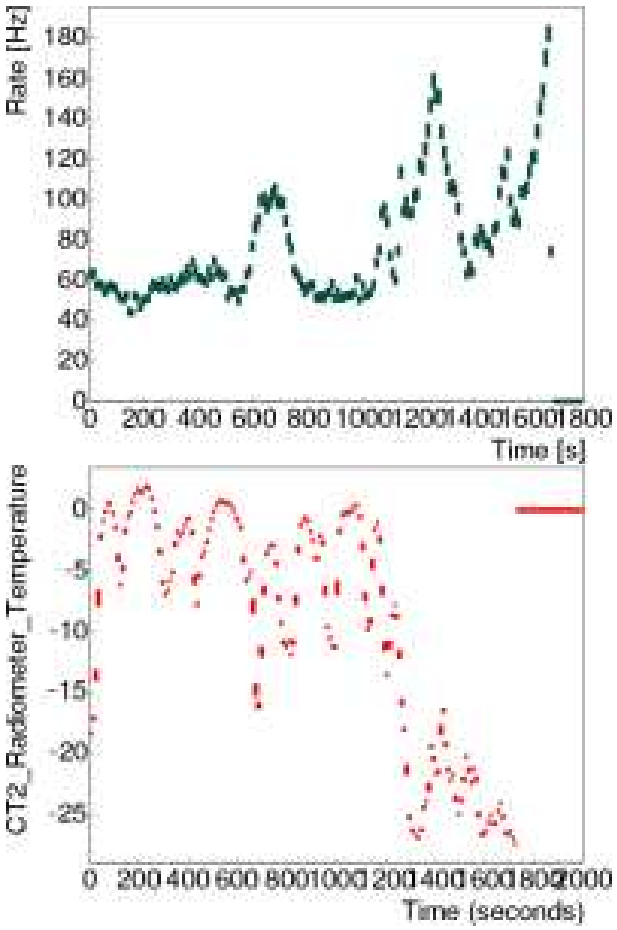

Figure 3.9: Central trigger rate (top) and radiometer readings (bottom) for the Run 23255 of PKS 2155-304 taken during the November 2004 campaign. This run was rejected as both the trigger rate and sky temperature are unstable.

about the Cherenkov image parameters can be obtained, the image recorded by the cameras must first be calibrated [3] and then cleaned.

The image is cleaned using the two-stage '5-10' criterion which removes any pixel signal from the image that is not associated with the Cherenkov shower image. The '5-10' requires that a PMT records a signal greater than 10 photo-electrons and have a neighbouring PMT with a signal greater than 5 photo-electrons. Conversely, PMTs with a signal greater than 5 photo-electrons are included if they have a neighbouring PMT with a signal greater than 10 photo-electrons. It should be noted that to ensure that the recorded shower images are not truncated by the edge of the camera, only images that are less than 2° from the centre of the camera are included in the analysis.

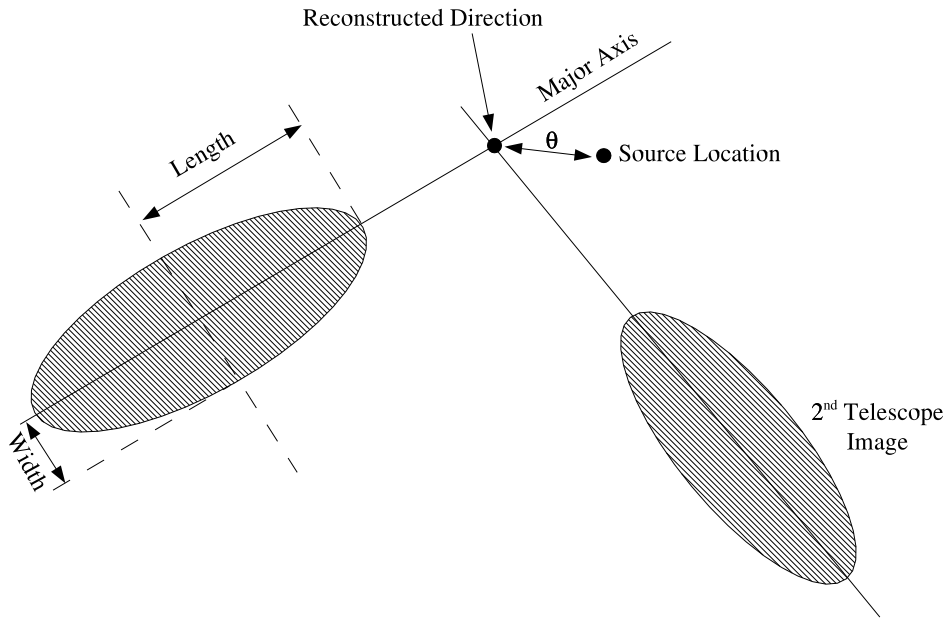

Figure 3.10: Graphical respresentation of the Hillas parameters. The two images are the same Cherenkov shower events recorded by two separate cameras.

Once the image is cleaned, the shower image can be parameterized using the *Hillas parameters* [94]. Figure 3.10 shows the graphical definition of the Hillas parameters[1], with the length, width and image amplitude all relating to

[1]A numerical definition of these parameters can be found in Appendix A

the image shape and θ relates to the orientation of the shower.

To obtain the physical characteristics of the shower, the reconstructed Hillas parameters are compared to a 'look-up' table of known results. These tables contain a range of different observational zenith angles and the associated predicted mean width and length for a given image amplitude and impact parameter. The image amplitude is the total light recorded from the shower event and the impact parameter defines the distance between the shower core on the ground and the telescope. The look-up tables have been compiled from the results of Monte Carlo simulations of EAS.

Once the shower characteristics have been parameterised, the numerous cosmic-ray-induced background is rejected by applying cuts to the mean reduced scaled width (MRSW) and the mean reduced scaled length (MRSL). Defined as the mean of the difference, in standard deviations, between the observed image length or width and the expected length or width from the look-up tables, the MSRL and MSRW are calculated from Eq 3.10 & Eq. 3.11.

$$MSRL = \frac{1}{N_{tel}} \sum_{i=0}^{N_{tel}} \frac{\text{length}_i - < \text{length}_i >}{\sigma_i} \tag{3.10}$$

$$MSRW = \frac{1}{N_{tel}} \sum_{i=0}^{N_{tel}} \frac{\text{width}_i - < \text{width}_i >}{\sigma_i} \tag{3.11}$$

Selection cuts are also placed on other shower parameters such as the image amplitude (the amount of photo-electrons detected by the PMT) and θ^2 (where θ^2 is the square of the angular separation between the reconstructed source position and the actual source position, as defined in Fig. 3.10). The H.E.S.S. analysis throughout this thesis was completed using the standard configuration of cuts, as shown in Table 3.2. It should be noted that other cuts can be applied to the data depending upon the source type and the nature of the observations.

3.6.3 Background Estimation

There are several methods employed to estimate the background, primarily the reflected background model and the ring background model. The model

Table 3.2: Standard selection cuts applied to the H.E.S.S. data.

$MRSL_{min}$ (σ)	$MRSL_{max}$ (σ)	$MRSW_{min}$ (σ)	$MRSW_{max}$ (σ)	θ^2 (deg^2)	Image Amp. (p.e)
-2.0	2.0	-2.0	0.9	0.0125	80

applied depends upon the object being observed (point source or extended) and the nature of the observations.

- *Reflected Background Model.* This model estimates the background from a number of background areas that are equidistant from the centre of the field of view, see Figure 3.11. The combined events from the background areas are scaled by the relative areas of the *on* and background regions.

- *Ring Background Model.* This model estimates the background from an annulus around the *on* source position, see Figure 3.11. The inner and outer radius of the annulus are chosen such that the background region is close to 7 times the *on* source area. Again a scaling factor is needed to take into account the difference in area between the *on* and background regions.

3.6.4 Flux & Spectrum Measurements

The $\gamma-$ray flux is calculated using the excess events after cuts and background subtraction, and takes into consideration the effective area of the telescopes. The effective area, modelled from Monte Carlo simulations, is essentially the area of the Cherenkov light pool on the ground and is a function of the zenith angle of observation, energy of primary $\gamma-$ray and selection cuts used. Note that the effective area also includes the probability of the telescope array being triggered when at least 2 telescopes lie within the Cherenkov light pool.

Assuming a spectral slope, Γ, for a power law, the integrated flux, ξ, above the threshold energy is calculated using Eq.3.12, where E_c is the maximum energy and is normally greater than 100 TeV. The integrated flux is given in units of VHE photons m^{-2} s^{-1}.

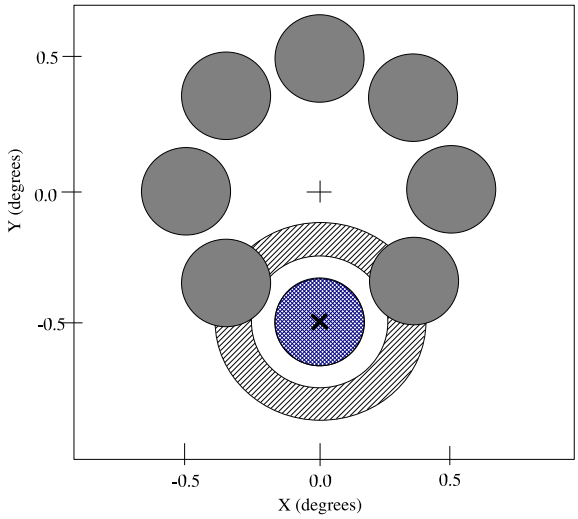

Figure 3.11: Schematic showing the background regions depending upon the background model used. The center of the field of view is marked with a cross, the source position is marked with an X. The *on* source position is denoted by the blue shading. The reflected background model is denoted by the identical grey shaded areas, while the ring background model is denoted by the hatched annulus around the *on* source position.

$$\xi = I_0 \int_0^{E_c} \int_{t_{start}}^{t_{stop}} \left(\frac{E}{E_0}\right)^{-\Gamma} A_{E_{true}}(E, Z(t)) dt dE \tag{3.12}$$

The spectral function is fitted using the least-squares method. The function fitted is usually a power law of form $\frac{\mathrm{d}N}{\mathrm{d}E} = I_0(\frac{E}{E_0})^{-\Gamma}$. The bin size for the spectrum is set depending upon the overall significance of the signal. It should be noted that the systematic errors are estimated to be 20% for the integral flux and ± 0.1 for the photon index.

Chapter 4

PKS 2155−304 October/November 2003 Campaign

At the beginning of the H.E.S.S. observing period for October 2003, a 5σ detection of PKS 2155−304 was made with the, then partially completed, H.E.S.S. telescope array, in 1 hour of observations. This triggered an approved Target of Opportunity programme with the Rossi X-ray Timing Explorer telescope (*RXTE*), as well as triggering a simultaneous optical campaign with the ROTSE-III telescope array and observations with the Nançay decimetric radio telescope.

While these observations, particularly those made with H.E.S.S. and *RXTE*, are important in their own right, considering simultaneous observations at VHE, X-ray, optical and radio wavelengths allows us to probe the behaviour of the particle population in great detail. This in turn provides a better constraint on some of the physical parameters of the jet and thus allows us to constrain possible emission mechanisms within the jet. In this chapter, the H.E.S.S. and *RXTE* observations of the October/November 2003 PKS 2155−304 campaign will be considered in-depth.

4.1 H.E.S.S. observations

The H.E.S.S. observations for this multi-wavelength campaign were taken while Phase I of the H.E.S.S. telescope array was still under construction. The third telescope was added to the array during September 2003. While three telescopes were in place during the campaign of October/November 2003, due to the recent installation of the third telescope, there were periods of data taking in which only 2 telescopes were used, CT3 and CT4. The rest of the time, all three telescopes were used, CT2, CT3 and CT4. The different telescope configurations need to be taken into consideration when reducing the data as the different telescopes have different effective areas and different 'look-up' tables.

The observations were taken in the stereoscopic *Wobble* mode, with PKS 2155−304 positioned $\pm 0.5^{\circ}$ in declination relative to the centre of the field of view of the camera during the observations. As described in Chapter 3, *Wobble* mode replaces the original ON/OFF technique, thus allowing us more time on source as both the *on*-source observations and *off*-source background estimation are done simultaneously.

The data were cleaned using the standard '5-10' criterion, with the parameterisation occuring after the standard cuts, described in Table 3.2, were applied. The background for these observations was estimated using the ring background model as described in Section 3.6.3. The different H.E.S.S. telescope configurations were taken into consideration by grouping the runs depending upon what specific telescopes were used for each individual observation. This resulted in 24 runs in CT3/CT4 configuration and 37 runs in CT2/CT3/CT4 configuration, with a total livetime on source of 14.8 hours. The two-dimensional significance sky map for the 3-telescope runs is shown in Figure 4.1, along with the θ^2 distribution of the observations. A summary of the 2- and 3- telescope data can be found in Table 4.1. It should be noted that the 2 telescope data cover only the first four nights of the campaign, the 3 telescope data cover the rest.

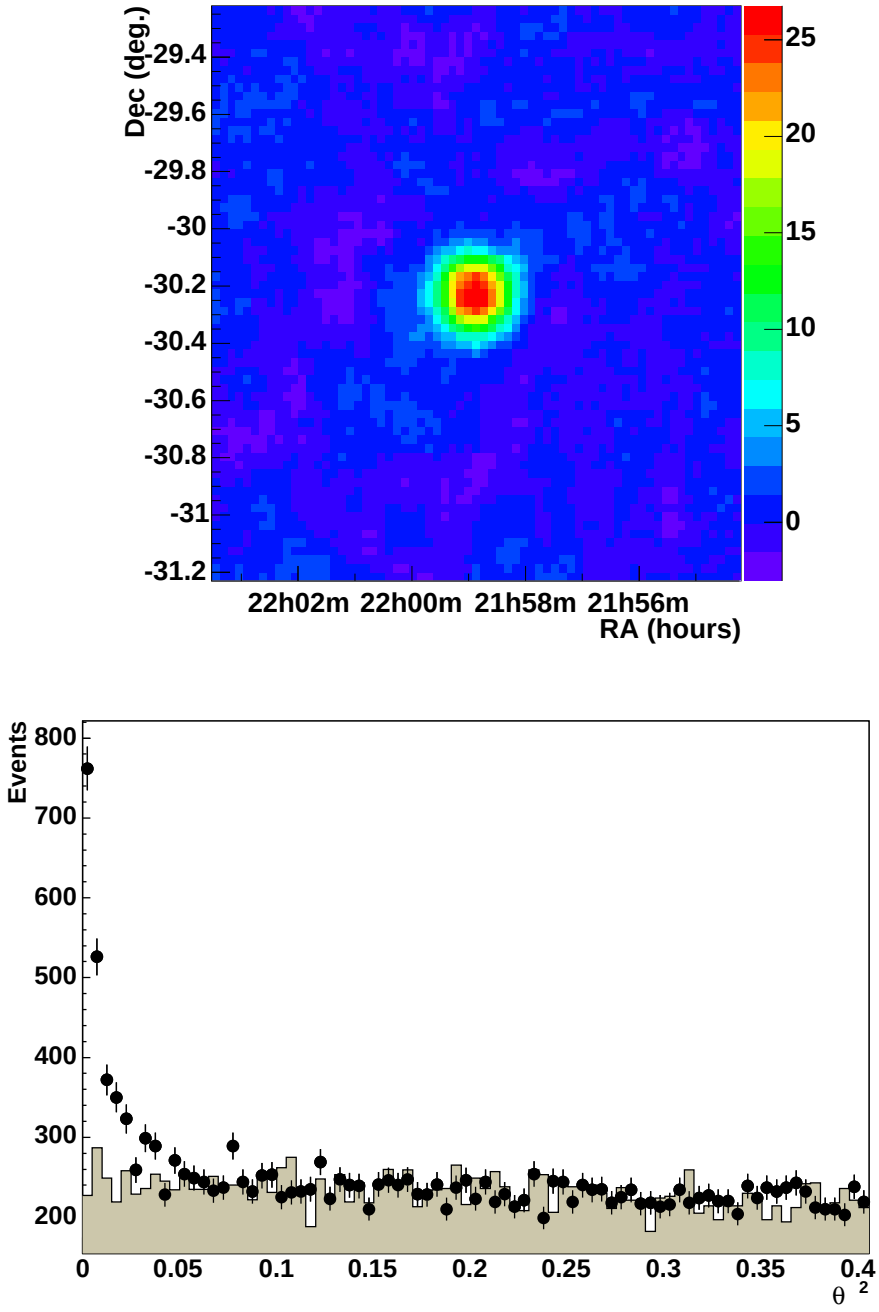

Figure 4.1: *Top:* The two-dimensional distribution of the excess events in the direction of PKS 2155 − 304 using the 3-telescope data. Right hand scale is the number of counts per unit angular area. *Bottom:* The θ^2 distribution of on source events (points) and normalised background events (shaded) for the 3 telescope data.

Table 4.1: Summary of observations for 2- and 3- telescope configurations.

	Livetime (hour)	Excess	Significance (σ)	Sign. rate ($\sigma/\sqrt{\text{h}}$)
2 tel.	8.68	329.5	14.6	5.0
3 tel.	6.12	872.7	27.3	11.0

4.1.1 H.E.S.S. results

Spectrum

As described in Section 3.6.4, the measured time-averaged spectrum is fitted by a power law, with the photon index of the power law then being used to estimate the integral flux above 300 GeV for each run. Note that this 300 GeV lower energy limit is just a conservative limit set to minimise any uncertainty associated with the energy threshold of the telescope system. Shown in Figure 4.2, the best-fitting power law (reduced χ^2 of 1.36 for 14 degrees of freedom), for the 3 telescope data is given by:

$$\frac{\mathrm{d}N}{\mathrm{d}E} = (6.37 \pm 0.50) \times 10^{-12} \left(\frac{E}{\mathrm{TeV}}\right)^{-3.48 \pm 0.07_{stat} \pm 0.1_{sys}} \mathrm{cm}^{-2}\ \mathrm{s}^{-1}\ \mathrm{TeV}^{-1} \quad (4.1)$$

There is a marginal ($\Delta\Gamma = 0.03$) difference between the best fit photon index for the 2-telescope data and the 3-telescope data. This photon index is marginally softer than the $\Gamma = 3.32 \pm 0.06$ previously reported by the H.E.S.S. collaboration during 2002 and early 2003, see [4].

To investigate the effect the absorption of VHE $\gamma-$rays by the extra-galactic background light has on the high energy tail of the VHE spectrum, a broken power law was also fitted to the data. It should be noted that the broken power law is correct to a first order approximation. Ideally, a power law with an exponential cut off would be a more accurate description. Nonetheless, a broken power law, with the spectral break close to the high energy tail would indicate that absorption by the EBL may be responsible. Furthermore, extra weight would be given to this arguement if the position of the break

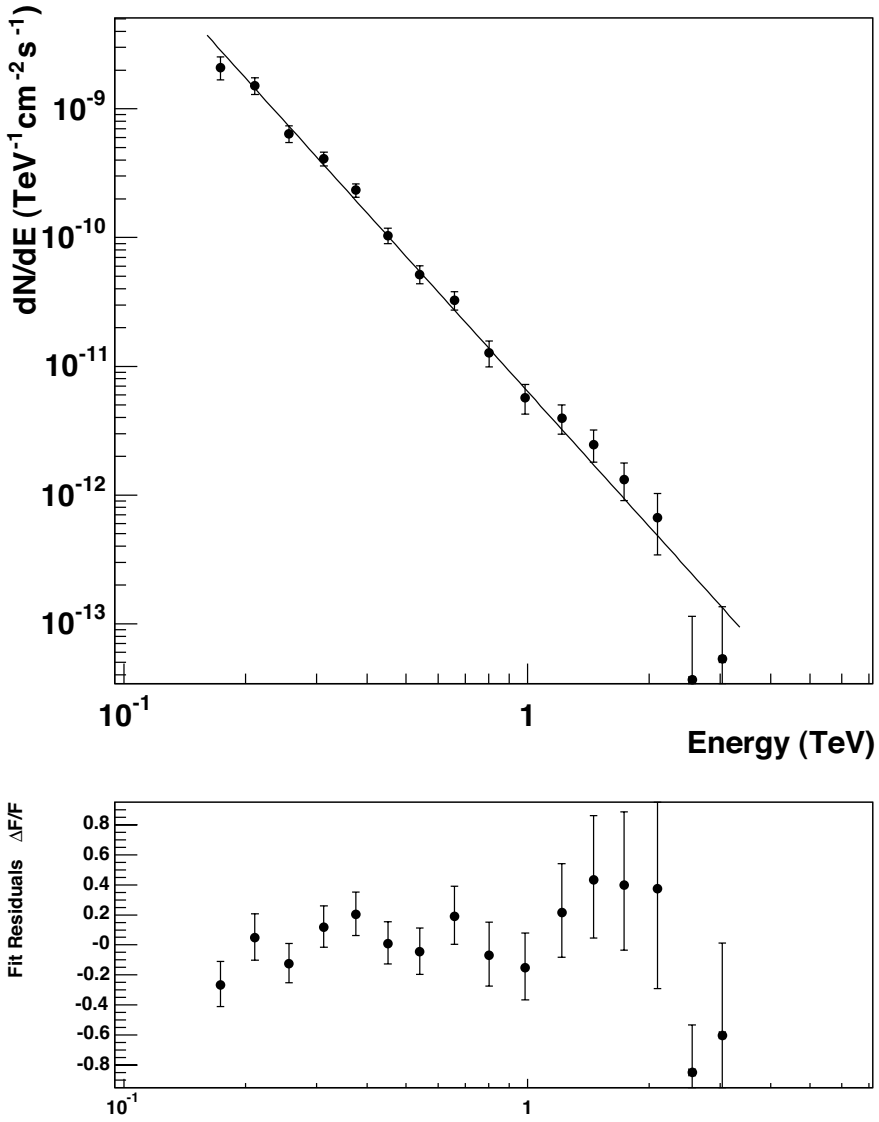

Figure 4.2: *Top:* Power law fit to the VHE data from the 3-telescope data. This fit yields a photon index, $\Gamma = -3.48 \pm 0.07$, with a reduced $\chi^2 = 1.36$ for 14 degrees of freedom. *Bottom:* The residuals to the power law fit.

was constant between the different campaigns within this thesis. The broken power law is of the form:

$$\frac{\mathrm{d}N}{\mathrm{d}E} = I_0 \left(\frac{E_{break}}{E_0}\right)^{(\Gamma_2-\Gamma_1)} \left(\frac{E}{E_0}\right)^{-\Gamma_2} \tag{4.2}$$

where E_{break} is the break point energy in TeV, Γ_1 and Γ_2 are the photon indices before and after the break and I_0 and E_0 are as before. Fitting a broken power law to the VHE data results in a only a slightly different reduced χ^2 of 0.96 for 11 degrees of freedom, with a better probability and a E_{break} of 1.75 ± 0.24 TeV, $\Gamma_1 = -3.37 \pm 0.08$ and $\Gamma_2 = -6.00 \pm 3.28$. Note that the large uncertainty in Γ_2 is due to the poor count rates at the high-energy tail of the VHE spectrum. Again, there is a $\Delta\Gamma = 0.1$ systematic uncertainty in the photon indices.

It should be pointed out that photon indices could not be derived on a run-by-run basis. This is due to the weak signal, especially at high energies. We are therefore unable to probe the harder-when-brighter characteristic demonstrated by Mkn 421 and Mkn 501 at very high energies [2, 62].

Lightcurve

Figure 4.3 shows the E> 300 GeV flux in units of photons m^{-2} s^{-1} for October, whilst Figure 4.4 shows the E> 300 GeV for November, both plots using good observation runs that pass all the selection criteria. The H.E.S.S. data have been binned using the original 28 minute observation length, with the flux being derived using a photon index of -3.48 for the 3-telescope data and photon index of a -3.45 for the 2-telescope data. Both of these photon indices were obtained earlier from the power law fit.

The E> 300 GeV flux of PKS 2155−304 throughout the campaign ranges from $\mathrm{F_{min}} = 2.6 \times 10^{-8}$ photons $\mathrm{m}^{-2}\mathrm{s}^{-1}$ to $\mathrm{F_{max}} = 1.2 \times 10^{-6}$ photons $\mathrm{m}^{-2}\mathrm{s}^{-1}$. While AGN are known to exhibit a large amount of variability, the VHE fluxes reported here are consistent with the past VHE observations by H.E.S.S. and Durham Mark 6 [4, 43]. As with these past observations, there is also clear evidence for intra-night variability. The fit of the individual observations to a constant flux yields a reduced χ^2 of 16.8 for 36 degrees of freedom, correspond-

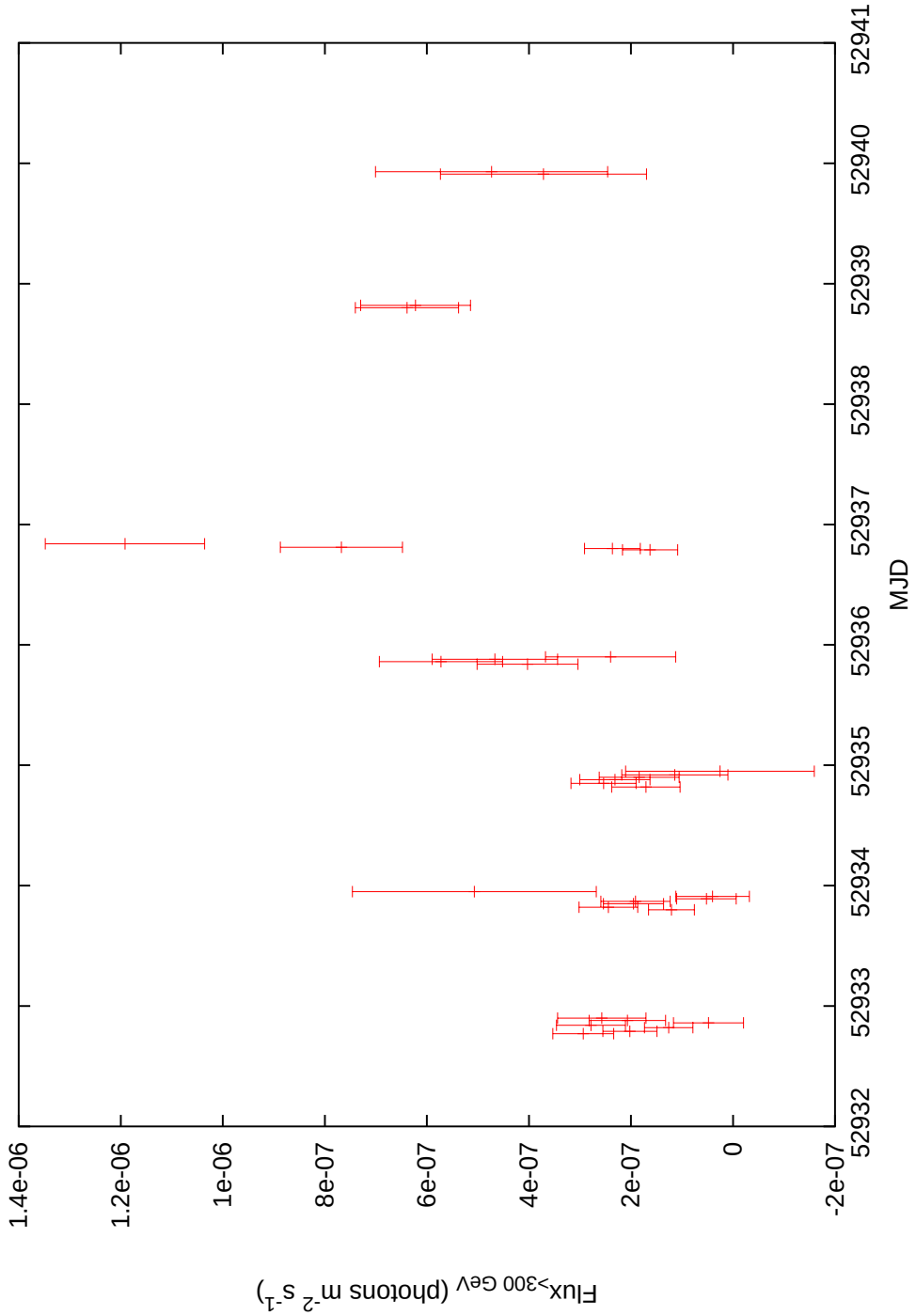

Figure 4.3: PKS 2155−304's E>300 GeV flux in units of photons m^{-2} s^{-1} during October 2003. The first 4 days of the VHE observations was completed with just 2 telescopes, there after, 3-telescopes were used. It should be noted that only the statistical errors are shown here, there is a further 20% systematic uncertainty in the fluxes.

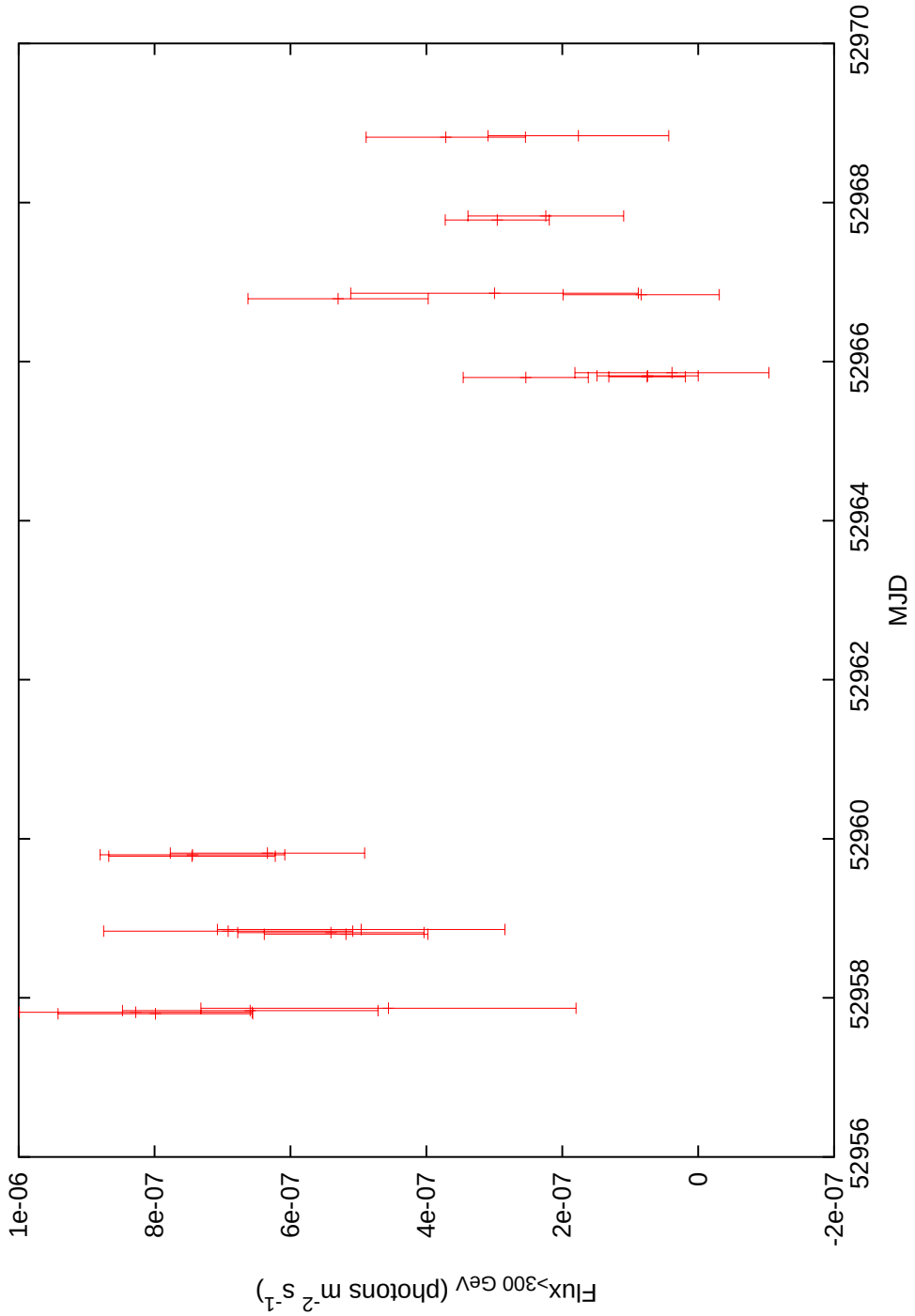

Figure 4.4: PKS 2155−304's E>300 GeV flux in units of photons m^{-2} s^{-1} during November 2003. It should be noted that only the statistical errors are shown here, there is a further 20% systematic uncertainty in the fluxes.

ing to a $(9.8 \pm 3.4) \times 10^{-10}$ χ^2 probability. The most extreme case intra-night VHE flux variability occurred during MJD = 52936, when the flux increased by a factor of 6.9 ± 0.9 in 1.2 hours.

4.2 X-ray Observations

Tracking the emission from the same relativistic electron population through two different observational techniques, such as simultaneous X-ray and VHE $\gamma-$ray observations, represents a powerful diagnostic tool to probe the inner regions of the jet. Simultaneous X-ray and VHE $\gamma-$ray observations can be used to constrain the timescales for injection, acceleration and cooling of the primary particles within the jet and the kinematics of the inner jet in general.

Furthermore, considering how the overall SED of the source reacts to, or indeed instigates, variations in the X-ray emission can help to determine the dominant model by which VHE γ-rays are produced, as described in Section 2.2. In this section, after a brief review of the Rossi X-Ray Timing Explorer (*RXTE*), we will look at the reduction of the *RXTE* observations taken as part of the October/November 2003 multi-wavelength campaign on PKS 2155−304.

4.2.1 *RXTE*

Launched on 30th December 1995, *RXTE* constitutes the largest X-ray detecting area ever sent into space [96]. With a moderate spectral resolution in the 2 - 250 keV range, *RXTE*'s strength lies in its unprecedented temporal resolution on timescales from microseconds to years. The excellent temporal resolution of *RXTE* is due to the large size of the detector, as sensitivity to temporal variations, for proportional counters, scales linearly with the detector surface area [97].

RXTE has 2 pointing instruments, the Proportional Counter Array, PCA, and the High Energy X-ray Timing Experiment, HEXTE [99, 155]. The PCA covers the lower end of the energy range, 2 - 60 keV, while the HEXTE covers the higher end of the energy range, 60 - 250 keV. Both instruments are equipped with a collimator giving a FWHM of one degree. In addition to PCA

and HEXTE, *RXTE* also carries an All-Sky Monitor, ASM. ASM consists of 3 scanning shadow cameras on a rotating boom. Observing 80% of the sky every 90 minutes, ASM is often used as a trigger for observations at other wavelengths when there is an increase in X-ray activity. With an effective area of 90 cm^2 ($3\times30cm^2$), the ASM has an energy of 1.5-12 keV and a sensitivity of 20 mCrab. For a review of the properties of each detector onboard *RXTE*, see Table 4.2.

During approximately half *RXTE*'s 16 daily orbits, the satellite passes through the South Atlantic Anomaly (SAA). The SAA is a region in the southern hemisphere where the Earth's magnetic field has a 'dip' in intensity. The reduced field strength allows cosmic rays and charged particles to travel further into the atmosphere. This increase in density of charged particles not only increases the background noise, but can also damage the instruments onboard *RXTE*. Therefore, during *RXTE*'s transit through the SAA, which usually lasts between 10-20 minutes, the observing instruments are put in a safe mode to protect against the high particle flux. These transit events need to be taken into consideration when placing quality control cuts on our *RXTE* observations.

The *RXTE* spacecraft was designed to be capable of slewing rapidly from one source to another in less than an hour. It is capable of pointing to any location of the sky bar a small region close to the Sun. This flexibility gives *RXTE* the ability to observe Targets of Opportunity, ToO, depending upon what sources are active in X-ray energies, and not be stuck to a rigid timetable. This is necessary to catch BL Lac objects in their high activity state, and thus allows us to probe the mechanisms behind the high activity.

Proportion Counter Array

As the name suggests, the Proportional Counter Array (PCA) consists of an array of 5 identical PCU detectors. These detectors, PCU 0-4, contain a xenon + 10% methane gas mixture. Consisting of a windowed gas cell, subdivided into a number of low and high electric field regions by an arrangement of electrodes, the PCUs follow the design principles of the HEAO-1 A2 experiment. In fact proportional counters in general have been the work-horse of the X-ray

Table 4.2: Properties of instruments onboard *RXTE* [96]

Property	PCA	HEXTE	ASM
Energy Range (keV)	2 - 60	15 - 250	1.5 - 12
Energy Resolution	18% at 6 keV	15% at 60 keV	3 channels
	9% at 22 keV		(1.5-3,3-5,5-12 keV)
Temporal Resolution	1 μs	8 μs	90 minutes
Spatial Resolution	1°	1°	$3' \times 15'$
Collecting Area	6250 cm^2	1600 cm^2	3×30 cm^2
Sensitivity	$\sim$0.1 mCrab	$\sim$1 mCrab	$\sim$20 mCrab
Background	$\sim$2 mCrab	$\sim$0.1 mCrab	$\sim$0.5 mCrab
Purpose	timing	timing	survey/monitor

community for a long time.

The X-rays are detected by the photoionisation of the xenon-methane gas mixture. Upon entering one of the cells, the X-ray ionises a number of atoms creating a small electron-ion cloud. The electrons in the cloud are accelerated towards the anode, causing ionisation of more atoms along the way, resulting in an 'avalanche' of electrons. This avalanche is detected as a pulse.

Each PCU consists of an Antico layer of propane, and 3 Xenon-Methane layers. The 'Antico', or anti-coincidence layer, is used to discriminate between cosmic ray triggers and X-ray triggers, thus keeping the fluctuations in the gain of the PCUs to a minimum. During data reduction, the signal from each of the three levels can be extracted separately. Since the majority of the signal is detected by the first layer and the first layer has around half of the background, both internal and external, noise, reducing data from the first Xenon-Methane layer alone maximises the signal-to-noise ratio and is ideal for faint sources such as AGN.

4.2.2 X-ray Data Reduction

The *RXTE* observations of PKS 2155−304 for the October/November 2003 campaign consisted of pointed observations using the PCA units [99] between October 22$^{\text{nd}}$ and November 23$^{\text{rd}}$ 2003 (52934 <MJD< 52966, where MJD

is the Modified Julian Date and is the Julian Date - 2400000.5). The total exposure time was $\sim$ 11 ks, with $\sim$ 10 ks during October and $\sim$ 1 ks of observations during November. Of these exposures, only the STANDARD2 data were extracted and reduced. The reduction was done using FTOOLS V.5.2, which are part of the HEASOFT 5.2 analysis software package provided by the NASA Goddard Space Flight Centre[1].

It should be noted that the the PCU configuration of the observations changed throughout the *RXTE* campaign. Much like the different configurations of telescopes for the H.E.S.S. observations, the different PCU configurations must be taken into consideration. During data reduction, background files, filter files and response matrices are calculated for each PCU separately. These files and matrices are dependent upon the PCU used. What is more, these matrices also depend upon the energy range in which you are observing and using the wrong response matrice can result in erroneous flux calculations and erroneous spectral fitting.

Throughout the *RXTE* observations, the PCU configuration was predominantly either PCU 0/2 or PCU 0/2/3. The PCU 0/2/3 observations were taken during the first half of the H.E.S.S. October observations, 52934 $<$ MJD $<$ 52940 in Figure 4.6, while the PCU 0/2 configured observations were taken MJD = 52940 onwards. During data reduction, the signal from each PCU was reduced separately, using the correct PCU-dependent response matrices and, when needed, were combined using the appropriate FTOOL routines.

While PCU 0 and PCU 2 were used for the majority of the RXTE campaign, the raw count rates from PCU 0 should be used with caution. As mentioned in Section 4.2.1, each PCU 0 has a propane layer to minimise fluctuations in the gain. However, due to a micro-meteor impact during May 2000, PCU 0 has lost its propane layer. Therefore the gain of PCU has been known to vary. Figure 4.5 shows the simultaneous raw count rates for PCU 0, 2 and 3 for 52934 $<$ MJD $<$ 52940. The effect the loss of the propane layer has on the count rates can easily be seen, with PCU 0 detecting $\sim$60% more counts than both PCU 2 and PCU 3. These different count rates, due to PCU 0 being more prone to contamination from low-energy electrons entering the detector, can result

[1]Available at http://heasarc.nasa.gov/lheasoft/download.html, last accessed 12/06/2006

in artifacts occuring within the X-ray lightcurve. While no alarming features are present in the ratio lightcurve, fluctuations are still present. However, to remove any uncertainty, only the signal from PCU 2 was considered for the October/November 2003 *RXTE* observations.

Before data reduction, quality control cuts have to be made. A number of recommended criteria are given by the *RXTE* Guest Observer Facility (GOF) to maximise the the signal to noise and to ensure the most accurate background subtraction can be obtained. These criteria are as follows:

- The Earth elevation should be $> 10^{\circ}$ to reduce the bright Earth effects. These effects are usually seen at around 5° elevation, and the limit of 10° is therefore a conservative cut.
- The pointing offset of the observations is $< 0.02^{\circ}$. This ensures that the source is in the centre of the field of view and simplifies the background estimations for the observations.
- The electron contamination should be < 0.1. This is to ensure that the background subtraction is accurate.
- The time since the peak of the last SAA passage should be > 30 minutes. Again this is a conservative cut to minimise the background noise from the SAA passage and for accurate background subtraction.

The quality control cuts used throughout our *RXTE* analysis of the October/November 2003 data are the same as those suggested by the GOF.

The STANDARD2 data was extracted using the FTOOL XDF, with only data from the left and right hand side of layer one being considered to maximise the signal-to-noise ratio. As mentioned in Section 4.2.1, the majority ($\sim$90%) of the low energy signal, E$<$ 10 keV, is detected by the top layer of the PCUs. Since the top layer detects only half of the noise (external and internal), using the top layer of the detector maximises the signal-to-noise of our observations, something that is particularly necessary for faint X-ray sources.

Once the data was extracted, the background must be subtracted. The background data were modelled using the FTOOL PCABACKEST V3.0, with

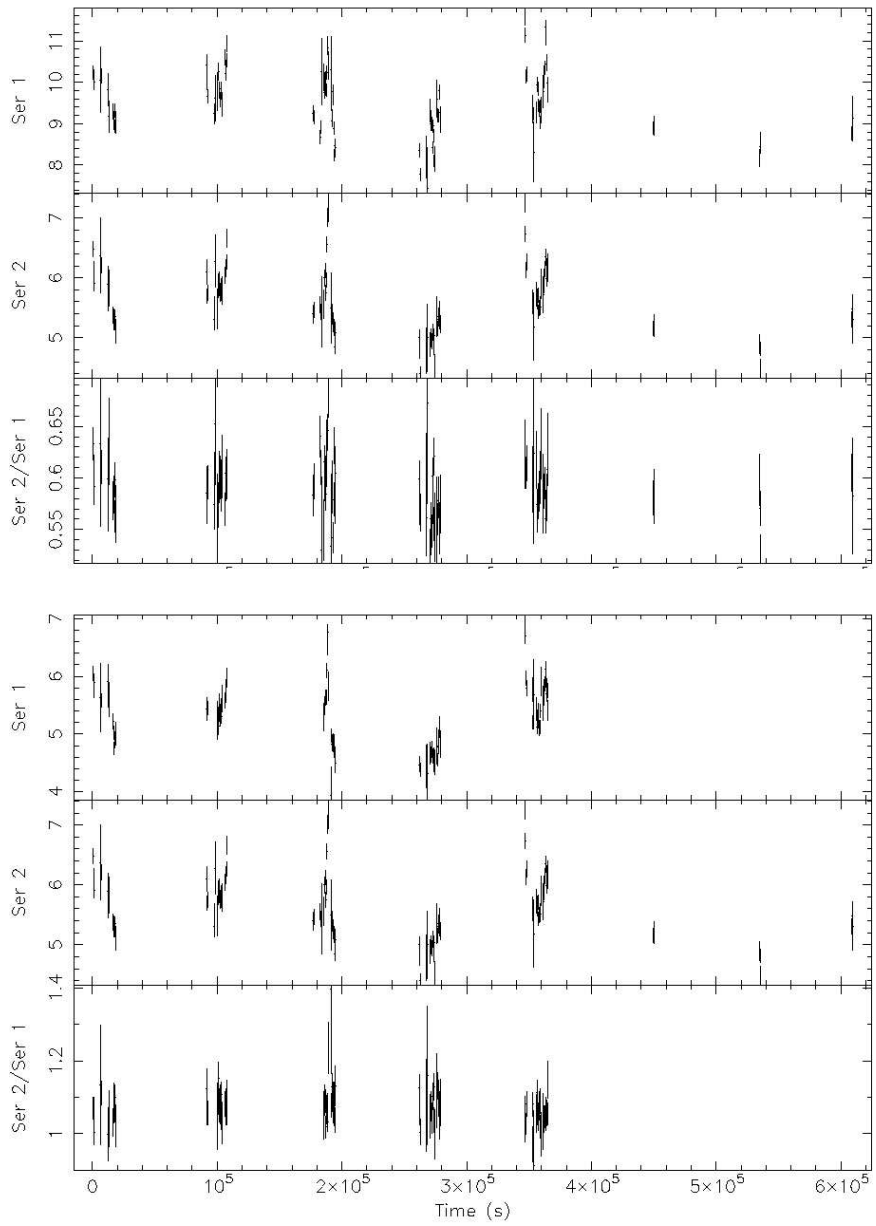

Figure 4.5: Top panel shows the simultaneous raw count rates for PCU 0 (Ser 1) and PCU 2 (Ser 2) as well as the ratio of the two count rates. The bottom panel is the same as the top, but Ser 1 represents the raw count rate from PCU 3. The ratio for the bottom panel, where both PCUs have their propane layer, is $\sim$1, while the ratio for the top panel (where PCU 0 has lost is propane layer and hence is susceptible to gain fluctuations), is $\sim$0.6.

a *faint source* background model. While the data were extracted from PHA channels 0-27 (corresponding to $2 - 11.45$ keV), only data in the energy range $3-10$ keV were considered for spectral fitting.

Using XSPEC v.11.2, an absorbed power law (WABS*PO) was fitted to the data, with the appropriate PCU configuration-dependent response matrices being generated using the FTOOL PCARSP v.8.0. Using a fixed column density of $N_H = 1.7 \times 10^{20} cm^{-2}$ obtained from PIMMS[2], a flux in the energy range $2-10$ keV was calculated, with an associated error corresponding to a 1σ confidence level. On closer inspection, when the data from each PCU is reduced separately the power law fit parameters for PCU 0 have systematically higher errors and χ^2. Considering that PCU 0 also detects systematically higher count rates due to the loss of its propane layer, only PCU 2 has been considered for analysis.

The photon index, and associated error, of the power law was also calculated using XSPEC v.11.2. (It should be noted that the fit to the data did not vary significantly when a broken power law was applied to the data.) The energy range of $3-10$ keV for photon index was used as this is the energy range in which the response matrices are the most reliable. The $2-10$ keV flux was extrapolated from the 3 down to the 2 keV limit, and is standard practice during *RXTE* analysis. What is more, the statistics of these *RXTE* observations above 10 keV are poor, adding unnecessary uncertainty to the high energy tail of the X-ray spectra. Likewise, the response matrix for the lower energies (1-3 keV) is poorly understood due to uncertainty in the low energy calibration of the PCA instrument.

4.2.3 X-ray Results

Lightcurve

Figures 4.6 and 4.7 shows the $2-10$ keV flux in units of 10^{-11} ergs $cm^{-2}s^{-1}$ for October and November 2003. While intra-night variability in X-ray emission is obvious, more so during October than November, it appears that no X-ray flare was completely resolved.

[2]See http://legacy.gsfc.nasa.gov/Tools/w3pimms.html

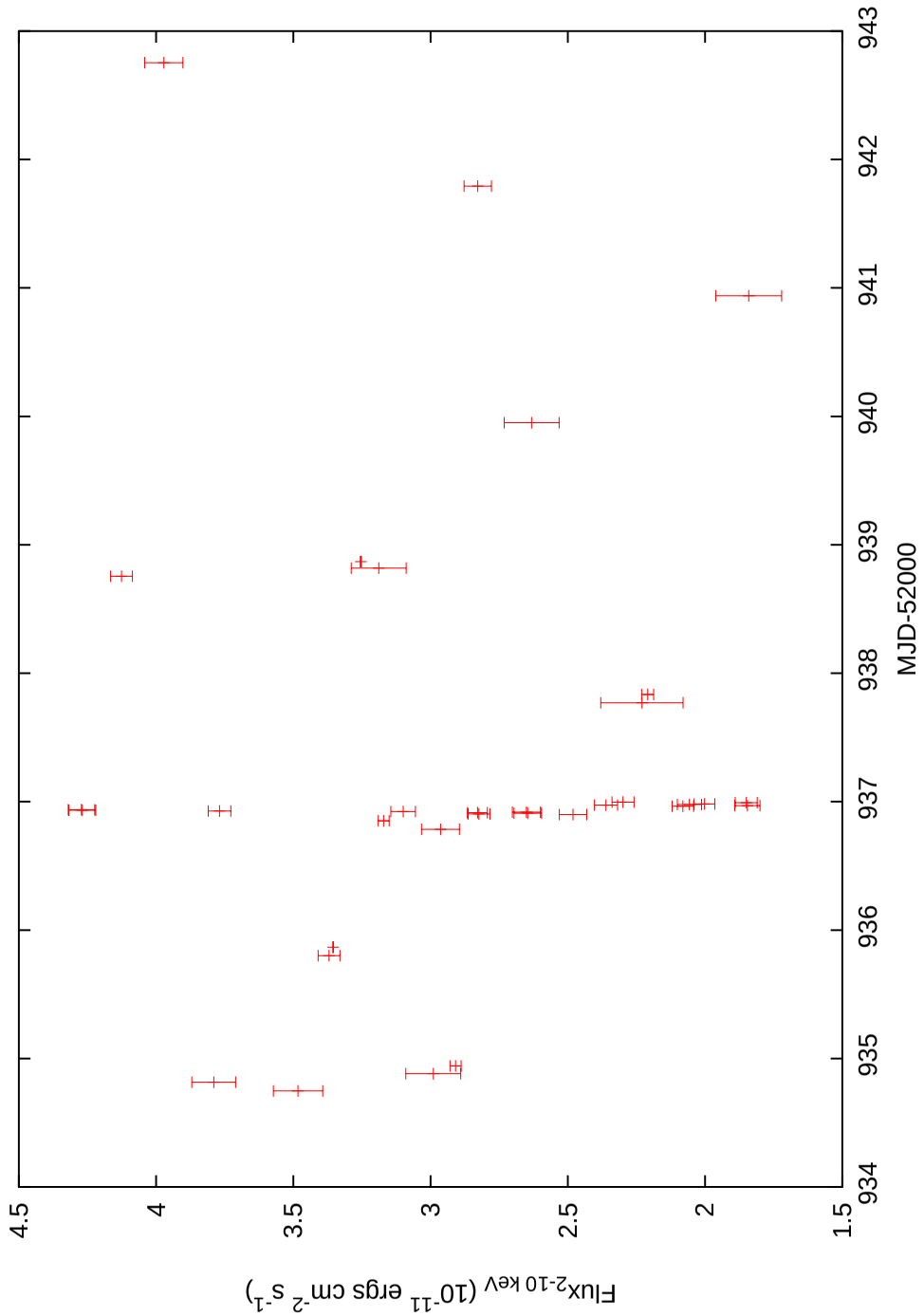

Figure 4.6: PKS 2155−304 2−10 keV flux in units of 10^{-11} ergs cm^{-2}s^{-1} during October, using data from PCU 2 only.

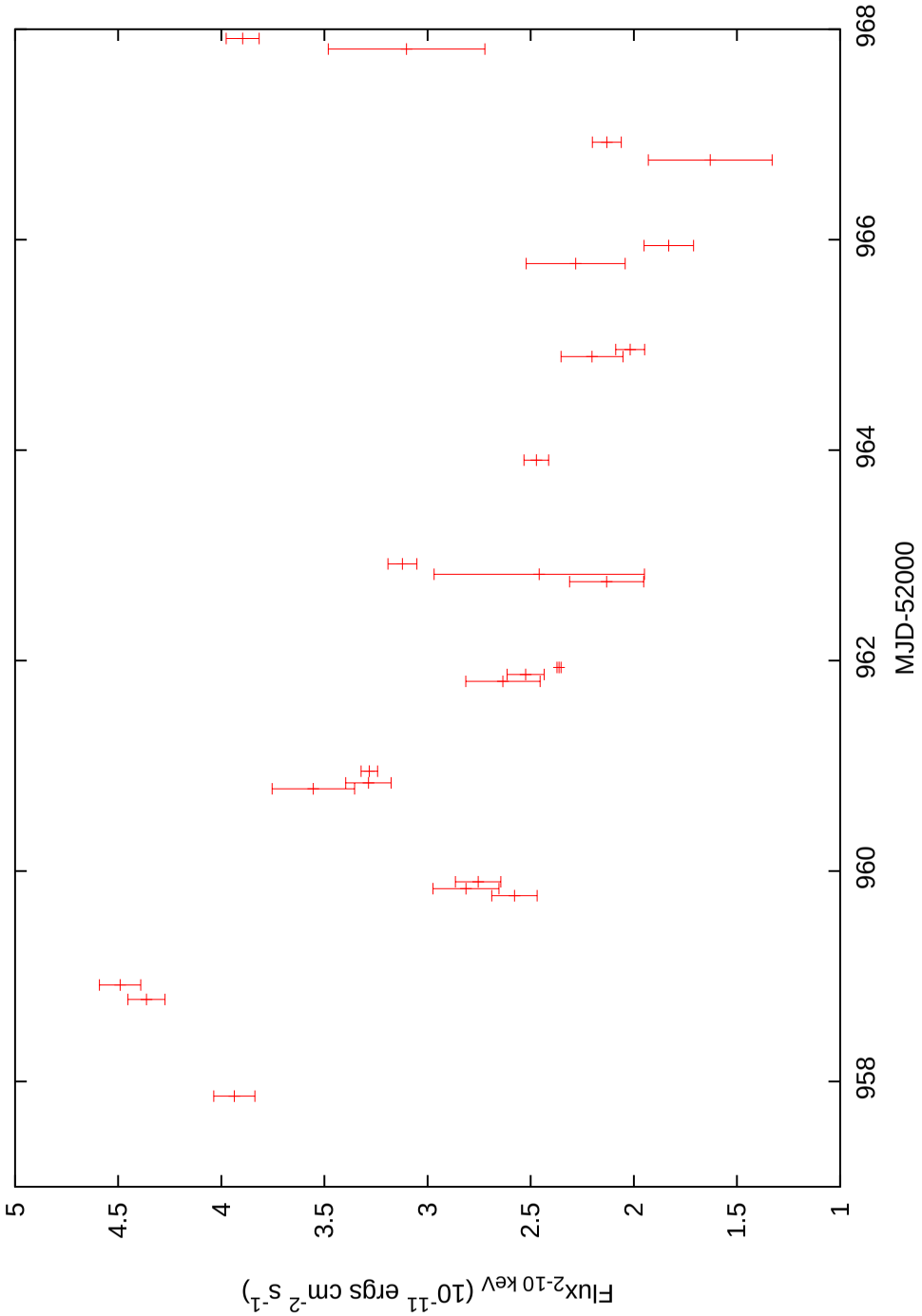

Figure 4.7: PKS 2155−304 2−10 keV flux in units of 10^{-11} ergs $cm^{-2}s^{-1}$ during November using data from PCU 2 only.

The 2−10 keV flux throughout the campaign ranges from $F_{min} = 1.6 \times 10^{-11}$ ergs cm^{-2} s^{-1} to $F_{max} = 4.5 \times 10^{-11}$ ergs cm^{-2} s^{-1}. Comparing these results to past X-ray observations, we see that PKS $2155-304$ was in a fairly low X-ray activity state throughout our multi-wavelength campaign [191, 197]. As we will see later, this quiescent state has important implications for the models we use to describe the overall emission from PKS 2155−304.

The highest 2−10 keV flux detected from PKS 2155−304 was detected with *RXTE* on the 20th November 1997, and measured to be 2×10^{-10} ergs cm^{-2}s^{-1}, an order of magnitude larger than the maximum flux detected during our campaign, [191]. What is more, the minimum 2−10 keV flux detected during the October/November campaign, 1.6×10^{-11} ergs cm^{-2} s^{-1}, is consistent with the historically low fluxes seen with *BeppoSax* [197].

As mentioned, while there is clear evidence in Figures 4.6 and 4.7 for intra-night variability, these flaring events are not completely resolved. Nonetheless, referring to Figure 4.6 we can see evidence for two flaring events, one at MJD $\sim$ 52937 and the other at MJD $\sim$ 52939. The former is more significant as a large amplitude of variability is observed in a shorter time, a $49 \pm 3\%$ increase in flux level, with a rise-time of $\approx 2\times10^3$ seconds, while the latter flare is only a $\sim 21\pm1\%$ increase in flux level, with a rise-time of $\approx 1\times10^4$ seconds. It should be noted that throughout this work the term 'flare' is a rather arbitary term used to describe an obvious flux variability event, whether it be a increase or a decrease in flux. When using the 'flaring' event to constrain jet parameters, the rise-time or fall-time will be specified depending upon what part of the 'flare' will be considered. Figure 4.8 shows the larger flaring event in greater detail.

Comparing this X-ray variability with past observations we find that our observed flux variability appears to be the fastest seen to date from PKS 2155−304. Kataoka et al. observed a doubling timescale of 3×10^4 seconds with *ASCA*, while Zhang et al. observed flaring event on the timescale of 5×10^4 seconds with *BeppoSax*, [102, 197]. However, care should be taken when comparing flares with different variability timescales. As we will see in Chapter 9, it is more appropriate to compare variability timescales for 'flaring' events with the same variability amplitude. Not doing so can introduce unnecessary

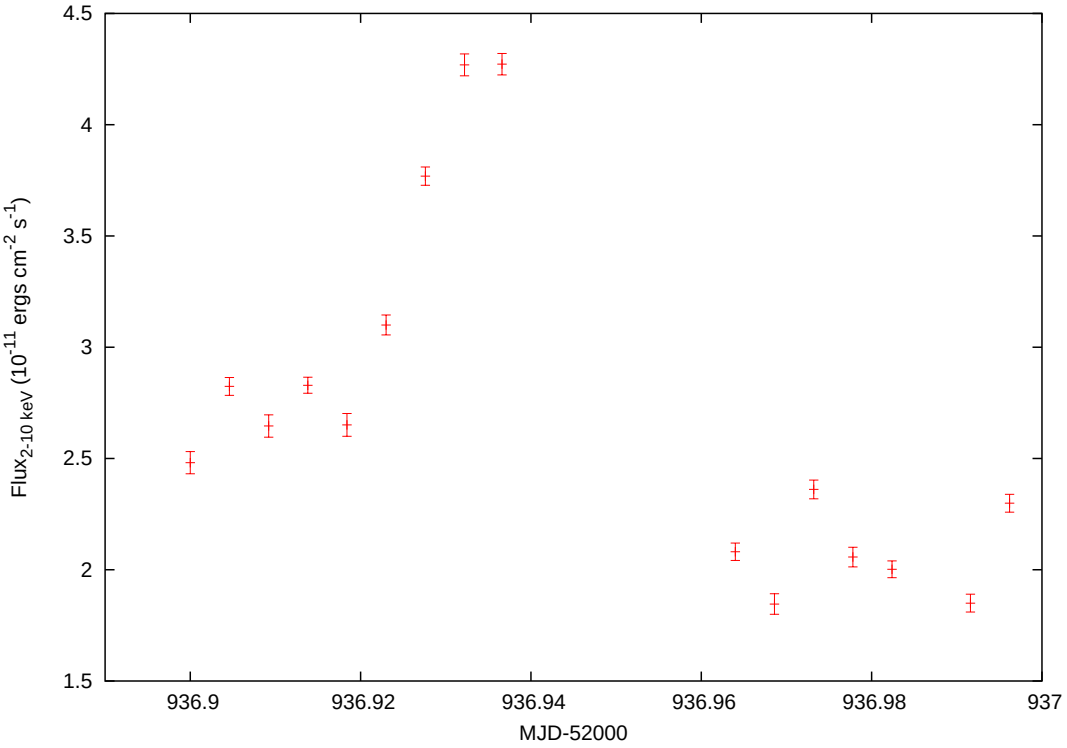

Figure 4.8: Flux versus MJD (52936.89< MJD <52937.00) showing the structure of the major flare of the campaign.

uncertainty, or bias, in the comparison.

In Section 5.1 the variability timescale will be used to derive physical parameters of the X-ray emission region. Coupled with the simultaneous H.E.S.S. observations, and assuming a co-spatial origin for both the X-ray and VHE emission, these derived parameters can be quite constraining on the physical characteristics of PKS 2155 − 304's relativistic jet.

Photon Index

Figure 4.9 shows the 3−10 keV power law fit and the residuals for the summed October and November data from PCU 2. For the energy range of 3−10 keV, this power law fit yields a photon index of $\Gamma = -2.88 \pm 0.03$, with a reduced χ^2 of 1.69 (14 degrees of freedom). Applying a broken power law to the same data set yields a slightly softer slope above the break energy, a slightly hard spectrum below the break energy and a marginally larger reduced χ^2 of 1.87 for 12 degrees of freedom, with an associated χ^2 probability of

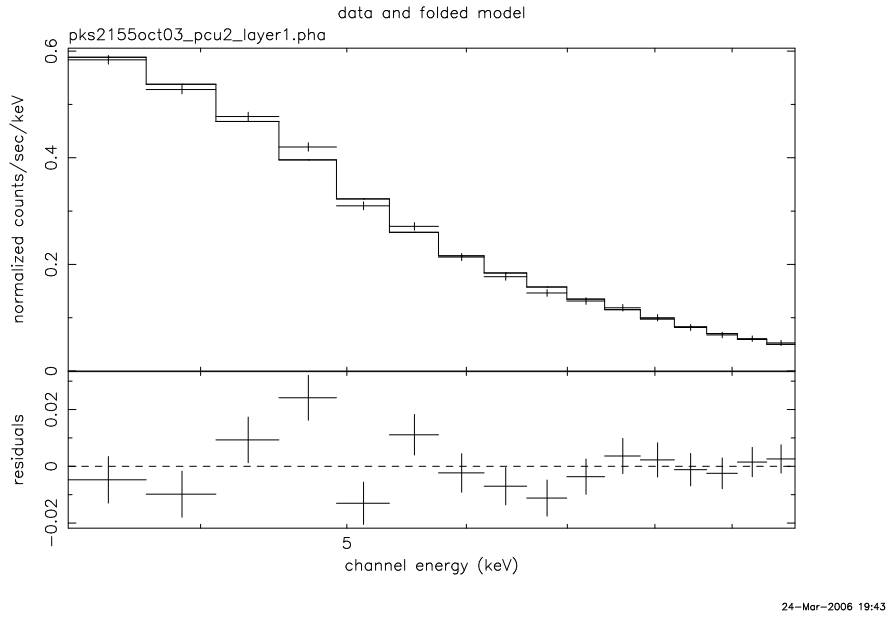

Figure 4.9: X-ray spectrum, 2−10 keV, derived from the summed October and November data from PCU 2, fitted by a power law. The top panel shows the data and the fit, while the bottom panel shows the residuals between the fit and the model.

0.05. To explore whether the poor reduced χ^2 is an artifact of summing over different spectral states throughout October and November, we considered each observation from PCU 2 separately, applying the same quality control criteria described in Section 4.2.2.

Figure 4.10 shows the photon index, Γ, versus MJD for a power law fit to each seperate pointed observation. As with the fluxes derived earlier on in this section, a power law was fitted to the data in the energy range of 3−10 keV. During October and November, the photon index varied from $\Gamma_{min} = 2.45 \pm 0.48$ to $\Gamma_{max} = 3.61 \pm 0.79$. Futhermore, the reduced χ^2 of the power law fit to the separate PCU 2 observations are close to 1. Therefore the poor reduced χ^2 for the summed October/November spectrum is likely to be due to summing over the different spectral states of PKS 2155−304 during the observing period. Again, the photon index values don't vary greatly if a broken power law is applied to the data.

It should be noted that the photon indices yielded from the power law fit are in good agreement with past measurements from *EXOSAT* during the 1980s, $2.44 < \Gamma < 3.02$ [181], and slightly higher then the $1.6 < \Gamma < 2.5$ measured by Urry et al., Giommi et al. and Sembay et al. [185, 84, 167]. All of these past photon indices are from a power law fit to the data.

In order to investigate any flux dependence of the spectral state variability, the 2−10 keV flux was plotted against the 3−10 keV photon index for the power law fit, Figure 4.11. Past X-ray studies of BL Lac objects have shown that, during a flaring state, the low energy peak of the SED shifts to higher energy. In particular, this behaviour has been observed in Mkn 421 by Takahashi et al. using *ASCA* and by Fossati et al. using *Beppo-SAX* [178, 71]. Both of these studies found that the low energy peak shifted to higher energies by approximately one order of magnitude. Likewise this 'harder when brighter' behaviour was observed in PKS 2155−304 by Chiappetti et al. with *Beppo-SAX* [49]. An extreme case occurred in Mkn 501, when during an exceptional flaring event, the low energy peak shifted 3 orders of magnitude from the sub-keV to the 100 keV range, [139].

The shift in the peak is often described as a shift in the break energy of the electron population to higher energies. However, how this shift occurs and

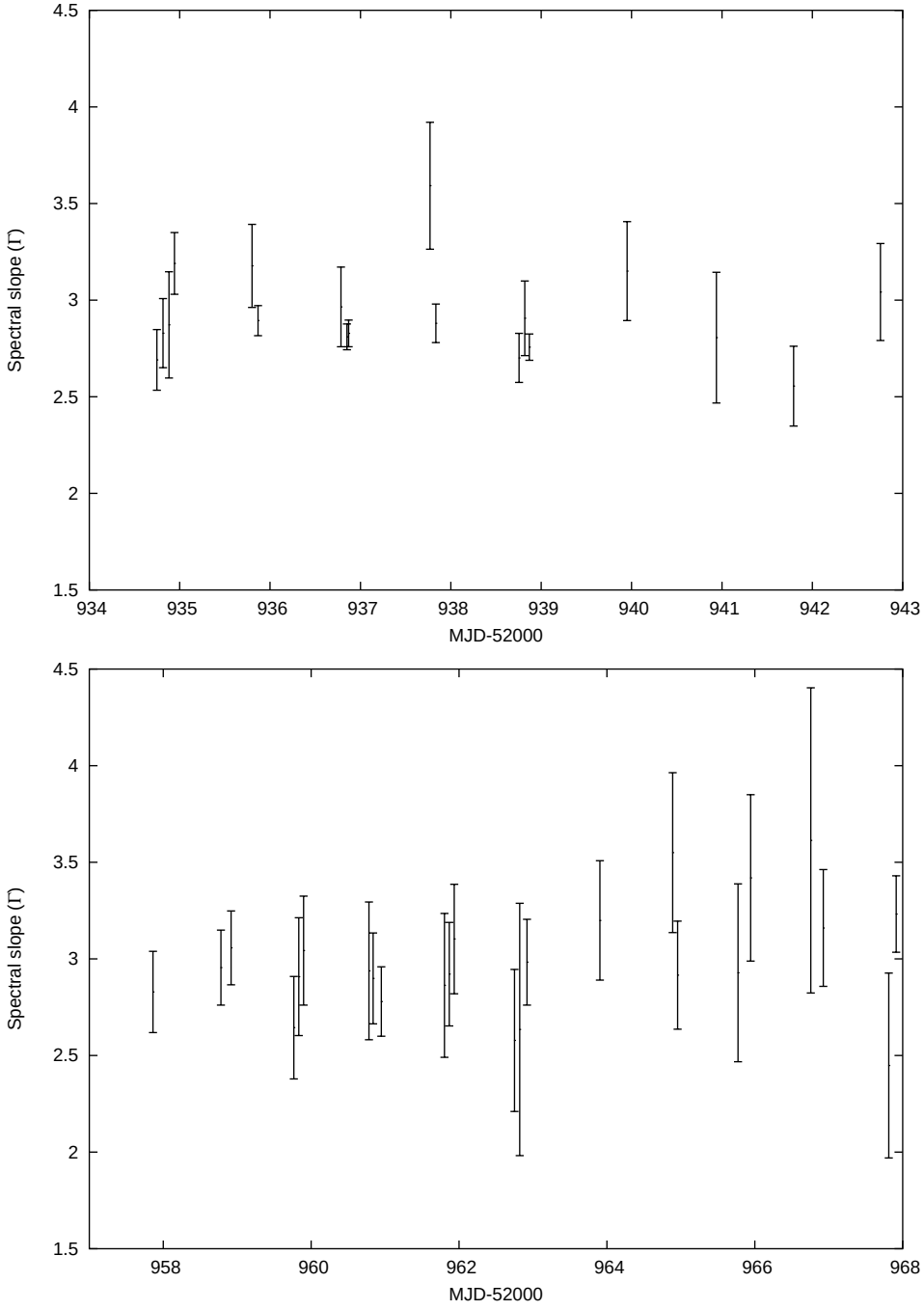

Figure 4.10: Photon index, Γ, versus MJD for a power law fit to each seperate pointed observation with PCU 2. The top panel shows the photon indices for the October observations, while the bottom panel shows the photon indices for the November observations.

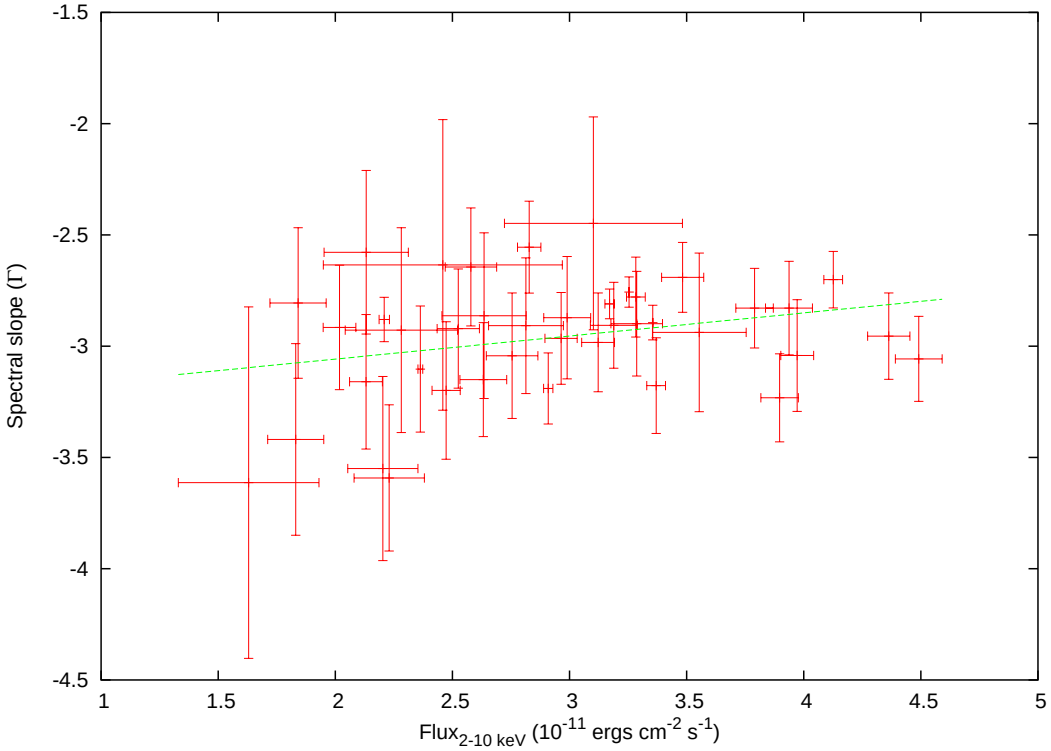

Figure 4.11: 2−10 keV flux versus the 3−10 keV photon index, Γ, from a power law fit to the observations from PCU 2. The dashed line is a linear fit to the data, with slope = 0.104 ± 0.057.

to what it is attributed is still an area of much debate.

Figure 4.11 has been fitted with a linear function using a least square fitting method. Although there is a large amount of scatter around the linear function, the reduced χ^2 is not unreasonable, 0.07 for 38 degrees of freedom. However, it should be pointed out that such a small reduced χ^2 indicates that the linear trend could probably be attributed to the large errors of the data points. Nonetheless, assuming that the linear trend of Fig. 4.11 is real, with a slope of 0.10 ± 0.06, the trend implies that $\Gamma_{3-10\mathrm{keV}} \propto 0.1 \times \ F_{2-10\mathrm{keV}}$.

It should be pointed out that, while the relationship between the flux and the spectral slope is often described as a linear function, the nature of this relation depends upon the area of the SED which we are observing. For a quadratic function and a small change in x, the change in the instantaneous slope is lowest around the turning point of the function. Therefore, if the low

energy peak is close to the energy range in which we are observing, which is indeed likely for PKS 2155−304 due to its brightness at UV and X-ray energies, any change in the spectral slope due to the 'harder when brighter' behaviour would be less obvious. In a flux versus slope graph, this would result in a softening of the 'harder when brighter' behaviour towards a constant horizontal line. There is evidence for this in Figure 4.11. A positive correlation between flux and spectral slope is most obvious with the data for fluxes less than 3×10^{-11} ergs cm^{-2} s^{-1}. Above this flux, there is no dramatic increase in the spectral slope.

Interestingly the softening of the 'harder when brighter' behaviour that is seen in Fig. 4.11 has been observed before. Using *BeppoSax*, Zhang et al. observed a simliar trend when the spectral index at 5 keV was plotted against the 2-10 keV flux. This plot can be seen in Fig. 4.12.

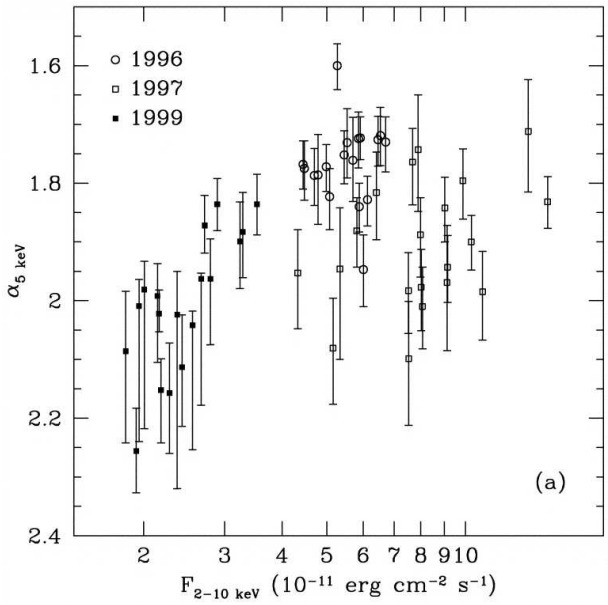

Figure 4.12: 2−10 keV flux versus the 5 keV spectral index from Zhang et al. [197]. The softening of the 'harder when brighter' behaviour can be seen at higher fluxes, with the trend tending towards a constant horizontal line. Image courtesy of [197].

4.3 Optical & Radio observations

4.3.1 Optical data reduction

The optical observations for the October/November 2003 campaign were made with the ROTSE-IIIa and ROTSE-IIIc telescopes. These telescopes are part of the ROTSE-III telescope array, a worldwide network of four 0.45 m robotic, automated telescopes. With a wide field of view ($1.85° \times 1.85°$), the ROTSE-III telescopes are designed for fast response to GRB triggers. Operated without filters, the large field of view of the ROTSE-III telescopes is imaged onto a Marconi 2048×2048 pixel back-illuminated thinned CCD. For an in-depth description of the ROTSE-III systems, see Akerlof et al. (2003) [13].

Throughout the October/November 2003 multi-wavelength campaign on PKS 2155−304, two ROTSE-III telescopes were operational in the Southern Hemisphere: ROTSE-IIIc, located in the centre of the H.E.S.S. telescope array, and ROTSE-IIIa, located at the Siding Spring Observatory, Australia. Both of these telescopes took part in this campaign.

During the campaign, the telescopes observed PKS 2155−304 typically 10 times per night, each observation consisting of 2×60 second exposures with a slight dithering of the pointing ($\sim$ 10 pixels) between each exposure to reduce the impact of noisy pixels. In total, 323 bias-subtracted and flat-field frames were used to construct the lightcurve shown in Figure 4.13. It should be noted that the ROTSE-III observations extend 3 weeks either side of the multi-wavelength campaign, such that the data shown in Figure 4.13 extends from the beginning of October to the end of November. The relative flux variations and associated error for each observation were calculated using 50 isolated comparison stars, all of which are similiar in brightness, in the field of view [5].

Evidence for flaring in the optical regime is clearly visible throughout the campaign, Figure 4.13. However, while the majority of these flares are completely resolved, the most active period for optical variability occurs during the 'moontime', 52940< MJD <52950. As stated in Chapter 3, due to the sensitivity of the PMTs used in the camera, the H.E.S.S. telescopes are unable

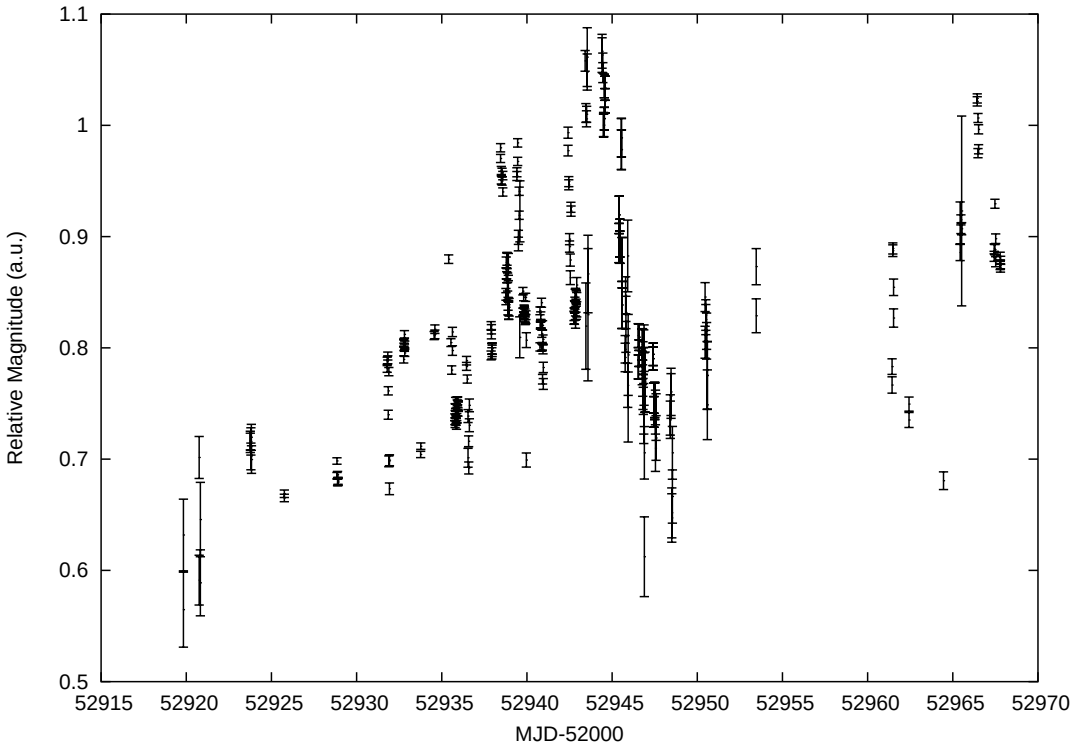

Figure 4.13: Relative fluxes of PKS 2155−304 during October and November 2003, using observations from both ROTSE-IIIa & ROTSE-IIIc.

to make observations when the Moon is above the horizon.

To compare the ROTSE-III observations with archival data, the relative fluxes were converted to absolute R-fluxes by comparing the instrumental magnitude of the source with the USNO catalogue, as described by Akerlof et al. [12, 5]. The absolute fluxes measured by ROTSE throughout the campaign are in the range $13.3 < \mathrm{m(R)} < 13.7$ magnitudes. These limits are lower than that of archival data and therefore the optical observations are also indicating that PKS 2155−304 was in a quiescent state throughout the campaign.

4.3.2 Radio data reduction

The radio observations of PKS 2155−304 throughout the October/November 2003 campaign were obtained using the Nançay decimetric radio telescope, NRT. The NRT is a single dish antenna with a collecting area of 200×34.56 m^2. In general, NRT observations consist of between 4 and 14 individual 1 minute drift scans. Flux calibration is done using the calibrated noise diode emission from the same individual 1 minute scan. The data processing for NRT observations is done on site, with the local Nançay software NAPS and SIR.

For the October/November 2003 campaign, the radio observations of the NRT consisted of a measurement every 2 or 3 days, with a total of 8 NRT observations throughout the campaign. These observations were taken at 11 cm wavelength (2695 MHz). For the 8 observations, an average flux of 0.30 ± 0.01 Jy was measured, with marginal evidence for variability [5].

Chapter 5

Discussion and Interpretation of 2003 Campaign

Previous to our 2003 campaign there had been numerous multi-wavelength studies of PKS 2155−304, see Section 1.5. However, these past studies did not include VHE observations and therefore did not study a substantial percentage of the total energy output from this object. More over, past VHE observations of PKS 2155−304 appear to have occurred during an active state, as indicated by the increased X-ray emission [43, 44]. As mentioned in Section 4.2.2 and Section 4.3.1, the X-ray and optical observations during October/November 2003 are close to historically low values for PKS 2155−304, indicating that the source is in a quiescent state. We are therefore able to, for the first time, probe the jet parameters and models of a quiescent HBL. The implications for this are quite important. The models for VHE emission from HBLs have evolved over the last 14 years since Mkn 421 was detected as a VHE emitter. However, the sensitivity of the past generations of VHE telescopes has only been sufficient to observe VHE emission from HBLs during apparent active states. These evolved models are therefore essentially high active state emission models. Since the sensitivity of H.E.S.S. now allows us to detect these objects in a quiescent state, the obvious question is, do the 'active state' models still accurately predict the SED and in particular, the VHE emission? In this Chapter the observations reported in Chapter 4 will be used to probe the emission models and jet physics for PKS 2155−304 during October/November 2003.

5.1 Constraints on Jet Parameters

5.1.1 Flux Variability

Since information cannot be transmitted at a speed greater than the speed of light, the variability timescale of a 'flaring' event can be used to derive an upper limit on the size and Doppler factor of the emission region. Referred to as causality, the upper limit of the emission region is given by Eq. 5.1, where R is the size of the emission region, t_{var} is the variability timescale and δ is the Doppler factor of the emission region. (Note that $\delta = (\Gamma(1 - \beta\cos\theta))^{-1}$ where Γ is the bulk Lorentz factor of the emission region, $\beta = \frac{v}{c}$ and θ is the angle to the line of sight).

$$R \leq ct_{var}\frac{\delta}{1+z} \tag{5.1}$$

Considering the biggest flaring event present at both X-ray and VHE $\gamma-$ray energies, taking the variability timescale to be the rise-time of the X-ray flare ($t_{var} \approx 2 \times 10^3$ seconds) from Section 4.2.3, and taking the redshift of PKS 2155−304 to be 0.117, the size of the emission region is:

$$R\delta^{-1} \leq 5.4 \times 10^{13}\text{cm} \tag{5.2}$$

5.1.2 Photon-photon pair production opacity

The detection of VHE photons implies that the emission region is transparent to photon-photon interactions between VHE $\gamma-$rays and NIR/O photons, with the opacity of photon-photon interactions, $\tau_{\gamma\gamma}$, being less than one. Relativistic beaming of the radiation emitted by the jet reduces the opacity of the emission region since the pair-production interaction cross-section tends to zero when the photons are travelling in the same direction. The opacity of the emission region is given by:

$$\tau_{\gamma\gamma} \approx \frac{\sigma_T}{5}\frac{1}{hc}\frac{d_L^2}{R}\frac{1}{\delta^3(1+z)}F(\nu_i) \tag{5.3}$$

where σ_T is the Thompson cross section, d_L is the luminosity distance to

the source given by Eq. 5.4 and $F(\nu_i)$ is the flux density of the radiation field that interacts with the VHE photons and is given by Eq. 5.5 [121, 64].

$$d_L = \frac{c}{H_o}\left(z + \frac{z^2(1-q_o)}{1+q_o z+\sqrt{1+2q_o z}}\right) \tag{5.4}$$

Throughout this thesis, for the luminosity distance calculation, a Freidmann universe is assumed with $q_o = 0.5$ and $H_o = 70$ km s^{-1}Mpc^{-1}.

$$h\nu_i \approx \frac{2(m_e c^2)^2}{h\nu_\gamma}\frac{\delta^2}{(1+z)^2} \tag{5.5}$$

Assuming that $F(\nu_i)$ is a power law, such that $F(\nu_i) \propto \nu^{-\alpha}$, then the spectral slope of the X-ray spectra can be used to calculate the flux density of the target photon field. It should be noted that the flux density of photons close to the threshold, where the $\gamma\gamma$ cross section is at its maximum, may differ slightly from that calculated from the X-ray slope, depending upon the amount of Doppler boosting of the emission region. However, interpolating the slope from a fit to the synchrotron bump shows little difference and thus the flux density calculated from the X-ray slope is satisfactory [142]. Imposing that $\tau_{\gamma\gamma} < 1$ for E_γ =1 TeV photons, we can derive an upper limit for δ and R. Taking the $h\nu_i$ to be Eq. 5.5 gives:

$$\frac{\sigma_T}{5}\frac{1}{hc}\frac{d_L^2}{R}\frac{1}{\delta^3(1+z)}\left(\frac{2(m_e c^2)^2}{h\nu_\gamma}\frac{1}{h}\frac{\delta^2}{(1+z)^2}\right)^{-\alpha} \leq 1 \tag{5.6}$$

$$\therefore R^{-1}\delta^{-3-2\alpha} \leq \left(\frac{\sigma_T}{5}\frac{1}{hc}\frac{d_L^2}{(1+z)}\right)^{-1}\left(\frac{2(m_e c^2)^2}{h\nu_\gamma}\frac{1}{h}\frac{1}{(1+z)^2}\right)^{\alpha} \tag{5.7}$$

Solving Eq. 5.7 numerically, with $\alpha = 1.7$ from the simultaneous X-ray observations, $h\nu_\gamma = 1$ TeV, $d_L = 1.59\times10^{25}$ m and z = 0.117, gives Eq. 5.8. It should be noted that the spectral slope (energy cm^{-2} s^{-1}), is slightly different to the photon index (number of photons cm^{-2} s^{-1}) derived from the spectral fitting.

$$R^{-1}\delta^{-6.4} \leq 5.6\times10^{-24}\text{cm}^{-1} \tag{5.8}$$

5.1.3 *Emission Model-Independent* Minimum δ

Assuming that the VHE $\gamma-$rays and X-rays emission regions are co-spatial, we are able to obtain a *emission model-independent* value for the minimum allowable Doppler factor, δ, by combining Eq. 5.2 and Eq. 5.8. The minimum allowable Doppler factor is given by Eq. 5.9.

$$\delta \geq 19.4 \tag{5.9}$$

The minimum Doppler factor calculated in Eq. 5.9 is marginally smaller than the Doppler factor derived in similiar fashion by Tavecchio et al. and Kino et al. [180, 103]. It is also slightly smaller than the value calcuated by Kataoka et al. for PKS 2155−304 using SSC modelling [102]. However, it should be pointed out that while Tavecchio et al. used similiar methods to those used here, they used a t_{var} of 2×10^4, one order of magnitude larger than the observed t_{var} during the October/November 2003 campaign. Compensating for this difference in t_{var}, we find that our minimum Doppler factor is larger than that derived by Tavecchio et al.

The two conditions that govern this model-independent Doppler factor, and their exclusion regions in the (R,δ) plane, are shown in Figure 5.1. The grey shaded regions are R and δ solutions that are do not satisfy Eq. 5.2 & 5.8, given a t_{var} of 2×10^3 seconds measured from the rise-time of the X-ray flare. It should be pointed out that these solutions are only viable if the VHE $\gamma-$ray and X-ray emission regions are co-spatial, that is, if the *single-zone model* is applicable. This assumption will be addressed in Section 5.2.

5.1.4 *Model-Dependent* Jet Parameter Constraints

Further constraints can be placed on the jet parameters by assuming that the broadband SED emission is dominated by a single-zone homogeneous Synchrotron Self-Compton model, as described in Section 2.2.1. Conversely the derived jet parameters can be used to probe the validity of the SSC model. In this section, we are assuming that the emission is dominated by a spherical blob, with radius R, a bulk Lorentz factor Γ and viewed at an angle θ.

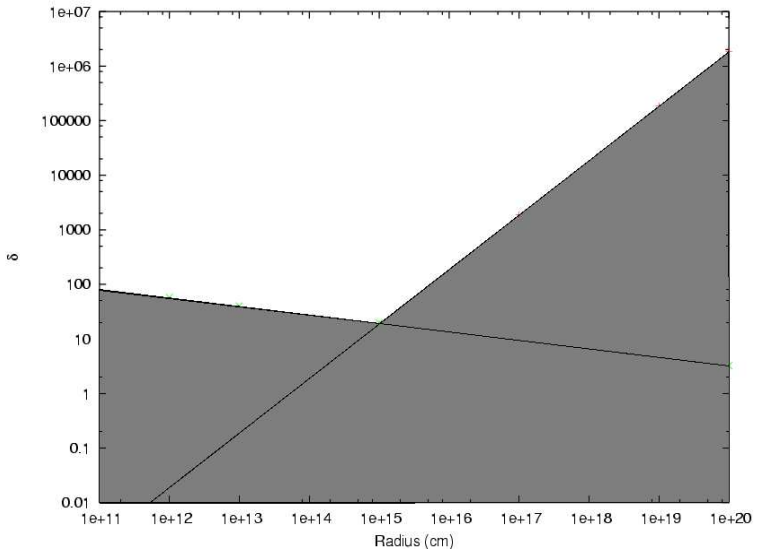

Figure 5.1: Exclusion regions in the (R,δ) plane which satisfy the causality and $\gamma\gamma$ opacity criteria of Eq 5.2 and 5.8 respectively. The minimum allowable Doppler factor, δ, is 19.4.

Isotropically filled with a relativistic electron population, the emission region has an associated magnetic field, B, that is randomly orientated.

Maximum electron energy

Assuming that the $2-10$ keV emission is due to synchrotron emission from the relativistic electron population, we can begin to constrain the magnetic field strength of the emission region. The observed synchrotron frequency of an electron with Lorentz factor γ_e is given by Eq. 5.10 [180, 102].

$$\nu_{syn} = 10^6 \left(\frac{\delta}{1+z}\right) B\gamma_e^2 \tag{5.10}$$

Taking the maximum observed synchrotron emission to be 10 keV, or 2.4×10^{18} Hz, the maximum Lorentz factor of the electron population is given by:

$$\gamma_{max} = 1.64 \times 10^6 B^{-\frac{1}{2}} \delta^{-\frac{1}{2}} \tag{5.11}$$

Within the SSC model, the same population of relativistic electrons are

responsible for boosting ambient photons to VHE energies. From Figure 4.2 we can see that while the VHE spectrum extends up to 3 TeV (in the reference frame of the observer), the residuals to the power law fit above 2 TeV are large. Therefore taking the maximum photon energy to be 2 TeV gives:

$$\gamma_{max} m_e c^2 \left(\frac{\delta}{1+z}\right) \geq 2 \text{ TeV} \tag{5.12}$$

Combining Eq. 5.11 and Eq. 5.12 gives:

$$B\delta^{-1} \leq 0.14 \text{ G} \tag{5.13}$$

Using Eq. 5.9, Eq. 5.11 and Eq. 5.13 we can constrain the Lorentz factor, γ_{max}, of the electrons to $\gamma_{max} = 2.2 \times 10^5$. This value is slightly less than the 5×10^5 calculated by Takahashi et al. for Mkn 421 and two orders of magnitude smaller than the $\gamma_e = 10^7$ calculated by Giebels et al. 1ES 1959+650 [178, 81]. It should be noted that the values for γ_e and δ_{min} calculated here are slightly different to those calculated by Aharonian et al. [5]. This is primarily due to Aharonian et al. considered the VHE $\gamma-$ray spectrum up to an energy of 3 TeV and the propagation of rounding off differences.

Spectral Energy Distribution Peaks

Past multi-wavelength campaigns on PKS 2155−304, have shown that the synchrotron component peaks at UV energies, $\sim 2 \times 10^{16}$ Hz [188]. Unfortunately no UV observations were taken as part of this campaign. Assuming that the position of the synchrotron peak during October and November 2003 was in a similiar position (proven *a posteriori* by the SSC fits in Section 5.3), then the peak synchrotron energy in the jet's rest frame is given by Eq. 5.14 [142].

$$e_{peak} \approx e_{peak}{}' \left(\frac{1+z}{\delta}\right) \tag{5.14}$$

In the SSC model, these synchrotron photons are then boosted to VHE energies via the Inverse Compton mechanism, see Section 2.1.2. Assuming that this interaction occurs in the Thompson regime, the photons are boosted, at most, by a factor of γ^2_{max} such that the maximum energy is $\gamma^2_{max} e_{peak}$. Since

the density of synchrotron photons decreases above e_{peak}, then the maximum energy from the IC process must be at most the rest frame energy of the Compton peak, $h\nu_{IC}$.

$$\gamma_{max}^2 e_{peak} \geq h\nu_{IC} \left(\frac{1+z}{\delta}\right) \tag{5.15}$$

Combining Eq. 5.10, Eq. 5.14 and Eq. 5.15, with $\nu_{syn} = 2 \times 10^{16}$ Hz and $\nu_{IC} = 2.4 \times 10^{25}$ Hz (again proven *a posteriori* by the SSC fits in Section 5.3), gives Eq. 5.16.

$$B\delta \leq 840 \text{ G} \tag{5.16}$$

Thompson/Klein-Nishina regime

As discussed in Section 2.1.2, due to the decrease in the IC interaction cross-section in the Klein-Nishina regime, the majority of the IC scattering occurs in the Thompson regime. A photon with rest frame energy of e_{peak} will be scattered in the Thompson regime if the scattering electron satisfies:

$$\gamma e_{peak} \leq 511 \text{ keV} \Longrightarrow \gamma \leq 6200 \left(\frac{\delta}{1+z}\right) \tag{5.17}$$

Using a similiar approach to Eq. 5.10 and Eq. 5.11, but using the synchrotron peak frequency of $\nu_{peak} \approx 2 \times 10^{16}$ Hz, instead of the maximum synchrotron frequency, gives:

$$\gamma_{peak} = 1.5 \times 10^5 B^{-\frac{1}{2}} \delta^{-\frac{1}{2}} \tag{5.18}$$

Combining Eq. 5.17 and Eq. 5.18, gives us the following constraint:

$$B\delta^3 \geq 730 \text{ G} \tag{5.19}$$

Maximum energy/SED peaks/Thompson–K-N Constraints

The limits from the maximum electron energy, the Spectral Energy Distribution peaks and the Thompson/K-N regime are summarised below.

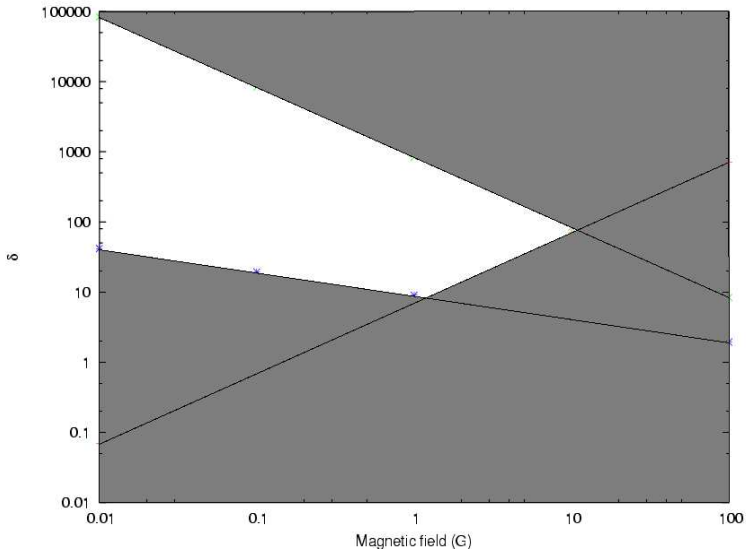

Figure 5.2: Exclusion regions in the (B,δ) plane which satisfy the criteria of Eq. 5.20, Eq. 5.21 and Eq. 5.22. The maximum allowed Magnetic field strength, assuming a single-zone SSC model, is ≈10.9 G. Notice that the minimum Doppler factor allowed is marginally smaller than that in Fig. 5.1.

$$B\delta^{-1} \leq 0.14 \text{ G} \tag{5.20}$$

$$B\delta \leq 840 \text{ G} \tag{5.21}$$

$$B\delta^{3} \geq 730 \text{ G} \tag{5.22}$$

Combining Eq. 5.20 and Eq. 5.21 gives us an upper limit for the magnetic field strength of the emission region, Eq. 5.23, assuming that the single-zone SSC model is dominant.

$$B \leq 10.9 \text{ G} \tag{5.23}$$

The exclusion regions in the (B, δ) plane, governed by Eq. 5.20, Eq. 5.21 and Eq. 5.22 are shown in Fig. 5.2. Again, the grey shaded regions indicate regions of the (B, δ) plane that are not allowed. Notice that the minimum Doppler factor, δ, from Fig. 5.2 is only marginally smaller than that allowed by the model independent causality/$\gamma\gamma$ opacity argument.

Synchrotron cooling

In attempt to further constrain the jet parameters, let us assume that the fall-time of the X-ray flare seen between 936.93 < MJD < 936.96 is associated with the cooling of the electron population via synchrotron emission. Taking the variability timescale to be the fall-time of the X-ray flare, $t_{var} \approx 2 \times 10^3$ seconds, we are able to constrain the magnetic field strength and the Doppler factor further. As described in Section 2.1.1, the synchrotron cooling timescale is given by Eq. 2.4. Substituting in the maximum Lorentz factor, given by Eq. 5.10, into Eq. 2.4 gives:

$$t_{syncool} = 515.9 B^{-\frac{3}{2}} \left(\frac{\delta}{1+z} \right)^{\frac{1}{2}} \tag{5.24}$$

Assuming that the observed fall in X-ray flux is purely due to synchrotron cooling of the electrons, such that $t_{syncool} \leq t_{var}$, gives:

$$B^{-3}\delta \leq 15 \text{ G}^{-3} \tag{5.25}$$

Taking Eq. 5.25 into consideration on the (B, δ) plane, gives Fig. 5.3. The region of the (B, δ) plane that does not statisfy Eq. 5.25 is shaded green. While at first glance the pure synchrotron cooling assumption does appear to constrain the B and δ parameters futher, it should be noted that Eq. 5.25 is the least robust of the constraints given so far. Cooling the relativistic electrons through synchrotron emission alone does not allow for cooling through the IC process. Therefore, the VHE emission cannot be produced via the IC scattering of ambient photons by the relativistic electron population and the SSC model would not apply.

Furthermore, if the cooling was purely due to synchrotron emission, one would expect spectral variations to accompany the flux variability, for which there is only marginal evidence for at best, see Fig 4.11. These expected spectral changes would be in the form of a breaking of the X-ray spectrum due to the higher energy electrons cooling quickest, see Section 2.1.1. As the electron population 'ages' one would expect to see a break in the spectrum, with the spectrum better described by a broken power law. The break energy

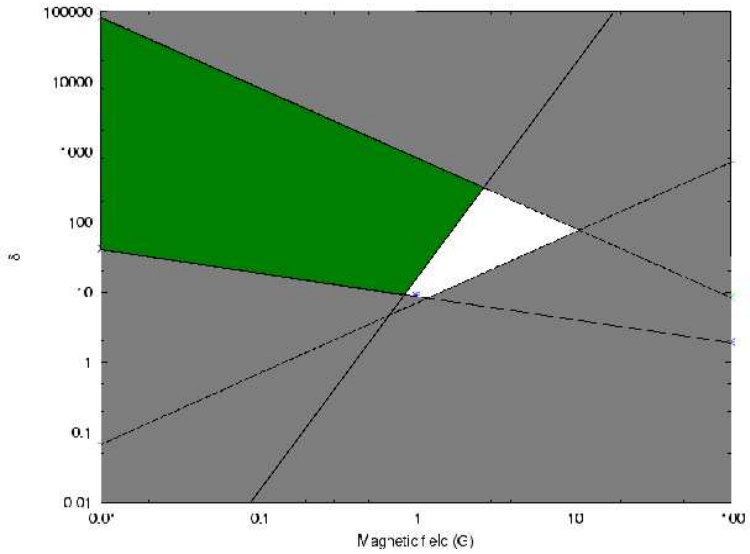

Figure 5.3: The addition exclusion regions in the (B,δ) plane associated with the synchrotron cooling constraint are filled green.

of the broken power law would shift to lower energies as the electron population is cooled by synchrotron emission. As discussed in Section 4.2.2, this is not seen.

Due to the unrealistic constraint imposed by assuming cooling through synchrotron emission alone, the following, assuming a single-zone SSC model, can be concluded:

- Cooling of the electron population is not through synchrotron emission alone.
- Variability could be due to changes in the number of accelerated particles injected into the emission region.

It should be noted that the constraint imposed by Eq. 5.25 will be relaxed hereon and thus the (B, δ) plane is described by Fig. 5.2.

5.2 Correlation studies

The jet parameters that have been constrained so far have been constrained under the assumption that the optical through to VHE emission regions are

co-spatial (*single-zone* model). To test whether this assumption is reasonable we can look for correlated flux variability at VHE, X-ray and optical energies. Correlated flux variability between two or more of these energy bands implies that the emission is from the same particle population and hence the emission regions for each energy band are co-spatial. Furthermore, as mentioned in Section 2.2.1, the SSC model predicts that any synchtrotron flux variation will be accompanied by a quasi-simultaneous variation in the IC flux. Thus, finding a correlation between the VHE flux and either the X-ray or optical flux would give weight to the SSC model.

In order to look quantitatively for correlated variability between the different energy bands, the measured VHE, X-ray and optical fluxes reported in Chapter 4 were plotted against each other, see Figures 5.4, 5.5 and 5.6. Only simultaneous data were considered, resulting in a total of 17 VHE/X-ray data points, 13 VHE/Optical data points and 9 X-ray/Optical data points. Figures 5.4, 5.5 and 5.6 show no obvious evidence of a correlation between any of the energy bands. At best, the VHE/X-ray data has a correlation factor of -0.18 ± 1.1, the VHE/Optical data has a correlation factor of 11 ± 7.4 and the X-ray/Optical data has a correlation factor of 1.6 ± 5.5. In all cases the uncertainty associated with the correlation factor is unacceptably large.

The lack of correlation between the flux levels of the different energy bands indicates that the assumption of a single emission zone may be incorrect and that the SSC model may not be dominant. However, it should be stressed that it is unclear whether the 'non-correlation' behaviour is characteristic of a quiescent HBL or whether it is due to the small dynamic range (1-2), of our observed variability. Past studies on Mkn 421 have indicated a strong VHE/X-ray correlation, but with a much larger amount of variability (dynamic range $\sim$30) [56]. Future observations of PKS 2155$-$304 with a higher variability range will give us insight into whether a highly variable PKS 2155$-$304 exhibits any correlation and hence whether the 'non-correlation' behaviour is just a characteristic of a quiescent PKS 2155$-$304 or of PKS 2155$-$304 in general. However it should be pointed out that quiescent HBLs, due to their low activity level, are unlikely to exhibit variability with a large dynamic range.

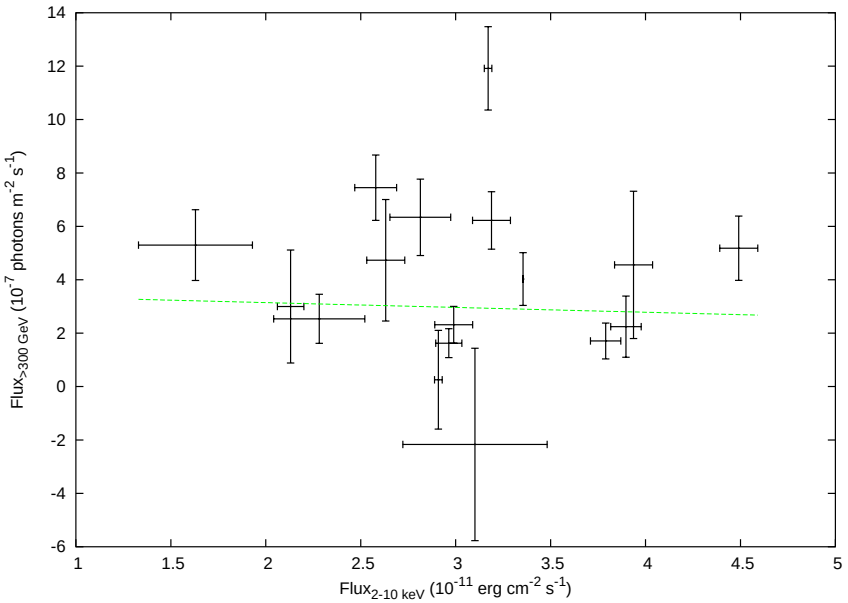

Figure 5.4: Simultaneous VHE $\gamma-$ray and X-ray flux measurements. No obvious correlation can be seen. Note that the linear function implies a correlation of -0.18 ± 1.1.

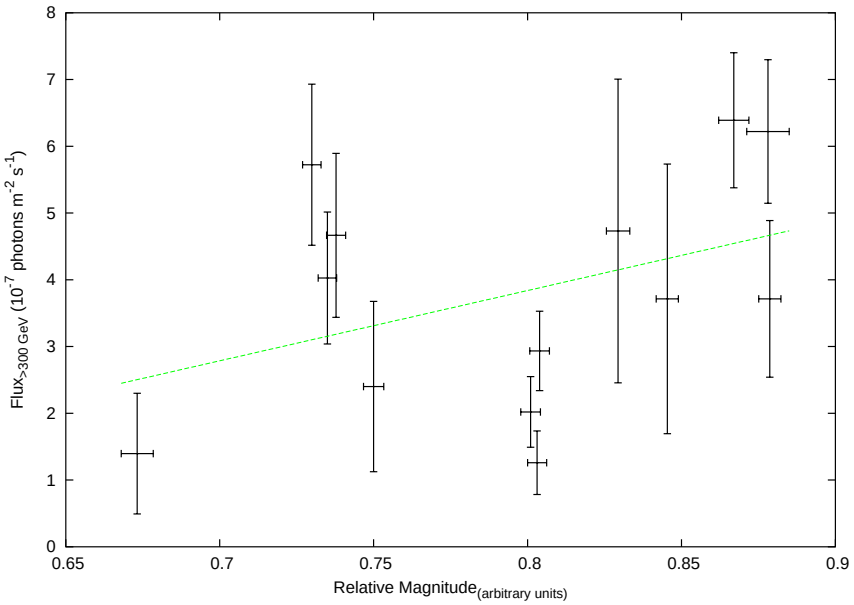

Figure 5.5: Simultaneous VHE $\gamma-$ray and optical flux measurements. No obvious correlation can be seen. Note that the linear function implies a correlation of 11 ± 7.4.

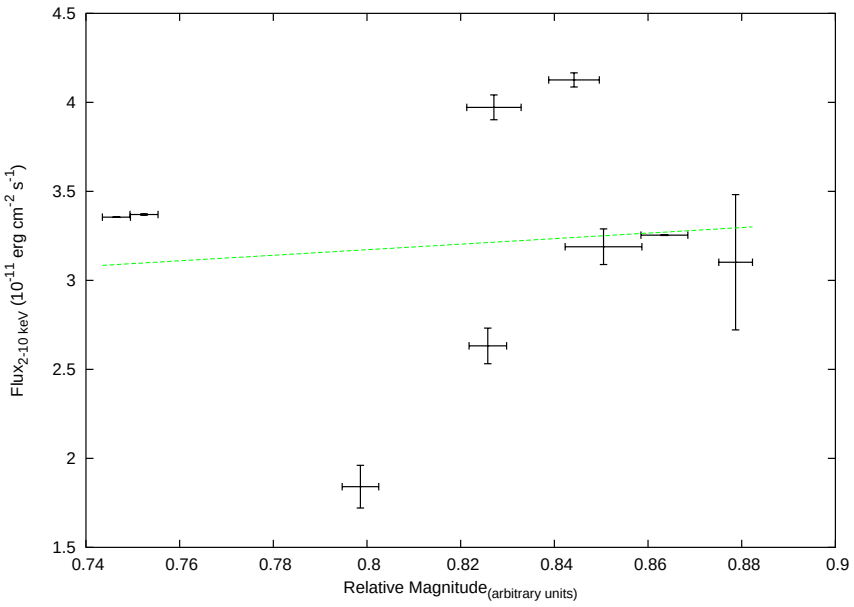

Figure 5.6: Simultaneous X-ray and optical flux measurements. No obvious correlation can be seen. Note that the linear function implies a correlation of 1.6 ± 5.5.

5.3 SED modelling

As discussed in Section 2.2, the broadband spectral energy distribution of PKS 2155−304 is typical of a High Energy BL Lac object, with double humped structure in the νF_ν representation. The emission from HBLs is often attributed to a population of highly relativistic electrons, in the form of the SSC model (see Section 2.2.1 for description). Figure 5.7 is the SED of PKS 2155−304 for October/November 2003, in units of power per logarithmic bandwidth versus frequency. Since PKS 2155−304 appeared to be in a quiescent state during our campaign, archival observations are unlikely to be representative of the activity state of PKS 2155−304 during the campaign and therefore are not considered for the SED modelling. It should be noted that the ROTSE data points have already been corrected for any host galaxy contribution which has been estimated to be no greater than 10^{-11} ergs cm^{-2} s^{-1} [5].

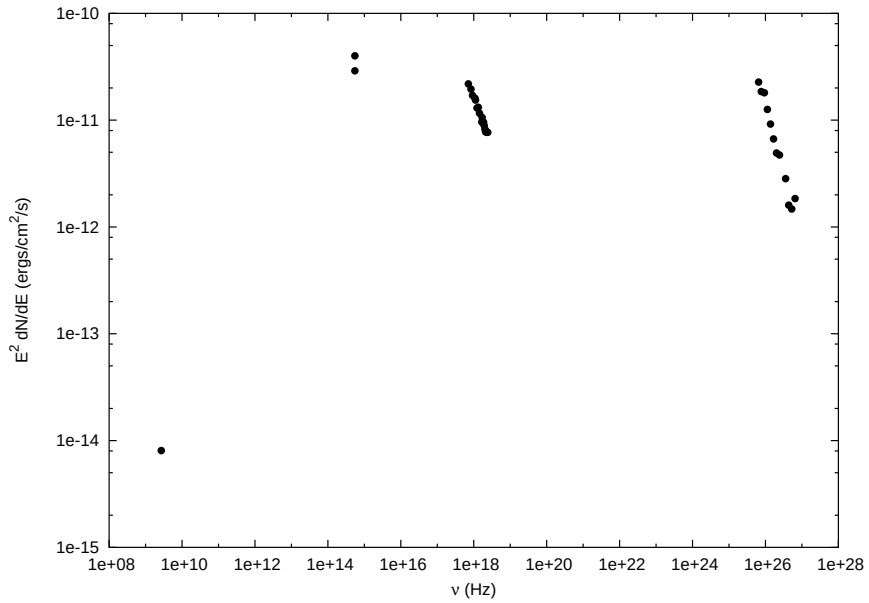

Figure 5.7: The spectral energy distribution of PKS 2155−304 during October and November 2003. Note that the H.E.S.S., RXTE and NRT data points are the averaged value from the observations during the campaign, whilst the ROTSE data is respresented by the highest and lowest measurements during the campaign.

5.3.1 Single-zone SSC interpretation

For consistency, the SED shown in Fig. 5.7 should be interpreted in relation to a single-zone SSC model, as was done in Section 5.1.4 regarding the variability. The model[1] applied assumes a single spherical emission region of radius, R, magnetic field, B and Doppler factor, δ. The spherical emission region is isotropically filled with an electron population described by a broken power law. Ranging from E_{min} to E_{max}, with the break at E_{break}, the spectral indices of the broken power law before and after the spectral break are fixed at $p_1 = 2$ and $p_2 = 3$ respectively [106]. It should be noted that the broken power law takes into consideration a certain amount of cooling of the electron population.

For the SSC modelling of the SED for October/November 2003, the magnetic field strength, Doppler factor and size of the emission region, along with the electron population distribution within the emission region, were all con-

[1]The SSC code is readily available at http://jelley.wustl.edu/multiwave, last accessed 12/06/2006

Table 5.1: Summary of fit parameters for the different emission constraints for the October/November 2003 campaign.

	Optical/X-ray/VHE fit	X-ray/VHE fit
δ	30	32
B (G)	0.145	0.25
R (m)	7×10^{13}	2×10^{13}
$E_{density}$ (ergs/cm^3)	0.135	0.3
$\log(E_{min}/\mathrm{eV})$	7.0	7.0
$\log(E_{break}/\mathrm{eV})$	9.25	9.95
$\log(E_{max}/\mathrm{eV})$	11.1	11.0
Reduced χ^2/d.o.f	1.31/31	1.73/30

sidered to be free parameters. The best model fit was found by varying the free parameters to minimise the reduced χ^2 of the model fit.

Initially an attempt was made to fit the complete SED with a single-zone SSC model. This implies that the radio, optical, X-ray and VHE $\gamma-$ray emission regions are co-spatial. With a reduced χ^2 of 1.31 for 31 degrees of freedom, the best single-zone SSC fit is shown in Fig. 5.8. The model parameters for this fit are shown in Table 5.1. It should be noted that the high energy tail of the VHE $\gamma-$ray observations contributing the most to the overall reduced χ^2 of the SED fit. Out of interest, an attempt was made to fit the low energy synchrotron curve, without considering the constraint of the VHE data. With a reduced χ^2 of 1.52 for 31 degrees of freedom, the only difference of the model parameters for the synchrotron fit to that of the 'Optical/X-ray/VHE' fit is a slight decrease in the energy density of the emission region ($E_{density} = 0.13$ ergs/cm^3). This smaller $E_{density}$ marginally decreases the reduced χ^2 to the synchrotron fit, but increases the $E_{density}$ to the VHE fit and thus to the overall fit.

Immediately obvious in Fig. 5.8 the large discrepancy between the model fit and the radio observation. Also seen in single-zone SSC fits to the SEDs of other HBLs, the discrepancy between the SSC model and the observations at low energies is often interpreted as an indication that the low energy emission orginates from a region different to that of the X-rays and VHE $\gamma-$rays [106,

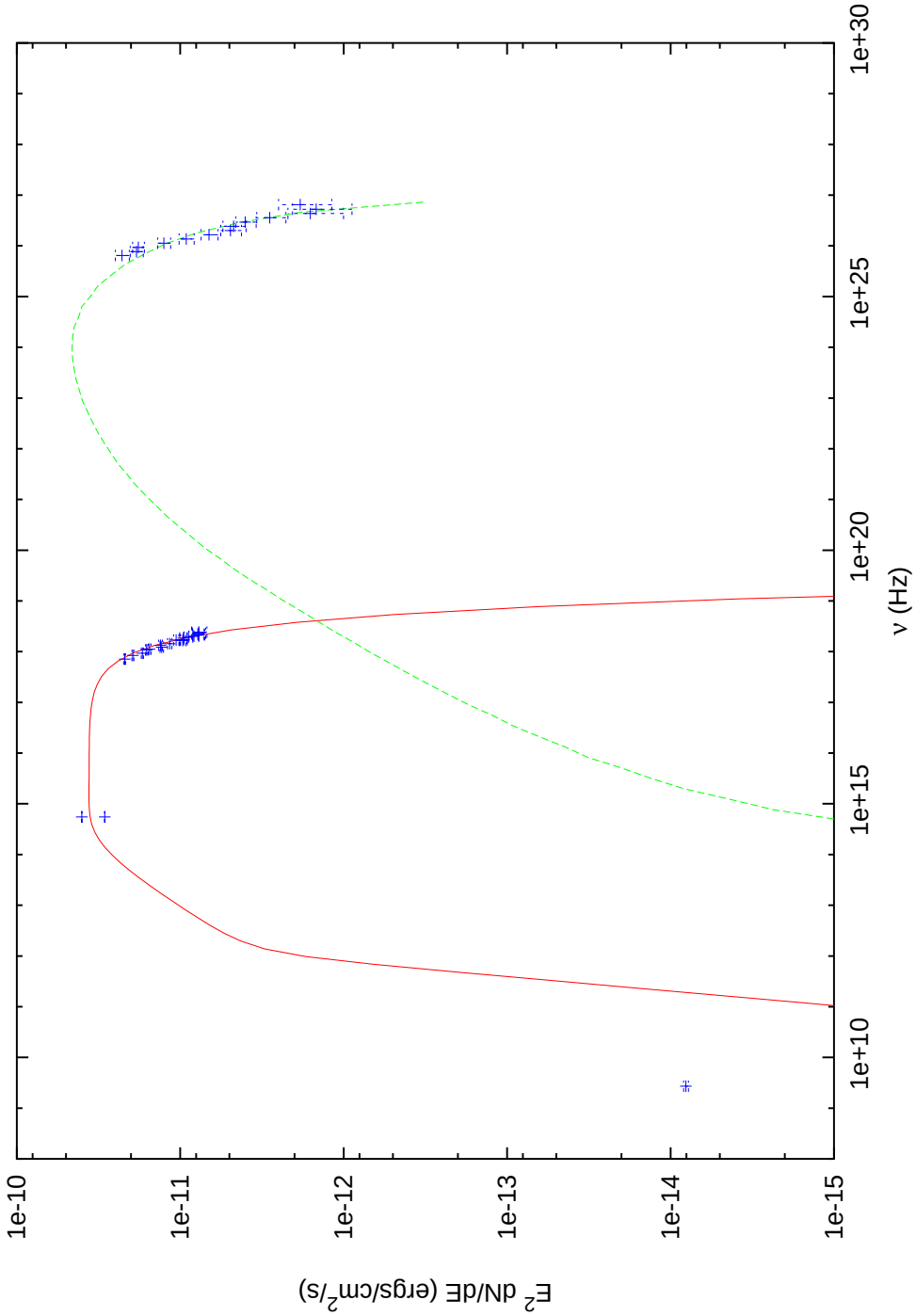

Figure 5.8: Using the same data as Fig. 5.7, the synchrotron continuum is described by the solid line and the IC continuum is described by the dashed line. The model parameters are $\delta = 30$, B = 0.145 Gauss, R = 7×10^{13} m, $\log(E_{min}/\mathrm{eV})$=7.0, $\log(E_{break}/\mathrm{eV})$=11.1, $\log(E_{max}/\mathrm{eV})$=9.25 and an electron energy density of 0.135 ergs cm^{-3}.

5, 140]. Indeed the lack of flux variation of the radio emission throughout the campaign also indicates a different origin for the radio emission, with the VLBI core being the most likely region responsible for the radio emission.

The Doppler factor and magnetic field strength for the fit in Fig. 5.8 are consistent with the constraints derived in Section 5.1. Interestingly however, the Doppler factor given by the best fit is at odds with radio VLBA observations of Piner & Edwards [140], which indicate only modest Doppler factor values of $\delta = 2 - 3$ for PKS 2155−304. Furthermore, the large Doppler factor is also at odds with the unification of BL Lac objects with the family of FR 1 sources [47, 187]. The discrepancies between the modelled Doppler factor, and the observations of Piner & Edwards and the unification model, possibly indicates that there are different velocity structures within the jet, similiar to the different magnetic field structures suggested in Section 1.2.2. The VHE observations probe the inner regions of the jet, with large velocity structures, while the radio observations probe the outer regions of the jet with low velocity structures.

To determine what effect the assumption that the low energy (radio and optical) emission region is co-spatial with that of the X-ray and VHE $\gamma-$ray emission region has on the high energy fit, the radio/optical/X-ray/VHE co-spatial constraint was relaxed. Fitting the same SSC model to just the X-ray and VHE $\gamma-$ray observations, the best fit was found by minimising the reduced χ^2 through varying the free parameters as before. With a reduced χ^2 of 1.73 for 30 degrees of freedom, the best fit to the X-ray and VHE data alone is shown in Fig. 5.9, with the parameters to this fit shown in Table 5.1.

Compared to the optical/X-ray/VHE $\gamma-$ray fit, the best fit parameters for the high energy fit indicate a smaller, more energetic and younger emission region than for the optical/X-ray/VHE $\gamma-$ray fit. Again the parameter values for the high energy SSC fit are consistent with those constrained in Section 5.1. However, it should be pointed out that the reduced χ^2 for the high energy fit is 30% larger (taking into consideration the difference in the number of degrees of freedom).

Interestingly, while the better reduced χ^2 implies that the optical, X-ray and VHE $\gamma-$ray emission regions are co-spatial, the lack of correlation be-

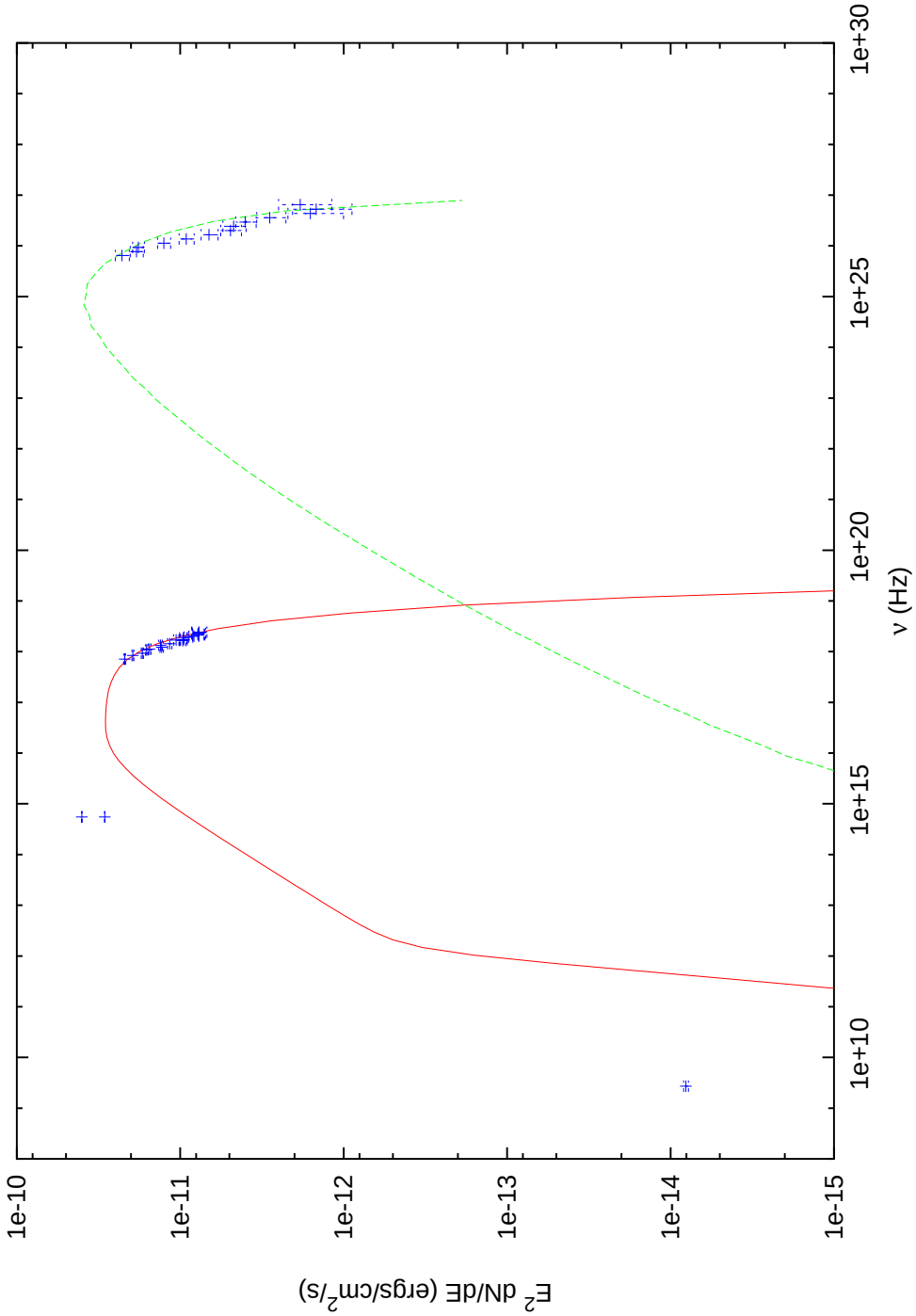

Figure 5.9: Using the same data as Fig. 5.7, the synchrotron continuum is described by the solid line and the IC continuum is described by the dashed line. The model parameters are $\delta = 32$, B = 0.25 Gauss, R = 2×10^{13} m, $\log(E_{min}/\mathrm{eV})$=7.0, $\log(E_{break}/\mathrm{eV})$=11.0, $\log(E_{max}/\mathrm{eV})$=9.95 and an electron energy density of 0.3 ergs cm^{-3}.

tween the different energy band fluxes (as discussed in Section 5.2), appears to indicate otherwise. However, as mentioned, this lack of correlation between the different energy band fluxes may be an artifact of the small dynamic range of variability observed during the October/November 2003 campaign.

5.3.2 Quiescent SSC model?

To investigate other possible models to describe the emission from quiescent HBLs, an inhomogenous jet SSC model[2] was applied [109, 78, 79]. The inhomogenous jet SSC model was chosen as the 'quiescent HBL model' because it assumes a constant injection of particles into the base of the jet. In a quiescent state, it is reasonable to assume that rather than having one large emission region dominant over the other, a steady injection of particles, or at least many small discrete 'blobs' of matter, has a significant contribution to the overall emission. An accurate fit of the inhomogenous jet SSC model to the SED for October/November would give weight to this assumption.

Rather than assuming that a single region is responsible for the overall emission, this jet model assumes emission along the inner 2×10^{18} cm of the jet. With the maximum particle density, local Lorentz factor and magnetic field strength being at the base of the jet, the inhomogenous jet SSC model assumes that the particle density, local Lorentz factor and magnetic field strength all decay along the jet in a power law fashion. To accurately model the effect the observation angle has on the amount of Doppler boosting, an observation angle of 4° between the line of sight and the jet was assumed. This angle is similiar to the one that was calculated by Piner & Edwards using radio observations, [140].

For the best inhomogenous jet SSC model fit, the particle density, magnetic field strength, local Lorentz factor and the bulk Lorentz factor were considered to be free parameters. Shown in Fig. 5.10, the best fit was found by varying the free parameters to minimise the reduced χ^2. The best fit parameters are an initial magnetic field strength of 0.5 G, an initial local Lorentz factor of 10.5×10^5, a particle density of 1.5×10^5 electrons cm^{-3} and an initial

[2]The inhomogenous jet SSC code was written by Dr Latham [109]

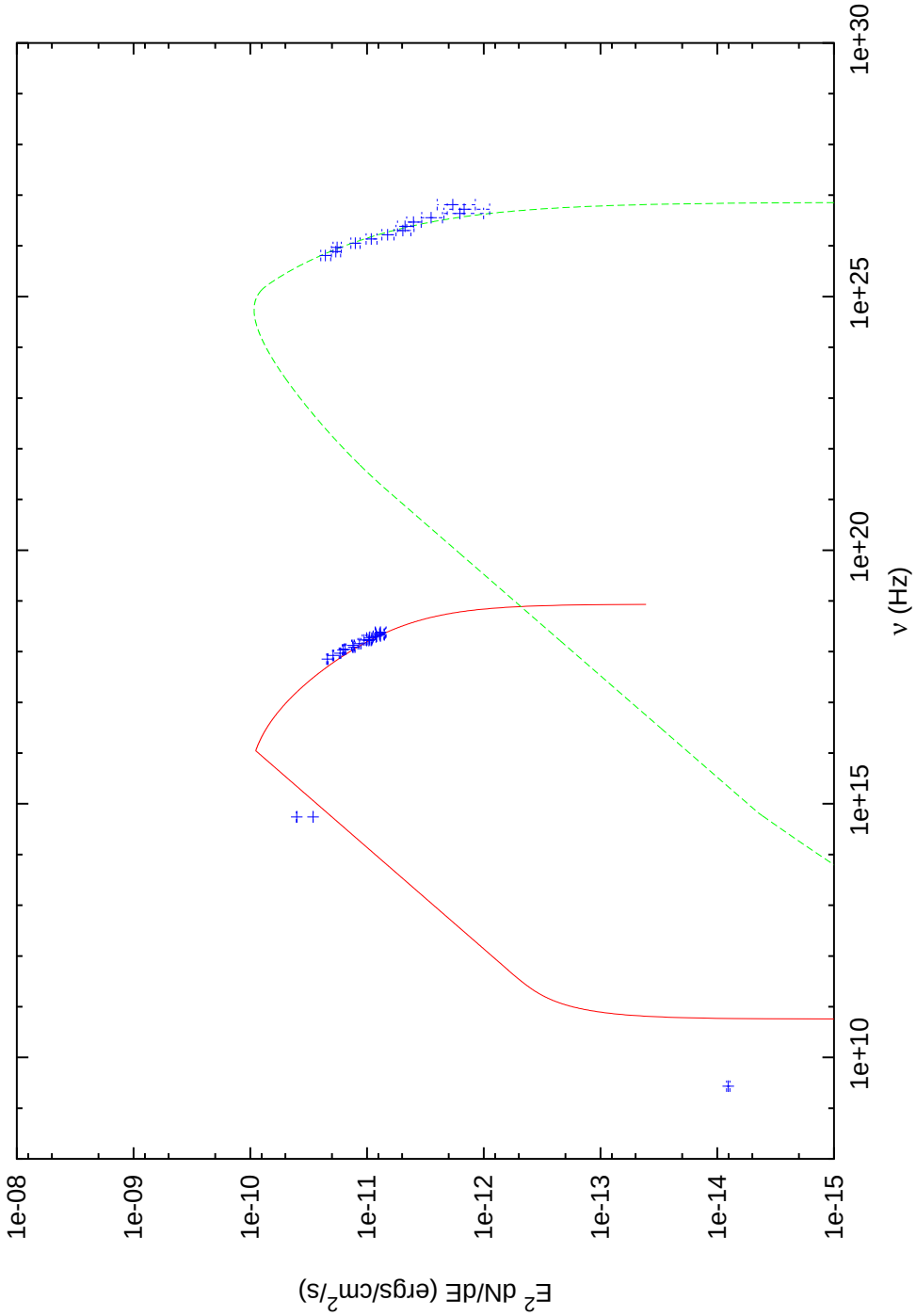

Figure 5.10: The inhomogenous jet SSC model fit to the October/November 2003 SED. The observation data points are as before, with the synchrotron continuum being described by the solid line, the IC continuum being described by the dashed line. Note that the sharp peak of the synchrotron continuum is just an artifact of the model used and is unphysical.

bulk Lorentz factor of 3. However, with a overall reduced χ^2 of 271 for 30 degrees of freedom, this 'best fit' is still inadequate. It should be pointed out that the majority of this reduced χ^2 stems from the poor fit of the model to the high energy tail of the VHE observations. It should also be noted that the discontinuity in the synchrotron spectrum at $\nu \sim 10^{16}$ Hz, is completely unphysical and is a characteristic of the algorithm used in the code.

Considering Fig. 5.10, it is immediately obvious that, just like the SSC fit of Section 5.3.1, the inhomogenous jet SSC model also fails to accurately describe the radio emission, giving further weight to the belief that the radio emission originates from a different location to that of the X-ray and VHE $\gamma-$ray emission. The inhomogenous jet SSC model also appears to under-predict the optical emission. Coupled with the absence of any obvious correlation between the optical and X-ray or VHE fluxes, the under-prediction of the optical flux appears to give weight to the separate emission regions for the low energy and high energy radiation. However, caution should be used with such an interpretation since the poor reduced χ^2 of the inhomogenous jet SSC model fit indicates that the single or multiple zone SSC model is more likely.

5.4 Conclusion

In this chapter, the results of the October/November 2003 multi-wavelength campaign of PKS 2155−304 have been discussed and interpreted. During the campaign, PKS 2155−304 appeared to be in a quiescent state, with both the optical and X-ray flux levels close to historically low values. However, irrespective of the quiet state, PKS 2155−304 was readily detected at very high energies during every night of the campaign.

While PKS 2155−304 appeared to be in a quiescent state throughout the campaign, several 'flaring' events were observed in both the X-ray and VHE energy bands. These flares were short and sharp, with the fastest X-ray flare from PKS 2155−304 being detected during the campaign. With a 50% increase in flux in less than 2000 seconds, the fast flare allowed us to constrain the Doppler factor and magnetic field of the emission region to $\delta \geq 19.4$ and $B \leq 10.9$ respectively. It should be noted that the Doppler factor constraint was

derived from model-independent methods using the causality and $\gamma\gamma$ opacity arguements, while the magnetic field strength constraint was derived assuming that the single-zone SSC model is dominant.

Although variability at optical, X-ray and VHE $\gamma-$ray energies was detected throughout the campaign, there was no obvious correlation between the optical, X-ray or VHE $\gamma-$ray flux levels. Further observations of PKS 2155$-$304, with a greater variability pattern, are needed to determine if the 'non-correlation' behaviour observed during October/November 2003 truly is characteristic of a quiescent PKS 2155$-$304 or just of PKS 2155$-$304 in general.

During the campaign, marginal evidence was found for the harder-when-brighter characteristic at X-ray energies seen in other HBLs. Again, this is believed to be due to the lack of large scale variability in the flux levels.

SED modelling of the October/November data, using both a single-zone SSC model and an inhomogenous jet SSC model, revealed that the radio emission observed during the campaign is most likely produced in a region different to that of the X-ray and VHE $\gamma-$rays. The most likely source of the radio emission is the VLBI core, which is two orders of magnitude larger in size than the emission region used to model the SED.

With a reduced χ^2 of 1.31 for 31 degrees of freedom, the best model fit to the observed SED for October/November 2003 is a single-zone SSC model. With a marginally larger reduced χ^2, a single-zone SSC fit to the X-ray and VHE $\gamma-$ray data also describes the observed SED fairly well. The fit to just the high energy data appears to attribute the X-ray and VHE $\gamma-$ray emission to smaller, faster, younger emission regions.

With descrepancies between the inhomogenous jet SSC model and the observed SED at radio and optical energies, as well as the high energy tail of the VHE observations, the reduced χ^2 for the inhomogenous jet SSC model fit is extremely poor. This indicating that whether it be a one-zone or two-zone variety, the SSC model fits the SED for October/November 2003 fairly well.

It should be noted that only leptonic models have been used to interpret the observations of this campaign. Probing hadronic emission models is beyond the scope of this thesis.

Chapter 6

PKS 2155−304 August/September 2004 Campaign

During August and September (5^{th} August − 16^{th} September) 2004, an extensive X-ray and VHE $\gamma-$ray monitoring campaign was completed on PKS 2155−304. Spanning 42.1 days, this campaign was unprecedented in its temporal coverage, with 287.3 kiloseconds of *RXTE* livetime and 172 separate 28-minute H.E.S.S. observations.

Unlike the October/November 2003 campaign, the H.E.S.S. observations of the August/September 2004 campaign were taken with the complete 4 telescope array. The *RXTE* observations were taken with the PCA detector. Unfortunately, due to high atmospheric dust content and bad weather, the majority of the H.E.S.S. observations were taken under poor atmospheric conditions. Nevertheless, the resulting temporal coverage, after selection cuts, at X-ray and VHE $\gamma-$ray energies allow us to constrain the physical parameters of the jet and probe correlations between X-rays and VHE $\gamma-$rays over both small and large time scales.

In this chapter the data reduction and results of both the H.E.S.S. and *RXTE/PCA* observations of the August/September 2004 campaign on PKS 2155−304 are reported.

6.1 H.E.S.S. observations

The VHE $\gamma-$ray observations were taken with the complete Phase 1 H.E.S.S. array of 4 telescopes. Each observation was taken in stereoscopic *Wobble* mode, with PKS 2155−304 positioned either $\pm 0.5^{\circ}$ in declination OR $\pm 0.579^{\circ}$ in right ascension, relative to the centre of the field of view of the camera. It should be noted that the amount of 'wobble' in right ascension is given by the amount of 'wobble' in declination divided by cosine of the declination of the target.

As described in Section 3.6.1, the stability of the central trigger rate was used as a means of quality control to only select runs taken under a stable sky. The radiometer data from each telescope were used to confirm that observations with an unstable central trigger rate were associated with clouds passing across the field of view. What is more, during the August/September 2004 campaign, there was a high dust content in the atmosphere due to large scale bush fires and dust storms in the region. This dust was clearly visible during the day and easily detected with the ceilometer in the centre of the H.E.S.S. array. Out of the 172 H.E.S.S. observation runs on PKS 2155−304 during the campaign, 60 runs were unaffected by the dust, 72 runs were severely affected by dust, while the remaining 40 runs were moderately affected by the dust. To remove any systematic uncertainty due to the atmospheric dust content and to make sure that any observed variability is intrinsic to the source, only the 60 H.E.S.S. observing runs unaffected by dust are considered.

As with the October/November 2003 campaign, the observations were cleaned using the standard '5-10' criterion. After cleaning, the standard image parameter cuts, described in Table 3.2, were applied to subtract the dominant cosmic ray background. As with previous H.E.S.S. observations, further background subtraction was estimated using the ring background model as described in Section 3.6.3. After cleaning, cuts and background subtraction for the 60 good runs, a total of 27.77 hours live time of observations remain; with an excess of 4362.1 $\gamma-$ray events, and a resulting significance of 68.9 σ. The two-dimensional excess sky map of the August/September 2004 observations is shown in Figure 6.1, along with the θ^2 distribution of these observations.

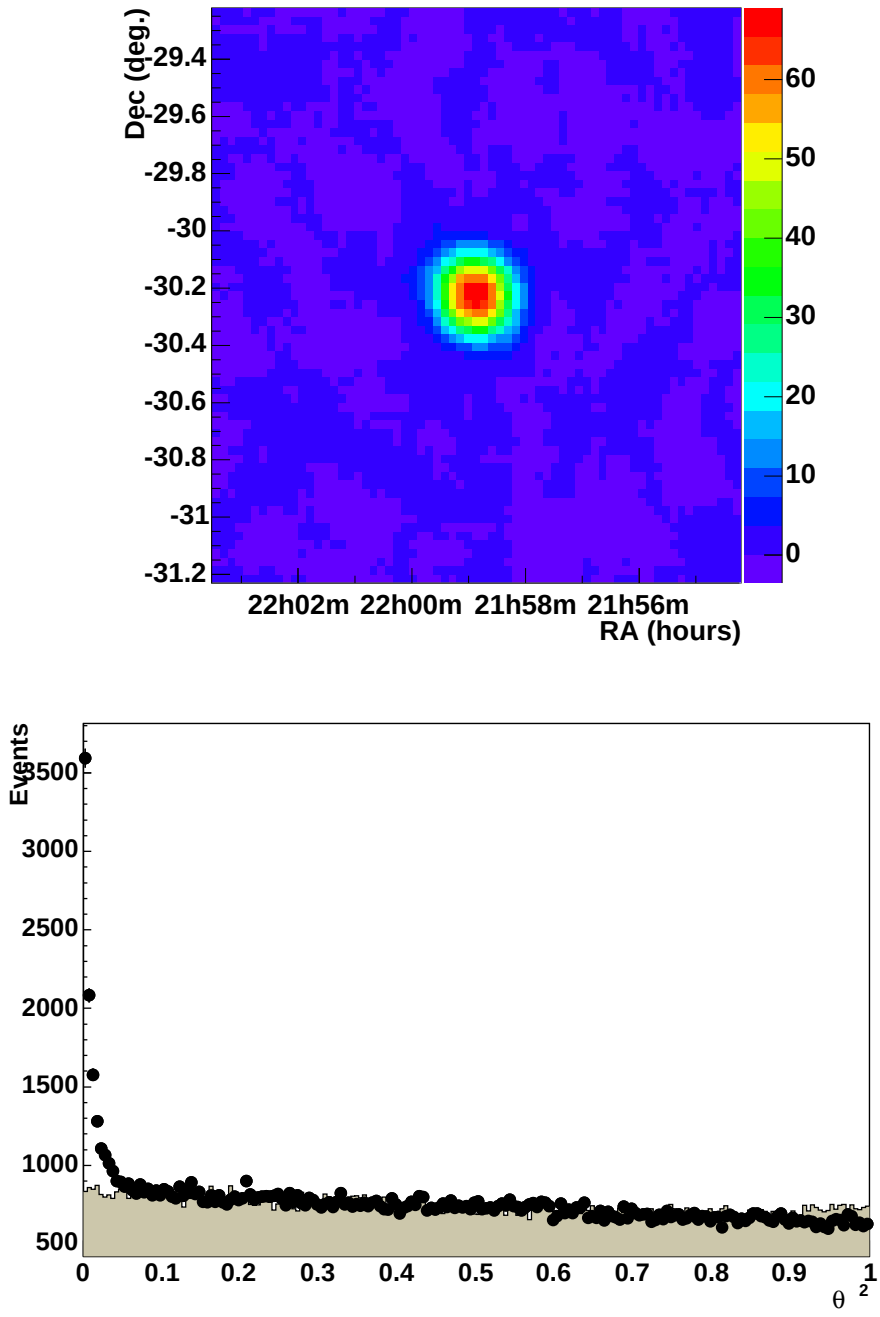

Figure 6.1: *Top:* The two-dimensional distribution of the excess events in the direction of PKS 2155 − 304 during August/September 2004. Right hand scale is the number of excess events. *Bottom:* The θ^2 distribution of on source events (points) and normalised background events (shaded).

6.1.1 H.E.S.S. results

Spectrum

The August/September 2004 data were fitted with both a power law and a broken power law function. Interestingly, unlike the October/November 2003 campaign, the broken power law is a better fit to the data with a reduced χ^2 of 2.36 for 23 degrees of freedom and associated χ^2 probability of 2.4×10^{-4}, compared to a reduced χ^2 of 4.93 for 26 degrees of freedom and associated χ^2 probability of 1.5×10^{-15}, though admittedly both large reduced χ^2 and small χ^2 probability indicate that these fits are quite poor. As with the time-averaged X-ray spectra in Chapter 4, the poor reduced χ^2 for both the power and broken power law fits implies that the spectrum shown in Figure 6.2 is the summation of different spectral states during the campaign.

Described by Eq. 6.1, the best broken power law fit is described by $\Gamma_1 = -1.00 \pm 0.39$, $\Gamma_2 = -3.78 \pm 0.12$, a break energy of $\mathrm{E_{break}} = 0.21 \pm 0.01$ TeV and a normalisation of $(9.0 \pm 2.1) \times 10^{-10}$.

$$\frac{\mathrm{d}N}{\mathrm{d}E} = I_0 \left(\frac{E_{break}}{E_0}\right)^{(\Gamma_2-\Gamma_1)} \left(\frac{E}{E_0}\right)^{-\Gamma_2} \tag{6.1}$$

Compared to the broken power law fit of the October/November 2003 data, we find that the break in the August/September 2004 spectrum is at an energy one order of magnitude smaller ($\mathrm{E_{break\ (2003)}} = 1.7$ TeV). However, the main spectral slope of the broken power law fits for both campaigns are quite similiar, with $\Gamma_2 = -3.78 \pm 0.12$ for August/September 2004 and $\Gamma_1 = -3.37 \pm 0.08$ for October/November 2003. Likewise, the spectral slope for the single power law fit, $\Gamma = -3.41 \pm 0.03$, is in very good agreement with the spectral slope of the single power law fit for the October/November 2003 campaign. It should be noted that as well as the statistical uncertainty of the spectral indices, there is also a systematic uncertainty of $\Delta\Gamma = \pm 0.1$.

As with the October/November 2003 campaign, the spectral indices could not be derived on a run-by run basis and thus we are unable to prove whether the poor spectral fit is indeed due to Figure 6.2 being the summation of different spectral states.

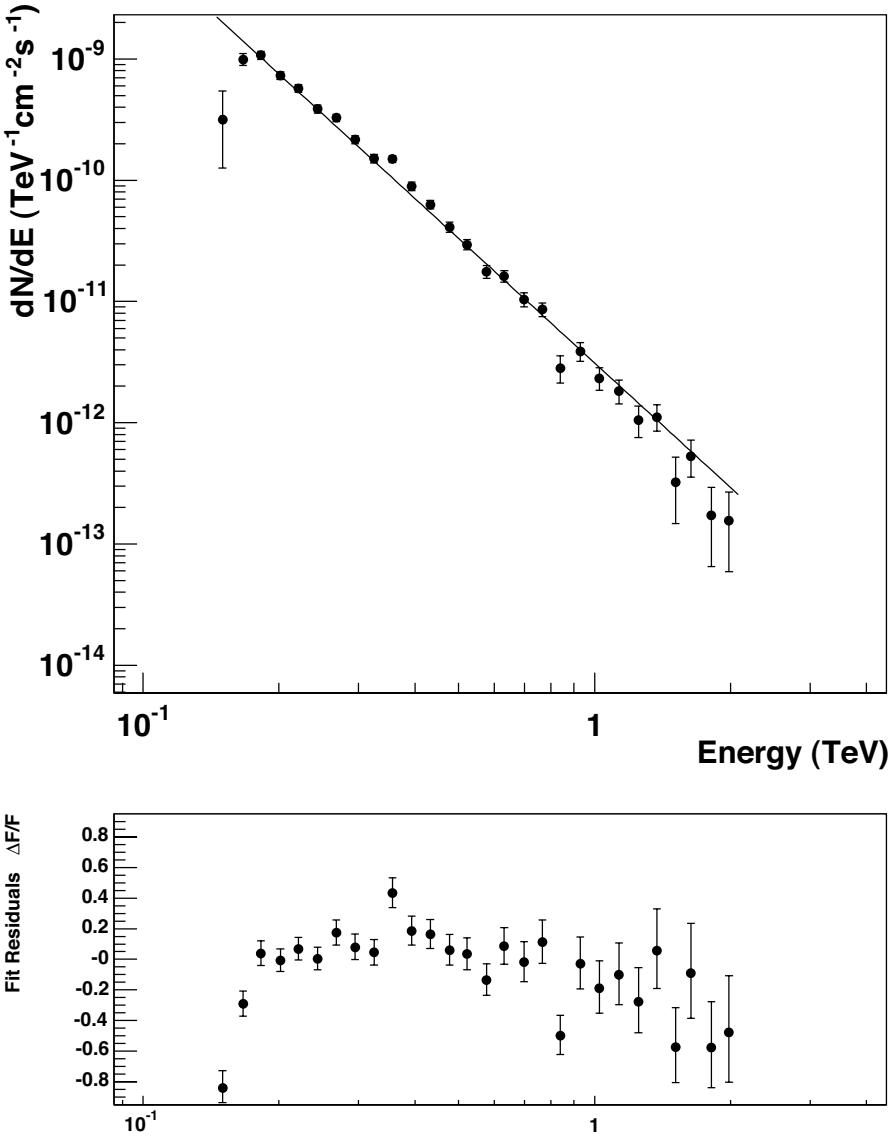

Figure 6.2: *Top:* Broken power law fit to the VHE data from August September 2004. This fit yields photon indices of $\Gamma_1 = -1.00 \pm 0.39$ and $\Gamma_2 = -3.78 \pm 0.12$, a break energy of $E_{break} = 0.21 \pm 0.01$ TeV and a reduced $\chi^2 = 2.36$ for 23 degrees of freedom. *Bottom:* The residuals to the broken power law fit.

Lightcurve

The E>300 GeV light curve for the August/September 2004 campaign is shown in Figure 6.3. As with the October/November 2003 campaign, the data were binned using the original 28 minute observation runs. During the campaign, the E>300 GeV flux varies from $F_{min} = 6.4 \times 10^{-8}$ photons $m^{-2}s^{-1}$ to $F_{max} = 4.3 \times 10^{-7}$ photons $m^{-2}s^{-1}$. Compared to the October/November 2003 campaign we find that the dynamic range of the VHE variability for the August/September 2004 campaign is smaller than that of the October/November 2003 campaign, though it should be noted that the VHE flux values for both campaigns are similiar, indicating that PKS 2155−304 was also in a quiescent state during the August/September campaign.

Evidence for inter-night variability of the flux level is clearly visible in Figure 6.3. Indeed, a constant flux fit to the complete campaign lightcurve has a very poor reduced χ^2 of 1.86×10^3 for 57 degrees of freedom. Evidence for intra-night variability is more obvious when we constrict the light curve to the most intensively sampled nights, see Figures 6.4 and 6.5.

Figure 6.4 clearly displays evidence for intra-night variability, with two major 'flaring' events occuring. As in Chapter 4, the term 'flare' is a rather arbitary term used to describe an obvious flux variability event, whether it be a increase or a decrease in flux. The first 'flaring' event occurred 53233.01< MJD <53233.12, with the E>300 GeV flux increasing by a factor of 1.9 ± 0.1 in 2.64 hours. The second 'flaring' event occurred 53234.06< MJD <53234.1 and saw the E>300 GeV flux decrease by a factor of 2.7 ± 0.5 in 0.96 hours. The large dynamic range of both of these 'flaring' events, coupled with the large amount of observations allows us to probe the evolution of the flaring event in great detail.

6.2 *RXTE* observations

The *RXTE* observations of PKS 2155−304 during the August/September campaign consisted of 96 separate pointing observations with the PCA detector (see Section 4.2.1 for description of the PCA). Spanning from August 5^{th} to

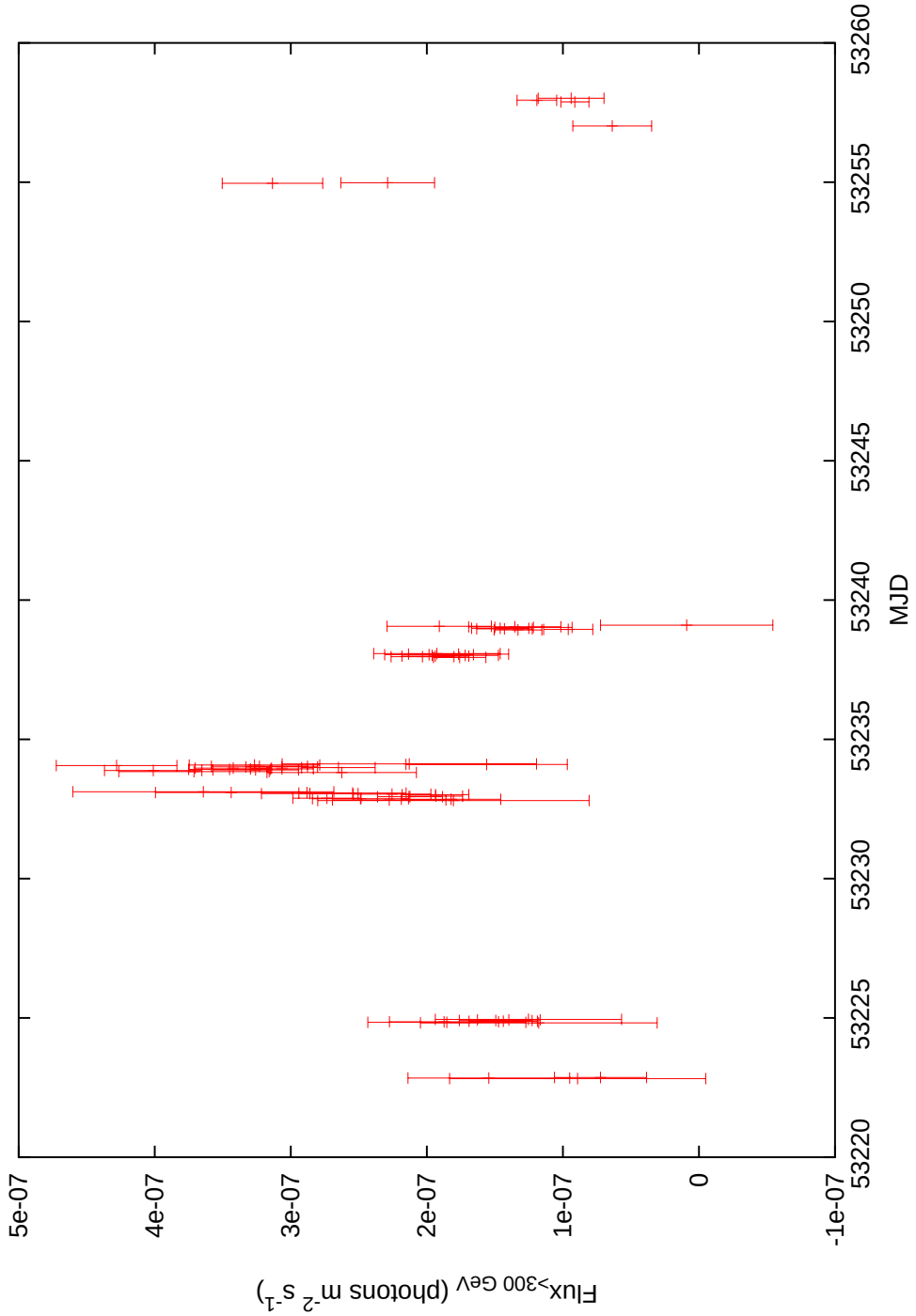

Figure 6.3: PKS 2155−304 E>300 GeV light curve in units of photons m^{-2} s^{-1} during August/September 2004. To minimalise the systematic uncertainty due to the poor atmospheric conditions, only the 60 runs that were unaffected by dust were considered, all of which are observation runs using all 4 telescopes.

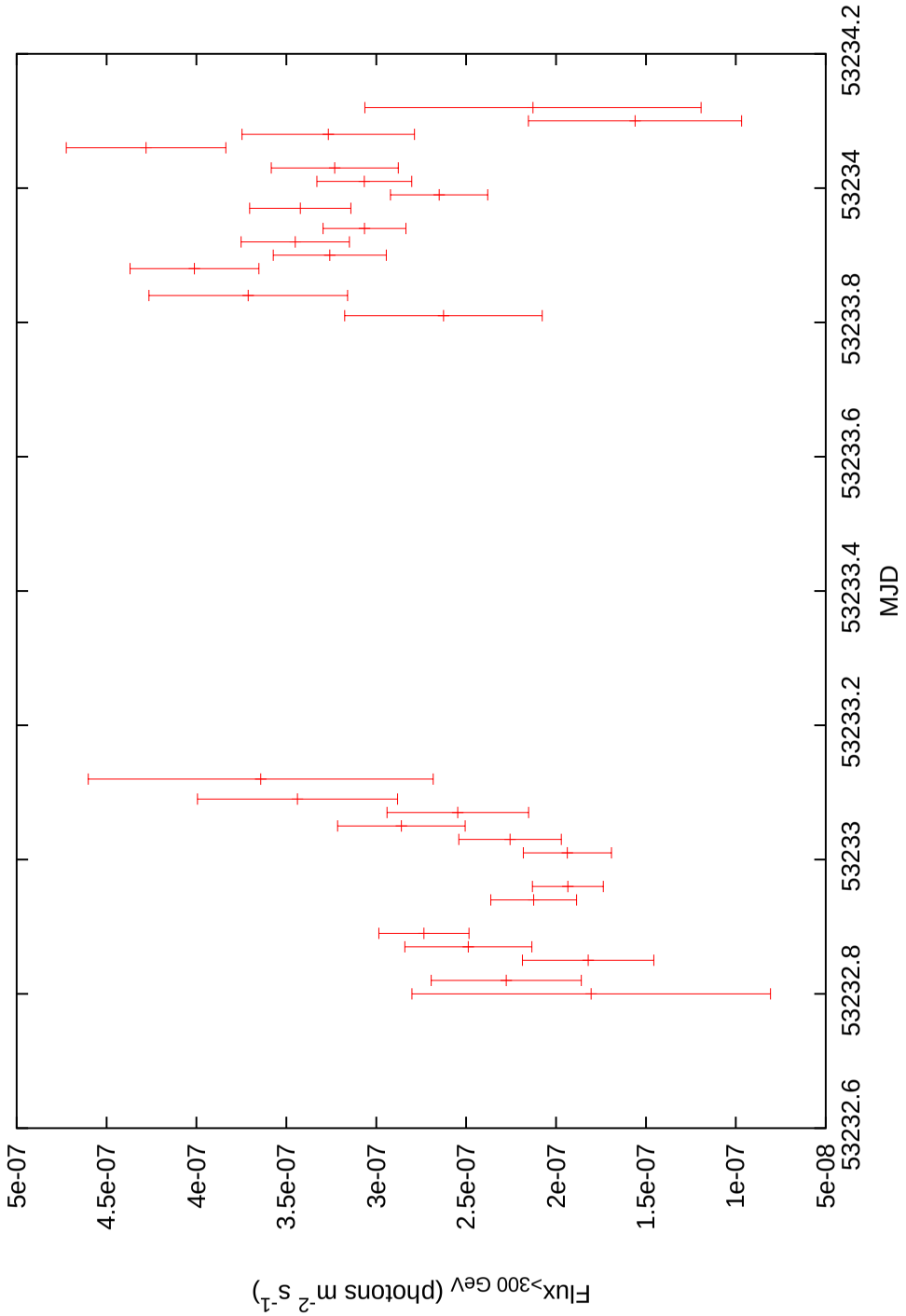

Figure 6.4: The E>300 GeV light curve in units of photons m^{-2} s^{-1} from MJD = 53232.6 to 53234.2. Evidence for intra-night variability is clearly visible.

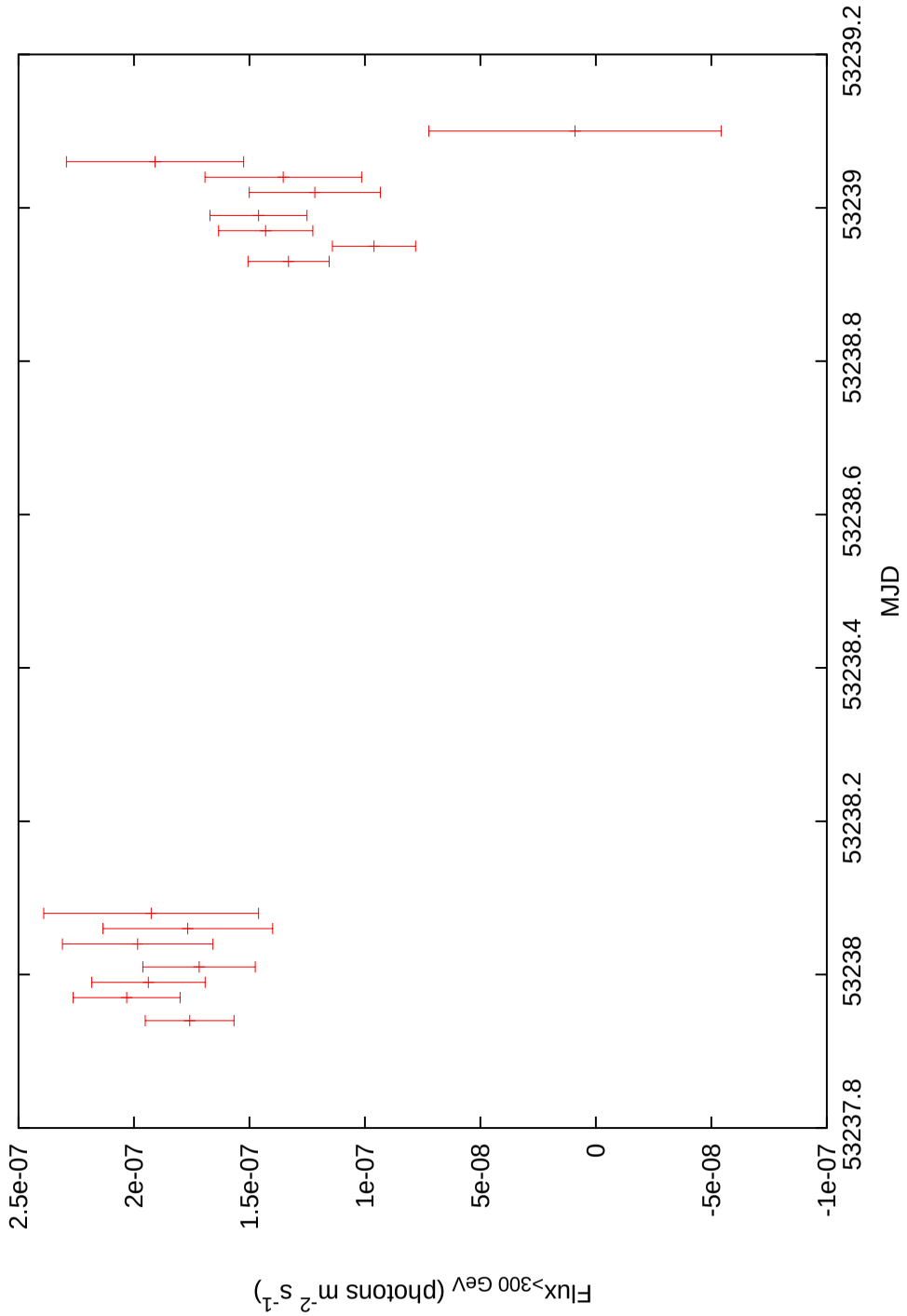

Figure 6.5: The E>300 GeV light curve in units of photons m^{-2} s^{-1} from MJD = 53237.8 to 53239.2. The intra-night variability is less obvious than in Fig. 6.4.

September 16th 2004 (53222 < MJD < 53264), the total lifetime of the X-ray observations is 287.3 kiloseconds. As with the October/November 2003 campaign, the dataset was dominated by observations with PCU 0 and PCU 2. While PCU 3 was briefly used during the campaign, the data reduction presented here focusses solely on the PCU 0 and PCU 2 observations.

Due to the loss of its propane layer, the gain in PCU 0 is known to fluctuate (see Section 4.2.2 for an in-depth discussion). To investigate the significance of the gain fluctuations in PCU 0 during the August/September 2004 campaign, the ratio of the raw counts from PCU 0 and PCU 2 was considered. Since there is very little variation in the gain of PCU 2, a varying PCU 0/PCU 2 count rate ratio would indicate a varying gain in PCU 0, with the varying gain possibly resulting in false artifacts occuring in the overall lightcurve. Any large scale variation in the ratio can be identified and excluded from the data reduction.

Figure 6.6 shows the raw counts of both PCU 0 and PCU 2 and the ratio of the two, with the data binned in 500 second intervals. With no alarming features visible, the gain fluctuations of PCU 0 appear to have had little effect during the *RXTE* observations in August/September 2004. Therefore the raw counts from both PCU 0 and PCU 2 were considered during data reduction, with the appropriate summed response matrix. It should be noted that using the counts from both PCUs decreases the statistical uncertainty associated with counting. However, as is shown in Chapter 8, there is little difference in the flux levels for the PCU 2 and PCU 0/2 data sets. Therefore, while it appears that the investigating the raw count rate from each detector is a moot point, it is a common practice in the reduction of *RXTE* data.

The same Good Time Interval (GTI) criterion that was applied to the October/November 2003 *RXTE* observations was also applied to the August/September observations. The STANDARD2 data was extracted using the FTOOL XDF, with signal from both the left and right hand side of layer 1 only, being considered. As described in Section 4.2.2, considering signal from just layer 1, maximises the signal to noise ratio.

As with the October/November 2003 campaign, the background data were modelled using PCABACKEST V3.0, with a faint background model. While

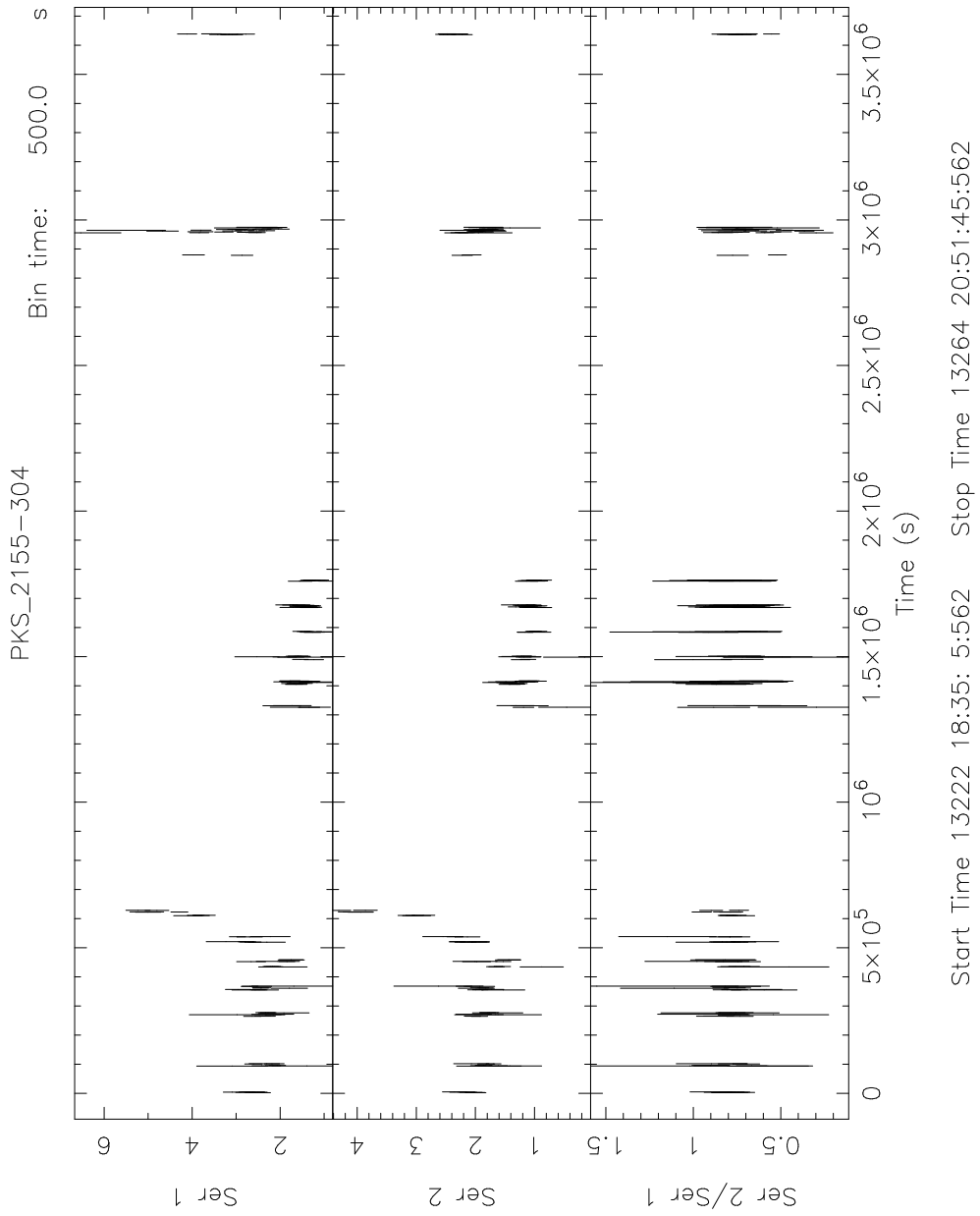

Figure 6.6: The raw counts of PCU 0 (top) and PCU 2 (middle) and the ratio of the two (bottom) for the August/September 2004 *RXTE* observations.

data were extracted from PHA channels 0-27 (corresponding to 2−11.45 keV), only data in the range 3−10 keV were considered for spectral fitting. This was done to remove the uncertainty associated with the low energy calibration of the PCA detector.

The appropriate PCU 0/PCU 2 response matrix was created using PCARSP v8.0. The spectral fitting was performed using XSPEC v11.2.0, with the resulting fit being used to calculate the 2−10 keV flux in units of ergs cm^{-2} s^{-1}. It should be noted that while the spectrum was fitted in the 3−10 keV energy range, the flux was extrapolated down to 2 keV. A common practice for RXTE data reduction, extrapolating the flux from 3 keV down to 2 keV removes the uncertainty associated with the poorly-understood low energy calibration of the PCA detector.

6.2.1 *RXTE* results

Lightcurve

The 2−10 keV lightcurve for the August/September 2004 campaign is shown in Figure 6.7. During the campaign, the 2−10 keV flux ranged from $F_{min} = 1.3 \times 10^{-11}$ ergs cm^{-2} s^{-1} to $F_{max} = 6.8 \times 10^{-11}$ ergs cm^{-2} s^{-1}, with clear evidence of inter-night variability. Comparing these flux levels to past X-ray observations, we see that much like the October/November 2003 campaign, PKS 2155−304 appears to be in a quiescent state during the August/September 2004 campaign.

However, while X-ray flux levels during the campaign suggests that PKS 2155−304 is in a quiescent state, there are still 3 major flaring events observed during the campaign, 2 of them in quick succession with 3 days between them. Unfortunately, only one of these flares (MJD $\sim$ 53233) was simultaneously observed at VHE γ−ray energies, the other two flares (MJD $\sim$ 53230 and MJD $\sim$ 53261) occurred during nights of poor atmospheric stability. Figure 6.8 shows the first two flares in greater detail (53228 < MJD < 53235), the latter of these flares was simultaneously observed at VHE γ−ray energies. Therefore it is the latter flare (MJD $\sim$ 53233), that will be used to constrain the physical parameters of PKS 2155−304's relativistic jet, as in Chapter 5.

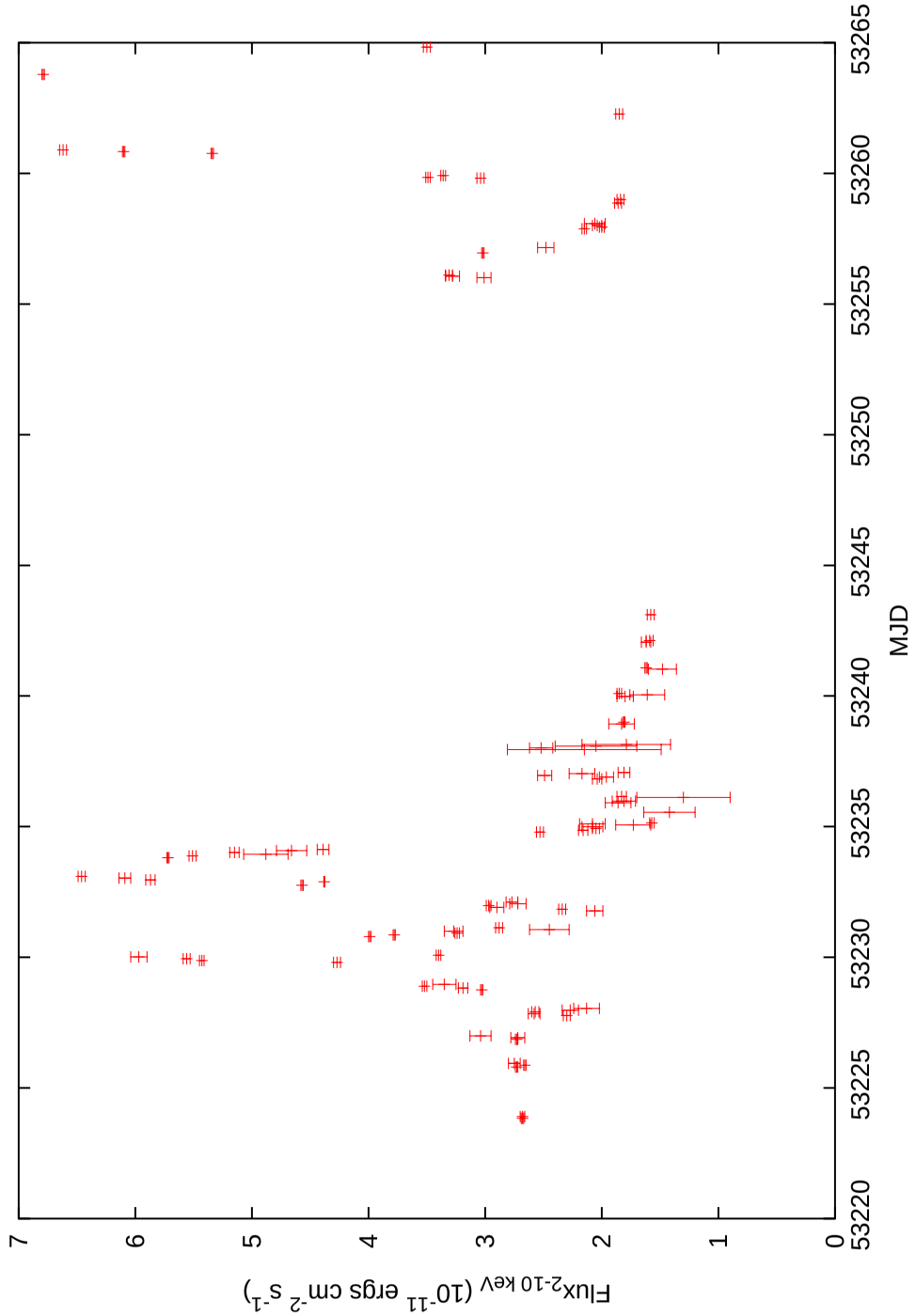

Figure 6.7: PKS 2155−304's 2−10 keV flux in units of 10^{-11} ergs cm^{-2} s^{-1} during the August/September 2004 campaign, using data from both PCU 0 and PCU 2.

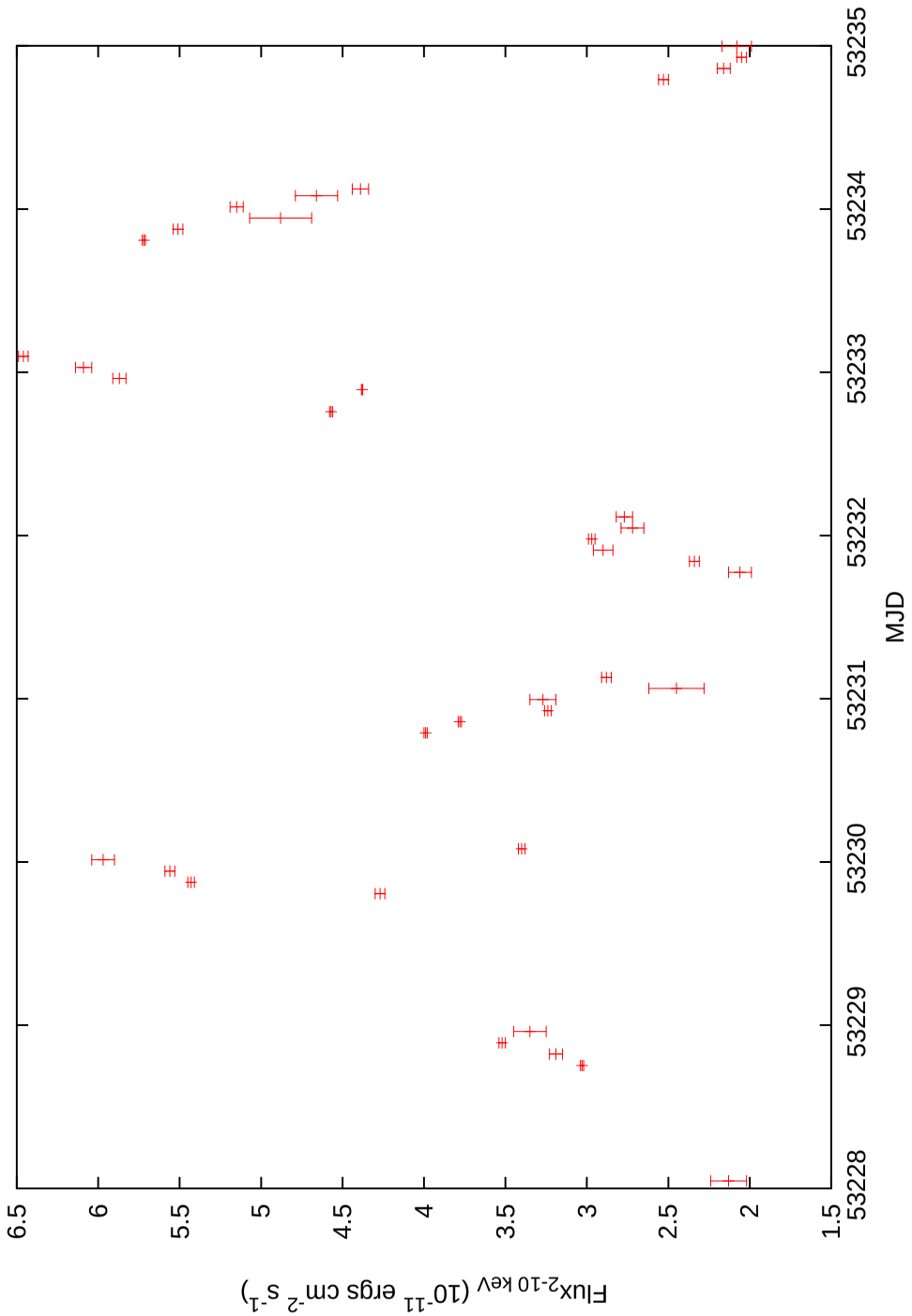

Figure 6.8: 2−10 keV flux versus MJD for two of the major flaring events during the August/September 2004 campaign.

Interestingly, while the X-ray flux during the campaign suggests that PKS 2155−304 was in a quiescent state, the dynamic range of variability during the campaign is quite large. Compared to the October/November 2003 campaign, which had a dynamic range of 2.75, the dynamic range of the August/September 2004 campaign is a factor of 2 greater, at 5.22. This larger range of variability should allow us to probe the harder-when-brighter phenomenon to a greater extent compared to October/November 2003.

Spectrum

Figure 6.9 shows the absorbed power law fit and residuals in the 3−10 keV energy range for the summed August/September 2004 observations, using both PCU 0 and PCU 2. As with the October/November 2003 data, the absorption was modelled by a fixed column density of $N_H = 1.7 \times 10^{20}$ cm^{-2}. The power law fit yields a photon index, Γ, of 2.97 ± 0.01 and a normalisation of $(4.7 \pm 0.1) \times 10^{-2}$. However, the reduced χ^2 of this fit is extremely poor, 15.4 for 14

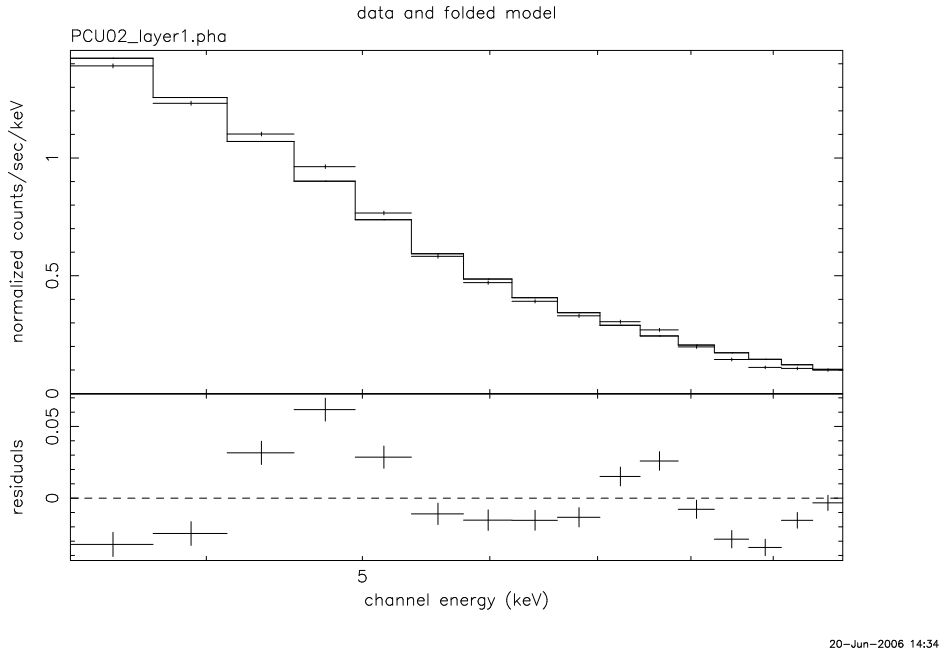

Figure 6.9: The summed 3−10 keV spectra for August/September 2004, fitted with an absorbed power law. The top pannel shows the data and fit, while the bottom panel shows the residuals between the fit and the model.

degrees of freedom and an associated χ^2 probability for the fit of 4.5×10^{-38}. An absorbed broken power law fit does not improve the reduced χ^2 to any great extent. The poor power law and broken power law fit to the summed August/September spectra is likely to arise from the high level of variability during the campaign, with Fig. 6.9 being the superposition of many individual well-fitted power laws. Indeed, the flux variability shown in Fig. 6.7 & Fig. 6.8 is further indication that Fig. 6.9 is likely to be the result of the superposition of different spectral states.

To investigate photon index variability throughout the campaign, a photon index for each individual pointed observation was calculated. As with the summed spectra, this photon index was calculated by fitting an absorbed power law, with a fixed column density of $N_H = 1.7 \times 10^{20}$ cm^{-2}. Shown in Fig. 6.10, the photon index of the X-ray observations clearly varies throughout the campaign, ranging from $\Gamma_{min} = 2.57 \pm 0.81$ to $\Gamma_{max} = 4.01 \pm 0.68$, with the reduced χ^2 at an acceptable level of $0.26 <$ reduced $\chi^2 < 1.85$ (both for 14 degrees of freedom). As with the October/November 2003 campaign, the statistical significance of the power law fits to the individual spectra indicates that the poor reduced χ^2 for the summed spectra is likely to be due to the superposition of different spectral states.

An interesting feature in Fig. 6.10 is the 'dip' in photon index between $53230 <$ MJD < 53235. A reduction in photon index is associated with a steepening of the photon slope. Temporally co-incident with the two flares shown in Fig. 6.8, it would appear that unlike the October/November 2003 campaign, the X-ray emission during this campaign is exhibiting the harder-when-brighter characteristic. To investigate the harder-when-brighter characteristic in more detail, the $2-10$ keV flux was plotted against the $3-10$ keV photon index, Γ, for each individual pointed observation, see Fig. 6.11.

As with Fig. 4.11 for the October/November 2003 campaign, Fig. 6.11 was fitted with a linear function using the least square fitting method. While there is scatter around the linear function, the reduced χ^2 of the fit is not unreasonable, 0.05 for 94 degrees of freedom. However, such a small reduced χ^2 implies that the linear fit to Fig. 6.11 is dominated by the large error bars of the data points.

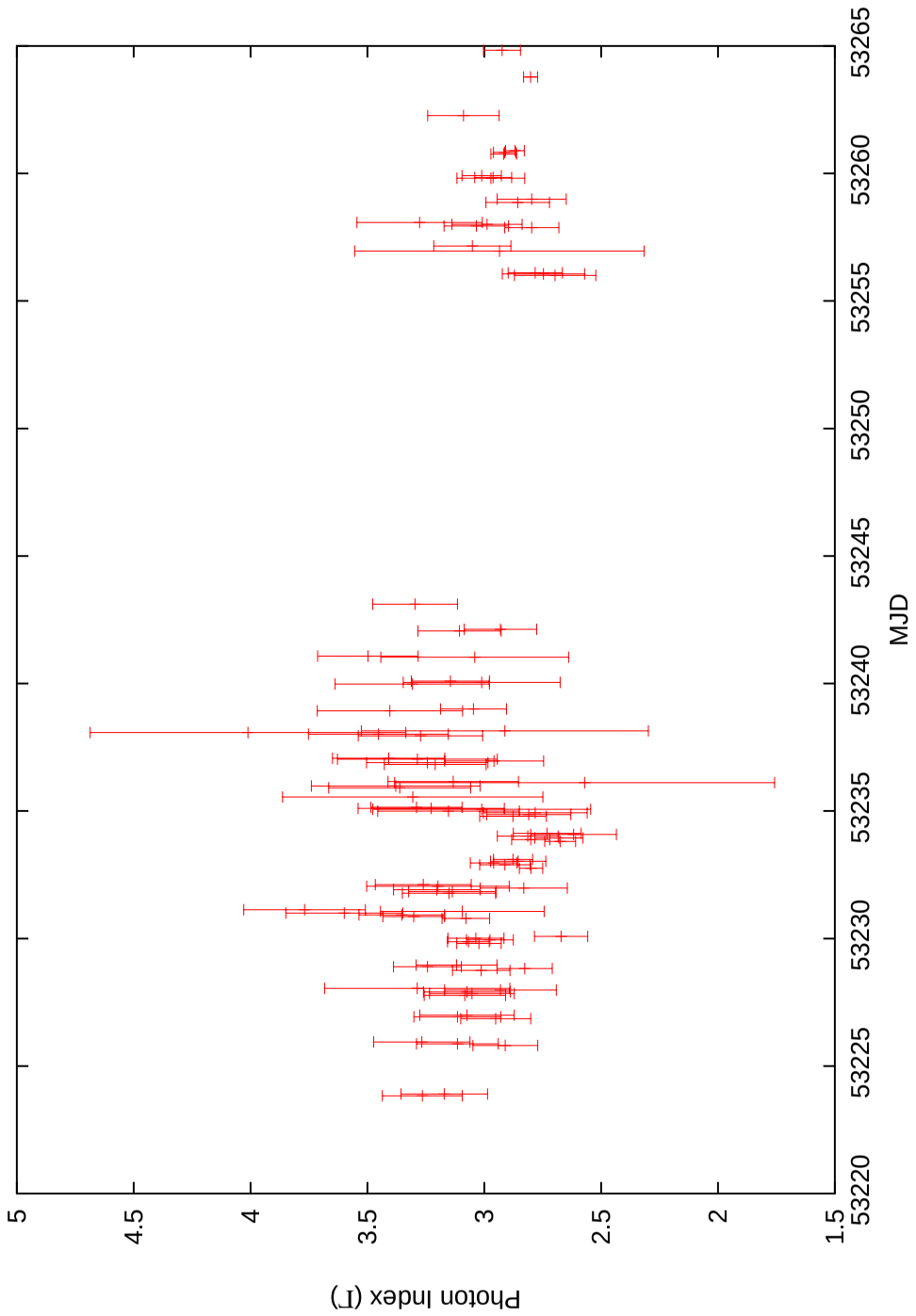

Figure 6.10: Photon index, Γ, versus MJD for a power law fit to the individual pointing observations for the August/September 2004 campaign.

With a slope of -0.07 ± 0.02, the linear trend of Fig. 6.11 implies that the X-ray observations do indeed exhibit a harder-when-brighter behaviour, with $\Gamma_{3-10\mathrm{keV}} \propto 0.07 \times \mathrm{F}_{2-10\mathrm{keV}}$. Compared to the *RXTE* observations of October/November 2003, we find that, while the linear trend is slightly shallower in August/September 2004, the uncertainty associated with the gradient of the linear fit is smaller, 24.3% compared to the 54.8% for October/November 2003, and the reduced χ^2 is slightly better. Nonetheless, the harder-when-brighter detected in both October/November 2003 and August/September 2004 are compatible with past observations [49, 198].

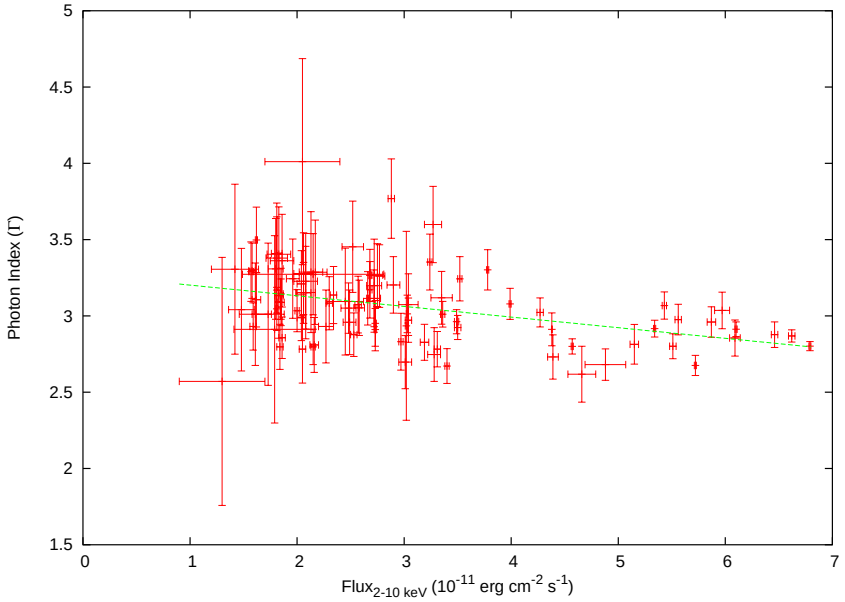

Figure 6.11: 2−10 keV flux versus the 3−10 keV photon index, Γ, for each individual pointing observation using data from both PCU 0 and PCU 2. The dashed line is a linear fit to the data, with a slope of -0.07 ± 0.02.

Chapter 7

Discussion and Interpretation of the August/September 2004 Campaign

As with the October/November 2003 campaign, the observations reported in Chapter 6 can be used to constrain the physical parameters of the emission region in the relativistic jet of PKS 2155−304 and probe possible emission models. Since PKS 2155−304 appeared to be in a quiescent state during the campaign, similar to October/November 2003 albeit with a larger amount of variability, the August/September 2004 campaign also allows us to probe whether the 'active state' models that have evolved over the last 14 years, are applicable to a quiescent HBL. Furthermore, comparing the model parameters of the August/September 2004 campaign to those of the October/November 2003 campaign will allow us a probe the differences between a variable quiescent HBL (2004) and a less variable quiescent HBL (2003).

In this Chapter, the observations reported in Chapter 6 will be used to probe possible leptonic emission models and constrain the physical jet parameters. While there were three major 'flaring' events during the campaign, only one of the flares, MJD $\sim$ 53233, was simultaneously observed at VHE γ−ray and X-ray energies. It is this flare that will be used to probe the emission models and jet parameters.

7.1 Constraints on Jet Parameters

The simultaneous VHE $\gamma-$ray and X-ray observations for 53232.6 < MJD < 53234.2 can be seen in Fig. 7.1. The variability timescale used in this chapter for constraining the jet parameters is associated with the sudden increase of both X-ray and VHE fluxes around MJD $\sim$ 53233. Admittedly, as before, this definition of flaring timescale is rather arbitrary, especially as the MJD $\sim$ 53233 flare may be a small section of a larger flare spanning several days (see 53232 < MJD < 53235 of Fig. 6.8). However we are unable to conclusively show whether Fig. 7.1 consists of 2 separate flares or one large one, and thus considering the variability around MJD $\sim$ 53233 to be one flare is a reasonable assumption to make.

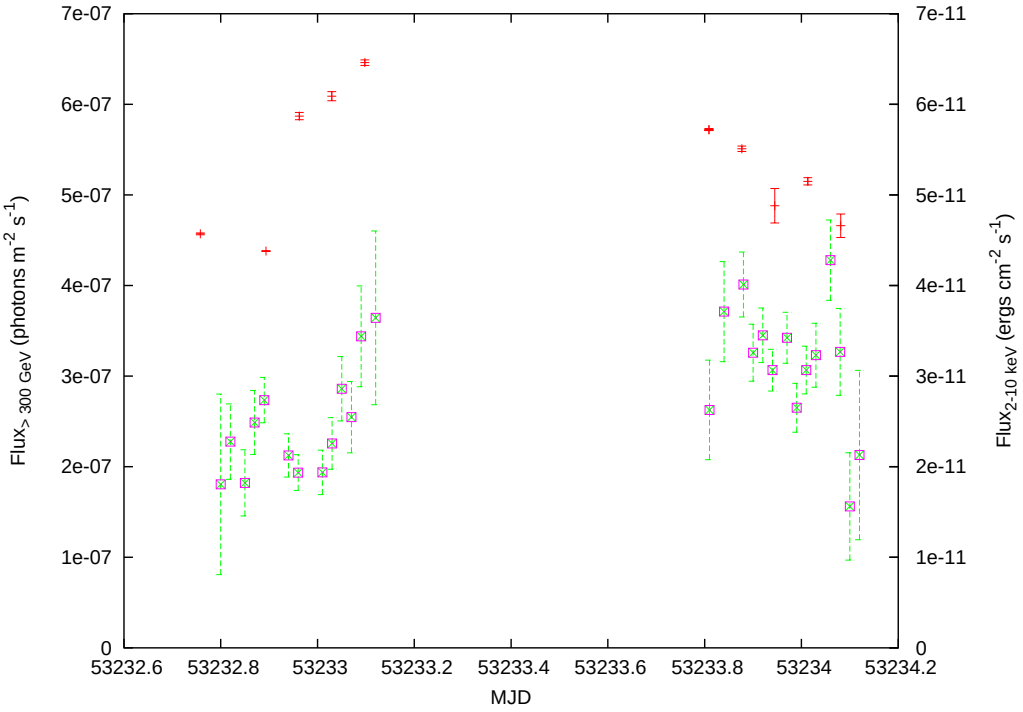

Figure 7.1: The simultaneous X-ray (red) and VHE $\gamma-$ray (green) observations around the peak of the large flare seen in Fig. 6.8. While it is a rather arbitrary definition of a 'flare', the variability timescale used for the following constraints is associated with the sudden increase in both X-ray and VHE $\gamma-$ray flux at MJD $\sim$ 53233. The flux scale for the VHE observations is on the left, while the flux scale for the X-ray observations is on the right.

The jet parameters constrained in this section are constrained using methods that are identical to those in Section 5.1, using the appropriate variability timescales, flux levels and spectral slopes from the August/September 2004 observations. For an in-depth discussion of the methods used, see Section 5.1.

7.1.1 Flux Variability

Using the causality argument, an upper limit on the size and Doppler factor of the emission region can be derived using the variability timescale of the flare. As with Section 5.1, the upper limit is given by Eq. 7.1, where R is the size of the emission region, t_{var} is the variability timescale and δ is the Doppler factor of the emission region.

$$R \leq ct_{var}\frac{\delta}{1+z} \tag{7.1}$$

Taking the variability timescale to be the rise-time of the flare from minimum to maximum X-ray flux around MJD $\sim$ 53233 (see Fig. 7.1), gives a $t_{var} = 1.72 \times 10^4$ seconds. Taking the redshift to be 0.117 and $t_{var} = 1.72 \times 10^4$ seconds gives:

$$R\delta^{-1} \leq 4.6 \times 10^{14}\text{cm} \tag{7.2}$$

7.1.2 Photon-photon Pair Production Opacity

The fact that VHE photons are observed, implies that the emission region is transparent to photon-photon interactions at VHE $\gamma-$ray energies, with $\tau_{\gamma\gamma} \leq 1$. As with Section 5.1.2, the opacity can be used to derive an upper limit for δ and R. The photon-photon pair production opacity is given by:

$$\tau_{\gamma\gamma} \approx \frac{\sigma_T}{5}\frac{1}{hc}\frac{d_L^2}{R}\frac{1}{\delta^3(1+z)}F(\nu_i) \tag{7.3}$$

Assuming a power law distribution for the photon field that the GeV-TeV photons interact with, such that $F(\nu_i) = \nu^{-\alpha}$, where $F(\nu_i)$ is given by Eq. 5.5, gives Eq. 7.4.

$$R^{-1}\delta^{-3-2\alpha} \leq \left(\frac{\sigma_T}{5}\frac{1}{hc}\frac{d_L^2}{(1+z)}\right)^{-1}\left(\frac{2(m_e c^2)^2}{h\nu_\gamma}\frac{1}{h}\frac{1}{(1+z)^2}\right)^{\alpha} \quad (7.4)$$

where σ_T is the Thompson cross section, d_L is the luminosity distance to PKS 2155−304, α is the spectral index of X-ray spectra and h, c and m_e represent Planck's constant, speed of light and mass of electron respectively. It should be noted that the spectral index is slightly different to the photon index calculated for each X-ray spectra in Section 6.2.1. As seen in Fig. 6.10, the photon index varied considerable throughout the campaign ($2.57< \Gamma <4.01$). To remove any uncertainty associated with photon index variability throughout the campaign, only the photon indices during the flaring event are consider. Summing the individual spectra during the flaring event and fitting an absorbed power law as before, the photon index is 2.9±0.1. This equates to a spectral index $\alpha = 1.9 \pm 0.07$. Using Eq. 7.4, with $\alpha = 1.9$, $h\nu_\gamma = 1$ TeV, $d_L = 1.59 \times 10^{25}$ m and z = 0.117 gives:

$$R^{-1}\delta^{-6.8} \leq 2.7 \times 10^{-22}\mathrm{cm}^{-1} \quad (7.5)$$

7.1.3 *Emission Model-Independent* Minimum δ

Assuming that the X-ray and VHE γ−ray emission regions are co-spatial, we are able to obtain a *emission model-independent* value for the minimum allowable Doppler factor, δ, by combining Eq. 7.2 and Eq. 7.5. The minimum allowable Doppler factor is given by Eq. 7.6.

$$\delta \geq 8.1 \quad (7.6)$$

This value is less than one order of magnitude smaller than the minimum Doppler factor calculated for the October/November 2003 campaign. While this is in part, due to the larger variability timescale of the August/September 2004 flaring event, it is the larger spectral index of the August/September that appears to have a greater effect, with a difference of 0.2 in spectral index resulting in 2 orders of magnitude difference between Eq. 5.8 and Eq. 7.5.

The exclusion regions, in the (R, δ) plane, associated with the two con-

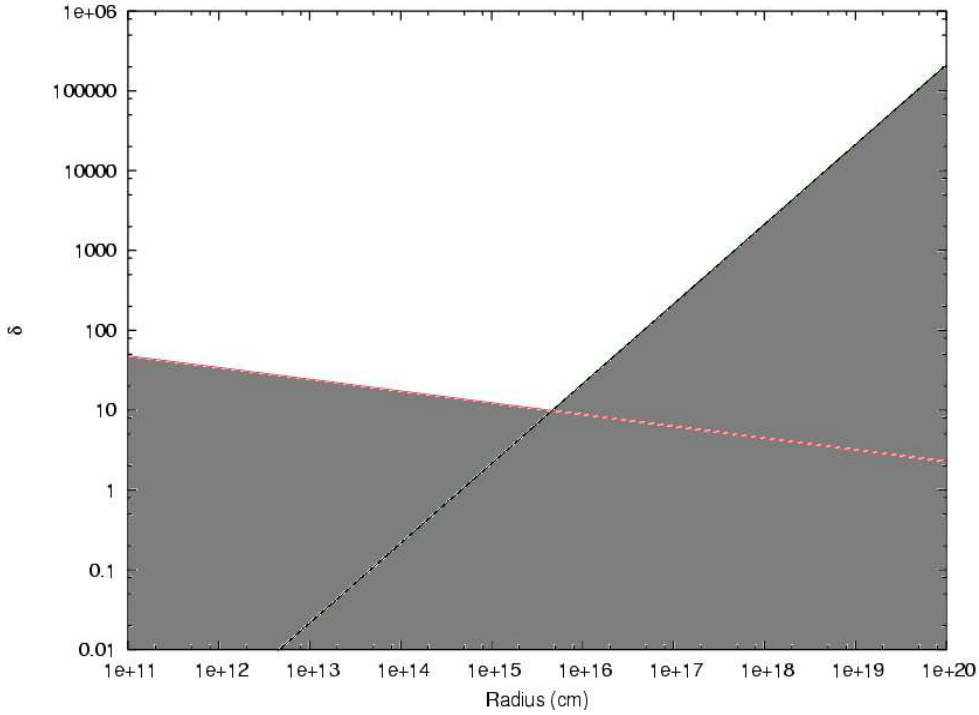

Figure 7.2: Exclusion regions in the (R,δ) plane which satisfy the causality and $\gamma\gamma$ opacity criteria of Eq. 7.2 and Eq. 7.5 respectively. The minimum allowable Doppler factor, δ, is 8.1.

ditions that govern this model-independent Doppler factor are shown in Fig. 7.2. The grey shaded areas are R and δ solutions that do not satisfy Eq. 7.2 and Eq. 7.5, given a t_{var} of 1.7 $\times 10^4$ seconds measured from the rise time of the X-ray flare. Fig. 7.2 is only valid if the X-ray and VHE $\gamma-$ray emission regions are co-spatial.

7.1.4 *Model-Dependent* Jet Parameter Constraints

As with Section 5.1.4, further constraints on the jet parameters can be made by assuming that the broadband emission is dominated by a single-zone SSC model, with a spherical emission region homogeneously filled with a relativistic electron population.

Maximum Electron Energy

As seen in Section 5.1.4, the maximum energy of the electron population is governed by Eq. 7.7 and Eq. 7.8.

$$\nu_{syn} = 10^6 \left(\frac{\delta}{1+z}\right) B\gamma_e^2 \tag{7.7}$$

$$\gamma_{max} m_e c^2 \left(\frac{\delta}{1+z}\right) \geq E_{\text{IC max}} \tag{7.8}$$

Since the maximum energy range of the synchrotron continuum and maximum energy of the IC continuum for the August/September 2004 campaign is identical to that of the October/November 2003 campaign, the inequality of the maximum energy of the electron population is also the same. Combining Eq. 7.7 and Eq. 7.8, with $\nu_{syn} = 2.4 \times 10^{18}$ Hz and $E_{\text{IC max}} = 2$ TeV, gives:

$$B\delta^{-1} \leq 0.14 \text{ G} \tag{7.9}$$

Using the model-independent Doppler factor for August/September 2004, Eq. 7.6, Eq. 7.8 and Eq. 7.9 we can numerically constrain the maximum Lorentz factor of the electron population to $\gamma_{max} = 5.5 \times 10^5$. This value is 2.5 times larger than the γ_{max} calculated in similiar fashion for the October/November 2003 campaign. Likewise, the γ_{max} calculated for August/September 2004 is similiar to the $5{\times}10^5$ calculated by Takahashi et al. for Mkn 421, but smaller than the $\gamma_e = 10^7$ calculated by Giebels et al. 1ES 1959+650 [178, 81].

Spectral Energy Distribution Peaks

Using the relative positions of both the synchrotron and IC peaks, in a ($\nu - \nu F_\nu$) plot, we are able to further constrain the magnetic field strength and Doppler factor of the emission region. In the jet's rest frame, the energy of the synchrotron peak is given by Eq. 7.10.

$$e_{peak} \approx e_{peak}\prime \left(\frac{1+z}{\delta}\right) \tag{7.10}$$

where $e_{peak}\prime$ is the observed energy of the synchrotron peak. Assuming that the IC scattering occurs in the Thompson regime, then the maximum energy boost of the IC process is given by $\gamma^2 e_{peak}$ (see Section 2.1.2). Since the density of target (synchrotron) photons decreases after the synchrotron peak, the energy of the IC peak, taking into consideration the $\gamma^2 e_{peak}$ energy boost and the change in reference frame, is given by:

$$\gamma_{max}^2 e_{peak} \geq h\nu_{IC} \left(\frac{1+z}{\delta} \right) \tag{7.11}$$

Combining Eq. 7.7, Eq. 7.10 and Eq. 7.11, with the synchrotron peak at 1.2×10^{16} Hz (49.7 eV) and the IC peak at 4.2×10^{24} Hz (170 GeV), gives Eq. 7.12. Again, the assumed positions of the synchrotron and IC peaks are proven *a posteriori* by the SSC fits in Section 7.3.

$$B\delta \leq 790 \text{ G} \tag{7.12}$$

Thompson/Klein-Nishina Regime

The IC scattering will occur in the Thompson regime if $\gamma e_\gamma \leq 511$ keV, where γ is the Lorentz factor of the electron involved in the IC process and e_γ is the energy of the photon involved in the photon involved in the IC process. Taking into consideration the change in reference frames, with an observed photon energy of 49.7 eV gives:

$$\gamma \leq 1.03 \times 10^4 \left(\frac{\delta}{1+z} \right) \tag{7.13}$$

The electron population associated with the synchrotron peak, $\nu_{syn} \approx 1.2 \times 10^{16}$ Hz, has a Lorentz factor governed by Eq. 7.14.

$$\gamma_{peak} = 1.16 \times 10^5 B^{-\frac{1}{2}} \delta^{-\frac{1}{2}} \tag{7.14}$$

Combining Eq. 7.13 and Eq. 7.14 gives the following constraint:

$$B\delta^3 \geq 160 \text{ G} \tag{7.15}$$

Maximum Energy/SED Peaks/Thompson–K-N Constraints

The limits placed on B and δ by the maximum electron energy, the positions of the Spectral Energy Distribution peaks and the Thompson/K-N regime are summarised below:

$$B\delta^{-1} \leq 0.14 \text{ G} \tag{7.16}$$

$$B\delta \leq 790 \text{ G} \tag{7.17}$$

$$B\delta^{3} \geq 160 \text{ G} \tag{7.18}$$

Combining Eq. 7.16 and Eq. 7.17 gives us an upper limit for the magnetic field strength of the emission region, Eq. 7.19, assuming that the single-zone SSC model is dominant.

$$B \leq 10.6 \text{ G} \tag{7.19}$$

The maximum magnetic field calculated for August/September 2004 is only marginally smaller than the maximum magnetic field calculated in similiar fashion for the October/November 2003 campaign (see Eq. 5.23). The exclusion regions in the (B, δ) plane, governed by Eq. 7.16, Eq. 7.17 and Eq. 7.18, is shown in Fig. 7.3. As before, the shaded regions in Fig. 7.3 indicated B and δ solutions that do not satisfy Eq. 7.16, Eq. 7.17 and Eq. 7.18. The minimum Doppler factor allowed by Fig. 7.3 is similiar to that calculated in Eq. 7.6 using the causality/$\gamma\gamma$ opacity argument.

7.2 Correlation studies

As mentioned, the jet parameters constrained in Section 7.1 have been done so under the assumption that the emission is dominated by a *single-zone* SSC model. As done in Section 5.2, to test whether this is a reasonable assumption to make, we can look for a correlation between the VHE $\gamma-$ray flux and X-ray flux levels; a correlation implying that the emission from the two seperate energy bands is due to the same particle population.

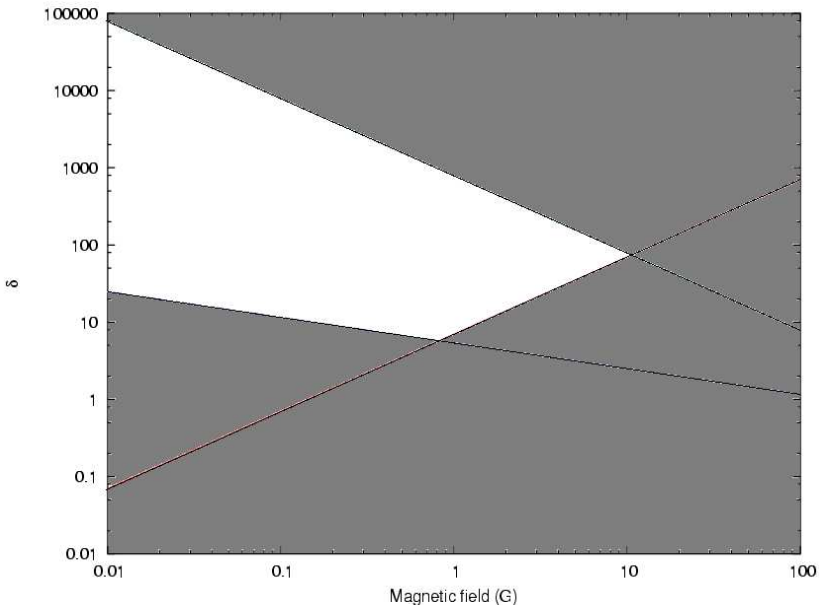

Figure 7.3: Exclusion regions in the (B,δ) plane which satisfy Eq. 7.16, Eq. 7.17 and Eq. 7.18. Assuming a single-zone SSC model, the maximum allowed magnetic field strength is ≈ 10.6 G.

In order to look quantitatively for correlated variability between the two energy bands, the simultaneous VHE $\gamma-$ray and X-ray fluxes were plotted against each other, see Fig. 7.4. Using the least square fitting method, a linear trend was fitted to Fig. 7.4. With a reduced χ^2 of 0.35 for 15 degrees of freedom for the linear fit, there is clear evidence for a correlation between the VHE $\gamma-$ray flux and the 2$-$10 keV flux levels during the August/September 2004 campaign. With a slope of 0.42 ± 0.08, the linear fit to Fig. 7.4 implies that $\mathrm{F_{VHE}} \propto 0.42 \times \mathrm{F_{X\text{-}ray}}$.

Furthermore, the correlation between the VHE $\gamma-$ray flux and X-ray flux levels during August/September 2004 implies that the emission in both energy bands is from the same population of particles and hence that the emission regions for both energy bands, are co-spatial. Therefore, assuming a single-zone emission region in Section 7.1.4 appears to be a reasonable assumption to make.

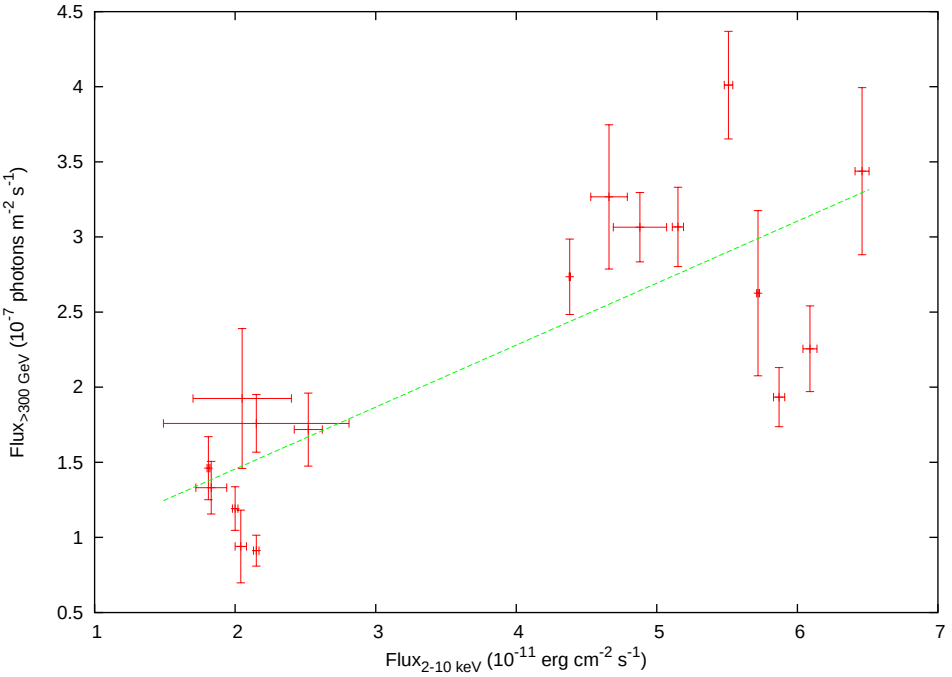

Figure 7.4: Simultaneous VHE $\gamma-$ray and X-ray flux measurements. With clear evidence for a correlation between the two, the slope of the linear fit is 0.42 ± 0.08. This implies that during the August/September 2004 campaign, $F_{\mathrm{VHE}} \propto 0.415 \times F_{\mathrm{X\text{-}ray}}$.

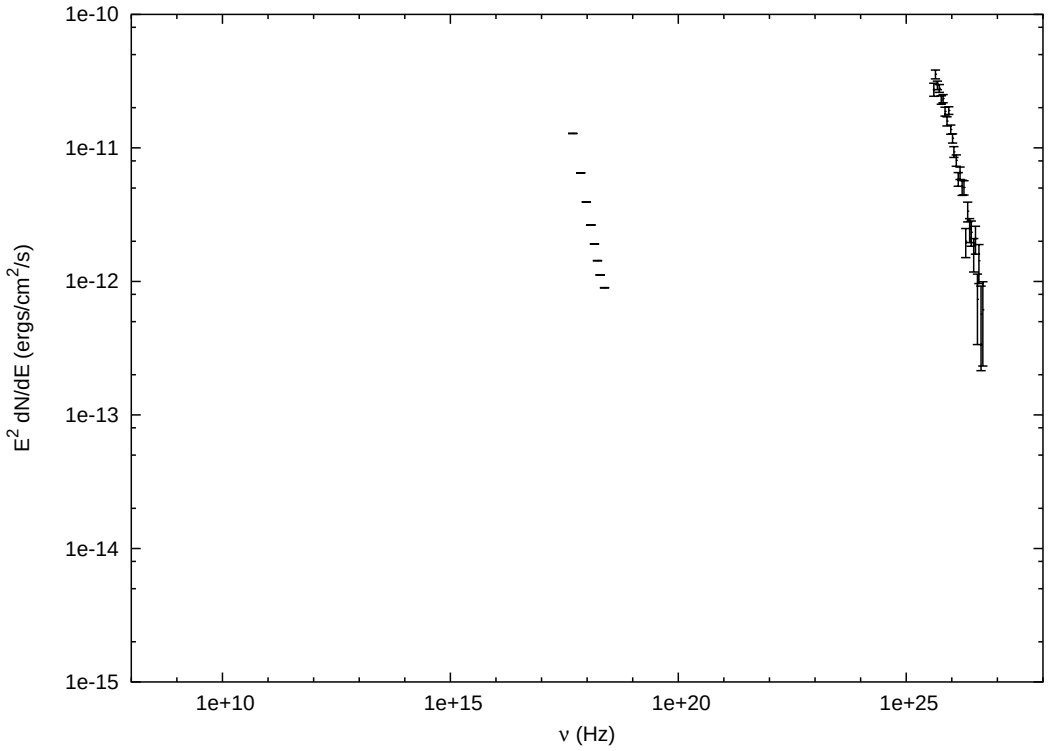

Figure 7.5: The spectral energy distribution of PKS 2155−304 during August and September 2004. Both the *RXTE* and H.E.S.S. data are averaged over the whole campaign.

7.3 SED modelling

The Spectral Energy Distribution for the August/September 2004 campaign is shown in Fig. 7.5, in νF_ν representation. Both the *RXTE* and H.E.S.S. data plotted in Fig. 7.5 has been averaged over the whole campaign. No archival data has been included in Fig. 7.5 since the observed X-ray and VHE γ−ray flux levels indicate that PKS 2155−304 was in a quiescent state during the campaign; like the October/November 2003 SSC modelling in Section 5.3, the archival data was not believed to be a true presentation of the flux levels at the other energy bands. Thus including archival data during the SSC modelling may introduce unnecessary uncertainty in the model fit.

7.3.1 Single-zone SSC interpretation

For consistency with the assumed model for the model-dependent jet parameters, the SED shown in Fig. 7.5 was interpreted with a single-zone SSC model. As with Section 5.3, the single-zone SSC model applied assumes a single spherical emission region of radius, R, magnetic field, B and Doppler factor, δ. The spherical emission region is isotropically filled with an electron population described by a broken power law. Ranging from E_{min} to E_{max}, with the break at E_{break}, the spectral indices of the broken power law before and after the spectral break are fixed at $p_1 = 2$ and $p_2 = 3$ respectively [106].

Starting with the fit parameters from the SSC fit to the October/November 2003 campaign, the best model fit was found by varying the magnetic field, the Doppler factor and the energy distribution of the electron population to minimise the reduced χ^2. While there are no optical or radio data to fit during the SSC modelling, both an X-ray/VHE fit and an 'X-ray/VHE + low energy' fit were considered (see Section 5.3 for the difference between the two). However, it should be stressed that with no low energy observations to verify the fit against, the 'X-ray/VHE + low energy' fit is simply a demonstration that, just like the October/November 2003 SSC modelling, the 'X-ray/VHE + low energy' fit can still fairly accurately predict the X-ray and VHE $\gamma-$ray observations of the August/September 2004 campaign. The best fit to the X-ray/VHE data can be seen in Fig. 7.6, with the best 'X-ray/VHE + low energy' fit is shown in Fig. 7.7. The fit parameters and reduced χ^2 for both of these fits are shown in Table 7.1.

With a better reduced χ^2, 0.961 for 33 degrees of freedom compared to 1.254 for 33 degrees of freedom, the X-ray/VHE fit (with the emission regions for the two energy bands being co-spatial), models the observations of the August/September 2004 campaign more accurately. Indeed, the correlation between X-ray and VHE $\gamma-$ray flux, shown in Section 7.2, also indicates that a single-zone model can be applied.

Compared to the best X-ray/VHE fit parameters for the October/November 2003 campaign, we find little difference in the best X-ray/VHE fit parameters for August/September 2004. Indeed the only major differences between the

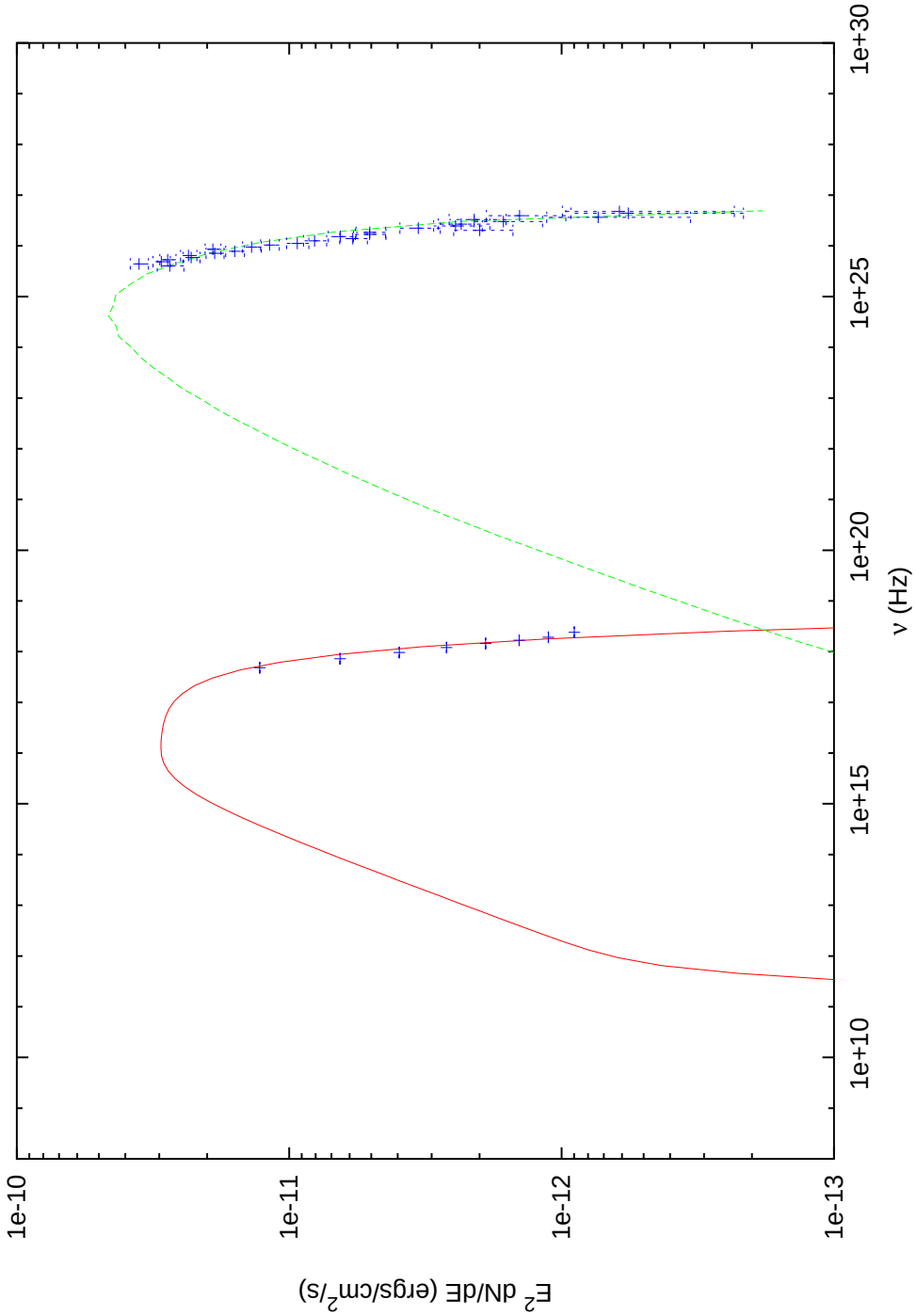

Figure 7.6: Using the same data as Fig. 7.5, assuming a X-ray/VHE fit, the synchrotron continuum is described by the solid line and the IC continuum is described by the dashed line. The model parameters are $\delta = 20$, B = 0.13 Gauss, R = 1×10^{14} m, $\log(E_{min}/\mathrm{eV})$=7.0, $\log(E_{break}/\mathrm{eV})$=9.95, $\log(E_{max}/\mathrm{eV})$=11.0 and an electron energy density of 0.06 ergs cm^{-3}.

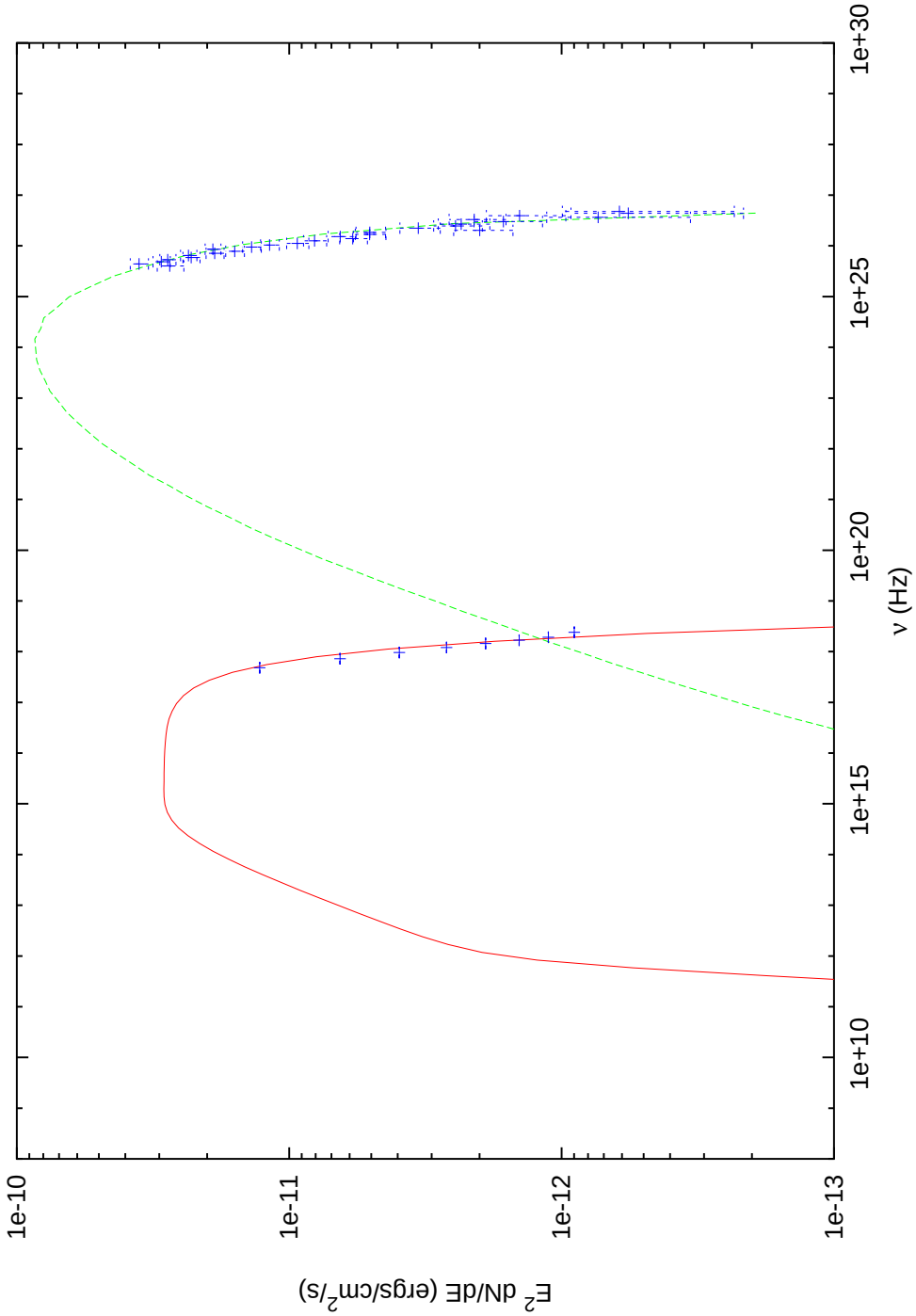

Figure 7.7: Using the same data as Fig. 7.5, a 'X-ray/VHE + low energy' fit was applied, assuming similiar optical flux to 2003. However, it should be stressed that this fit is simply a demonstration that, just like the 2003 SSC modelling, the 'X-ray/VHE + low energy' fit can still fairly accurately predict the X-ray and VHE $\gamma-$ray observations of the 2004 campaign.

Table 7.1: Summary of fit parameters for the different emission constraints for the August/September 2004 campaign.

	X-ray/VHE fit	'X-ray/VHE + low energy' fit
δ	20	18
B (G)	0.13	0.15
R (m)	10^{14}	10^{14}
$E_{density}$ (ergs/cm^3)	0.06	0.18
$\log(E_{min}/\mathrm{eV})$	7.0	7.0
$\log(E_{break}/\mathrm{eV})$	9.95	9.45
$\log(E_{max}/\mathrm{eV})$	11.0	11.0
Reduced χ^2/d.o.f	0.961/33	1.25/33

two fits are the Doppler factor and the energy density of the emission region.

The Doppler factor for 2003 is somewhat higher than that for August and September 2004 ($\delta_{2003} = 32$ compared to $\delta_{2004} = 20$). At first glance, this difference in Doppler factor is counter-intuitive considering that August/September 2004 exhibits far more variability, over a greater dynamic range, at both X-ray and VHE $\gamma-$ray energies. However, it should be noted that the model-independent minimum Doppler factor calculated for August/September 2004 is over 2 times smaller than that for 2003 ($\delta_{2003} \geq 19.4$ compared to $\delta_{2004} \geq 8.1$). More to the point, while there was greater variability in both energy bands during the August/September 2004 campaign, this variability is fairly steady over the whole campaign period. The variability observed in October/November 2004 was in essence short and sharp, with both flares on a smaller timescale than the variability timescale used in Section 7.1. (These short sharp flares possibly being associated with sudden discrete mass ejection into the base of the jet.)

Since the SED data in both the 2003 and the August/September 2004 campaigns are averaged over the whole campaign, the type of flaring observed in 2003 appears to have a greater impact on the global SSC fit for the whole campaign. The parameters for 2003 indicating the emission is dominated by smaller, faster 'blobs' of matter, while the August/September 2004 campaign is dominated by steady variabililty associated with larger, slower moving 'blobs'.

It should be noted that, from the X-ray/VHE fit to the global SED fit for August/September, we find that the synchrotron peak is located at 1.2×10^{16} Hz ($\sim$49.7 eV) and that the Inverse Compton peak is located at 4.2×10^{24} Hz ($\sim$170 GeV). These values were used in Section 7.1 to constrain B and δ.

7.3.2 Quiescent jet SSC model?

As with Section 5.3.2 for October/November 2003, an inhomogenous jet SSC model was also applied to the SED for August/September 2004. With a constant injection of particles into the base of the jet, the inhomogenous jet SSC model assumes SSC emission along the first 2×10^{18} cm of the jet. Along this length, both the local Lorentz factor and the local magnetic field strength decrease in a powerlaw fashion, as does the particle density due to adiabatic expansion. The inhomogenous jet SSC model was applied to investigate if a constant injection of particles could accurately model the overall SED, though the large amount of variability observed during the campaign already indicates that a constant injection of particles is unlikely.

The best model fit was found by varying the local Lorentz factor, magnetic field strength, particle density and bulk Lorentz factor to minimise the reduced χ^2. As with Section 5.3.2, the angle between the jet and the line of sight was frozen at 4°, which agrees with the radio observation of Piner & Edwards [140]. Shown in Fig. 7.8, the best fit parameters are an initial magnetic field strength of 0.6 G, an initial local Lorentz factor of 4.25×10^5, a particle density of 1.6×10^5 electrons cm^{-3} and an initial bulk Lorentz factor of 4.

While at first glance these parameters produce a good fit to the observed SED, on closer inspection of the high energy tail of the VHE data in particular, we find large discrepancies between the model and the data. The reduced χ^2 for the fit to the X-ray data is reasonable at 0.7 for 7 degrees of freedom. The reduced χ^2 for the fit to the VHE data, for all bar the 5 highest energy data points is also quite reasonable at 1.5 for 20 degrees of freedom. However, the high energy tail of the VHE observations significantly increases the reduced χ^2 , with the last two data points not being fitted by the model fit at all.

Compared to the quiescent fit parameters for October/November 2003,

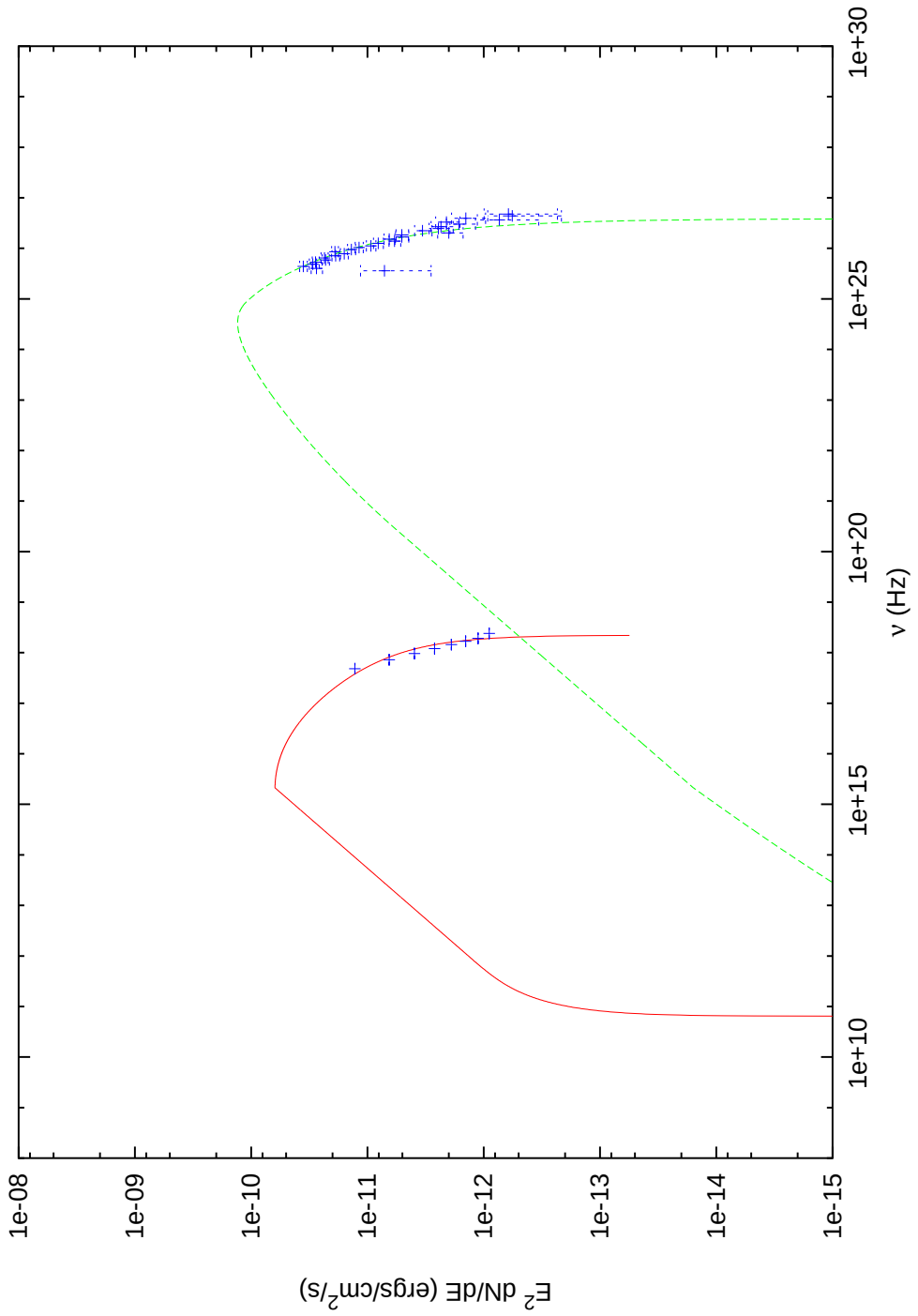

Figure 7.8: The inhomogenous jet SSC model fit to the August/September 2004 SED. Ths synchrotron continuum is described by the solid red line while the IC continuum is described by the dashed green line.

both the particle density and the initial local Lorentz factor for August and September 2004 are similiar. However, there is marked difference between the two campaigns in the magnetic field strength and the bulk Lorentz factor at the base of the jet, with the magnetic field being a factor of two smaller, and the bulk Lorentz factor being a factor of two bigger during August/September 2004. While the larger bulk Lorentz factor for August/September indicates that matter is being injected into the jet at a greater rate (possibly indicating that the larger amount of variability during this campaign is due to an increase into injection rate) the extremely poor reduced χ^2 of the fit indicates that caution should be used when interpreting the inhomogeneous jet SSC model fit.

7.4 Conclusion

In this Chapter, the results of the August/September 2004 H.E.S.S. and *RXTE* campaign on PKS 2155−304 have been discussed and interpreted. As with the October/November 2003 campaign, the 2−10 keV flux levels are close to historically low values indicating that the source appears to be in a quiescent state throughout the campaign. Nonetheless, 3 large X-ray flares were detected throughout the campaign, these flares having a much larger dynamic range of variability compared to the X-ray flares of the October/November 2003 campaign.

The large dynamic range of variability during August/September campaign allowed a clear detection of correlated VHE γ−ray/X-ray variability. It would therefore appear that the lack of correlation between the VHE γ−ray and X-ray flux during the October/November 2003 campaign was an artifact of the small dynamic range of variability during the October/November 2003 campaign. It is possible that the larger dynamic range also allowed a more obvious correlation between 2−10 keV flux and 3−10 keV photon index, this correlation indicating that $\Gamma_{3-10\mathrm{keV}} \propto 0.07 \times \mathrm{F}_{2-10\mathrm{keV}}$.

Although 3 flaring events were observed during the campaign, only one was simultaneously observed in both energy bands. The rise-time of this flare was used to constrain, through a model-independent method, the minimum

Doppler factor, δ, to 8.12. Assuming a single-zone SSC model, the maximum magnetic field strength was calculated to be 10.58 Gauss. While there is little difference in maximum magnetic field strength between the 2003 and 2004 campaign, there is marked difference in the minimum Doppler factor, ($\delta_{2003} \geq 19.4$ compared to $\delta_{2004} \geq 8.1$).

SED modelling of the August/September 2004 data reveals that, like the October/November 2004 campaign, the broadband emission for PKS 2155−304 is best described by a single-zone SSC fit to the X-ray and VHE $\gamma-$ray data alone. With fit parameters described by Table 7.1, the reduced χ^2 for the single-zone SSC fit is 0.96 for 33 degrees of freedom compared to the >900 for the inhomogeneous jet SSC model.

Chapter 8

PKS 2155−304 November 2004 Campaign

During the first 10 days of November 2004 another multi-wavelength campaign was completed on PKS 2155−304. While this campaign was not extensive in temporal resolution or coverage, large spectral coverage was achieved with observations at VHE $\gamma-$ray, X-ray, infrared, sub-millimeter and radio energies.

As with the August/September 2004 campaign, the complete 4 telescope H.E.S.S. array was used, while the X-ray observations were completed using *RXTE*. The infra-red observations were taken with the *Spitzer* Space Telescope, the sub-mm observations were completed with the JCMT and as before the NRT was used for the radio observations. The sparse temporal coverage during this campaign, coupled with the high percentage of weather affected runs means that there is little scope for in-depth correlation and variability studies. However, the strength of the November 2004 campaign is its large spectral coverage. Particularily true at energies less than 2−10 keV X-rays, this coverage will allow us to constrain possible emission models through the use of SED modelling.

In this chapter the results of quasi-simultaneous VHE $\gamma-$ray, X-ray, infrared, sub-millimeter and radio observations will be presented. These results will then be used to probe possible emission models through SED modelling. In particular, the distribution of the electron population will be investigated, assuming that a SSC model is dominant.

8.1 Observations

8.1.1 H.E.S.S. observations

As with the August/September 2004 campaign, the VHE $\gamma-$ray observations were taken with the full array of four telescopes. Each observation was taken in stereoscopic *Wobble* mode, with PKS 2155−304 positioned either $\pm 0.5^{\circ}$ in declination OR $\pm 0.579^{\circ}$ in right ascension relative to the center of the field of view of the camera.

As described in Section 3.6.1, the stability of the central trigger rate was used during quality control to only select runs taken under a stable sky. The radiometer data were used to confirm that data with an unstable central trigger rate were associated with clouds passing across the field of view. After the central trigger rate cuts were applied to the data, only 8 observation runs remain ($5^{\text{th}} - 9^{\text{th}}$ November).

The data was cleaned using the standard '5-10' criterion, with the image parameterisation occuring after the standard cuts, described in Table 3.2, applied. As with previous H.E.S.S. observations, the background was estimated using the ring background model as described in Section 3.6.3. The 8 observation runs gave a total live time of 3.46 hours, with an excess of 265 $\gamma-$ray events and a resulting significance of 9.0 σ. The two-dimensional excess sky map of the November 2004 observations is shown in Figure 8.1, along with the θ^2 distribution of the observations.

Spectrum

The November 2004 data were fitted with both a power law and a broken power law function. The power law was found to be a better fit with a reduced χ^2 of 1.00 for 5 degrees of freedom and a χ^2 probability of 0.42, compared to the broken power law reduced χ^2 of 2.5 for 2 degrees of freedom and a χ^2 probability of 0.08. Shown in Fig. 8.2, the power law fit is described by Eq. 8.1.

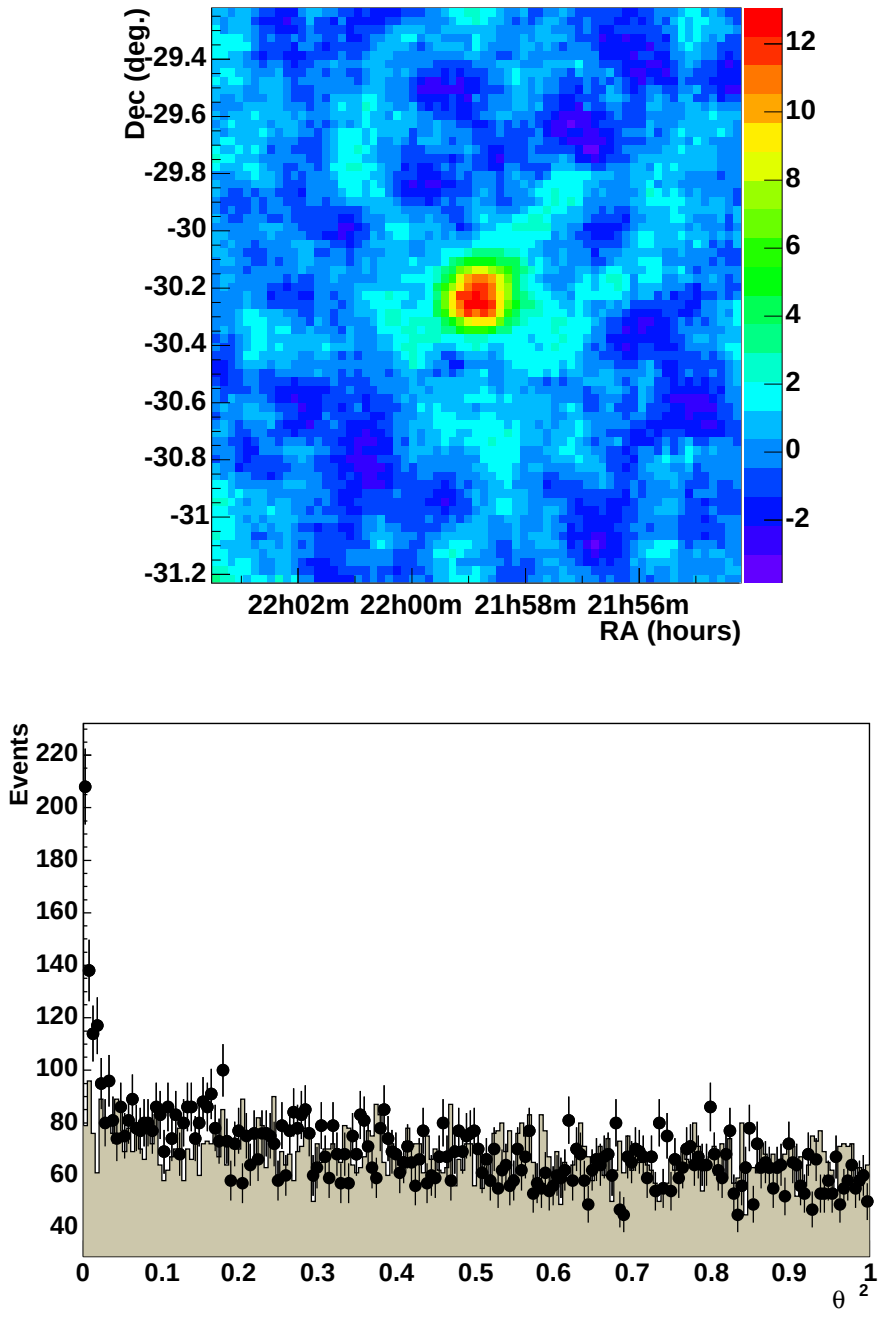

Figure 8.1: *Top:* The two-dimensional distribution of the excess events in the direction of PKS 2155 − 304 during November 2004. Right hand scale is the number of excess events. *Bottom:* The θ^2 distribution of on source events (points) and normalised background events (shaded).

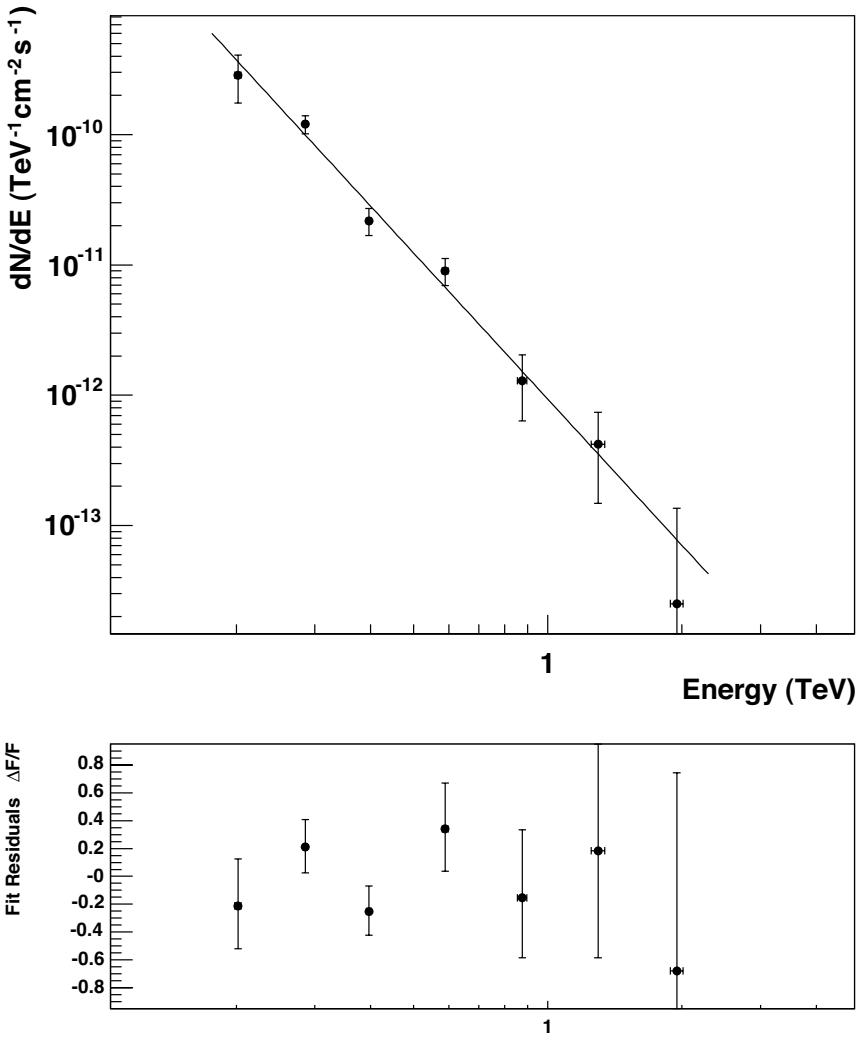

Figure 8.2: *Top:* Power law fit to the VHE data for November 2004. This fit yields a photon index, $\Gamma = -3.73 \pm 0.22$, with a $\chi^2 = 1.00$ for 5 degrees of freedom. *Bottom:* The residuals to the power law fit.

$$\frac{\mathrm{d}N}{\mathrm{d}E} = (9.3 \pm 2.6) \times 10^{-13} \left(\frac{E}{\mathrm{TeV}}\right)^{-3.73 \pm 0.22_{stat} \pm 0.1_{sys}} \mathrm{cm}^{-2}\ \mathrm{s}^{-1}\ \mathrm{TeV}^{-1} \quad (8.1)$$

Lightcurve

The H.E.S.S. lightcurve of PKS 2155−304 during November 2004 campaign is shown in Figure 8.3. The data have been binned using the orignal 28 minute observation length, with flux being derived using the photon index of 3.727 from the power law fit. The E> 300GeV flux of PKS 2155−304 during the campaign ranges from $F_{min} = 3.7 \times 10^{-8}$ photons $m^{-2}s^{-1}$ to $F_{max} = 1.4 \times 10^{-7}$ photons $m^{-2}s^{-1}$. Note that these fluxes are comparable to the VHE fluxes from the October/November 2003 and August/September 2004 campaigns indicating that the source is likely to have been in a quiescent state during November 2004.

As with previous H.E.S.S. observations of PKS 2155−304, there is evidence for inter-night variability. Fitting Fig. 8.3 with a constant flux yields a χ^2 of 44.7 for 7 degrees of freedom, corresponding to a $(1.8 \pm 0.2) \times 10^{-9}$ χ^2 probability. Unfortunately the small number of observations do not allow probing of any intra-night variability.

8.1.2 *RXTE* observations

The X-ray emission from PKS 2155−304 during early November 2004 was monitored using PCA onboard *RXTE*, as part of the proposal P91118. A total of 6.2×10^4 seconds livetime was recorded from MJD = 53311 to MJD = 53318. The whole of the data set obtained by *RXTE* during November 2004 is dominated by observations using PCU 0 and PCU 2, though PCU 3 was very briefly used. The data reduction therefore is focused upon data from PCU 0 and PCU 2 only.

As described in previously, PCU 0 is known for gain fluctuations. These fluctuations are associated with the loss of its propane layer and must be taken into consideration. While the background modelling can attempt to take these fluctuations into consideration, as we will see, it does not remove the effects

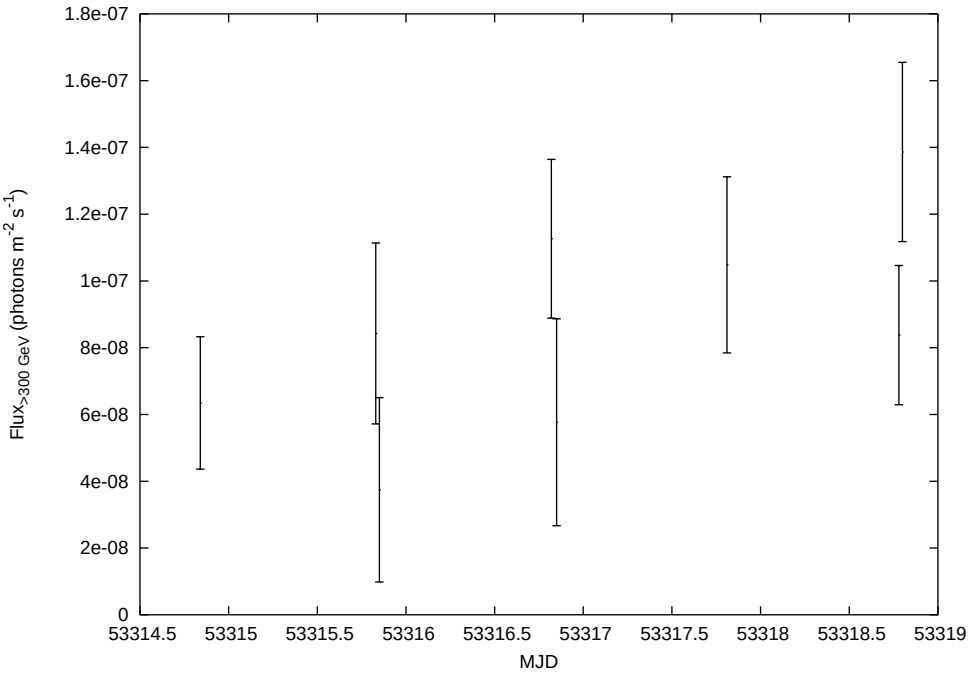

Figure 8.3: PKS 2155−304's E>300 GeV flux during November 2004 in units of photons m^{-2} s^{-1}.

completely, especially when the source is close to quiescence at X-ray energies. The effects of the using PCU 0 was investigated by reducing data with both PCU 0 & 2 active and just PCU 2 on its own.

As before, the X-ray data were reduced using the FTOOLS V5.2. The STANDARD2 data was extracted using the FTOOLS XDF, with signal being considered from the left and right hand side of layer one only. The same good time interval criteria as described in Section 4.2.2 were applied to the extracted data. As with the *RXTE* data reduction for the previous campaigns, the background was modelled using PCABACKEST V3.0, with a faint background model being used. After background subtraction, data were extracted from PHA channels 0-27, with only data in the energy range 3−10 keV being considered for spectral fitting.

The reduced data were then fitted using XSPEC 11.2. The PCU 0 & 2 data were reduced first and fitted with an absorbed power law (WABS*PO), using a fixed column density of 1.7×10^{20}. The power law fit and residuals to the summed PCU 0 & 2 are shown in Fig. 8.4. Note that the appropriate

response matrix for combined PCU 0 and PCU 2 data was modelled using the FTOOLS PCARSP V8.2. With a reduced χ^2 of 1.67 for 14 degrees of freedom and an associated χ^2 probability of 0.06, the power law fit gives a photon index, $\Gamma = 3.04 \pm 0.08$.

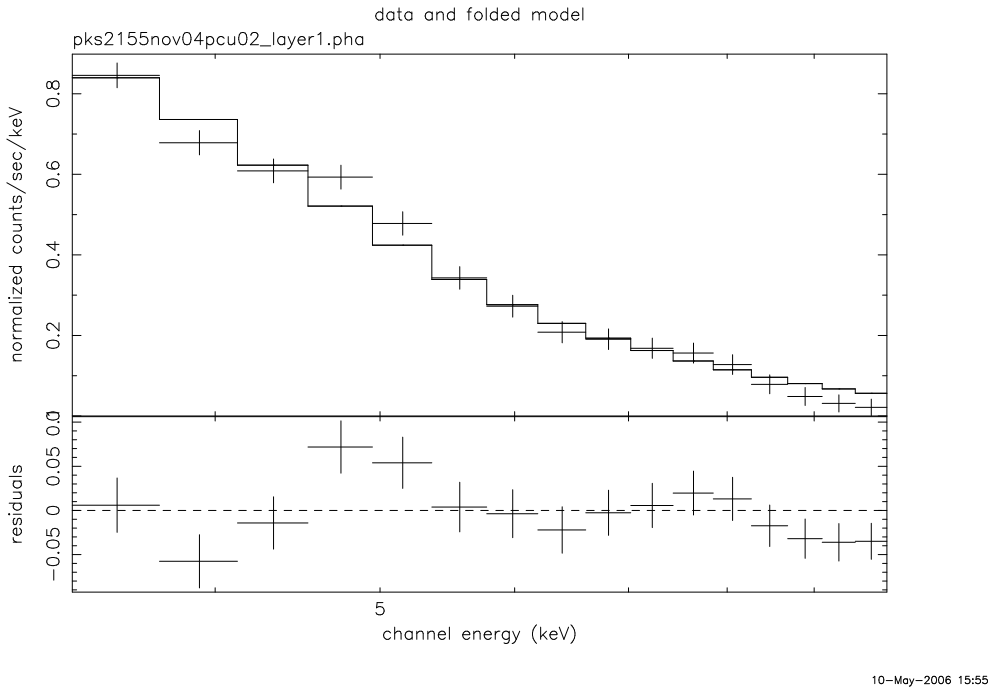

Figure 8.4: *Top*: Power law fit to the summed data from PCU 0 & 2, resulting in a $\Gamma = 3.04 \pm 0.08$. *Bottom*: Residuals to the data set from the power law fit.

Interestingly, while the residuals to the power law fit are small, there are two excess features at 4.8 and 7.8 keV. Upon inspection, we also find these features present in the background spectra modelled for these observations, leading us to believe that rather than being intrinsic to the source, both excess features are an artifact of the background modelling and subtraction. What is more, these excess features are present in past *RXTE* observations of PKS 2155-304 made by Vestrand & Sreekumar in 1999 [191]. Vestrand & Sreekumar associated these features to the background modelled for a quiescent PKS 2155−304. Indeed an 'active' state spectrum of PKS 2155−304 using *RXTE* presented in the same paper was void of such excess features. Since the excess features were present in the quiescent spectra before PCU 0 lost its propane layer, it

is safe to assume that the excess features are not purely due to modelling the background for PCU 0 incorrectly.

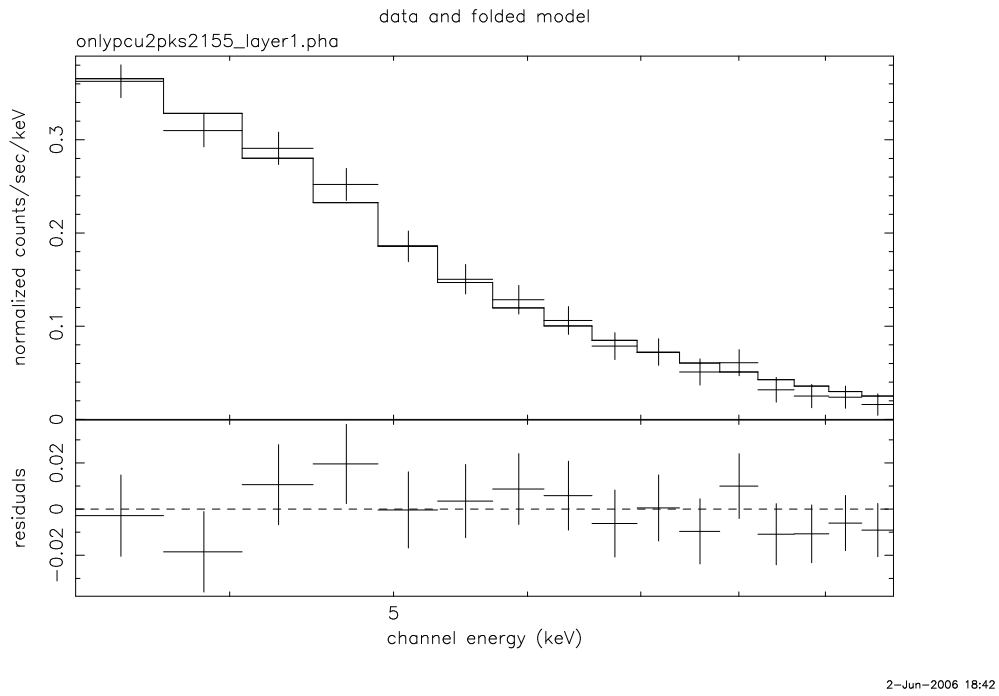

Figure 8.5: *Top*: Power law fit to the summed data from PCU 2, resulting in a $\Gamma = 3.11 \pm 0.11$. *Bottom*: Residuals to the data set from the power law fit.

To investigate the effect the poorly modelled background has on the flux levels and spectrum fit, the raw data were reduced again with the same good time intervals, but only considering data from PCU 2. Fitting a power law to the 3−10 keV PCU 2 data only results in a better reduced χ^2 of 0.48 for 14 degrees of freedom and a χ^2 probability of 0.94, see Fig. 8.5. Again note that the appropriate response matrix for PCU 2 data was modelled using the FTOOLS PCARSP V8.2. There is little difference in the 2−10 keV flux calculated for both data sets.

However, it should be pointed out that by only considering the signal from one PCU instead of two, we essentially halve the counts detected. Since the source is in quiescence and the total data set only consists of 6.2×10^4 seconds livetime, halving the counts can dramatically increase the statistical uncertain associated with the counting, especially for some of the short exposures.

Therefore, for the November 2004 *RXTE* data set, data from both PCU 0 & 2 will be considered, resulting in the 2-10 keV flux lightcurve shown in Fig 8.6.

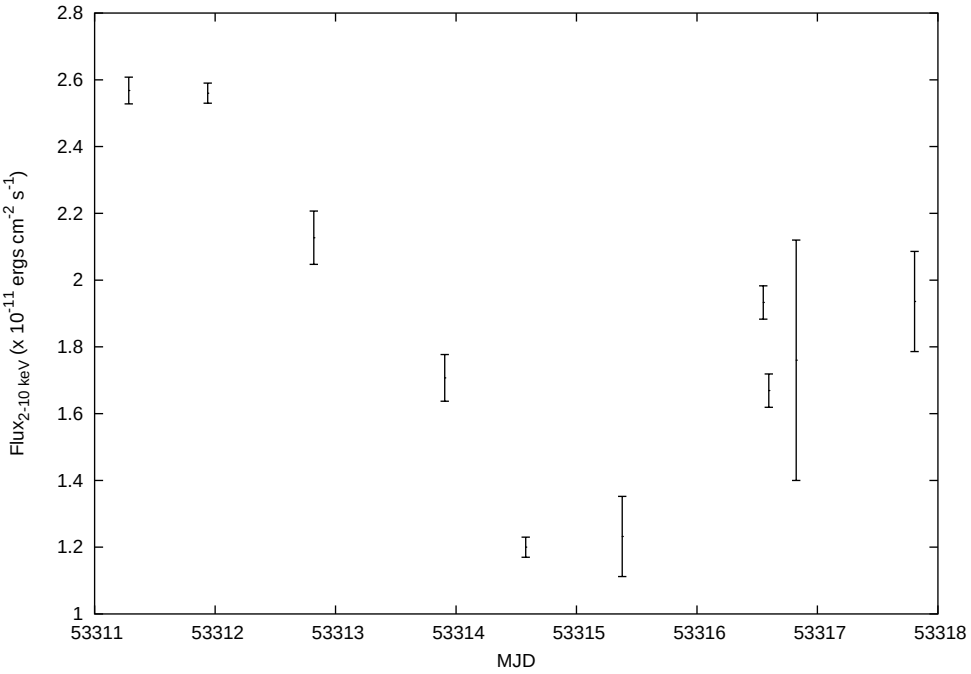

Figure 8.6: The 2-10 keV lightcurve for PKS 2155−304 during November 2004 using both PCU 0 and PCU 2.

From Fig 8.6 we can see that there is evidence for inter-night variability, however, due to the limited number of observations, we are unable to probe intra-night variability to any great extent. During the November 2004 campaign, the 2−10 keV flux varied from $F_{min} = 1.2 \times 10^{-11}$ ergs cm^{-2}s^{-1} to $F_{max} = 2.6 \times 10^{-11}$ ergs cm^{-2}s^{-1}. Compared to past values, we see that the X-ray emission is close to historically low values, again indicating that PKS 2155−304 is in a quiescent state during the November 2004 campaign.

8.1.3 *Spitzer* observations

The mid to far infra-red flux of PKS 2155−304 was monitored using the Multiband Imaging Photometer (MIPS) onboard the *Spitzer* Space telescope from $2^{nd} - 10^{th}$ November. PKS 2155−304 was observed 16 times during this time, with each visit comprising of a single flux measurement at 24, 70 and 160 μm.

Variability on shorter timescales was also probed on two separate occasions with 20×3s exposures at 24 μm and 20×10s exposures at 70 μm [142].

The basic calibrated data were processed with the standard Spitzer Science Center software pipeline S11.0.1. A median flatfield was calculated for each 24 μm observation and was then applied to all the data. After data reduction, a total of 16×160 μm and $54 \times (24$ & $70)$ μm images was obtained, with PKS 2155−304 being readily identified in all energy bands observed. Photometry from these images was extracted using APEX, with a signal to noise ratio of 7−15.

Lightcurves & Fluxes

The 24, 70 and 160 μm lightcurves of PKS 2155−304 are shown in Fig. 8.7, with the well-sampled periods at 24 and 70 μm enlarged in Fig. 8.8 and Fig. 8.9. From Fig. 8.7 we can see that neither the 70 or 160 μm lightcurves show significant evidence for variability during the November 2004 campaign. A constant flux fit to the 70 or 160 μm lightcurves has a reduced χ^2 of 0.7 for 53 degrees of freedom and 0.2 for 15 degrees of freedom respectively. (It should be noted that the uncertainty in the 160 μm data is dominated by the background). However, the 24 μm lightcurve does show evidence for variability, with a reduced χ^2 of 3.3 for 53 degrees of freedom for a constant flux fit. Further investigation showed the 24 μm flux to vary at 5% level on timescales of $\sim$1 day [142].

The average fluxes for each energy band over the 8 day observing period are shown in Table 8.1. The certainty of the absolute flux calibration of *Spitzer* is dependent upon the wavelength observed, with the 24 μm observations accurate to 10% and the 24 & 70 μm observations accurate to 20%. Comparing to the archival flux measurements of 90.8 ± 3.2 mJy (14.3 μ m), 315 ± 27 mJy (60 μm), 250 ± 34 mJy (90 μm) and an upper limit of 1.2 Jy (170 μm) from the Infrared Space Observatory (*ISO*) and the InfraRed Astronomical Satellite (*IRAF*) [98, 22], we see that during November 2004 PKS 2155−304 appears to be in a quiescent state at mid to far infra-red energies.

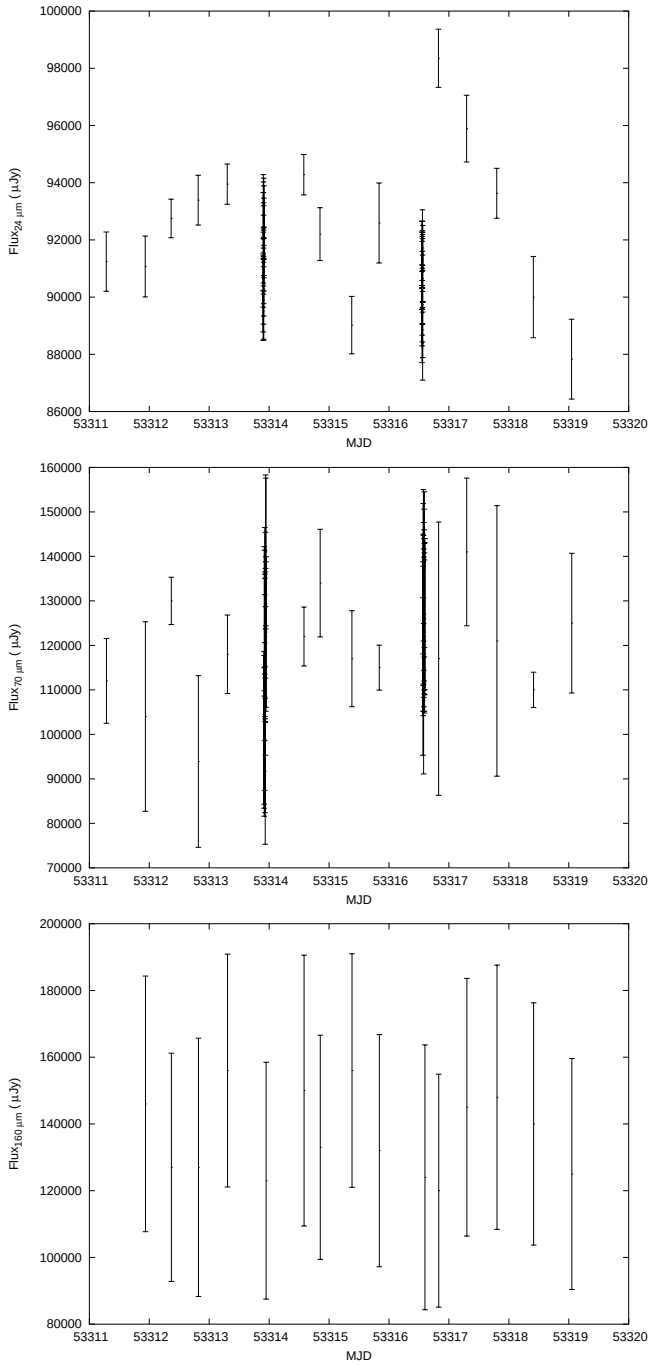

Figure 8.7: Lightcurve at 24μm (top), 70μm (middle) and 160μm (bottom) of PKS 2155−304 during $2^{\text{nd}} - 10^{\text{th}}$ November.

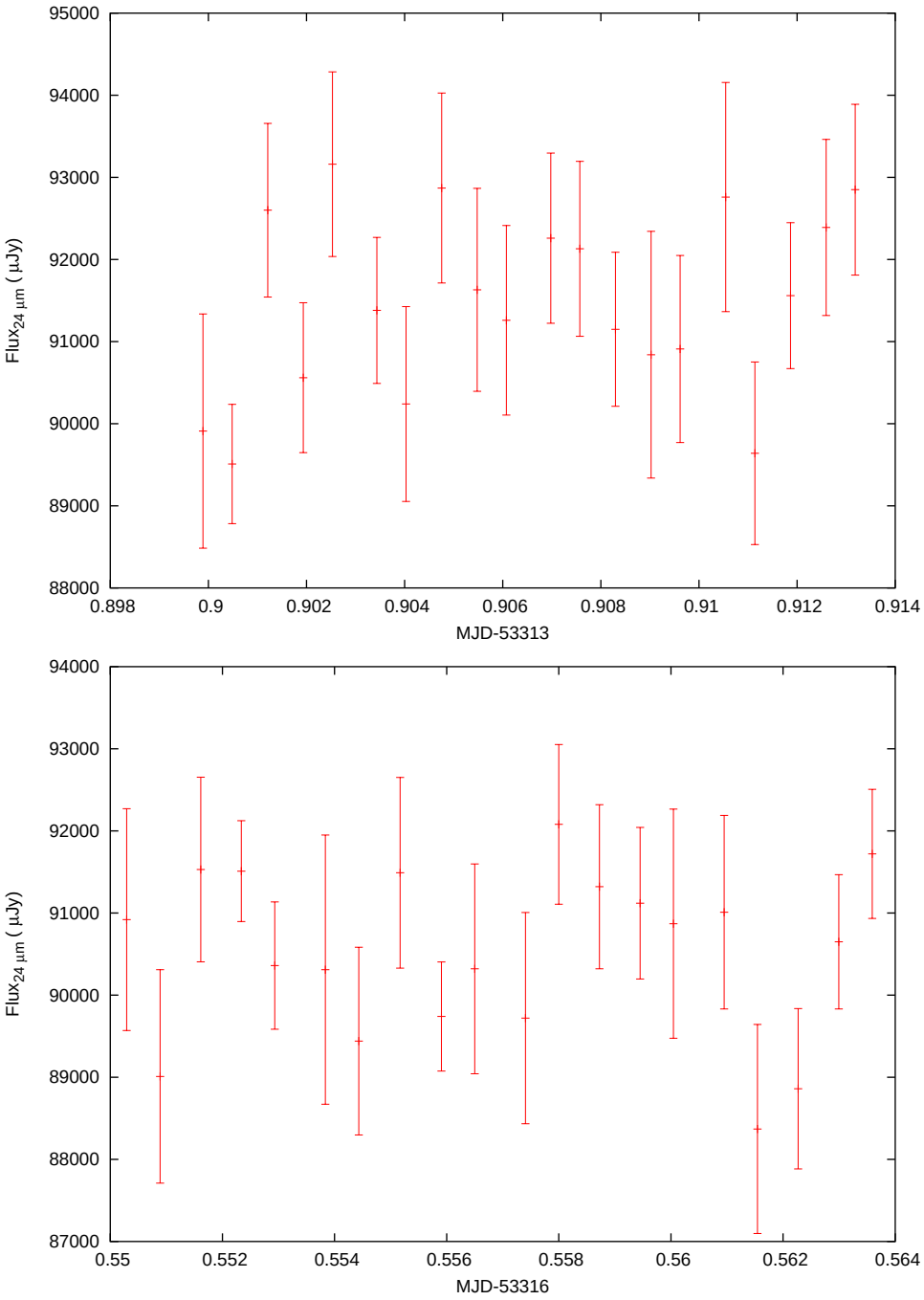

Figure 8.8: 24μm lightcurve during the extended, well-sampled visits. The first well-sampled visit (MJD = 53313) is shown in the top panel, while the second visit (MJD = 53316) is shown in the bottom panel.

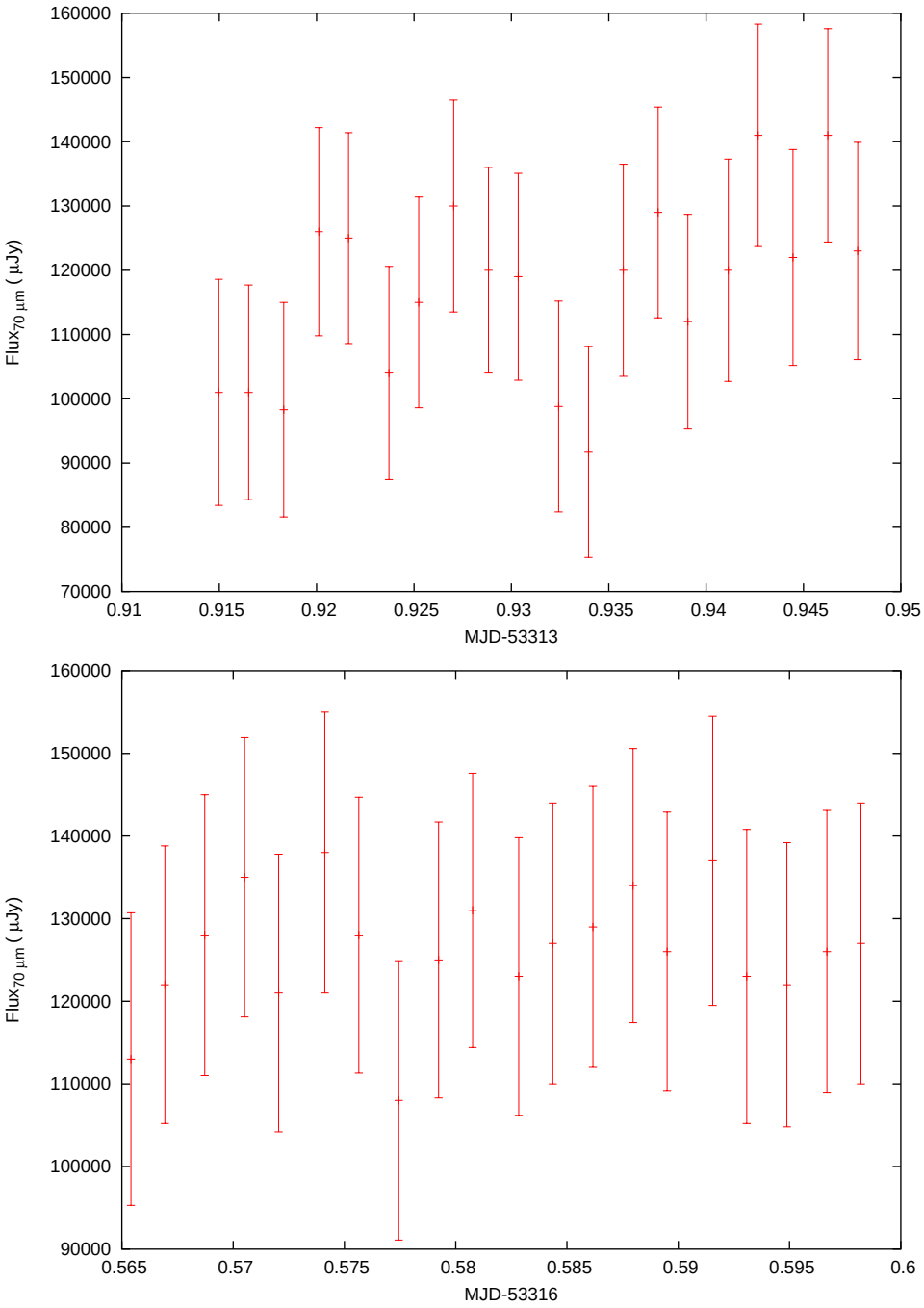

Figure 8.9: 70μm lightcurve during the extended, well-sampled visits. The first well-sampled visit (MJD = 53313) is shown in the top panel, while the second visit (MJD = 53316) is shown in the bottom panel.

Table 8.1: Average fluxes at 24,70 and 160 μm

Wavelength	Flux (ergs cm^2 s^{-1})
24 μm	$(12.4 \pm 1.2) \times 10^{-12}$
70 μm	$(5.4 \pm 1.1) \times 10^{-12}$
160 μm	$(2.7 \pm 0.6) \times 10^{-12}$

8.1.4 JCMT sub-mm observations

The submillimeter observations were made with the SCUBA detector on the James Clerk Maxwell Telescope (JCMT). The JCMT is a single 15 m diameter dish telescope on an alt-azimuth mounting, located on Mauna Kea in Hawaii, at an altitude of 4.2 km. With a field of view of 2.3 arcminutes, SCUBA (Submillimetre Common User Bolometer Array) consists of two hexagonal arrays of bolometric detectors ('pixels'). One array consists of 37 pixels and is dedicated to 850 μm observations (LW), the other array consists of 91 pixels dedicated to 450 μm observations (SW). Limited by diffraction, the LW array has a resolution of 14" and the SW array has a resolution of 7.5". The SCUBA detector is cooled to 100 mK and as such the sensitivity of SCUBA is limited by the photon noise from sky. Nevertheless, SCUBA gives unprecedented sensitivity at sub-mm wavelengths. For an indepth review of the SCUBA detector, see [95].

As with the H.E.S.S. observations, the SCUBA observations were affected by weather conditions, primarily in the form of high water vapour content. Only 2 observing runs were acceptable: a 45 minute exposure on 4$^{\text{th}}$ November 2004 and a 15 minute exposure on the 11$^{\text{th}}$ November 2004, at both 450 and 850 μm. All of these observations were taken in *jiggle-map* mode. Used to minimise undersampling of the sky background, jiggle mode consists of 4 cycles of 16 pointed jiggle positions, each jiggle position offset by $\sim$3 arcsec from the last. A single jiggle cycle takes 64 seconds to complete and is repeated until an adequate signal to noise ratio is obtained.

The SCUBA observations were reduced using the SCUBA User Reduction Facility (SURF) software, version 1.6-11. While the usual data reduction steps,

Table 8.2: Zenith opacities at 450 and 850 μm for the two observations.

	450 μm	850 μm
04/11/2004	2.72 ± 0.59	0.53 ± 0.09
11/11/2004	2.59 ± 0.51	0.44 ± 0.002

such as flatfielding and background subtraction, are also applied during sub-mm data reduction, there are two additional and crucial steps that need to be considered during sub-mm data reduction. The first is the correction for atmospheric extinction, primarily due to water vapour, and the second is flux calibration using point sources of known sub-mm flux.

Extinction correction

Observations at both 450 and 850 μm are very sensitive to atmospheric extinction. The amount of extinction correction needed to be applied is given by $S(z) \propto \exp^{-\tau \sec(z)}$, where z is the zenith angle of the observation and τ is the zenith opacity. The zenith opacities for each observation were calculated using the SURF skydip routine and are shown in Table 8.2. Note that the zenith opacity at 450 μm is significantly larger than at 850 μm and as such only the brightest of AGN at 450 μm are detected by SCUBA.

Once the zenith opacity is calculated for each image separately, the extinction correction can be applied to the corresponding observation. An example of a flatfield, sky background and extinction corrected image of PKS 2155−304 at 850 μm can be seen in Fig. 8.10. Note that PKS 2155−304 is in the centre of the field of view of Fig. 8.10 and that several bad pixels have been removed so as to get an accurate measurement of the sky background level.

Flux calibration

Once the observations have been reduced and extinction-corrected, they must be flux calibrated. Using a flux calibration observation of a point source of known sub-mm flux, a conversion factor from bolometer voltage to Jansky is calculated. For our SCUBA observations, the planet Uranus was used for

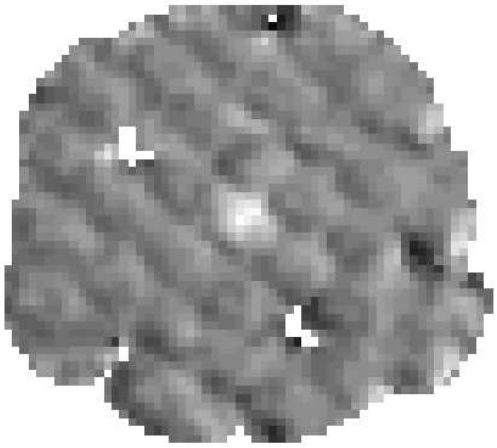

Figure 8.10: A flatfield, sky background and extinction corrected image of PKS 2155−304 at 850 μm. Note that PKS 2155−304 is in the center of the field of view. Several bad pixels have been removed to obtain a more accurate measurement of the sky background level.

calculating the conversion factor. The conversion factors for the 850μm observations are given in Table 8.3.

Since PKS 2155−304 is a non-extended source, in the centre of the field of view for all the observations, applying the conversion factor to the peak voltage of the central pixel gives us the flux. It should be noted that no signal was detected from PKS 2155−304 at 450 μm during either observation. The peak voltages and flux values of the 850 μm observations are given in Table 8.3. The error associated with a 200-299 mJy flux level is set at 14% as described in [154].

Within the uncertainty, there is no evidence for variability of the 850 μm emission from PKS 2155−304. What is more, compared to a past SCUBA observation of PKS 2155−304 during May 1998, which detected a flux of 252±35 mJy [154], we find little evidence for variability on longer timescales.

Table 8.3: Peak voltage, conversion factor and resulting flux for both 850 μm observations.

	Conversion factor (Jy/beam V^{-1})	Peak Voltage (mV)	Flux (mJy)
04/11	264.8	0.99	262.7±36.8
11/11	260.7	0.97	253.1±35.4

8.1.5 Radio observations

The radio observations of PKS 2155−304 throughout the November 2004 campaign were obtained using the Nançay decimetric radio telescope, NRT. See Section 4.3.2 for a description of the Nançay decimetric radio telescope observation technique.

During the November 2004 campaign, the NRT observed a total of 27 times ($1^{st} - 13^{th}$ November). As with October/November 2003, the NRT radio observations were taken at 11 cm wavelength (2695 MHz). During the 27 observations there was little evidence for variability with an average flux of 0.31 ± 0.01 Jy [142].

8.2 Discussion and Interpretation

The Spectral Energy Distribution of the November 2004 campaign in νF_ν representation, is shown in Fig. 8.11. Since there is little evidence of large scale variability during the campaign, the data points in Fig. 8.11 are averaged over the whole campaign. The *RXTE* data are averaged over the whole campaign using PCU 2 data only; this was done to remove any uncertainty associated with the background modelling of PCU 0 and the apparent excess features at 4.8 and 7.8 keV.

8.2.1 One/Two Zone SSC

As before, Fig. 8.11 was first interpreted with a single-zone SSC model using the same code as in Section 5.3. Since there is little variability to constrain the

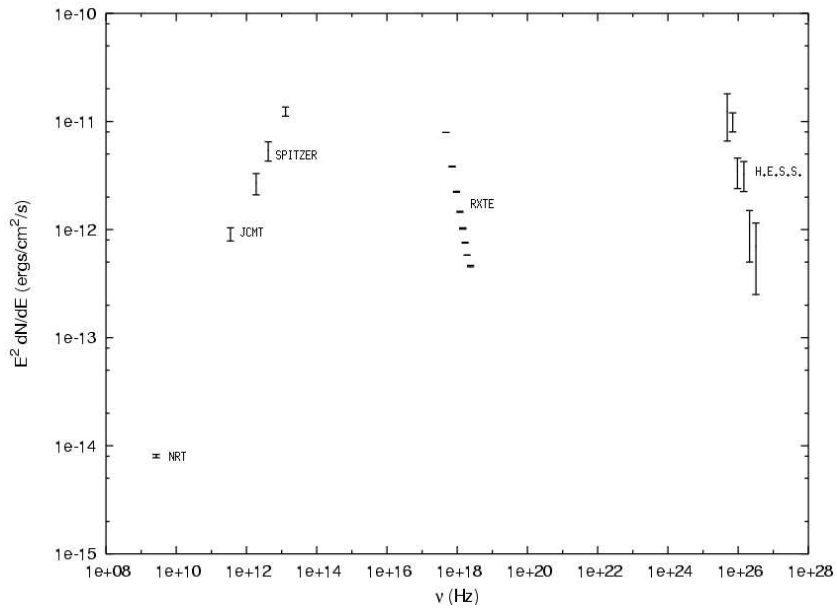

Figure 8.11: The Spectral Energy Distribution of PKS 2155-304 during November 2004.

emission region size and the flux levels are similiar to the October/November 2003 campaign, we assume initial model parameters similiar to those in Chapter 5; $R = 1 \times 10^{14}$ m, $\delta = 22$ and $B = 0.2$ G. To find the best model fit to the observed SED, the free parameters of B, R, δ and the electron distribution, were allowed to vary to minimise the reduced χ^2 of the fit.

Initially an attempt was made to fit the entire broadband SED with a single emission region described by the SSC code. Seen in Fig. 8.12, the best single-zone fit was found to have a magnetic field of 0.13 Gauss, a radius of 1×10^{14} m and energy density of 0.09 ergs cm^{-3}, (see Table 8.4 for best fit model parameters). The reduced χ^2 for this fit was 3.64 for 17 degrees of freedom. While the X-ray and VHE $\gamma-$ray data are reasonably well described by this fit, there is a clear discrepancy at the lower energies of IR, sub-mm and radio. Indeed, the majority of the contribution to the reduced χ^2 arises from the IR and sub-mm fit which has a reduced χ^2 of 17.7 for 3 degrees of freedom; note that like the October/November 2003 campaign, the single-zone model fails to describe the radio observations.

It should be noted that like Chapter 5, an attempt was also made to fit the

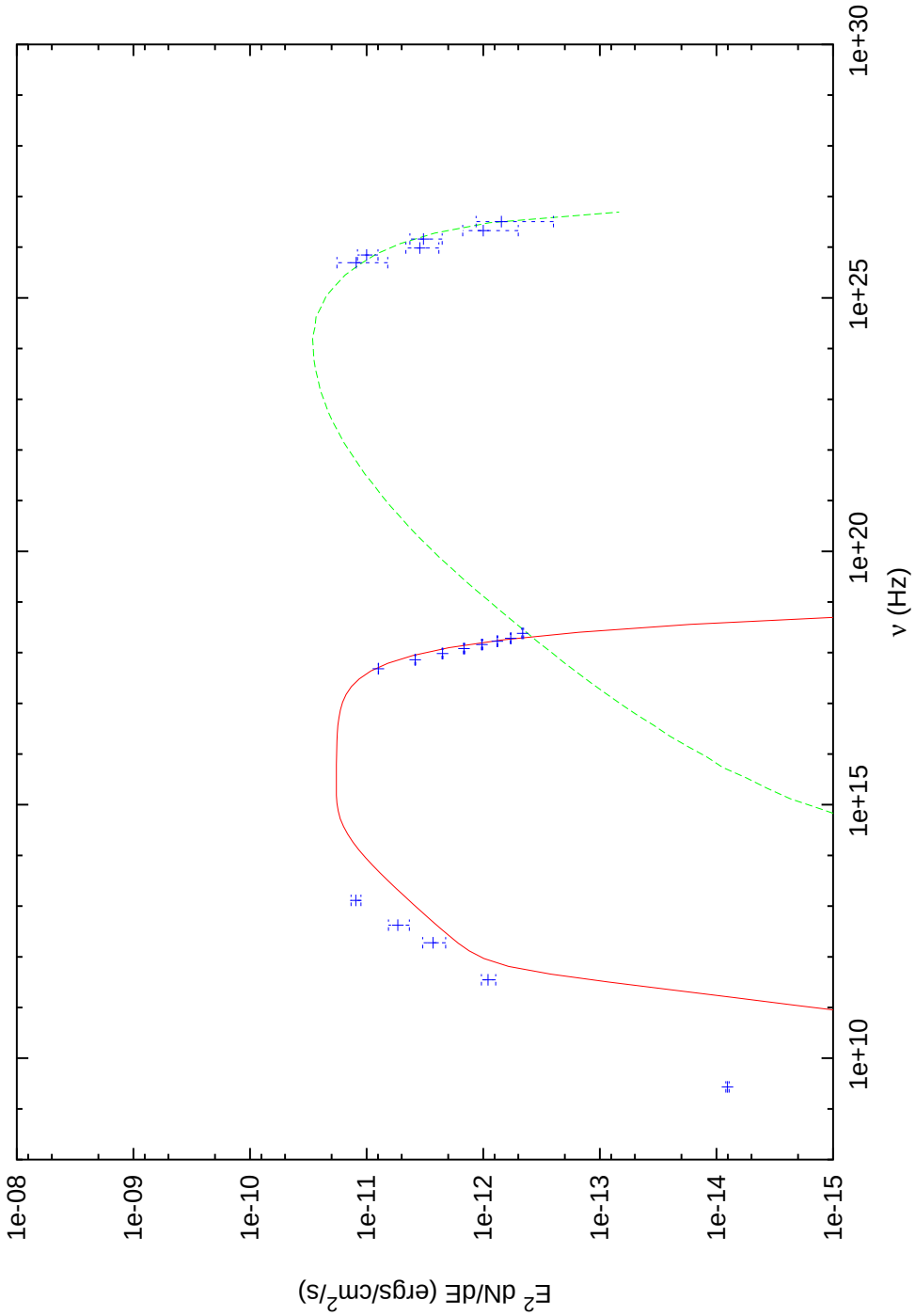

Figure 8.12: Using the same data as Fig. 8.11, the synchrotron continuum is described by the solid line and the IC continuum is described by the dashed line. The best fit parameters for the single-zone model are described in Table 8.4.

Table 8.4: Parameters for the SED fit for the assumptions that the all emission regions are cospatial (Model 1), that the low energy part of the SED emanates from the radio lobe (Model 2 + Model $2_{\text{Low energy}}$) or assuming a fit to the synchrotron continuum only.

Parameter	Model 1	Model 2	Model $2_{\text{Low Energy}}$	Syn. fit
$R_{blob}(10^{14}\text{m})$	1	1	100	0.7
B (G)	0.13	0.11	0.004	0.13
δ	20	22	2	30
p_1	-2.0	-2.0	-1.3	-2.0
p_2	-3.0	-3.0	–	-3.0
$E_{density}$(ergs cm^{-3})	0.09	0.035	0.065	0.12
E_{min} (log(E_{max}/eV))	7.0	7.0	4.0	6.9
E_{break} (log(E_{break}/eV))	9.5	10.0	10.5	9.0
E_{max} (log(E_{max}/eV))	11.0	11.0	10.5	10.9
Reduced χ^2/d.o.f	3.64/17	1.03/13	0.167/3	4.21/17

synchrotron continuum without being constrained by the VHE observations. Shown in Table 8.4, the best fit parameters to the synchrotron continuum imply a smaller faster moving emission region, with a slightly truncated electron distribution. However, it should be pointed out that while there is a marginal improvement in the reduced χ^2 for the IR and sub-mm data points, the deterioration of the reduced χ^2 to the high energy data points is far greater resulting in an overall reduced χ^2 of 4.21 for 17 degrees of freedom.

To address the discrepancy between the model and the observations at low energy, the low energy emission (radio to infrared) was assumed to originate in the radio lobes and was modelled as a single spherical emission region, two orders of magnitude bigger in radius than the emission region assumed for the single-zone modelling. The emission from this 'radio lobe' was believed to be synchrotron in origin. The high energy emission (X-ray and VHE $\gamma-$ray) was assumed to be attributed to a single-zone SSC mechanism. As before, the best fit was found by varying the magnetic field strength, Doppler factor and electron distribution to minimise the reduced χ^2. It should be noted that the best fit for the low and high energy components were found separately, essentially assuming that the two emission regions are isolated from each other.

Shown in Fig. 8.13, the dotted line represents the low energy emission associated with the radio lobe while the solid line represents the synchrotron continuum of the X-ray/VHE $\gamma-$ray emission region and the dashed line represents the Inverse Compton continuum of the X-ray/VHE $\gamma-$ray emission region. The fit parameters for these fits are shown in Table 8.4. It should be highlighted that the two-zone fit shows a considerable improvement in the overall reduced χ^2 of 0.8 for 17 degrees of freedom.

The best fit Doppler factor of the 'radio lobe' emission region was found to be low, 2, which is in line with the VLBI radio observations of Piner & Edwards [140]. While the energy distribution of the particle population was truncated to take into consideration that the particles have cooled, the *Spitzer* and JCMT data could only be fitted if the particle distribution had a single power law slope of $p_1 = -1.3$. Since the slope of the distribution is meant to steepen with cooling, the shallower slope implies that the particles have been heated. This re-heating could be associated with shock turbulence of the relativistic jet as it encounters the inter galactic medium. Admittedly, however, this is a rather *ad hoc* solution with no evidence for or against it.

Interestingly, this radio lobe assumption still does not adequately model the radio observations. While the lobe assumption is a marked improvement over the single zone fit at radio energies, there is still $\sim$1 order of magnitude difference between the model and the observed flux.

Compared to the model parameters for the single-zone fit, the high energy parameters for the two-zone fit show a slight increase in Doppler factor and a slight decrease in magnetic field strength. While there is little difference in the particle distribution, the energy density of the particle population for the X-ray/VHE $\gamma-$ray fit is a factor of $\sim$3 times smaller.

Compared to the X-ray/VHE $\gamma-$ray fits for both the October/November 2003 and August/September 2004 campaigns, we find that the fit parameters for November 2004 primarily agree with the SED fit parameters for August/September 2004. Indeed there is little difference between the Doppler factor, magnetic field strength and particle distribution for the two campaigns, with the only major difference being the energy density of the electron population ($E_{densityAug/Sept} = 0.06$ compared to $E_{densityNov} = 0.035$). Unfortunately,

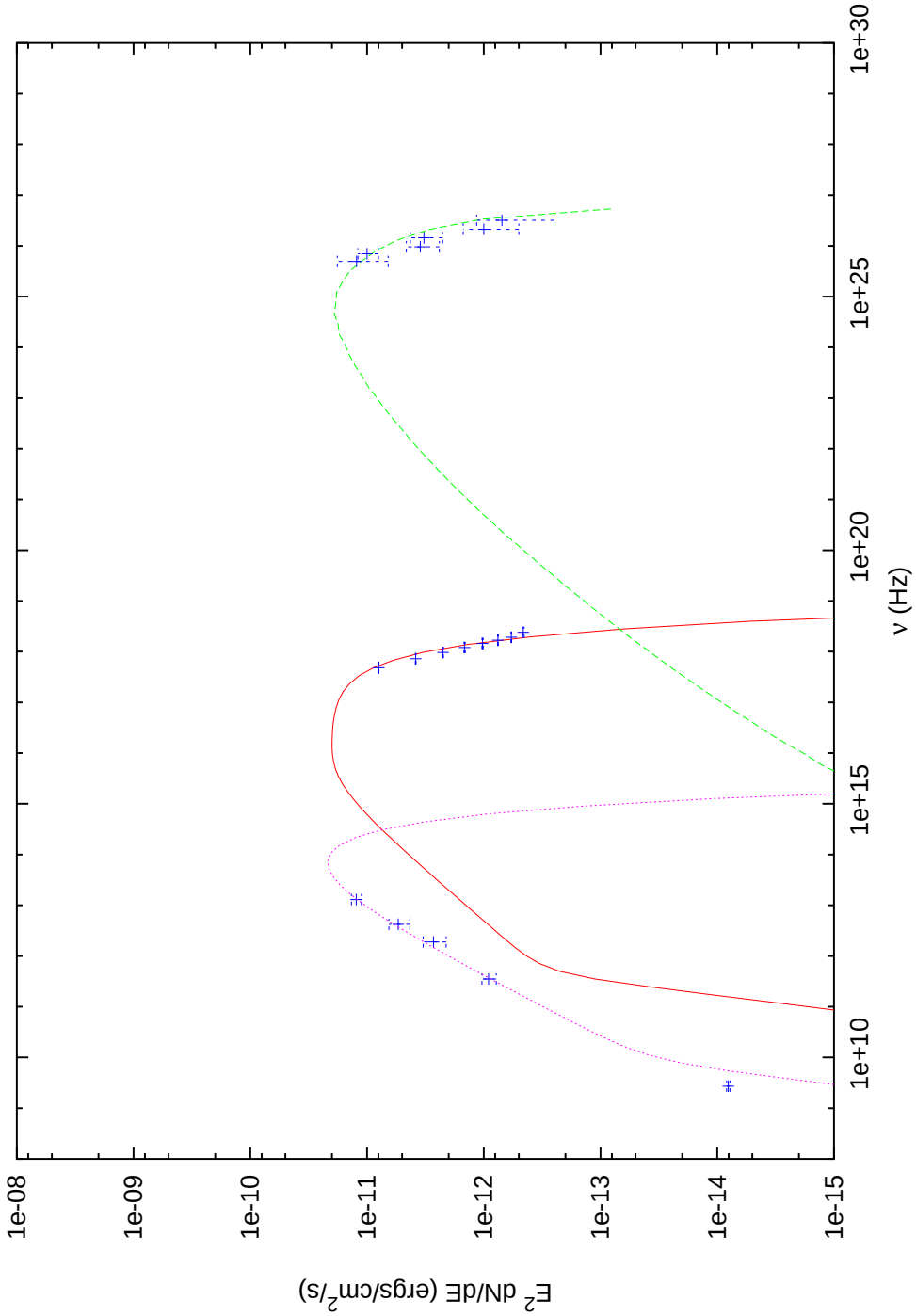

Figure 8.13: Using the same data as Fig. 8.11, the low energy 'radio lobe' emission is described by the dotted line, the synchrotron continuum is described by the solid line and the IC continuum is described by the dashed line. The best fit parameters for each of these models are described in Table 8.4.

while the X-ray and VHE $\gamma-$ray flux levels for November 2004 indicate the same activity state as the past 2003 and 2004 campaigns, the sparse temporal sampling of the November 2004 campaign does not allow us to determine if PKS 2155−304 exhibited short, sharp, small flares or larger, broader flares during the November 2004 campaign, if at all. We are therefore unable to show where the fit parameters for both August/September and November 2004 are associated with large, broad flares.

8.2.2 Quiescent SSC model

As with the October/November 2003 campaign, an inhomogenous jet SSC model was also applied to the SED as a quiescent model. With the lack of flaring events at either X-ray or VHE $\gamma-$ray energies during the campaign and with the flux levels close to historically low values, even more so than in 2003, one would expect the inhomogenous jet SSC model to describe the observed SED fairly well. Shown in Fig. 8.14, the best fit model parameters were an initial magnetic field of 0.6 Gauss, an initial Lorentz factor of 3.0×10^5, a particle density of 1.5×10^5 and an initial bulk Lorentz factor of 5. Again this best fit was found by varying the initial parameters to minimise the reduced χ^2.

It should be noted that the steep nature of the SED at X-ray energies could only be taken into consideration by increasing the initial bulk Lorentz factor of the jet. While the initial bulk Lorentz factor for the quiescent model fit to the October/November 2003 SED was 2, a initial bulk Lorentz factor of 5 was needed for the November 2004 SED. This larger bulk Lorentz factor implies that the matter is injected into the jet at a higher rate. Considering that the months preceding the November 2004 campaign marked a period of large scale variability of PKS 2155−304's X-ray and VHE $\gamma-$ray flux (see Chapter 6), it is not unreasonable to model matter being injected into the base of the jet with a larger initial bulk Lorentz factor.

As with the single-zone SSC model, the 'quiescent' inhomogenous jet SSC model is unable to accurately predict the IR, sub-mm and radio observations. However, the poor nature of the inhomogenous jet SSC model fit is apparent

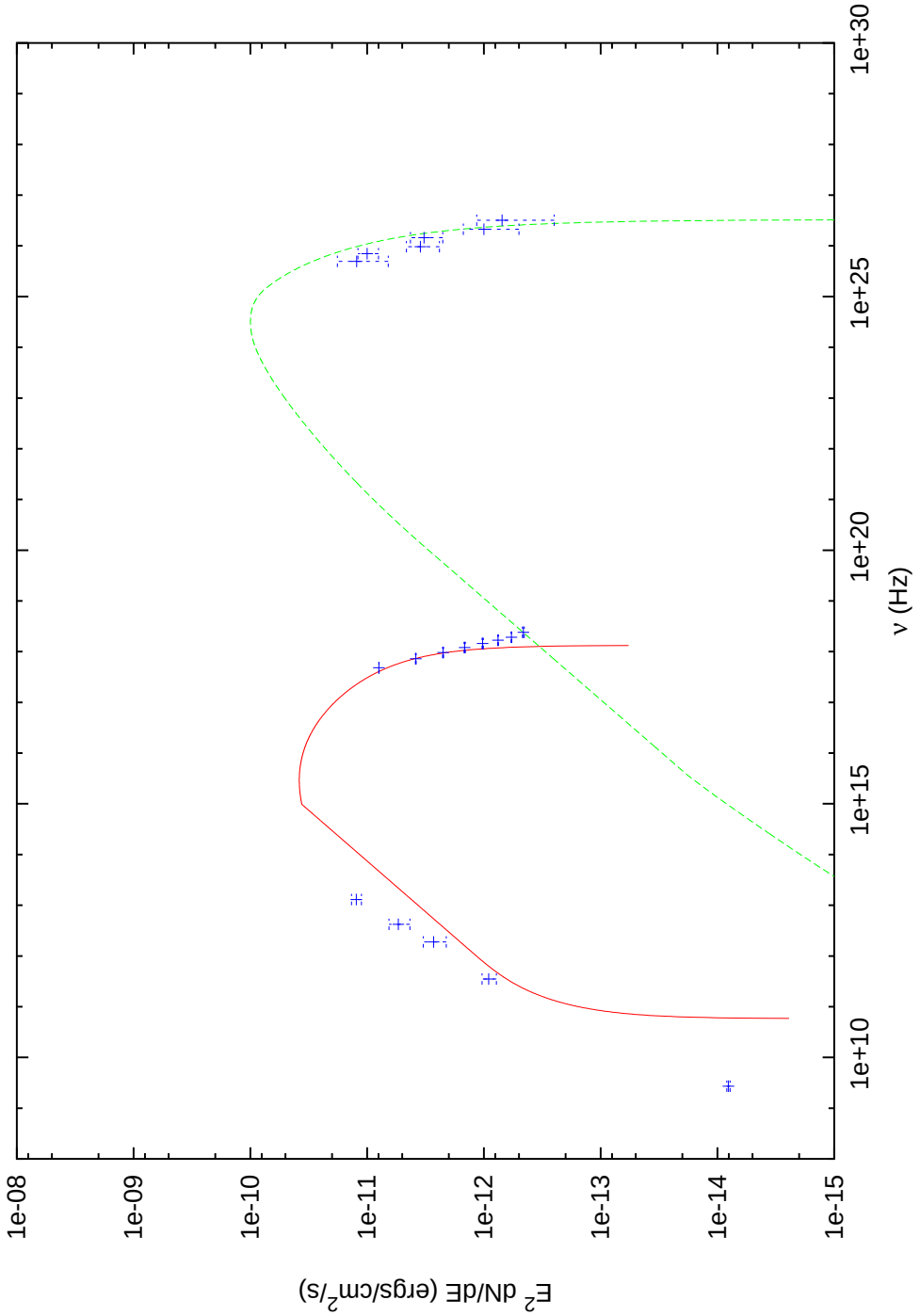

Figure 8.14: The inhomogenous jet SSC model fit to the November 2004 SED. The observation points are as before, with the synchrotron continuum being described by the solid line and the IC continuum being described by the dashed line. As before, the viewing angle is 4° to the line of sight, and the sharp turnover of the synchrotron continuum is merely an artifact of the model.

at all energies with an overall reduced χ^2 of 284 for 17 degrees of freedom. The major contribution to this poor reduced χ^2 is the high energy tail of the VHE $\gamma-$ray observations.

8.3 Conclusion

During November 2004, another multi-wavelength campaign was completed on PKS 2155−304. While a combination of bad weather and a quiescent activity state left little scope for in-depth variability studies, observations with H.E.S.S., *RXTE*, *Spitzer*, JCMT and the NRT provided unprecedented spectral coverage, over 18 orders of magnitude in energy. This spectral coverage allowed us to produce an accurate SED, with no need for archival data. Modelling the SED with a SSC code, we are able to accurately model the X-ray and VHE $\gamma-$ray observations with either a one-zone or two-zone emission model. While it is difficult to differentiate between the fits of the two models, future experiments, such as H.E.S.S. phase II and *GLAST*, will allow us to directly observe the IC peak and thus help to constrain the different models (see Chapter 10).

As with the previous campaigns, the single-zone SSC model is unable to fit the low energy emission. In an attempt to address this, we assumed the low energy emission was emitted by low energy synchrotron radiation in the radio lobe. While this assumption does fit the *Spitzer* and JCMT data well, it still wasn't able to accurately fit the radio observations. What is more, the slope of the particle distribution needed to accurately model the synchrotron emission is shallow, indicating an amount of re-heating of the particle population has occurred. While this re-heating could be associated with the termination shocks of the jet as it encounters the inter galactic medium, this is an *ad hoc* solution and we are more inclined to take the unusual particle distribution as an indication that the low energy emission cannot be associated with the radio lobe, or that the radio lobe has been incorrectly modelled.

As with Section 5.3.2, an inhomogenous jet SSC model was applied to the SED as a 'quiescent' model. The continous injection of matter into the base of the jet assumed by the inhomogenous jet SSC model is believed to be a more

accurate prediction of a 'quiescent' HBL than a dominant single-zone model. Indeed, assuming a slightly larger initial bulk Lorentz factor compared to the quiescent fits of past campaigns, the inhomogenous jet SSC model fit is quite reasonable. The larger initial bulk Lorentz factor is a reasonable requirement since the months preceding the November 2004 campaign saw an increase in activity of PKS 2155−304, see Chapter 6. However, while PKS 2155−304 does appear to be in a more quiescent state when compared to October/November 2003, the SED for the November 2004 campaign is more accurately model led by a single-zone or two-zone SSC model. This seems to imply that the quiescent nature of PKS 2155−304 during November 2004 cannot necessarily be attributed to a steady-state, with a continous injection of matter into the base of the jet.

Chapter 9

PKS 2155−304 Optical Spectroscopic Campaign

In this chapter the results of recent optical spectroscopic observations of PKS 2155−304, made during July and September 2005 are reported. When possible, these observations were taken simultaneously with the H.E.S.S. telescope array to allow the greatest insight into mechanisms present within the jet. Quick-look results from the All Sky Monitor onboard the *RXTE* satellite were also used to determine the activity state of PKS 2155−304.

The original motivation for this study was to look for optical emission lines from PKS 2155−304 during different states of activity, with the belief that this will allow us to probe the external contribution to a possible seed photon population. Time was successfully obtained on the ESO 3.58 m New Technology Telescope (NTT) in Target of Opportunity format. The large primary mirror size of the NTT and the efficiency of the EMMI spectrograph allowed us to obtain good Signal-to-Noise (S/N) ratios in a short exposure times. In Section 9.2 the NTT observations and the data reduction technique are discussed and the H.E.S.S. and *RXTE/ASM* observations are presented. In Section 9.4 the results of NTT observations are presented. The implications of the results of this campaign are discussed in Section 9.5.

9.1 Introduction

Historically, BL Lac objects were distinguished from other AGN by their large scale flux variability and featureless optical spectra, with no or extremely weak (EW $<$ 5Å), observable absorption or emission lines (see Section 1.3.4). The large variability of BL Lac objects is believed to be associated with a relativistic jet that is aligned close to the line of sight. It is the emission from this jet that dominates the total emission from BL Lac objects.

Presumably as a result of the original featureless description, there have been very few spectroscopic studies of BL Lac objects; rather they are often used as a featureless sources needed for calibration of spectroscopic observations. This practice inadvertently led to the detection of strong emission lines from the low energy peaked BL Lac object, BL Lacertae, with Hα, Hβ, O[III] and N[II] emission lines being detected during May 1995 and over an extended period during 1997 [189, 51, 52]. On both occasions, the Hα emission line was clearly visible with a flux between 1.7 $\times 10^{-14}$ ergs cm^{-2} s^{-1} and 4.8 $\times 10^{-14}$ ergs cm^{-2} s^{-1} and an equivalent width between 1.6 and 7.3 Å. Furthermore, during the 1995 observations, BL Lacertae was not particularly faint, with a V band magnitude of 16.0, and the Hα emission line would have still been detected even if BL Lacertae's continuum was 3-4 magnitudes brighter [189]. Emission lines have also been detected from other low energy peaked BL Lac objects, PKS 0521$-$365 and OJ 287, albeit slightly weaker [184, 172].

The detection of these emission lines not only brings into question the original classification of BL Lac objects as being spectrally featureless, but also the strength of the external photon field from the broad line region (BLR) and the role it may play in the dynamics and emission from the relativistic jet of this class of AGN. While an external photon field provides a greater population of target photons for Comptonisation than just synchrotron photons alone, the larger population of target photons also have a great cooling effect on the jet, extracting more energy from the relativistic particles within the jet. Thus, while an increase in radiation from the BLR should result in an increase in VHE emission, it will also cool the jet more. This extra cooling could effect the evolution of the relativistic jet at larger distances from the central SMBH,

[35] and references therein.

Broad emission lines hold fundamental clues about the kinematics, structure and composition of the broad line regions of AGN. Understanding the structure of the broad line region helps us to probe the contribution of the external photon field to the production of VHE photons in the jet. The principal broad lines in the optical domain from a source at redshift 0.117 are Hα and Hβ, both of which are low ionisation lines (LILs). The medium from which these LILs are emitted is optically thick, being photoionised by radiation from the accretion disc, [16, 176, 65]. The photons principally responsible for the photoionising are the Lyman and He[I] continua and 'soft' 300-800 eV X-rays, [107]. Observing the Hα and Hβ emission lines can therefore be used as an indicator to probe the contribution to the external photon field from a range of photon energies, not just the 1.88 and 2.54 eV of the Hα and Hβ emission lines.

9.2 Optical Spectroscopic Observations and data reduction

9.2.1 Optical Spectroscopic campaign

Five spectroscopic observations of PKS 2155−304 were obtained with the EMMI spectrograph on the 3.58 m New Technology Telescope (NTT), at the ESO La Silla observatory, Chile during July and September 2005 (see table 9.1). Each of the spectroscopic observations was carried out in photometric conditions, with airmass < 1.26 and < 0.8" seeing.

Each observing block consisted of a 300 second integration split into five equal observations, with a slight dithering along the slit between observations to reduce the impact of individual noisy pixels. The spectra were taken with a 1" wide slit on Grism #1 covering a wavelength range of 385-1000 nm, at a resolution of $\lambda/\Delta\lambda$=1000. To ensure that the possibility of second order contamination could not affect the results, the first two sets of observations were also accompanied by higher resolution ($\lambda/\Delta\lambda$=300) spectra taken with the #646 RG-715 order sorting filter (which covers a wavelength range >7210 Å).

However, it was noted that the effect of second order contamination was negligible (<1%) and thus the order sorting filter was not used for the remaining 3 sets of observations.

9.2.2 Optical Spectroscopic Data Reduction

All of the spectroscopic observations were reduced using the standard NOAO ONEDSPEC package in IRAF[1]. The data reduction steps include bias subtraction, wavelength calibration (using an internal Helium/Argon arc lamp), flat-fielding, sky subtraction (which was performed using sky regions adjacent to the object on the spectrograph) and spectral extraction. The final data have an output pixel scale of 28 Å/FWHM (measured from the widths of the sky-lines).

Flux calibration was performed using spectroscopic observations of a standard star, either LTT9239 or Feige 110, taken at either the beginning or the end of the observation sequence. It should be noted that no standard star observations were taken during the second set of observations (MJD=53,618.082) and as such, it is not possible to obtain absolute flux calibration for these spectra. The second set of observations will therefore not be considered. A summary of the optical spectroscopic observations can be found in Table 9.1.

9.3 X-ray/VHE $\gamma-$ray observations

9.3.1 *RXTE* observations

To determine the X-ray activity throughout the optical spectroscopic campaign, the All Sky Monitor, ASM, onboard the *RXTE* satellite was used, (for a full description of *RXTE*, see Chapter 4). In short, the ASM scans 80% of the sky, in the 2−10 keV energy range, every 90 minutes, with a sensitivity of 30 milliCrab. Using the quick-look results from the *RXTE/ASM* team, it is possible to determine the X-ray activity state of PKS 2155−304.

[1]IRAF is distributed by the National Optical Astronomy Observatory, which is operated by the Association of Universities for Research in Astronomy, Inc., under the co-operative agreement with the National Science Foundation.

Table 9.1: Summary of optical spectroscopic observations

Date	MJD	Instrument	Filter	T_{Exp} [s]
03-07-2005	53,554.3809	EMMI/Gr 1	none	1×60
	53,554.4321		none	1×60
	53,554.4331		none	1×60
	53,554.4342		none	1×60
			#646 RG-715	3×60
05-09-2005	53,618.0821	EMMI/Gr 1	none	3×60
			#646 RG-715	3×60
23-09-2005	53,636.2324	EMMI/Gr 1	none	1×60
	53,636.2344			1×60
	53,636.2356			1×60
	53,636.2366			1×60
	53,636.2376			1×60
25-09-2005	53,638.2210	EMMI/Gr 1	none	1×60
	53,638.2230			1×60
	53,638.2242			1×60
	53,638.2252			1×60
	53,638.2262			1×60
01-10-2005	53,644.1226	EMMI/Gr 1	none	1×60
	53,644.1248			1×60
	53,644.1260			1×60
	53,644.1270			1×60
	53,644.1281			1×60

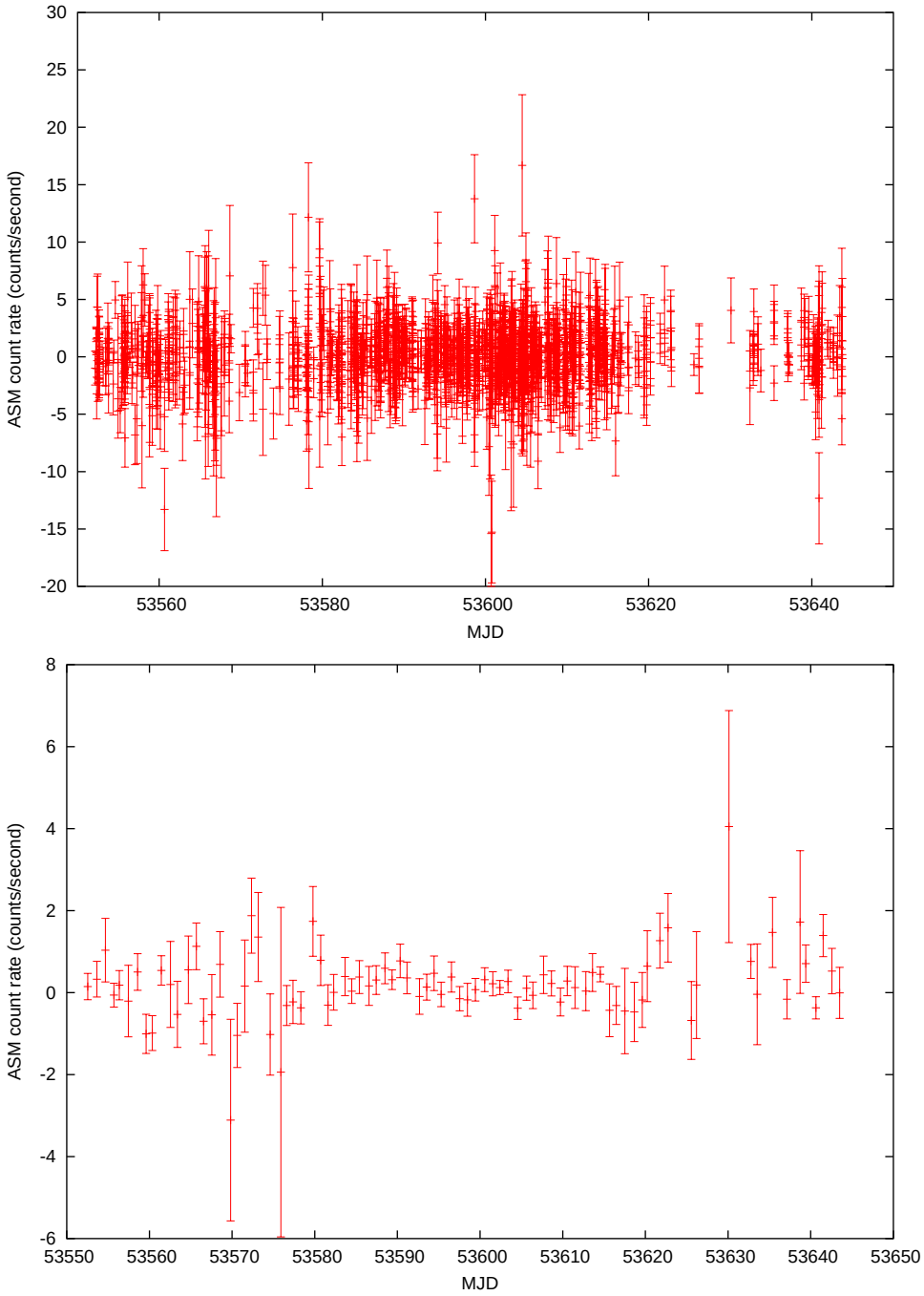

Figure 9.1: The dwell-by-dwell count rate (top) and day average (bottom) count rate of PKS 2155−304 July 1st to October 1st. ASM data are courtesy of the Quick-look *RXTE/ASM* team.

As can be seen in Figure 9.1, during the optical spectroscopic campaign (July 1st through to October 1st), the X-ray activity of PKS 2155−304 did not increase significantly as it fluctuated around 0 counts/second. Indeed, due to the poor sensitivity of the ASM, 30 mCrab compared to the 0.1 mCrab of the PCA, a large increase in X-ray flux would need to occur for PKS 2155−304 to be detected by ASM. The null detection of PKS 2155−304 by the ASM indicates that the X-ray emission is close to the low values detected in a quiescent state. It should be noted that lightcurve shown in Figure 9.1 is similiar to the ASM lightcurves of PKS 2155−304 during the October/November 2003 and August/September and November 2004 campaign.

9.3.2 H.E.S.S. observations

When it was possible, the optical spectroscopic observations were taken simultaneously with H.E.S.S. observations so as to allow the greatest insights into the mechanisms present within the jet. The H.E.S.S. observations were taken in the standard *Wobble* mode, with PKS 2155−304 positioned $\pm 0.5^{\circ}$ in declination relative to the field of view.

As with the previous H.E.S.S. observations, the observations that satisfied the quality control criteria were cleaned using the standard '5-10' criterion, (see Chapter 3 for in-depth discussion on the quality control and '5-10' criteria). After cleaning, the standard image cuts, described in Table 3.2, were applied to subtract the dominant cosmic ray background. Further background subtraction was completed using the ring background model, see Section 3.6.3. After cleaning, cuts and background subtraction for the 7 good runs, a total 2.85 hours live time, an excess of 316.46 $\gamma-$rays and an associated significance of 18.7 σ was achieved. The two-dimensional excess sky map and θ^2 distribution of the 2005 observations are shown in Fig. 9.2.

As with October/November 2003 and August/September and November 2004, the usual quality control criteria were applied to minimise the systematic uncertainties. Unfortunately, due to the stringent observing conditions set for the spectroscopic observations, near simultaneous observations were only possible for the third optical ToO trigger (MJD = 53,636.9), when 4 H.E.S.S.

Table 9.2: Summary of H.E.S.S. observations during the optical spectroscopic campaign

Date	Run No.	Accepted	Comments
2005-09-23	28784	No	Run cut short
	28785	No	Doubtful trigger rate on CT3
	28786	Yes	
	28787	Yes	
2005-09-24	28805	Yes	
	28806	Yes	
	28807	Yes	
	28808	Yes	
	28809	Yes	

observation runs were taken. A further 5 H.E.S.S. observation runs were taken on PKS 2155−304 the following night, MJD = 53,637.8. A summary of the H.E.S.S. runs can be found in table 9.2.

9.3.3 H.E.S.S. results

Spectrum

The 2005 VHE observations were fitted with both a power law and a broken power law function. As with the October/November 2003 and November 2004 campaign, the power law fit described the VHE spectrum more accurately, with a reduced χ^2 of 1.91 for 4 degrees of freedom and an associated χ^2 probability of 0.11. Shown in Figure 9.3, the best-fitting power law is given by:

$$\frac{\mathrm{d}N}{\mathrm{d}E} = (1.05 \pm 0.24) \times 10^{-12} \left(\frac{E}{\mathrm{TeV}}\right)^{-3.59 \pm 0.17_{stat} \pm 0.1_{sys}} \mathrm{cm}^{-2}\ \mathrm{s}^{-1}\ \mathrm{TeV}^{-1} \quad (9.1)$$

It should be noted that the majority of the contribution to the reduced χ^2 stems from the 0.9 TeV data point which is approximately 1.25 σ from the power law fit. Compared to the 2003 and 2004 H.E.S.S. observations of

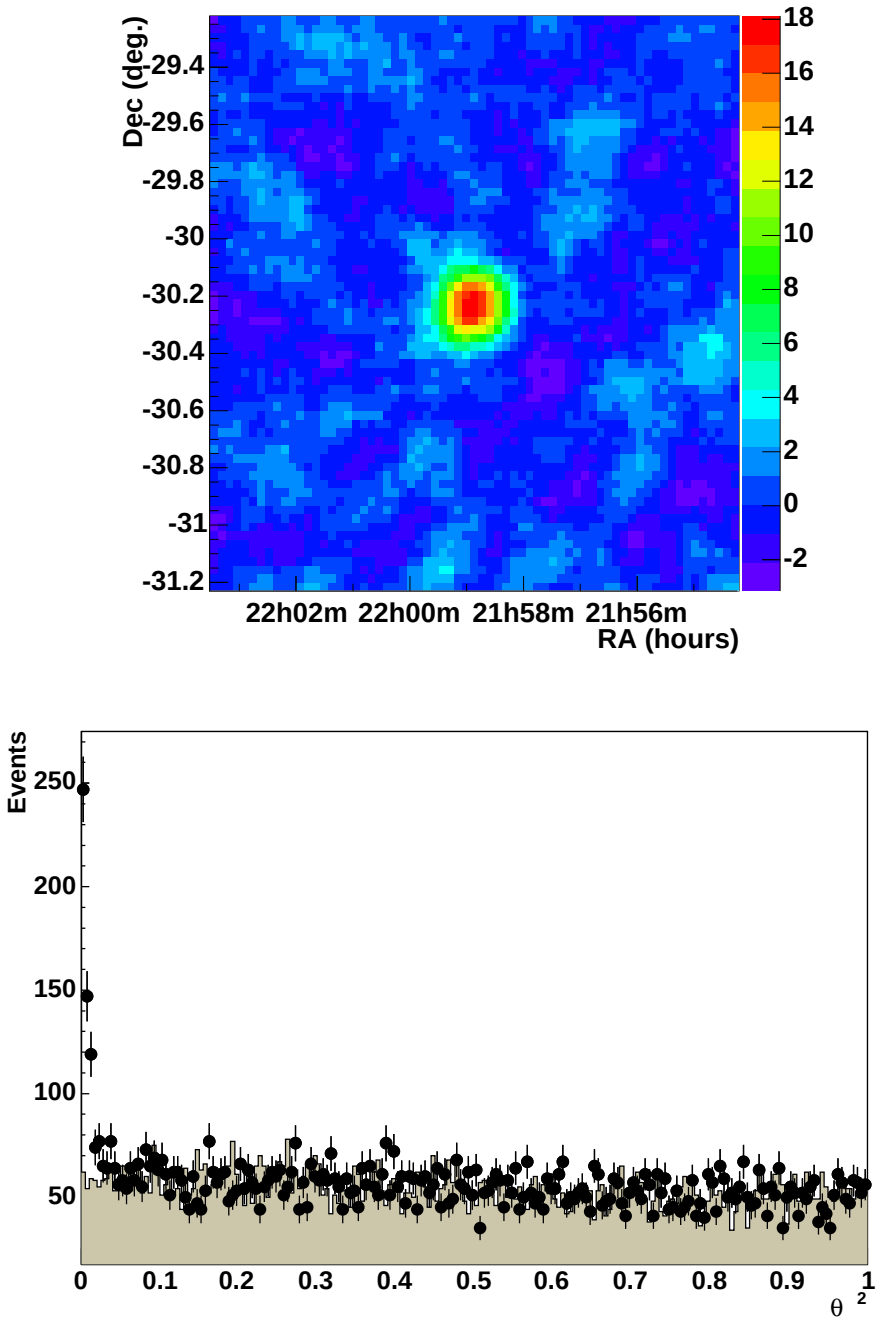

Figure 9.2: *Top:* The two-dimensional distribution of the excess events in the direction of PKS 2155 − 304 during July and September 2005. Right hand scale is the number of excess events. *Bottom:* The θ^2 distribution of on source events (points) and normalised background events (shaded).

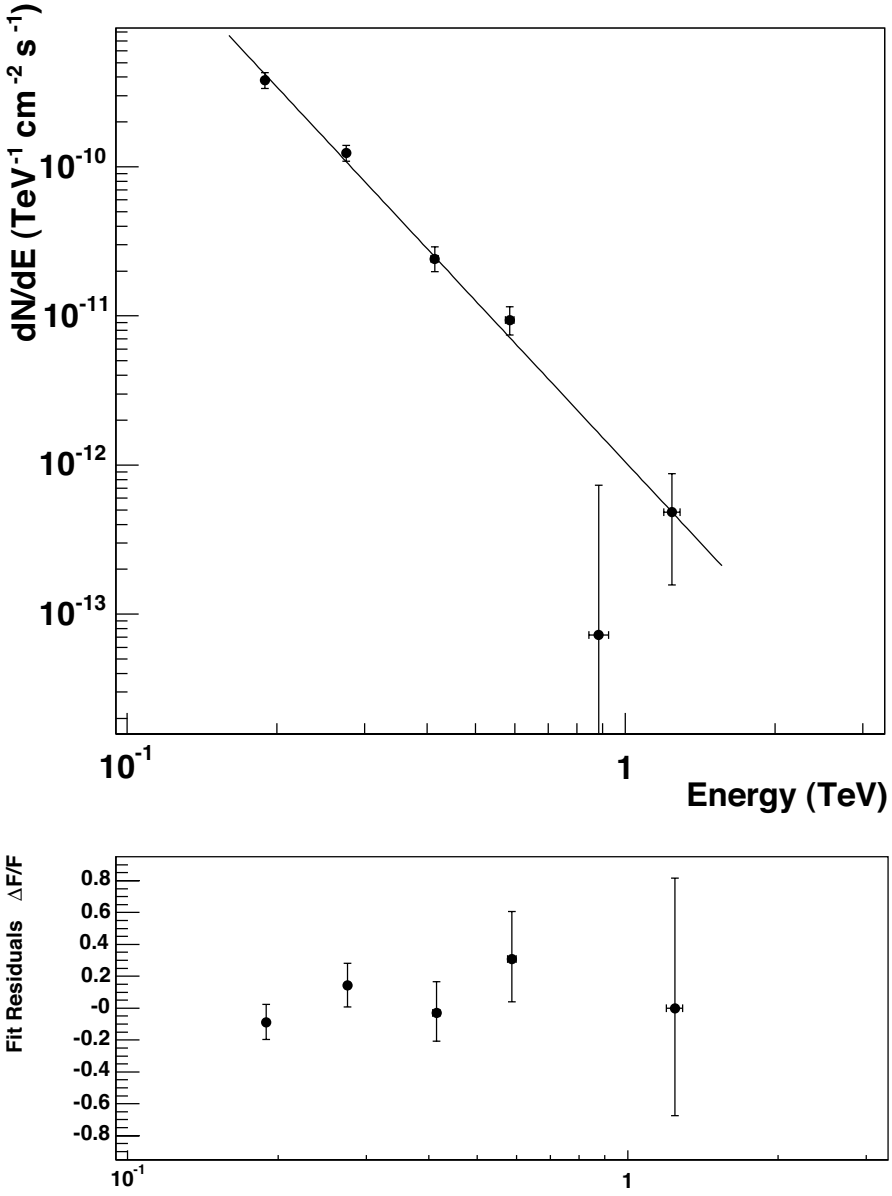

Figure 9.3: *Top:* Power law fit to the VHE data for the July and September 2005 observations. This fit yields a photon index, $\Gamma = -3.59 \pm 0.17$, with a reduced $\chi^2 = 1.36$ for 4 degrees of freedom. *Bottom:* The residuals to the power law fit.

PKS 2155−304, there is little difference in spectral index. As before, the poor reduced χ^2 possible indicates that there is different VHE spectral states present in the summed spectra of Fig. 9.3. Again, it is not possible to derive spectral indices for each individual observation run due to the low flux.

Lightcurve

The E>300 GeV lightcurve for September 2005 is shown in Fig. 9.4, in units of photons m^{-2} s^{-1}. As before, the data was binned using the original 28 minute observation runs. During the September 2005 observations, the E>300 GeV flux varies from $F_{min} = 2.6 \times 10^{-8}$ photons $m^{-2}s^{-1}$ to $F_{max} = 1.3 \times 10^{-7}$ photons $m^{-2}s^{-1}$. These flux levels are similiar to the November 2004 campaign, but less than the levels observed during October/November 2003 and August/September 2004. Therefore, PKS 2155−304 again appears to be in a quiescent state during the optical spectroscopy campaign.

As with all the 2003 and 2004 campaigns, there is clear evidence for inter-night variability. A constant flux fit to the run by run flux levels results in a reduced χ^2 of 3.93 for 6 degrees of freedom and an associated χ^2 probability of 4.2×10^{-9}.

9.4 Optical Spectroscopic Results

9.4.1 Spectral features

The spectral features of the BL Lac objects are, to first approximation, a combination of the absorption and emission lines from the elliptical host galaxy and the broad emission lines from the central engine [182]. The relative strength of any of these lines depends upon the strength of the non-thermal continuum from the relativistic jet of the AGN. Overlaid on top of the intrinsic spectrum are features external to the source, such as absorption features from gas clouds in the line of sight and the telluric absorption from the Earth's atmosphere.

To maximise the S/N ratio in order to look for spectral features, the spectra in each set of observations were combined. It was noted that the difference

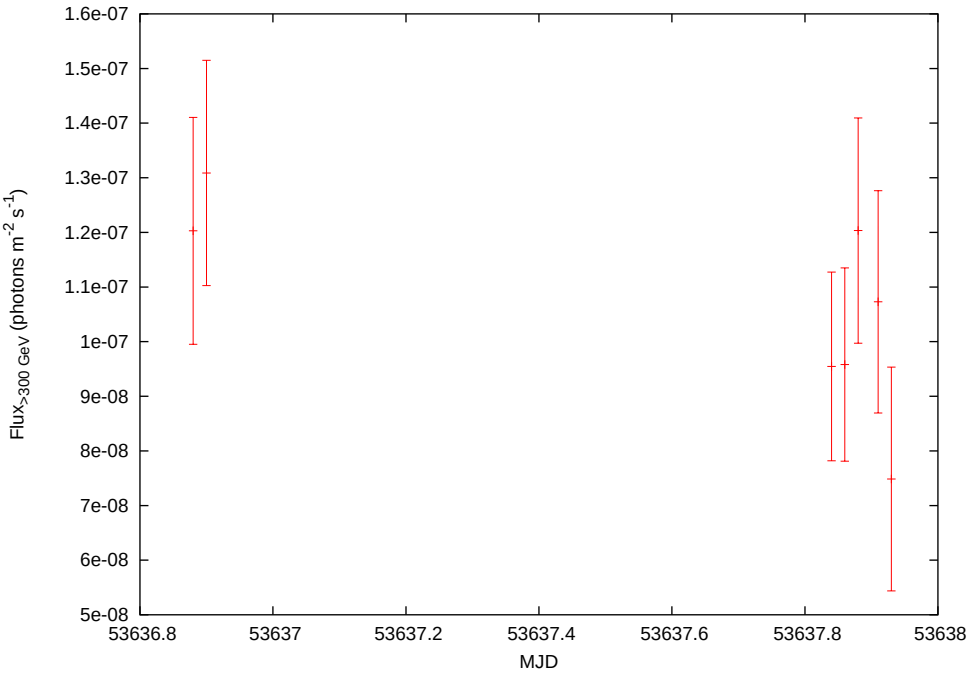

Figure 9.4: Run by run lightcurve of the H.E.S.S. observations for the September 23$^{\text{rd}}$ and September 24$^{\text{th}}$ 2005.

between the average and the median spectra was negligible. The averaged spectra for each set of observations are shown in Figures 9.5 and 9.6.

Immediately obvious are the three strong absorption features shaded in grey. Referred to as telluric absorption lines, their presence is due to molecular absorption, such as water vapour and ozone, in the atmosphere. Apart from telluric absorption lines, the Na absorption line can be seen at $\lambda \approx 6280$ Å. Believed to be due to the host galaxy, the Na absorption line is also present in spectra recently reported by Sbaruffatti et al. [160].

Vertical dashed lines have been placed on Figures 9.5 and 9.6 to indicate the position of some common emission lines, such as Hα, from a z=0.117 object. Whilst there is no evidence for Hβ or O[III] emission lines being present in the spectra, there is some evidence for Hα.

To investigate this possible emission feature further, each one minute observation was considered separately, seen in Figures 9.7 and 9.8. The signficance of this apparent feature varies between separate one minute exposures. This is either due to statistical fluctuations or an increase in the relative strength of a

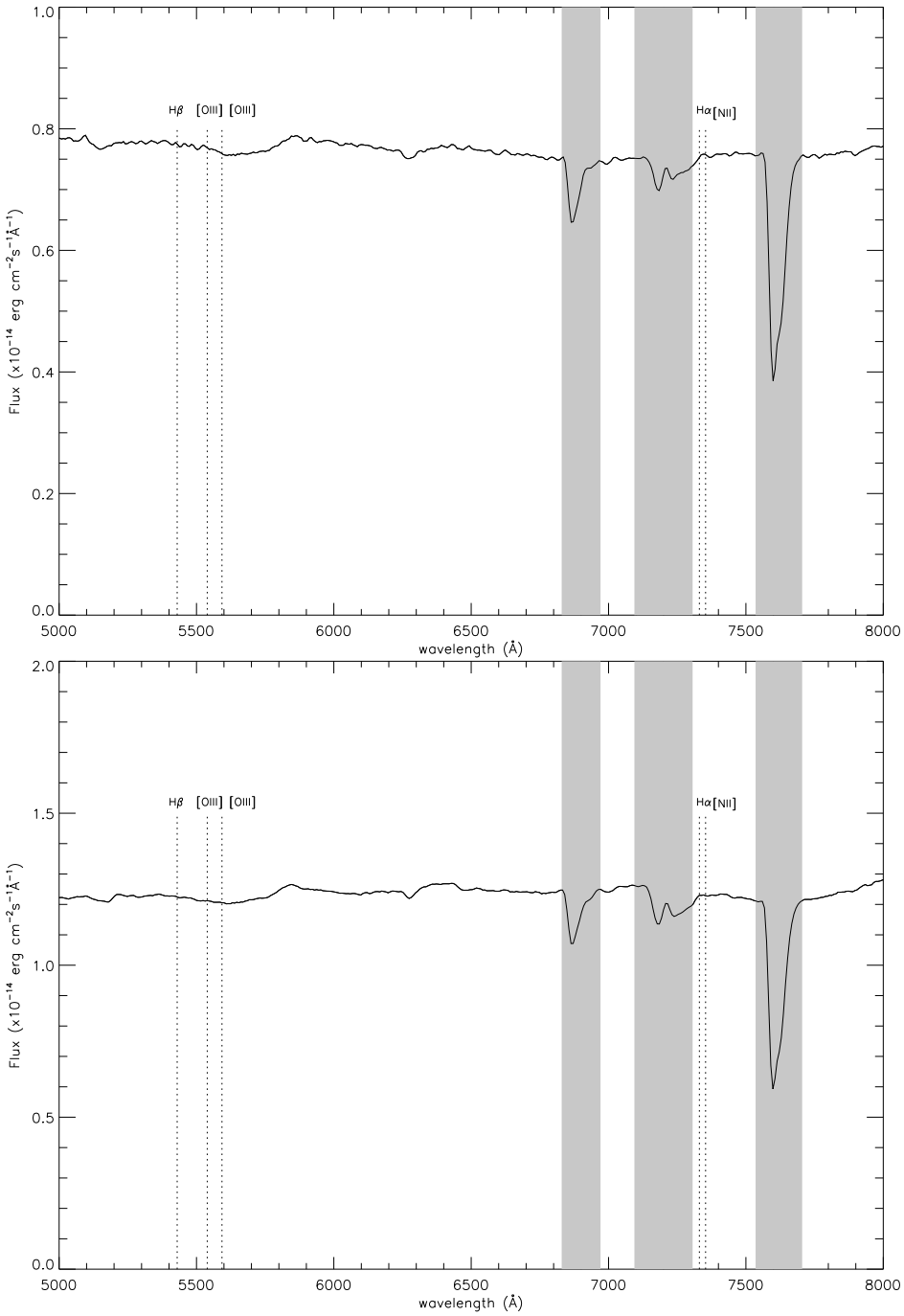

Figure 9.5: The average spectrum of the 4 exposures from the 03-07-2005 (top) and 23-09-2005 (bottom) observations. Typical features expected from the BLR clouds, at z=0.117, are indicated by the dashed vertical lines. The shaded regions indicate regions of the spectrum affected by atmospheric absorption.

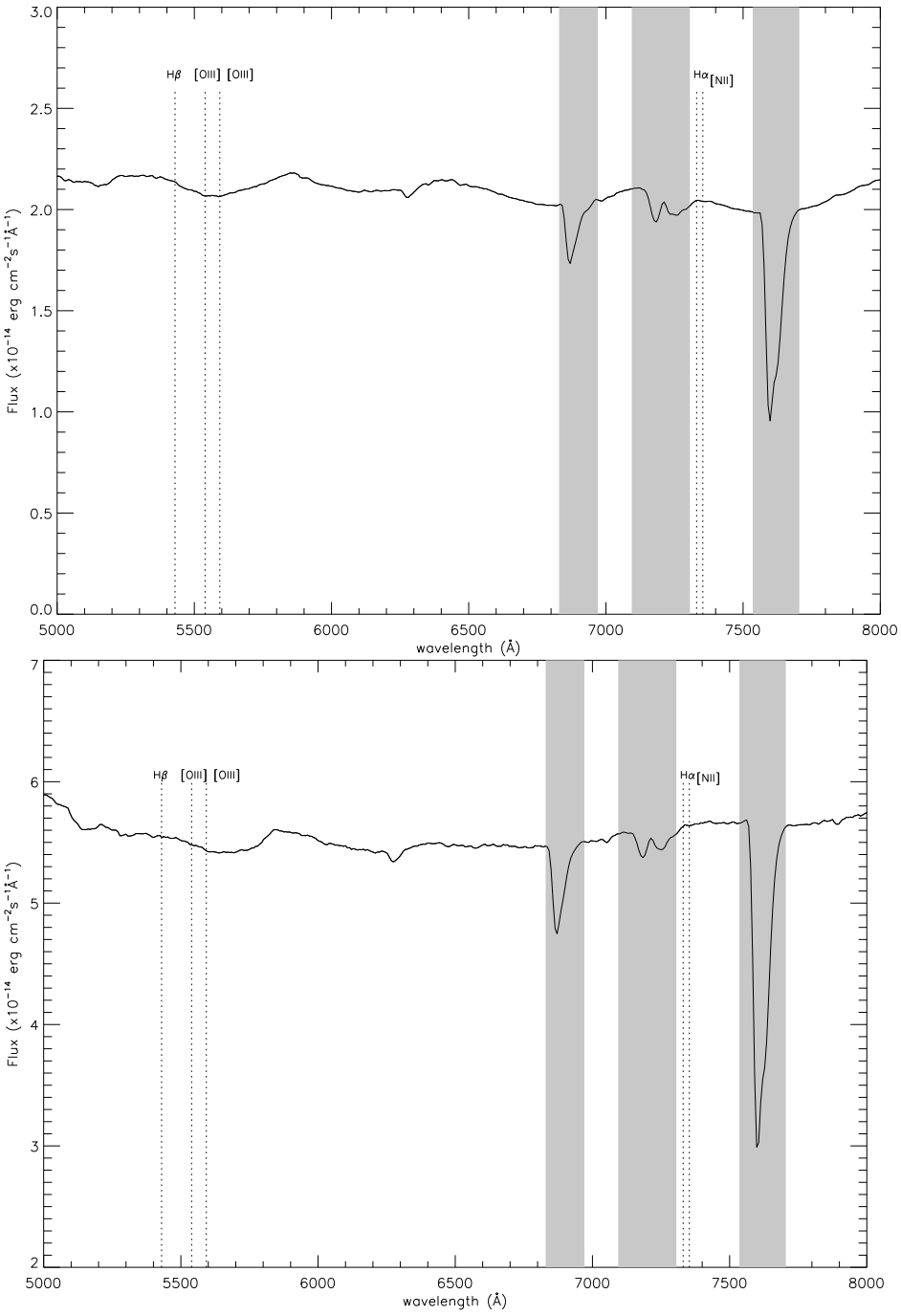

Figure 9.6: The average spectrum of the 5 exposures from the 25-09-2005 (top) and 01-10-2005 (bottom) observations. Typical features expected from the BLR clouds, at z=0.117, are indicated by the dashed vertical lines. The shaded regions indicate regions of the spectrum affected by atmospheric absorption.

weak Hα emission line compared to the optical continuum. If it is indeed the latter, then the significance of the feature would be greatest when the continuum is close to its weakest. This is because we would not expect the strength of the BLR emission lines to vary significantly on minute timescales.

Whilst it is true that the brightest set of spectra show no trace of the Hα emission feature, this trend is not uniform across the complete set of exposures. It should be noted that there is 85 days between the first set and third set of exposures shown in Fig. 9.7. Assuming the Hα emission feature originated in the BLR and assuming a BLR radius of 0.1 parsec, it is possible that the intrinsic strength of the emission lines increased from the first to the third set of observations. Therefore, only considering the spectroscopic observations taken towards the end of September, the significance of the Hα emission feature is greatest when the continuum is at its lowest.

Only considering the feature when it is $\sim 2\sigma$ above the continuum, an upper limit can be placed on the Hα emission line from PKS 2155−304. Using the SPLOT tool from the NOAO ONEDSPEC package in IRAF, an upper limit of $F_{H\alpha} < 7.1 \times 10^{-15}$ ergs cm^{-2} s^{-1} is found for the flux of the Hα emission line, and EW < 0.58 Å for the equivalent width of the Hα emission line.

9.4.2 Variability

Interestingly, there appears to be an appreciable amount of variability in the continuum flux level between the separate one minute exposures, see Figures 9.7 and 9.8. This variability appears to be uniform across the whole optical continuum.

At its greatest variation, the continuum flux decreased by 42% in ∼3 minutes between successive runs, corresponding to 0.6 magnitudes in the V band. This occurred at MJD = 53644.1226 through to MJD = 53644.1248. All the other sets of observations also showed a large amount of variability, albeit on a smaller scale, with the maximum change being ∼18%, ∼17% and ∼16% for the 1st, 3rd and 4th sets of observations respectively. Again these variations were observed on ∼3 minute timescales. Such rapid variations in the optical continuum, if real, are the fastest seen to date from any BL Lac object.

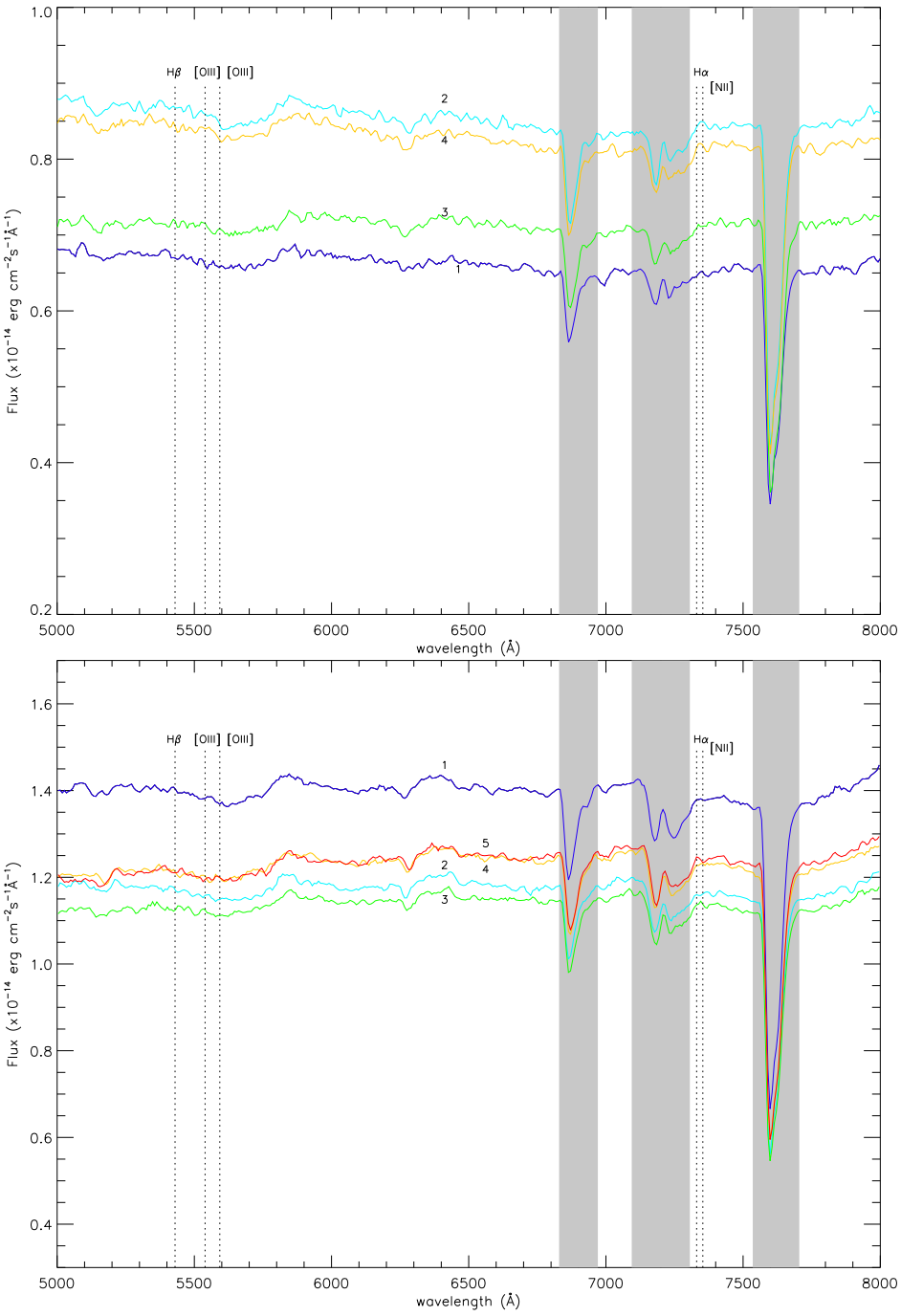

Figure 9.7: Each 60 second exposure from the first (top) and third (bottom) set of observations plotted separately, with the order of the observations shown by the numbers at ∼6500Å.

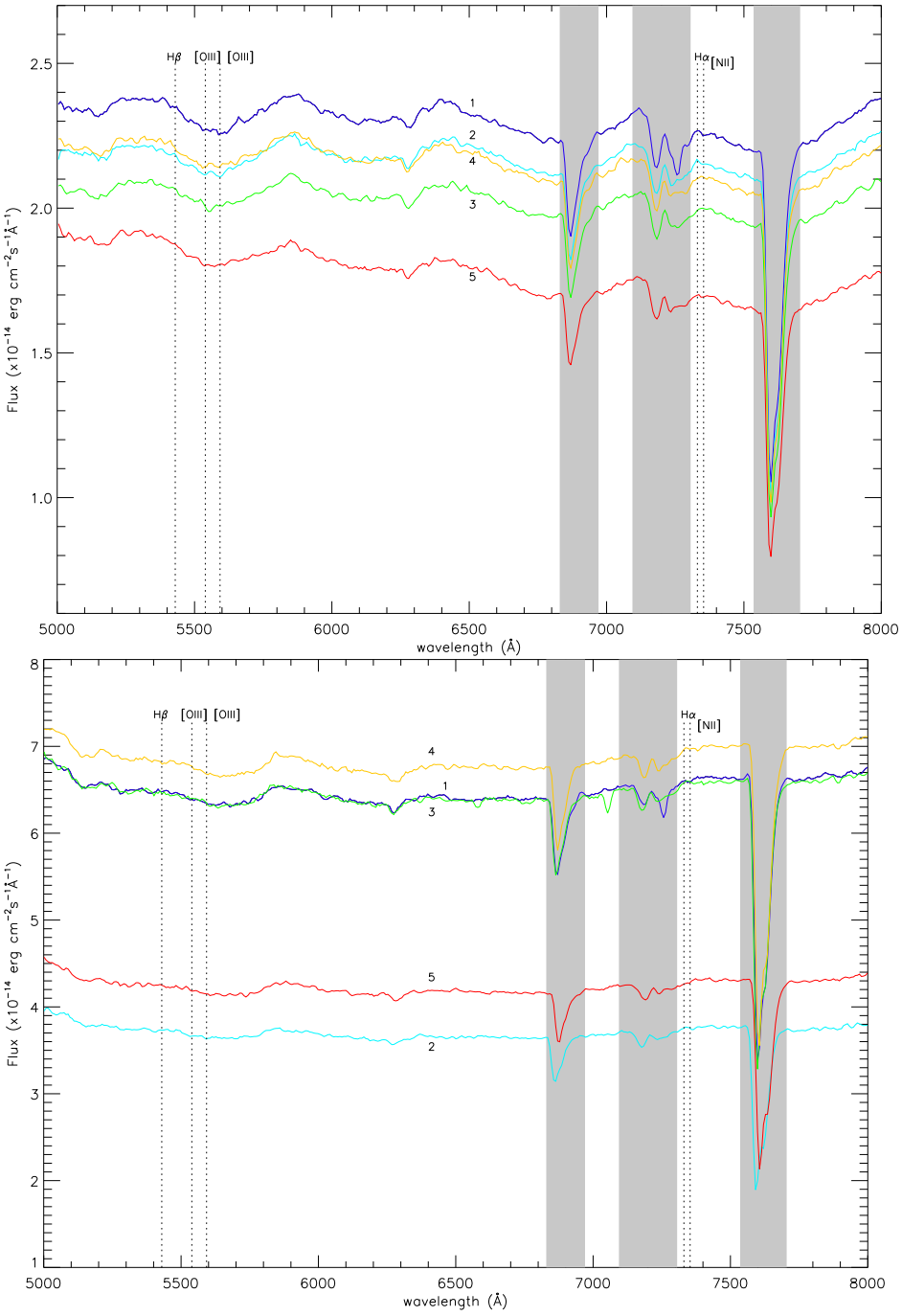

Figure 9.8: Each 60 second exposure from the fourth (top), and fifth (bottom) set of observations plotted separately, with the order of the observations shown by the numbers at ∼6500Å.

Traditionally, to confirm that any observed variability is intrinsic to the source, simultaneous observations of a constant optical source are taken. Variability that is due to changes in the atmosphere, such as variations in seeing or atmospheric extinction, appear in the light curves of both sources. However, since this campaign was originally aimed towards looking for the presence of spectral features, no simultaneous observations of a standard source were taken during our spectral campaign. Rather, a flux standard was observed immediately before or after the science observations, simply for flux calibration.

To confirm that the variability detected was intrinsic to PKS 2155−304, the FWHM of the source image and the strength of the sky-lines for each separate spectrum was considered. The FWHM of the source image depends upon both the intrinsic source width and the source width due to atmospheric seeing, see Eq. 9.2.

$$\sigma^2_{image} = \sigma^2_{seeing} + \sigma^2_{source} \tag{9.2}$$

Throughout the spectroscopic campaign, the FWHM of the source, σ_{source}, was 2.5", with no significant variation from this value being observed. Therefore any variation observed in the FWHM of the image, σ_{image}, is due to variations in atmospheric seeing, σ_{seeing}. To determine if the observed variability is due to variations in the relative transmission of the atmosphere, we considered the strength of the sky-lines. An increase in the transmissivity of the atmosphere would be associated with an increase in the strength of the sky-line. Any strong correlation between either the FWHM, the strength of the sky-lines or the strength of the continuum, would indicate an underlying atmospheric component to the observed variability of the source.

The FWHM of the image varied by no more than 5% between observing runs and the strength of the sky-lines varied by no more than 2% between observing runs, with no correlation between the two. What is more there is no evidence of a correlation between either the FWHM of the image or the strength of the sky-lines and the range of variability of the optical continuum. As such, the observed variability in the optical continuum of PKS 2155−304 is believed to be intrinsic to the source. It should be noted that it is not

possible to rule out other extrinsic sources of variability, such as micro-lensing from foreground stars [46] or jet precession [32, 40]. However, the frequency of the variability and, more to the point, the timescale of the variability, means that both micro-lensing and jet precession are unlikely explanations for the observed variability.

9.5 Discussion

9.5.1 Spectral features

Apart from the the very strong telluric atmospheric absorption lines, the only other spectral features present in the spectra are the Na absorption feature, and in some cases, a possible Hα emission feature. Associated with PKS 2155−304's elliptical host galaxy, the Na absorption feature was originally used to calculate the redshift of PKS 2155−304 [30, 68]. More recently, observations in 2001 also found the Na absorption feature to be present in an otherwise featureless spectrum [160].

At its brightest, the Hα emission feature has a flux of $F_{H\alpha} < 7.1 \times 10^{-15}$ ergs cm^{-2} s^{-1} and an associated equivalent width of <0.58 Å. Using the luminosity distance calculated in Section 5.1.2, $d_L = 1.59 \times 10^{25}$ m, this flux limit equates to a luminosity of $L_{H\alpha} < 1.8 \times 10^{40}$ ergs s^{-1}. This value is fully consistent with the upper limits calculated for other HBLs; 1H 0323+022 ($L_{H\alpha} < 1.8 \times 10^{40}$ ergs s^{-1}) and PKS 2005-489 ($L_{H\alpha} < 1.9 \times 10^{41}$ ergs s^{-1}) [160].

If the September Hα emission feature had been present during the July spectral observations, it would have been seen clearly above the continuum flux level. The continuum flux level at the start of July was $\sim 35\%$ lower than the 23$^{\text{rd}}$ September when the apparent feature was at its most significant. Therefore, the non-detection of the Hα emission line, particularly during the first set of observations, cannot be attributed to the dominance of the relativistic jet alone.

The non-detection during July also raises questions about the variability of the external photon field strength and variability of the broad line region in general. Variations in the strength of the external photon field can occur

through changes in the amount of matter (or number of BLR clouds) emitting the radiation, variations in the photoionising continuum incident upon the matter in the broad line region or possible changes in the efficiency of reprocessing the continuum radiation by the BLR clouds. While the last point is possible, through a change in chemical composition for example, there is unlikely to be process by which such a dramatic variation in efficiency occurs on a timescale as short as 85 days. Therefore, the variation in the external photon field strength is more likely attributed to a change in the amount of matter reprocessing the light, or an increase in the amount of light to process. Either way, the varying detection of emission lines from BL Lacertae and other LBLs are evidence of the dynamic nature of the BLR, with continual loss and gain of BLR matter through processes such as photoionisation, turbulence and magnetic reconnection induced mass ejection events from the accretion disk.

If the non-detection of the Hα feature during July, and subsequent upper limit calculated during September, are an indication of a varying external photon field strength, it may have interesting consequences for the unification of blazars. The current model for the unification of blazar subclasses has a combination of accretion rates and jet cooling by an external photon field as the dominant difference between Flat Spectrum Radio Quasars (FSRQ), LBLs and HBLs [72]. Starting as FSRQs with large accretion rates, blazars age to HBLs as the accretion rate steadily decreases and the broad line region is cleared up. However, the BLR is dynamic region as discussed in [189]. While it is likely that processes such as the photoionisation of matter off the accretion disc scale with the accretion rate, over a very large fraction of the blazar's lifetime the accretion rate is believed to be approximately constant. Its only during the birth of the disc, and its final death throws, that the mass outflow rate changes to any great degree. So if the accretion rate and cooling of the jet by external photons are the dominant differences between the blazar subclasses, then we would not expect the see a smooth transition from FSRQ to HBL, but rather a staggered one.

However, it should be noted that since the flux level calculated for Hα is only an upper limit, caution should be used when interpreting the different between the July and September spectral observations. A more in-depth

spectroscopic survey of blazars will give us insights into the validity of the blazar unification theory and indeed the validity of these optical spectrscopic observations.

9.5.2 Continuum Variability

Comparing the results of our campaign on PKS 2155−304 with past observations, [181, 41], we find that while we have found evidence for a small variability timescale, the dynamic range of the variability is not unusual. The variability dynamic range, d, is defined as

$$d = F_{max}/F_{min} \tag{9.3}$$

and the variability timescale, t_D, is defined as

$$t_D = F(\Delta F/\Delta t)^{-1} \tag{9.4}$$

The variability dynamic range of our observations varied from 1.2 to 1.8 (see Table 9.3). Compared with the earlier studies of Treves et al. and Carini & Miller, both of which quote a dynamic range of ∼2 in the optical regime, the dynamic range of the spectroscopic observations presented here are consistent with, if not slightly smaller than, previous observations [41, 181].

There is however a significant difference, 3 orders of magnitude, between the variability timescale quoted in the Treves et al. and Carini & Miller papers and that calculated from our observations. During the 2005 optical spectroscopic campaign, the variability timescale varied between 0.12 and 0.31 hours (see Table 9.3). In the optical regime, Treves et al. detected a t_D of 90 days and Carini & Miller detected a t_D of approximately 100 hours. However, it should be noted that it is best to compare variability timescales from data sets with the same dynamic range. The largest dynamic range for our campaign is 1.82 from the 5^{th} set of observations.

Compared to the previous studies of Carini & Miller and Treves et al., our observations are taken with a higher temporal resolution. This is in part due to the brightness of the source and in part due to the large size of the telescope

Table 9.3: Summary of variability parameters

Date	d	t_D	Max. Var
2005-07-02	1.3	0.21 h	18±1%
2005-09-22	1.2	0.29 h	17±1%
2005-09-24	1.3	0.31 h	16±1%
2005-10-01	1.8	0.12 h	42±1%

mirror, allowing us to obtain a high S/N ratio in a short exposure. This high temporal resolution allows us to provide tighter constraints on the characteristic variability timescale for high energy BL Lac objects such as PKS 2155−304. Therefore, it appears that for bright sources, the observed variability timescale is limited only by the temporal resolution of the observations. With higher temporal resolution it is possible to observe variability that would have otherwise been masked over or averaged out. It should be noted that the observed variability timescale of this campaign is of the same order of magnitude as that detected by Treves et al. for their 3 keV X-ray observations. In fact Treves et al. found evidence of the variability timescale being a function of photon energy, with the X-ray flux having a smaller timescale than the UV flux, which in turn has a smaller variability timescale then the optical flux [181]. So while a variability timescale of 0.3 hours is not unheard of, it is unprecedented in the optical regime for BL Lac objects.

9.6 Conclusion

Here the results of a recent optical spectroscopic observations of the high energy BL Lac object, PKS 2155−304, are presented. The detection of a Na absorption feature is consistent with the few past observations made on PKS 2155−304. Interestingly, some of the optical spectra, with fainter continuum levels, show evidence of a Hα emission feature. At its brightest, this feature has a flux upper limit of $F_{H\alpha} < 7.1 \times 10^{-15}$ ergs cm^{-2} s^{-1} and associated equivalent width of <0.58 Å. This feature doesn't appear in spectra taken in July when the continuum was 35% fainter. With 85 days between observations, the

non-detection during July could possibly be due to an intrinsic reduction in the flux of the BLR radiation.

It should be noted that the upper limit on the luminosity of the Hα feature, $L_{H\alpha} < 1.8 \times 10^{40}$ ergs s^{-1}, is consistent with those calculated for other HBLs. This gives further weight to the belief that the Hα emission feature is real.

Considering intra-night fluctuations, there is evidence of up to 42% variability in the optical continuum on a timescale of $\sim$3 minutes, even though the source appeared to be in a low or quiescent activity state. While the dynamic range of variability is not unusual for this source, the timescale for the variability is. While the lack of a correlation between the the FWHM of the source image, the strength of the sky-line and the strength of the continuum indicates that the contribution to the variability by atmospheric fluctuations is minimal, further spectroscopic observations are needed to confirm this.

The observed variability should not be dismissed on the grounds of atmospheric variability as the high temporal resolution of this campaign, compared to previous studies, allows the provision of tighter constraints on the characteristic variability timescale for high energy BL Lac objects such as PKS 2155−304.

The next logical step in this study is to continue with further spectroscopic studies of PKS 2155−304 with a constant source also on the spectrograph slit, to confirm that any variability observed is intrinsic to the source. This study should be expanded to a larger list of target sources as well as observing over a larger span of time. This will allow us to probe the effects of external photon fields on the dynamics of these jet dominated sources to a greater extent, something that is fundamental to the unification of blazars.

Chapter 10

General Conclusions

10.1 Summary

Four multi-wavelength campaigns were completed on PKS 2155−304 from October 2003 to September 2005. With the VHE γ−ray, X-ray, optical, infra-red, sub-mm and radio fluxes all close to historically low values, PKS 2155−304 appears to be in a quiescent state during all of these campaign. It is therefore possible, for the first time, to probe the jet parameters and emission models for a quiescent BL Lac object for the first time.

The October/November 2003 campaign consisted of H.E.S.S., *RXTE*, NRT and ROTSE observations. During the campaign, the fastest X-ray flare from PKS 2155−304 was observed, with a 50% increase in the 2−10 keV flux in less than 2000 seconds. This flare allowed us to derive a model-independent minimum Doppler factor of 19.4. Assuming a single-zone SSC model as the dominant emission model, an upper limit of 10.9 Gauss was derived for the magnetic field of the emission region. With no correlation found between the different energy band fluxes, the optical, X-ray and VHE γ−ray emission regions are believed to be separate. Interestingly however, the SED modelling of the October/November 2003 campaign indicates that the optical, X-ray and VHE γ−ray emission regions are co-spatial. With a reduced χ^2 of 1.31 for 31 degrees of freedom, the best model fit is a single-zone SSC model, with a Doppler factor and emission region of 32 and 2×10^{13} m respectively. These values are

Table 10.1: Summary of fit parameters for the different emission constraints for the October/November 2003 campaign.

	Optical/X-ray/VHE fit	X-ray/VHE fit
δ	30	32
B (G)	0.145	0.25
R (m)	7×10^{13}	2×10^{13}
$E_{density}$ (ergs/cm^3)	0.135	0.3
$\log(E_{min}/\mathrm{eV})$	7.0	7.0
$\log(E_{break}/\mathrm{eV})$	9.25	9.95
$\log(E_{max}/\mathrm{eV})$	11.1	11.0
Reduced χ^2/d.o.f	1.31/31	1.73/30

consistent with the short, sharp flares exhibited during October/November 2003 being attributed to small, fast emission regions. The fit parameters for the SSC modelling of the October/November 2003 campaign are summarized in Table 10.1.

The August/September 2004 campaign consisted of H.E.S.S. and *RXTE* observations. Spanning over 32 days, the August/September 2004 campaign was unprecedented in temporal resolution. During this campaign, 3 large X-ray flaring events were observed, these flares exhibiting a much larger dynamic range of variability compared to the X-ray flares of the October/November 2003. This large dynamic range allowing us to observe a clear correlation between both VHE and X-ray fluxes as well as between the X-ray flux and X-ray spectral slope. Using the variability timescale and assuming a single-zone SSC model, a minimum Doppler factor and maximum magnetic field strength was calculated to be 8.1 and 10.6 Gauss respectively. While there is little difference between the maximum magnetic field strength between the 2003 and August/September 2004 campaign, there is a 2.4 factor difference between the minimum Doppler factor calculated for the two campaigns ($\delta_{2003} \geq 19.4$ compared to $\delta_{2004} \geq 8.1$).

The SED modelling of the August/September indicates that a single-zone SSC model adequately describes the observed emission. With a reduced χ^2 of 0.96 for 33 degrees of freedom, the best fit Doppler factor and emission region

radius are 20 and 10^{14} m respectively. These values are consistent with the larger, longer flares exhibited during August/September 2004 being attributed to larger, slower emission regions compared to October/November 2003. The fit parameters for the SSC modelling of the August/September 2004 campaign are summarized in Table 10.2.

Table 10.2: Summary of fit parameters for the different emission constraints for the August/September 2004 campaign.

	X-ray/VHE fit	'X-ray/VHE + low energy' fit
δ	20	18
B (G)	0.13	0.15
R (m)	10^{14}	10^{14}
$E_{density}$ (ergs/cm^3)	0.06	0.18
$\log(E_{min}/\mathrm{eV})$	7.0	7.0
$\log(E_{break}/\mathrm{eV})$	9.95	9.45
$\log(E_{max}/\mathrm{eV})$	11.0	11.0
Reduced χ^2/d.o.f	0.961/33	1.25/33

The November 2004 campaign consisted of H.E.S.S., *RXTE*, *Spitzer*, JCMT and NRT observations. Extending over 18 orders of magnitude in energy, the large spectral coverage of the November 2004 campaign allowed us to produce an accurate SED, with no need for archival data. As with the two previous campaigns, a single-zone SSC model was applied to the observed SED. This model was found to fit the X-ray and VHE $\gamma-$ray observations, but not the low energy observations of radio through to infra-red. In attempt to address this, the low energy emission was assumed to be associated with synchrotron emission from the radio lobe. This assumption accurately described the sub-mm and infra-red observations, but as with the previous campaigns, it still didn't describe the radio observation. As before, an inhomogenous jet SSC model was also applied to the observed SED. With a reduced χ^2 of 284 for 17 degrees of freedom, the inhomogenous jet SSC model was found to be the least accurate of the three applied models. The fit parameters for the SSC modelling of the August/September 2004 campaign are summarized in Table 10.3.

Table 10.3: Parameters for the SED fit for the assumptions that the all emission regions are cospatial (Model 1), that the low energy part of the SED emanates from the radio lobe (Model 2 + Model $2_{\text{Low energy}}$) or assuming a fit to the synchrotron continuum only.

Parameter	Model 1	Model 2	Model $2_{\text{Low Energy}}$	Syn. fit
δ	20	22	2	30
$R_{blob}(10^{14}\text{m})$	1	1	100	0.7
B (G)	0.13	0.11	0.004	0.13
p_1	-2.0	-2.0	-1.3	-2.0
p_2	-3.0	-3.0	–	-3.0
$E_{density}$(ergs cm^{-3})	0.09	0.035	0.065	0.12
E_{min} (log(E_{max}/eV))	7.0	7.0	4.0	6.9
E_{break} (log(E_{break}/eV))	9.5	10.0	10.5	9.0
E_{max} (log(E_{max}/eV))	11.0	11.0	10.5	10.9
Reduced χ^2/d.o.f	3.64/17	1.03/13	0.167/3	4.21/17

The optical spectroscopic campaign of July and September 2005 consisted of 5 sets of spectroscopic observations with the New Technology Telescope at the ESO La Silla observatory. Apart from the telluric absorption lines, due to molecular absorption within the Earth's atmosphere, these spectroscopic observations detected a Na absorption feature believed to be from the host galaxy, as well as detecting evidence for Hα emission feature when the optical continuum was faintest. At its strongest, this feature was $\sim 2\sigma$ above the continuum level, allowing us to derive an upper limit of $F_{H\alpha} < 7.1 \times 10^{-15}$ ergs cm^{-2} s^{-1} and associated equivalent width of <0.58 Å. This flux limit equates to a luminosity limit of $L_{H\alpha} < 1.8 \times 10^{40}$ ergs s^{-1}, which is fully consistent with those calculated for other HBLs. Assuming that the Hα emission line is a good indication of the external photon field strength from the BLR, we can begin to constrain the external radiation field density, U_{rad}. As mentioned in Chapter 2, if $U_B < U_{rad}$ then an External Compton model is dominant over an SSC model. Unfortnately, due to the lack of simultaneous pointed X-ray observations, it is not possible to constrain U_B for September 2005.

10.2 General Conclusions

The importance of the studies completed here is that the source, PKS 2155−304, appeared to be in a quiescent state during the observations, which is implied by the flux values at X-ray and optical energies being close to historically low values. This has allowed us to, for the first time, probe the mechanics, through SED modelling and variability/opacity arguements, of the VHE emission regions of a quiescent HBL. Past studies of this nature have only been completed on HBLs that are in an active state, due to the sensitivity of past Cherenkov telescopes.

Considering each SED fit separately, we find that in each campaign, the SSC model describes the observed emission quite well, whether it be a single-zone model as in October/November 2003 and August/September 2004, or by a two-zone SSC model as with November 2004. Interestingly however, the correlation between flux levels at different energies that is implied by having a common origin, does not appear to be present in the October/November 2003 data set, while it is in August/September 2004. With the SSC model describing the overall emission fairly well during these campaigns, we can conclude that even though PKS 2155−304 is in a quiescent state throughout the observations, the 'active' state SSC model can still describe the observed emission to an accurate level.

Comparing the fit parameters between each of the 2003 and 2004 campaigns, we find that the best fit model parameters are characteristic of the global emission trends during the campaign. For example, for the October/November 2003 campaign, the best fitting SSC model has a Doppler factor of 32 and a radius of 2×10^{13} m. These values are consistent with the short, sharp flares exhibited during October/November 2003 being attributed to small, fast emission regions. Likewise, the best fitting SSC model for August/September 2004 has a Doppler factor of 20 and a radius of 10^{14} m. These values are consistent with the larger, longer flares exhibited during August/September 2004 being attributed to larger, slower emission regions compared to October/November 2003.

Comparing the SSC fit parameters for the 2003 and 2004 campaigns with

that of other HBLs, we find some interesting results. Similiar work by the H.E.S.S. collaboration done on another quiescent HBL, H 2356−309, describes the overall emission by SSC model parameters similiar to those of the X-ray/VHE fit for August/September 2004 albeit a smaller emission and slightly larger E_{min} and E_{max} [10]. However, a similiar study completed on an apparent *active* HBL, 1ES 1101-232, has SSC model parameters similiar to those of the October/November 2003 optical/X-ray/VHE fit, albeit a smaller magnetic field and slightly larger E_{min} and E_{max} [11]. Note that the apparent active state of this HBL is assumed from the historically high X-ray flux levels observed during this campaign. Finally, SSC modelling of another active HBL, 1ES 1959+650, by Krawczynski et al. showed that while the model parameters are somewhat different to those in Table 10.1, Table 10.2 and Table 10.3, a single-zone SSC model could still satisfactorily describe the observations [106].

It would therefore appear that, regardless of the state of the HBL, a single-zone SSC can describe the broadband SED to a satisfactory level. Indeed, the number of parameters of the single-zone SSC model allows for a large number of degrees of freedom. Thus, with an insufficient number of constraints the SSC model should be able to describe most SEDs to some level. The insufficient number of constraints can be addressed by further SSC studies of more HBLs in different activity states so that phenomenological studies can be undertaken. Also, as can be seen in Figure 10.3, extending the observations to MeV energies will allow us to produce a more complete SED and thus constrain the SSC fit futher.

10.3 The Future

With the continual success of the H.E.S.S. Phase I telescope array over the last 3 years, the future is definitely bright for VHE extra-galactic astronomy. A natural evolution of this success is to improve the performance of the current Phase I array. This can be done by increasing the sensitivity of the H.E.S.S. telescope array and lowering the energy threshold of the array. These improvements will allow us to not only detect fainter AGN, possibly detecting new types of extra-galactic VHE sources, but arguably more importantly, the

lower energy threshold will allow us to bridge the gap between the energy threshold of current ground based experiments and the GeV energy range of satellite instruments.

With the foundations being dug in early 2006, the next step in H.E.S.S. development has begun with the construction of H.E.S.S. Phase II. Seen in Fig. 10.1, H.E.S.S. Phase II consists of a single large dish at the centre of the current H.E.S.S. array. With a total mirror surface of 596 m^2, the energy threshold of Phase I, in stand alone mode, is 20 GeV.

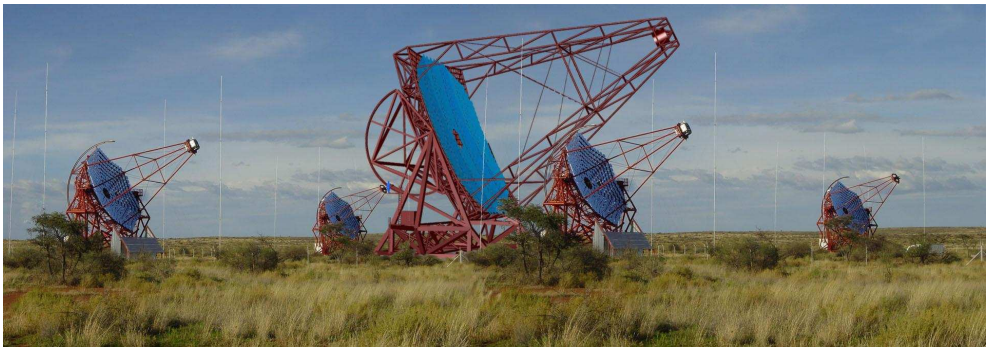

Figure 10.1: Picture of current Phase I array with a drawing of the proposed Phase II telescope at its intended location in the center of the H.E.S.S. array.

While H.E.S.S. Phase II will close the gap between the energy threshold of current ground based experiments and the GeV energy range of satellite instruments, the imminent launch of GLAST in 2007 will also close the gap by increasing the GeV range of satellite instruments; though it should be pointed out that there is currently no satellite which observes in the GeV energy range. The overdue successor to the EGRET satellite, the Large Area Telescope detector on GLAST will have a large field of view (> 2.5 steradians), with a sensitivity 50 times greater than EGRET at 100 MeV. As can be seen in Fig. 10.2, with the increase in performance characteristic, GLAST and H.E.S.S. Phase II will allow, for the first time, continuous observations from 10 MeV to 10s of TeV.

The ability to observe $\gamma-$rays 10 MeV to 10s TeV in energy will allow us to observe the whole of the IC continuum, giving us the ability to differentiate between the different models discussed in Chapter 2. For example, while it is

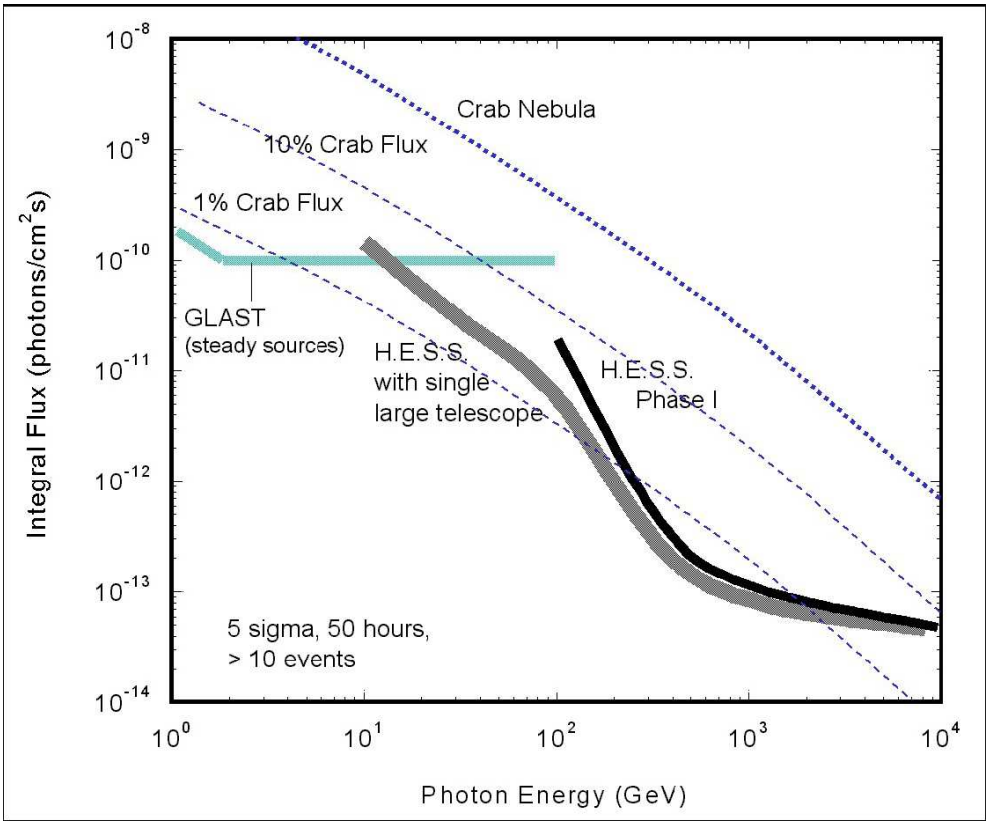

Figure 10.2: Minimum observable flux for a given energy threshold, for 50 hours of observations and a resulting significance of 5σ. The sensitivity of H.E.S.S. Phase I is shown, along with the predicted sensitivity for both H.E.S.S. Phase II and GLAST. There is clear overlap between H.E.S.S. Phase II and GLAST in the 10−100 GeV energy range.

difficult to differentiate between the single-zone and two-zone SSC model fits using VHE data alone, there is a marked different between the two at energies below VHE $\gamma-$rays (see Fig. 10.3).

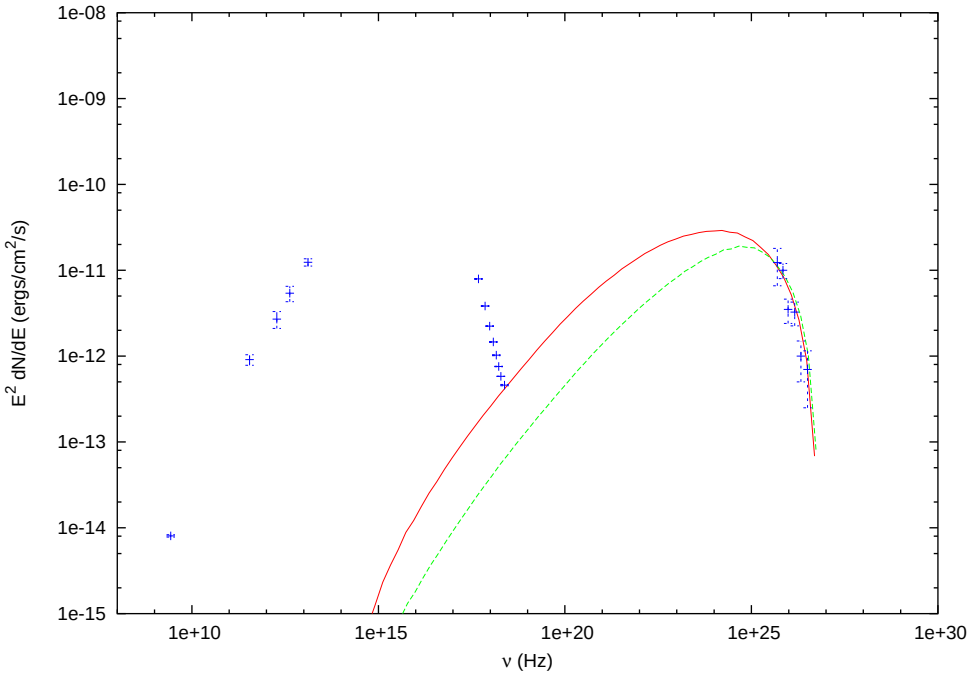

Figure 10.3: The different IC continua for the single-zone X-ray/VHE fit and two-zone fits for the November 2004 observations. The dashed continuum is the IC continuum for the single-zone X-ray/VHE fit, while the solid line is the IC continuum for the two-zone fit.

Future observations aside, the work presented in this thesis can be extended further through several avenues of research.

- *Modelling the observed SEDs from the 2003, August/September 2004 and November 2004 campaigns with a hadronic model.* Throughout this thesis, only variations of the leptonic SSC model have been applied. Considering hadronic models, or indeed other leptonic models such as the external compton model, will allow us to probe the dominant broadband emission mechanism further.

- *Consider a more intensive correlation analysis.* Calculating the Discrete Correlation Function (DCF) for the different campaigns will allow us to

look for time lags between flaring events in the different energy bands. Discrete Correlation Function are analogous to the classical correlation function, except that the DCF is able to work with unevenly sampled data. A DCF analysis was completed by Edelson et al. for a low energy multi-wavelength campaign on PKS 2155−304 during the early 1990's [66]. Applying a DCF analysis to the campaigns reported in this thesis will allow an even greater insight into possible emission mechanisms.

10.4 July/August 2006 flare

Towards the end of July 2006, H.E.S.S. observed an increase in VHE $\gamma-$ray (E>300 GeV) from PKS 2155−304 varying between 40−700% of the Crab flux. Reported in an astronomer's telegram, during the night of the 24/25th July, preliminary analyses of H.E.S.S. observations indicate a significance of 30 sigma/$\sqrt{h}$, or an average 89% of H.E.S.S. Crab flux above 200 GeV. On the night of 25/26th July PKS 2155−304 was observed with a significance of 25 sigma/$\sqrt{h}$ or an average of 62% Crab. On the night of 27/28th July the brightness of PKS 2155−304 was seen to decrease with a significance of 14 sigma/$\sqrt{h}$.

This high activity state triggered a large multi-wavelength campaign consisting of H.E.S.S., *Chandra*, *RXTE*, *Integral*, ROTSE, NRT and SALT observations. Optical spectroscopic observations were also taken as part of this campaign, thus allowing us to probe U_B versus U_{rad}. Preliminary H.E.S.S. results indicate an extremely active state not seen from PKS 2155−304 before. Coupled with the results of this thesis, the July/August 2006 flare will allow us to study the differences between an extremely active state HBL and an quiescent HBL.

Appendix A

Definition of Hillas Parameters

A.1 Definition of Hillas Parameters

The PMT positions are given coordinates x and y (in degrees), with the origin of the co-ordinate system at the centre of the field of view of the camera. The number of digital counts after calibration for tube i is given by n_i. An ellipse is fitted to the image and the first and second order Hillas parameters are calculated relative to the centre. The various moments are then defined as:

$$\langle x \rangle = \frac{\Sigma n_i x_i}{\Sigma n_i} \qquad \langle y \rangle = \frac{\Sigma n_i y_i}{\Sigma n_i}$$

$$\langle x^2 \rangle = \frac{\Sigma n_i x_i^2}{\Sigma n_i} \qquad \langle y^2 \rangle = \frac{\Sigma n_i y_i^2}{\Sigma n_i}$$

$$\langle xy \rangle = \frac{\Sigma n_i x_i y_i}{\Sigma n_i}$$

The spread of the image in different directions are then defined by the following moments:

$$\begin{aligned} \sigma_{x^2} &= \langle x^2 \rangle - \langle x \rangle^2 \\ \sigma_{y^2} &= \langle y^2 \rangle - \langle y \rangle^2 \\ \sigma_{xy} &= \langle xy \rangle - \langle x \rangle \langle y \rangle \end{aligned}$$

Given the following definitions:

$$\begin{aligned} d &= \sigma_{y^2} - \sigma_{x^2} \\ s &= \sqrt{d^2 + 4(\sigma_{xy})^2} \\ w &= \sqrt{(\langle y^2 \rangle - \langle x^2 \rangle)^2 4 \langle xy \rangle^2} \\ u &= 1 + \frac{d}{s} \\ v &= 2 - u \end{aligned}$$

the Hillas parameters are calculated from:

$$\begin{aligned} Size &= \Sigma n_i \\ Length &= \sqrt{\frac{\sigma_{x^2} + \sigma_{y^2} + s}{2}} \\ Width &= \sqrt{\frac{\sigma_{x^2} + \sigma_{y^2} - s}{2}} \\ Miss &= \sqrt{\frac{1}{3}(u\langle x \rangle^2 + v\langle y \rangle^2) - \left(\frac{2\sigma_{xy}\langle x \rangle \langle y \rangle}{s}\right)} \\ Distance &= \sqrt{\langle x \rangle^2 + \langle y \rangle^2} \\ Alpha &= \sin^{-1}\left(\frac{Miss}{Distance}\right) \\ Azwidth &= \sqrt{\frac{\langle x \rangle^2 \langle y \rangle^2 - 2\langle x \rangle \langle y \rangle \langle xy \rangle + \langle x^2 \rangle \langle y^2 \rangle}{(Distance)^2}} \end{aligned}$$

where, as represented in Fig(A.1),

Size is the total integrated light content of the shower,

Length is the RMS light spread along the major axis of the image,

Width is the RMS light spread across the minor axis of the image,

Miss is the orthogonal distance of the the major axis of the ellipse from the centre of the field of view,

Distance is the distance of the centroid of the image to the centre of the field of view,

Alpha is the angle between the major axis of the image and the line drawn between the centroid of the image and the centre of the field of view,

Azwidth is the RMS spread of light perpendicular to the line drawn between the centroid of the image and the centre of the field of view.

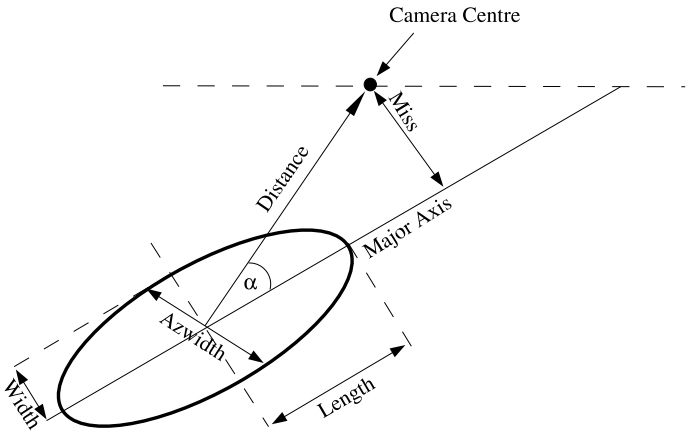

Figure A.1: Graphical representaion of Hillas parameter definitions as seen in Figure 3.10.

Bibliography

[1] Aharonian, F.A. 2000, New Astronomy, 377

[2] Aharonian, F.A., et al. 2002, A&A, 393, 89

[3] Aharonian, F.A., et al. (H.E.S.S. Collaboration) 2004, Astroparticle Physics, 22, 109

[4] Aharonian, F.A., et al. (H.E.S.S. Collaboration) 2005a, A&A, 430, 865

[5] Aharonian, F.A., et al. (H.E.S.S. Collaboration) 2005b, A&A, 442, 895

[6] Aharonian, F.A., et al. (H.E.S.S. Collaboration) 2005c, A&A, 437, 95

[7] Aharonian, F.A., et al. (H.E.S.S. Collaboration) 2006a, in preparation

[8] Aharonian, F.A., et al. (H.E.S.S. Collaboration) 2006b, accepted by Nature

[9] Aharonian, F.A., et al. (H.E.S.S. Collaboration) 2006c, submitted to A&A

[10] Aharonian, F.A., et al. (H.E.S.S. Collaboration) 2006d, A&A, 455, 461

[11] Aharonian, F.A., et al. (H.E.S.S. Collaboration) 2006e,in preparation

[12] Akerlof, C.W., et al. 2000, ApJ, 542, 251

[13] Akerlof, C.W., et al. 2003, PASP, 115, 132

[14] Aye, K.-M., et al. 2001, ICRC Conf. Proc. 7, 2676

[15] Aye, K.-M., et al. 2005, AIP Conf. Proc. 745, 724

[16] Baldwin, J.A. 1997, ASP Conf. Ser., 113, 80

[17] Baring, M. G 1997, arXiv:astro-ph/9711177, v1

[18] Beall, J.H., & Bednarek, W. 1999, ApJ, 510, 188

[19] Bednarek, W. 1993, ApJ, 402, L29

[20] Bednarek, W., & Protheroe, R.J. 1997, MNRAS, 287, L9

[21] Bernlöhr, K. et al. 2003, Astroparticle Physics, 20, 111

[22] Bertone, E. et al. 2000, A&A, 356, 1

[23] Blandford, R.D. et al. 1974, MNRAS, 169, 395

[24] Blandford, R.D. 1976, MNRAS, 176, 465

[25] Blandford, R. D. & Znajek, R. L., 1977, MNRAS, 179, 433

[26] Blandford, R. D. & Payne, D. G., 1982, MNRAS, 199, 883

[27] Bolton, J.G. et al. 1964, Australia Journal of Physics, 17, 340

[28] Bottcher, M., & Schlickeiser, R. 1995, A&A, 302, L17

[72] Bottcher, M., & Dermer, C.D., 2002, ApJ, 564, 86

[30] Bowyer, S., Brodie, J., Clarke J. & Henry J.P 1984, ApJ, 278, 103

[31] Brinkmann, W., et al. 1994, A&A, 288, 433

[32] Brinkmann, W., et al. 2000, A&A, 362, 105

[33] Brinkmann, W., et al. 2003, A&A, 402, 929

[34] Brown, A.M., et al. 2006, submitted to A&A

[35] Brown, A.M., et al. 2005a, Proc. of the 29^{th} ICRC (Pune), 4, 403

[36] Brown, A.M., et al. 2005b, Proc. of the 29^{th} ICRC (Pune), 4, 411

[37] Brown, A.M., et al. 2005c, Proc. of the 29^{th} ICRC (Pune), 5, 403

[38] Burbidge, G.R. 1956, ApJ, 124, 416

[39] Canizares, C.R., & Kruper, J. 1984, ApJ, 278, L99

[40] Caproni, A & Abraham, Z. 2000, MNRAS, 349, 1218

[41] Carini, M. & Miller, H. 1992, ApJ, 385, 146

[42] Chadwick, P.M., et al. 1987, VHE Conf. Proc. 199, 115

[43] Chadwick, P.M., et al. 1999, ApJ, 513, 161

[44] Chadwick, P.M., et al. 1999, Astroparticle Physics, 11, 145

[45] Chadwick, P.M., et al. 2000, AIP Conf. Proc. 515, 393

[46] Chang, K. & Refsdal, S. 1979, Nature, 282, 561

[47] Chiaberge, M., et al. 2000, A&A, 358, 104

[48] Chiappetti, L. & Torroni, V. 1997, IAU Cirular, 6776

[49] Chiappetti, L., et al. 1999, ApJ, 521, 552

[50] Cooke, B.A., et al. 1978, MNRAS, 189, 489

[51] Corbett, E.A., et al. 1996, MNRAS, 281, 737

[52] Corbett, E.A., et al. 2000, MNRAS, 311, 485

[53] Cornils, R., et al. 2003, Astroparticle Physics, 20, 129

[54] Costamante, L. & Ghisellini, G. 2002. A&A, 384, 56

[55] Courvoiser, T.J-L., et al. 1995, ApJ, 438, 108

[56] Cui, W., et al., AIP Conf. Proc. (arXiv:astro-ph/0410160)

[57] Dar, A., & Laor, A. 1997, ApJ, 478, L5

[58] Davies, J. & Cotton, E. 1957, Journal of Solar Energy, 1, 16

[59] Dermer, C.D., et al. 1992, A&A, 256, L27

[60] Dermer, C.D., & Schlickeiser, R. 1993, ApJ, 416, 458

[61] Dermer, C.D., et al. 1997, ApJS, 109, 103

[62] Djannati-Atai, A., et al. 1999, A&A, 350, 17

[63] Dominici, T.P., et al. 2004, ApJ, 128, 47

[64] Dondi, L., & Ghisellini, G. 1995, MNRAS, 273, 583

[65] Dultzin-Hacyan, D., et al. 2000, Rev. Mex. AA 9 308

[66] Edelson,R., et al. 1995, ApJ, 438, 120

[67] Ekers, J.A. 1969, Australia Journal of Physics, 7, 3

[68] Falomo, R., et al. 1993, ApJ, 106, 11

[69] Felten, J.E. 1968, ApJ, 1551,861

[70] Fermi, E. 1949, Phys. Rev., 75, 1169

[71] Fossati, G., et al. 1998, Nucl. Phys. B, 69, 423

[72] Fossati, G. 1999, ASP Conf. Ser. Vol 159, 351

[73] Funk, S., et al. 2004, Astroparticle Physics, 22, 285

[74] Frank, I. & Tamm, I. 1937, Dokl, Akad, Nauk. 14, 109

[75] Gaidos, J.A., et al. 1996, Nature, 383, 319

[76] Galbraith, W. & Jelley, J.V. 1953, Nature, 171, 349

[77] Georganopoulos, M. & Marscher, A. 1998, ApJ, 506, L11

[78] Ghisellini, G., et al. 1985, A&A, 146, 204

[79] Ghisellini, G., & Maraschi, L. 1989, ApJ, 340, 181

[80] Ghisellini, G., & Madau, P. 1996, MNRAS, 280, 67

[81] Geibels, B., et al. 2002, ApJ, 571, 763

[82] Gilmore, D. M.& Urry, C. M. 1994, AIPC, 313, 429

[83] Ginzburg, V.L., & Syrovatskii, S.I. 1969, ARA&A, 7, 375

[84] Giommi, P., et al. 1998, A&A, 333, L5

[85] Goeckel, H. 1910, Phys. Zeits., 11, 280

[86] Gower, J.F.R. 1966, MNRAS, 133, 151

[87] Grazian, A., et al. 2000, ApJ, 119, 2540

[88] Griffiths, R.R., et al. 1979, ApJ, 234, 810

[89] Hamuy, M., & Maza, J. 1987, A&AS, 68, 383

[90] Hanna, D.S., et al. 2002, Nucl. Inst. & Methods, A491, 126

[91] Haswell, C.A., et al. 1992, ApJ, 401, 495

[92] Heidt, J., Wagner, S. J., & Wilhein-Erkes, U. 1997, A&A, 325, 27

[93] Hess, V. 1911, Phys. Zeits., 12, 998

[94] Hillas, A. 1995, Proc. of the 19^{th} ICRC (La Jolla), 3, 445

[95] Holland, W.S. et al. 1999, MNRAS, 303, 659

[96] $http://www.gsfc.nasa.gov/gsfc/service/gallery/factsheets/general/40th.pdf$ (last accessed 11/11/2004)

[97] $http://imagine.gsfc.nasa.gov/docs/science/how_l2/proportional.html$ (last accessed 11/11/2004)

[98] Impey, C.C., & Neugebauer, G. 1988, AJ, 95, 307

[99] Jahoda, K. et al. 1996, Proc. SPIE, 2808, 59

[100] Jelley, J.V. 1966, Nature, 211, 472

[101] Jones, T.W., et al. 1974, ApJ, 188, 353

[102] Kataoka, J., et al. 2000, ApJ, 528, 243

[103] Kino, M., et al. 2002, ApJ, 564, 97

[104] Konigl, A. 1981, ApJ, 446, 598

[105] Krawczynski, H., et al. 2002, MNRAS, 336, 721

[106] Krawczynski, H., et al. 2004, ApJ, 601, 151

[107] Krolik, H.J. & Kallman, T.R. 1998, ApJ, 324, 714

[108] Laing, R.A., et al. 2006, arXiv:astro-ph/0601328

[109] Latham, I.J. 2005, PhD Thesis, University of Durham, VHE $\gamma-$rays from Microquasars

[110] Lesch, H., & Pohl, M. 1992, A&A, 254, 29

[111] Long, R.J. & Stewart, P. 1967, MNRAS, 135, 361

[112] Longair, M.S. 1992, High Energy Astrophysics Volume 1: Particles, photons and their detection. Second Edition, Cambridge University Press

[113] Longair, M.S. 1992, High Energy Astrophysics Volume 2: Stars, the Galaxy and the interstellar medium. Second Edition, Cambridge University Press

[114] Lovelace, R.V.E. 1976, Nature, 262, 649

[115] MacDonald, G.H., et al. 1968, MNRAS, 138, 259

[116] Mannheim, K. & Biermann, P.L. 1992, A&A, 253, L21

[117] Mannheim, K. 1993, A&A, 269, 67

[118] Marscher, A. 1977, ApJ, 216, 244

[119] Marscher, A., & Gear, W. 1985, ApJ, 298, 114

[120] Marshall, M.L., et al. 2001, ApJ, 549, 938

[121] Mattox, J.R., et al. 1993, ApJ, 410, 609

[122] McEnery, J.E. 1997, PhD Thesis, University College Dublin, TeV gamma-ray variability of the BL Lacertae object Markarian 421

[123] Miller, H.R, & McAlister, H.A. 1983, ApJ, 272, 26

[124] Mori, K., et al. 1998, ApJ, 493, 175

[125] Morini, M., et al. 1986, ApJ, 307, 486

[126] Morrison, P., et al. 1984, ApJ, 280, 483

[127] Mueke, A., et al. 2003, Astroparticle Physics, 18, 593

[128] Mushotzky, R. 2004, astro-ph/0405144

[129] Nakase, T. et al. 2003, Proc. of the 28^{th} ICRC (Tsukuba), 2811

[130] Nellen, L., et al. 1993, Phys. Rev. D., 47, 5270

[131] Nicastro, F., et al. 2002, ApJ, 573, 157

[132] Nishijima, K. et al. 2001, Proc. of the 27^{th} ICRC (Hamburg), 2626

[133] Paltini, S., Courvvoiser, T. J.-L., Blecha, A. & Bratschi, P. 1997, A&A, 327, 539

[134] Perlman, E.S., et al. 2003, AAS, 2031 4605P

[135] Pesce, J.E., et al. 1997, ApJ, 486, 770

[136] Peir, E.A., & Krolick, J.H. 1992, ApJ, 401, 99

[137] Peir, E.A., & Krolick, J.H. 1993, ApJ, 418, 673

[138] Pian, E, et al. 1997, ApJ, 486, 784

[139] Pian, E, et al. 1998, ApJ, 492, L17

[140] Piner, B.G. & Edwards, P.G. 2004, ApJ, 600, 115

[141] Pohl, M., & Schlickeiser, R. 2000, A&A, 354, 395

[142] *Private Communication* Guilluame Dubus (H.E.S.S. Collaboration)

[143] Romanova, M.M., & Lovelace, R.V.E. 1992, A&A, 262, 26

[144] Pounds, K., et al. 1975, MNRAS, 1972, 473

[145] Price, R.M. & Milne, D.K. 1965, Australia Journal of Physics, 18 329

[146] Proga, D., et al. 2000, ApJ, 543, 686

[147] Proga, D., & Kallman, T.R. 2004, ApJ, 324, 714

[148] Punch, M., et al. 1992, Nature, 358, 477

[149] Quinn, J., et al. 1996, ApJ, 456, L83

[150] Ravasio, M., et al. 2004, A&A, 424, 841

[151] Reimer, A., et al. 2004, A&A, 419, 89

[152] Resvanis, L. et al. 1987, VHE Conf. Proc. 199, 105

[153] Roberts, M. D. et. al. 1999, A&A, 343, 691

[154] Robson, E.I., et al. 2001, MNRAS, 327, 751

[155] Rothschild, R.E., et al. 1998, ApJ, 496, 538

[156] Rowell, G., et al. 2005, arXiv:astro-ph/0512523

[157] Rybicki, G.B., & Lightman, A.P. 1979, Radiative Process in Astrophysics, 1st Edition, Wiley-Interscience

[158] Salpeter, E.E. 1964, ApJ, 140, 796

[159] Sandage, A. et al. 1965, ApJ, 142, 1307

[160] Sbarufatti, B. et al. 2006, arXiv:astro-ph/0605448

[161] Schmidt, M. 1963, Nature, 197, 1040

[162] Schmidt, M. & Green, R.F.L. 1983, ApJ, 269, 352

[163] Schopper, R., et al. 1998, A&A, 335, 26

[164] Schroedter, M. 2005, arXiv:astro-ph/0504397

[165] Schwartz, D. A., et. al. 1979, ApJ, 229, L53

[166] Schwartz, D. A. 2002, ApJ, 569, L23

[167] Sembay, S., et al. 1993, ApJ, 404, 112

[168] Sikora, M., et al. 1987, ApJ, 320, L81

[169] Sikora, M., et al. 1994, ApJ, 421, 153

[170] Sikora, M. 1997, ApJ, 484, 108

[171] Sikora, M., et al. 2005, arXiv:astro-ph/0509685

[172] Sikto, M., & Junkkarinen, V.T. 1985, PASP, 97, 1158

[173] Smith, P.S., et al. 1992, ApJ, 400, 115

[174] Sokolov, A., & Marscher, A. 2005, ApJ, 629, 52

[175] Stecker, F.W., & de Jager, O.C. 1997, ApJ, 476, 712

[176] Sulentic, J.W., et al. 2000, Annu. Rev. Astron. Astrophysics, 38, 521

[177] Swanenburg, B.N., et al. 1978, Nature, 275, 298

[178] Takahashi, T., et al. 1996, ApJ, 470, L89

[179] Tanihata, C. et al. 2001, ApJ, 563, 569

[180] Tavecchio, F., et al. 1998, ApJ, 509, 608

[181] Treves, A., et al. 1989, ApJ,341,733

[182] Treves, A., et al. 2006, arXiv:astro-ph/0601506

[183] Tsvetanov, Z.I., et al. 1998, ApJ, 493, 83

[184] Ulrich, M.-H. 1981, A&A, 103, L1

[185] Urry, C.M., et al. 1986, ApJ, 305, 369

[186] Urry, C.M., et al. 1993, ApJ, 411, 614

[187] Urry, C.M. & Padovani, P. 1995, PASP, 107, 803

[188] Urry, C.M., et al. 1997, ApJ, 486, 799

[189] Vermeulen, R.C., et al. 1995, ApJ, 452, L5

[190] Vestrand, W.T., et al. 1995, ApJ, 454, L93

[191] Vestrand, W.T. & Sreekumar, P. 1999, Astroparticle Physics, 11, 197

[192] Wagner, S.J., & Witzel, A. 1995 ARA&A, 33, 163

[193] Wandel, A. & Urry, C.M. 1991, ApJ, 367, 78

[194] Weekes, T.C. 1989, ApJ, 342, 379

[195] White, R.L., et al. 2000, ApJS, 126, 133

[196] Xhang, Y.H., & Xi, G.Z. 1996, A&AS, 116, 289

[197] Zhang, Y.H., et al. 2002, ApJ, 572, 762

[198] Zhang, Y.H., et al. 2006, arXiv:astro-ph/0607138

[199] Zeldolvich, Ya.B., & Novikov, I.D. 1964, Sov. Phys. Dokl., 158, 811